Titre: Title:	Optimisation of snow management practices on tailings storage facilities to reduce spring freshet intensity and geoenvironmental risks
Auteur: Author:	Mohammad Mahdi Karamouzian
Date:	2025
Type:	Mémoire ou thèse / Dissertation or Thesis
Référence: Citation:	Karamouzian, M. M. (2025). Optimisation of snow management practices on tailings storage facilities to reduce spring freshet intensity and geoenvironmental risks [Mémoire de maîtrise, Polytechnique Montréal]. PolyPublie. https://publications.polymtl.ca/61979/

URL de PolyPublie: PolyPublie URL:	https://publications.polymtl.ca/61979/
Directeurs de recherche: Advisors:	Vincent Boulanger-Martel, & Jean Côté
Programme: Program:	Génie minéral

POLYTECHNIQUE MONTRÉAL

affiliée à l'Université de Montréal

et

l'Université du Québec en Abitibi-Témiscamingue

Optimisation of snow management practices on tailings storage facilities to reduce spring freshet intensity and geoenvironmental risks

MOHAMMAD MAHDI KARAMOUZIAN

Département des génies civil, géologique et des mines

Mémoire présenté en vue de l'obtention du diplôme de Maîtrise ès sciences appliquées

Génie mineral

Décembre 2024

POLYTECHNIQUE MONTRÉAL

affiliée à l'Université de Montréal

et

l'Université du Québec en Abitibi-Témiscamingue

Ce mémoire intitulé:

Optimisation of snow management practices on tailings storage facilities to reduce spring freshet intensity and geotechnical risks

présenté par **Mohammad Mahdi KARAMOUZIAN**

en vue de l'obtention du diplôme de Maîtrise ès sciences appliquées

a été dûment accepté par le jury d'examen constitué de:

Li LI, président

Vincent BOULANGER-MARTEL, membre et directeur de recherche

Jean CÔTÉ, membre et co-directeur

Daniel NADEAU, membre

DEDICATION

My dearest, your unwavering love and support have been my rock throughout this academic journey. This achievement is as much yours as it is mine.

ACKNOWLEDGEMENTS

I wish to extend my heartfelt gratitude to everyone who contributed to the completion of my master's thesis. This project stands as a significant personal and professional milestone for me, and I am deeply thankful to all who supported me throughout this journey.

I would like to extend my deepest gratitude to my research director, Vincent Boulanger-Martel, for his exceptional supervision and invaluable guidance throughout this work. His vision, expertise, and wise counsel have greatly enriched my research experience and significantly contributed to the quality of this dissertation. I am also profoundly grateful to my co-director, Jean Côté, whose expertise, and advice have been immensely helpful.

I would like to extend my heartfelt gratitude to all my professors and the URSTM staff, with special thanks to Sylvette Awoh, Jean Christophe, and Pierre Alain. Their invaluable contributions, relevant advice, and constructive suggestions were instrumental in refining my ideas and enhancing the coherence of my work.

I am also deeply grateful to the UQAT-Polytechnique Montréal Institute for Research in Mines and Environment and the CRSNG-UQAT Industrial Research Chair on the Restoration of Mining Sites for their generous financial support.

I am also deeply thankful to my colleagues and friends for their unwavering support and the stimulating, enriching discussions we shared. Their moral support, innovative ideas, and constant encouragement have been invaluable to me throughout this journey.

I am profoundly grateful to my family and loved ones for their unwavering support, love, and understanding during this challenging period. Their presence and constant encouragement provided me with the strength and determination needed to complete this project.

I extend my heartfelt thanks to the Agnico-Eagle Mines mine staff for their invaluable assistance in constructing and monitoring the snow management piles. Their support and collaboration were crucial throughout this process. I would also like to thank Bernard Swarbrick and Mike Heino Jr from Mine Tailing Solutions for their exceptional contribution, notably with respect to snow grooming.

RÉSUMÉ

La gestion de l'eau est un défi important pour l'industrie minière et plus particulièrement au printemps lors de la fonte de la neige. Une quantité importante de l'inventaire annuel de l'eau peut être stocké sous forme de neige à la surface des parcs à résidus miniers. Ceci fait qu'u dégel, une quantité d'eau important est libérée sur une période relativement courte, appelée crue printanière. La durée et l'intensité de la crue peut varier d'une année à l'autre, mais entraîne des défis importants en gestion de l'eau sur les parcs à résidus. La grande quantité d'eau à gérer fait que les infrastructures de gestion et de traitements des eaux ainsi que les ouvrages de retenue des résidus miniers sont sollicitées à pleine capacité durant cette période. Dans un contexte de changements climatiques où il y a une augmentation dans la variabilité et les extrêmes de plusieurs variables du cycle de l'eau, les crues printanières représentent un risque grandissant sur la stabilité des infrastructures de gestion de l'eau et des rejets miniers. Cette étude explore l'utilisation de piles de gestion de la neige comme solution pour contrôler l'intensité et les taux de fonte de la neige lors de la crue printanière. Ces piles sont conçues pour contrôler le taux de fonte et ainsi réduire les débits de pointe des eaux de fonte. En gérant le moment et le volume d'eau entrant dans les installations de stockage des résidus, les piles de gestion de la neige peuvent aider à maintenir l'intégrité des infrstructures ges gestion des rejets minier et à atténuer les risques géotechniques et environnementaux qui y sont associés

L'objectif principal de cette recherche est d'évaluer l'efficacité des piles de gestion de la neige à contrôler la fonte de la neige sur les parcs à résidus miniers. Plus précisément, l'étude vise à évaluer comment les piles de gestion de la neige peuvent contrôler les taux de fonte de la neige, réduire les pics de débit de fonte et prolonger le temps de fonte. Pour ce faire, six piles de gestion de la neige ont été construites à l'échelle pilote sur deux sites miniers sur une période de deux ans. Les méthodes utilisées ont évaluer la capacité d'équipements civils conventionnels et d'équipement spécialisés à construire des piles de gestion de la neige de manière optimale. Les piles de gestion de la neige ont été conçues avec des profils cubiques, coniques et en crête. La fonte des piles de gestion de la neige a été suivie par des mesured de changements de volume, hauteur et d'empreinte à l'aide de

techniques de photogrammétrie et de relevés LiDAR. Des mesures de densité de la neige ont également été obtenues par échantillonnage de carottes de neige à différents intervalles.

Les résultats ont indiqué que les piles de gestion de la neige permettent d'augmenter la durée de la fonte de la neige en prolongeant le processus d'environ quatre à six semaines. Le volume et la hauteur des piles de gestion de la neige se sont révélés être des facteurs critiques influençant leur capacité à réguler la fonte des neiges.

Un modèle numérique simplifié décrivant la fonte des piles de gestion de la neige a été développé. Les résultats ont montré que la prédiction du comportement en fonte avait une erreur moyenne de 6,75 % par rapport aux mesures de terrain, tandis l'erreur de la prédiction de la durée totale de la période de fonte des piles de gestion de la neige était inférieur à 4 %. Sur la base de ces résultats de modélisation, des graphiques de prédiction de la fonte des piles de gestion de la neige ont été développés, prenant en compte les dimensions, la forme et le coût de construction des piles de neige. Des équations décrivant la performance anticipée de piles de gestion de la neige en fonction de la hauteur ou du volume des piles de gestion de la neige ont été développées basées sur les résultats de 35 configurations de piles modélisées. Il a été constaté que les piles de gestion de la neige en forme de cône sont très sensibles aux changements de température, tandis que les piles de gestion de la neige en forme de crête sont moins sensibles et présentent des performances plus stables sous différentes sollicitations climatiques. Ces graphiques pourraient être utilisés pour concevoir des piles de gestion de la neige et réduire les risques géotechniques des parcs à résidus miniers durant la fonte printanière.

L'étude a conclu que les piles de gestion de la neige peuvent aider à atténuer les risques environnementaux et géotechniques associés à la fonte rapide des neiges, réduisant potentiellement le besoin d'installations de stockage et de traitement supplémentaires lors d'événements extrêmes. Cela est particulièrement important dans le contexte des changements climatiques, où la prévision des futurs schémas météorologiques devient de plus en plus difficile. En abordant ces aspects, l'étude améliore la compréhension des dynamiques de fonte des neiges et fournit des solutions pratiques pour améliorer la résilience des infrastructures minières dans un contexte des changements climatiques.

ABSTRACT

Water management is among the mains challenges facing the mining industry, particularly in the spring when the snow melts. A significant amount of the annual water inventory can be stored as snow on the surface of tailings storage facilities. As a result, a significant part of the water balance is released over a relatively short period, known as spring freshet. The duration and intensity of spring freshet can vary from year to year, but typically represent significant water management challenges for tailings storage facilities. The large quantity of water to be managed means that water management and treatment infrastructures, as well as tailings storage facilities, are highly sollicitated during this period. In a context of climate change, where variability and extremes of most water balance variables are on the rise, springrunoff represent a growing risk to the stability of water management and tailings storage facilities. This study explores the use of snow management piles as a solution for controlling snowmelt intensity and rates during spring freshet. Snow management piles are designed to control meltwater release rates and thus reduce peak meltwater flows and prolong runoff. By managing the timing and volume of water to be managed on tailings storage facilities, snow management piles can help maintain the integrity of mine waste management infrastructures and mitigate associated geotechnical and environmental risks.

The primary objective of this research was to evaluate the effectiveness of snow management piles in controling spring runoff on tailings storage facilities. Specifically, the study aims to assess how snow management piles can control snowmelt rates, reduce peak meltwater flows, and extend spring runoff. To achieve this, six pilot-scale snow management piles were constructed at mine sites over a two-year period. The ability of conventional civil equipment as well as specialized equipment to construct snow management piles was also investigated. The snow management piles wer designed with cubic, conical, and ridge-shaped configurations. Snow melt was monitored for changes in volume, height, and footprint using LiDAR and Structure-from-Motion (SfM) photogrammetry techniques. Snow density measurements were also obtained through core sampling at different intervals.

The results indicated that snow management piles effectively increased the duration of snowmelt, prolonging the process by approximately four to six weeks. The volume and

height of snow management piles emerged as critical factors influencing their ability to regulate snowmelt. Simplified phase change numerical modeling was done to represent field observations. The results showed that the prediction of the snowmelt process had an average error of 6.75% with respect to in situ results, while the error for predicting the entire length of the snow melting period was less than 4%. Based on these modeling results, snowmelt prediction charts were developed, considering the dimensions, shape, and cost of snow pile construction. Equations were developed to predict the melting behaviour of snow management piles configurations based on air temperature. To do so, the snowmelt of 35 piles configurations was modeled. It was found that cone-shaped snow management piles are highly sensitive to temperature changes, while ridge-shaped snow management piles are less sensitive and exhibit consistent performance across different temperature settings. This study concludes that snow management piles can help mitigate environmental and geotechnical risks associated with rapid snowmelts. This is particularly important in the context of climate change, where predicting future weather patterns is becoming increasingly challenging. By addressing these aspects, the study enhances the understanding of snow melting dynamics and provides practical solutions for improving the resilience of mine storage structures in the context of climate change.

TABLE OF CONTENTS

LIST OF TABLES

LIST OF FIGURES

LIST OF ACRONYMS AND ABBREVIATIONS

$(\rho_f C_{pf})_{eff}$	Effective Volumetric Heat Capacity at Constant Pressure [J m^{-3} K^{-1}]
Ø	Volumetric Liquid Water Content in Snow [m^3 m^{-3}]
a_r	Adjusted Degree-Day Factor [cm ∘ C^{-1} day^{-1}]
C_a	Specific Heat of Air at Constant Pressure [J kg^{-1} K^{-1}]
C_i	Specific Heat Capacity of Ice [J kg^{-1} K^{-1}]
COE	Army Corps of Engineers
$C_{p,f}$	Fluid Heat Capacity at Constant Pressure [J kg^{-1} K^{-1}]
$C_{p,solid}$	Solid Heat Capacity at Constant Pressure [J kg^{-1} K^{-1}]
CRSNG	Conseil de Recherches en Sciences Naturelles et en Génie du Canada
C_s	Specific Heat Capacity of Snow [J kg^{-1} K^{-1}]
D	Melting Duration [Day]
d	Average Particle Diameter [m]
D_0	Coefficient of Water Vapor Diffusion in Air [m^2 s^{-1}]
Da	Darcy Number
DD	Degree-Day [°C day]
DDF	Degree-Day Factor for Snowmelt [cm $°C^{-1}$ day^{-1}]
DEM	Digital Elevation Model
DF	Decomposing and Fragmented Precipitation Particles
DH	Depth Hoar
DHSVM	Distributed Hydrology Soil Vegetation Model
DWHC	Distributed Water-Heat Coupling Model
e_a	Saturation Vapor Pressure [Pa]
E_i	Poisson's ration

FC	Faceted Crystals
FT	Net Turbulent Flux [W m^{-2}]
g	Acceleration of Gravity [m s^{-2}]
G	Incoming or Global Shortwave Radiation [W m^{-2}]
GBHM	Geomorphology-Based Hydrological Model
G_{con}	Conductive Energy Flux [W m^{-2}]
G_h	Ground Heat Flux [W m^{-2}]
GIS	Geographic Information Systems
GPR	Gaussian Process Regression
H	Snow Management Pile Height [m]
H_i	Ice Thickness [m]
H_t	Layer Thickness [m]
H_s	Snow Thickness or Snow Depth [m]
H_{sen}	Sensible Energy Flux [W m^{-2}]
h_{sf}	Interstitial Heat Transfer Coefficient between Solid and Fluid Phases [J m^{-2} K^{-1}]
HSPF	Hydrological Simulation Program – HFORTAN
ICSSG	The International Classification for Seasonal Snow on the Ground
IDE	Integrated Development Environment
IDS	Integrated Drainage Systems
IF	Ice Formations
IR	Infrared Reflectance
K	Permeability [m^2]
K_a	Coefficient of Air Permeability [m s^{-1}]

K_h	Coefficient of Eddy Conductivity [$m^2\ s^{-1}$]
K_m	Vertical Transfer of Momentum [$m^2\ s^{-1}$]
K_v	Coefficient of Volumetric Expansion
L	Latent Energy Flux [$W\ m^{-2}$]
Lidar	Light Detection and Ranging
L_s	Latent Heat of Sublimation [$J\ m^{-2}$]
LSTM	Long Short-Term Memory
LTE	Local Thermal Equilibrium
LTNE	Local Thermal Nonequilibrium
M	Snow Ablation Quantity [$cm\ day^{-1}$]
M_{adv}	Advective Energy Flux [$W\ m^{-2}$]
MF	Melt Forms
MLP	Multilayer Perceptron Neural Network
MM	Machine Made Snow
M_{mel}	Quantity of Melted Snow [$cm\ day^{-1}$]
m_Q	Depth-Specific Energy-to-Water Conversion Constant [$cm\ m^2\ J^{-1}\ day^{-1}$]
n	Porosity
NARX	Nonlinear Autoregressive Exogenous
n_i	Ice Porosity
n_s	Snow Porosity
n_{solid}	Solid Porosity
Θ_a	Air Volume Fraction [-]
Θ_f	Fluid Volume Fraction [-]
Θ_i	Ice Volume Fraction [-]

Θ_P	Volume Fraction of Solid Material in Porous Media [-]
Θ_s	Snow Volume Fraction [-]
Θ_{solid}	Solid Volume Fraction [-]
Θ_w	Water Volume Fraction [-]
OGS	Optical-equivalent Grain Size
Pa	Atmospheric Pressure [Pa]
PBSM	Prairie Blowing Snow Model
PP	Precipitation Particles
Pr	Prandtl Number
PRMS	Precipitation Runoff Modelling System
Q	Complete Runoff Quantity
q	Conductive Heat Flux [W m^{-2}]
Q_{cc}	Amount of Energy Necessary to Raise the Temperature of Snow to its Melting Point
q_f	Fluid Conductive Heat Flux [W m^{-2}]
Q_f	Solid Heat Source [W m^{-2}]
Q_G	Heat Flux from the Soil [W m^{-2}]
Q_I	Change in Heat Storage of Snowdrifts [W m^{-2}]
Q_{Lin}	Incoming Longwave Radiation [W m^{-2}]
Q_{Lout}	Outgoing Longwave Radiation [W m^{-2}]
Q_m	Amount of Energy Accessible for Snow Melting [W m^{-2}]
Q_n	Net All-Wave Radiation at the Surface [W m^{-2}]
Q_{NR}	Net Radiant Flux [W m^{-2}]
Q_P	Heat Transferred into the Snow Pile by Rainfall [W m^{-2}]

Q_{Sin}	Incoming Shortwave Radiation [J m^{-2}]
Q_{solid}	Fluid Heat Source [W m^{-2}]
q_{solid}	Solid Conductive Heat Flux [W m^{-2}]
Q_{Sout}	Reflected Shortwave Radiation [W m^{-2}]
r	Dry Adiabatic Lapse Rate [K km^{-1}]
r_o	Grain Size
Ra	Rayleigh Number
R_{ep}	Particle Reynolds Number
RG	Rounded Grains
r_h	hydraulic radius [m]
r_H	Resistance to Heat Flux [s m^{-1}]
r_{opt}	Effective Radius [μm]
ROS	Rain-on-Snow
SAC	Sacramento Model
SCA	Snow-Covered Area
SEM	Scanning Electron Microscopy
SFM	Structure from Motion
Sg	Conducted Heat from Underlying Ground
SH	Surface Hoar
SHAW	Simultaneous Heat and Water Model
SHE	European Hydrological System
S_l	Latent Heat of Vaporization from Condensation or Evaporation /Sublimation [W m^{-2}]
SMP	Snow management piles

$S_{net,lw}$	Net Thermal Radiation [W m^{-2}]
$S_{net,sol}$	Net Solar Radiation [W m^{-2}]
S_p	Sparrow Number
SRM	Snow Runoff Model
SSA	Specific Surface Area [m^2 kg^{-1}]
S_{sen}	Sensible Heat Flux [W m^{-2}]
SVR	Support Vector Regression Model
SWAT	Soil and Water Assessment Tool
SWE	Snow water equivalent [mm]
T_a	Air Temperature [˚C]
T_{avg}	Average Temperature of the Day [˚C]
T_b	Temperature Threshold [˚C]
T_d	Degree-Day Index [˚C]
T_f	Freezing Temperature [˚C]
T_i	Ice Temperature [˚C]
T_m	Melting Temperature or Melting Point [˚C]
$T_{pc,\ 1 \rightarrow 2}$	Phase Change Temperature Between Phase 1 and Phase 2 [˚C]
T_{ref}	Reference Temperature [˚C]
T_{SF}	Tailings storage facilities
T_{solid}	Temperature of Solid Phase [˚C]
T_{sr}	Radiometric Snow Surface Temperature [K]
T_{ss}	Aerodynamic Surface Temperature [˚C]
u	Velocity Field [m s^{-1}]
UEB	Utah Energy Balance

u_f	Fluid Velocity Field [m s^{-1}]
UNECE	United Nations Economic Commission for Europe
u_p	Porous Velocity [m s^{-1}]
UQAT	Université du Québec en Abitibi-Témiscamingue
URSTM	Unité de Recherche et de Service en Technologie Minérale
U_Z	Wind Velocity [m s^{-1}]
V	Snow Management Pile Volume
V_h	Heat of Vaporization of Water [KJ mol^{-1}]
V_i	Ice Volume [m^3]
VIC	Variable Infiltration Capacity
V_s	Snow Volume [m^3]
V_{solid}	Solid Volume [m^3]
V_z	Vertical Wind Speed [m s^{-1}]
Z_o	Roughness Parameter
α	Standard Deviation of the Elements from the Symmetry Axes
γ	Psychrometric Constant [Kpa K^{-1}]
δ	Phase Lag Angle Between Stress and Strain [°]
ΔQ	Change in Snowpack Energy [W m^{-2}]
ΔT	Temperature Difference [°C]
ε	Emissivity of Snow
ε_o	Strain
η	Dynamic Viscosity [Pa s]
κ_{2p}	Empirical Parameter
λ	Thermal Conductivity [W m^{-1} K^{-1}]

λ_a	Air Thermal Conductivity [W $m^{-1} K^{-1}$]
λ_{eff}	Effective Thermal Conductivity [W $m^{-1} K^{-1}$]
λ_f	Fluid Thermal Conductivity [W $m^{-1} K^{-1}$]
λ_m	Porous Medium Thermal Conductivity [W $m^{-1} K^{-1}$]
λ_{peff}	Equivalent Thermal Conductivity of Porous Medium [W $m^{-1} K^{-1}$]
λ_{rel}	Relative Thermal Conductivity [W $m^{-1} K^{-1}$]
λ_s	Snow Thermal Conductivity [W $m^{-1} K^{-1}$]
$\lambda_{s,f\,eff}$	Solid-Fluid Thermal Conductivity [W $m^{-1} K^{-1}$]
λ_{solid}	Solid Thermal Conductivity [W $m^{-1} K^{-1}$]
νi	Young's modulus [Pa]
ρ_a	Air Density [Kg m^{-3}]
ρ_f	Fluid Density [Kg m^{-3}]
ρ_i	Ice Density [Kg m^{-3}]
ρ_s	Snow Density [Kg m^{-3}]
ρ_{solid}	Solid Density [Kg m^{-3}]
ρ_v	Water Vapor Density [Kg m^{-3}]
ρ_w	Water Density [Kg m^{-3}]
φ	Heat Source [J]

LIST OF APPENDICES

CHAPTER 1 INTRODUCTION

The methods employed to extract valuable minerals from ore generate substantial volumes of solid and liquid waste, such as mine tailings, throughout the mining of mineral deposits (Bussiere and Guitonny, 2020). Tailings are typically stored at the surface in large areas designated as tailings storage facilities (TSFs). Despite advancements in TSF design (e.g., Azam and Li, 2010; Caldwell, 2017), geotechnical instability and TSF failures still occur. Although the causes of these failures vary, inadequate water management often plays a significant role (Strachan and Goodwin, 2015). Therefore, careful planning and effective implementation of water management infrastructure are crucial to TSF safety, from construction to reclamation (Kuyucak, 2021). This includes integrating measures for controlling surface water flows and managing water levels into the design and operation of water management practices, storage, and treatment facilities (Environment Canada, 2009).

Regular assessment and maintenance of tailings dams are important for long-term performance. Water balances for tailings dams should be developed and updated often as the centerpiece of these efforts. To minimize the risk of catastrophic failure in a TSF, it is crucial to reduce the water content. This includes supernatant water released from the slurry and held in the tailing's basin, pore water within the tailings' interstices, and water from rainfall and surface runoff (East and Fernandez, 2021). Quantifying and contrasting all water inflows and outflows is necessary to build a water balance for a specific tailings dam (Figure 1.1). Precipitation, infiltration, evaporation, seepage, groundwater flow, and potential flood events are variables that need to be quantified (Geris et al., 2022).

1.1 Water balance on TSFs

The surface area of TSFs can vary significantly depending on the size of the mining operation and the number of tailings produced. The surface area of TSFs can range from a few hectares to several square kilometers (Williams, 2016). For example, smaller TSFs might cover around 10-20 hectares, while larger TSFs can extend over several hundred hectares. Some of the largest TSFs in the world can even exceed 1,000 hectares (Williams, 2016). In cold regions, where seasonal freezing and thawing occurs, snow is critical to

many hydrological processes, including water supply, erosion, and flood control (Gray and Male 1981; Walter et al., 2005). In these regions, there are generally two periods of high-water flows: the spring runoff and the significant fall precipitation (Boulanger-Martel et al., 2022). During winter, substantial snow accumulates on the surface of TSFs, contributing notably to the annual water inventory such as reservoir storage, and groundwater recharge. As a result, TSFs frequently have the highest annual flow rates during spring snowmelt, which puts potentially excessive demands on the water management infrastructure and puts tailings dams, flumes, and treatment capacity at risk (Boulanger-Martel et al., 2022).

To effectively manage precipitation, infiltration, evaporation, seepage, ground water flow, and potential flood events in tailings dams, several strategies can be employed (Kiedrzyńska et al., 2015). Implementing diversion channels and drainage systems helps manage rainfall, while covering the tailings surface with impermeable materials reduces infiltration. Enhancing evaporation can be achieved by increasing the surface area of water exposed to air, such as through shallow ponds or spraying techniques (Hu et al., 2024). Seepage can be controlled by installing collection systems like drains and wells and monitoring seepage rates and water quality. Groundwater flow can be managed using interception wells and cutoff walls, with regular monitoring to assess effectiveness. Designing the tailings dam to withstand extreme weather events, including constructing spillways and overflow channels, is crucial for managing potential flood events. Figure 1.1 shows the main elements of water balance of a tailings dam.

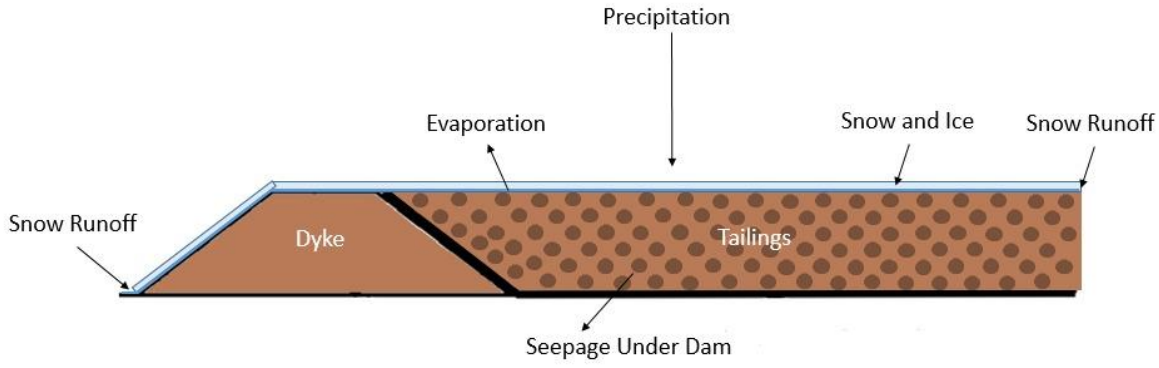

Figure 1.1 Elements of the water balance of a tailings dam.

The management of water resources and the assessment of the risk of spring snowmelt flooding depends on accurate snowfall and melt forecasting. A comprehensive water balance management system includes all waters and water cycles on a mine site, as well as those affected by the mine site, interconnected as building blocks (Figure 1.2). Generally, mine-site water cycles can be categorized into two main types (Punkkinen et al., 2016):

- Natural waters encompass groundwater, surface water, rainfall, snowfall, and evaporation, collectively referred to as clean waters. Mine dewatering waters, primarily groundwater, often require treatment due to potential salinity, high concentrations of metals and metalloids, and significant levels of nitrogen compounds.
- Tailings, dams, ponds, and seepage waters, which include wastewaters and used waters that may require treatment, along with the associated treatment facilities.

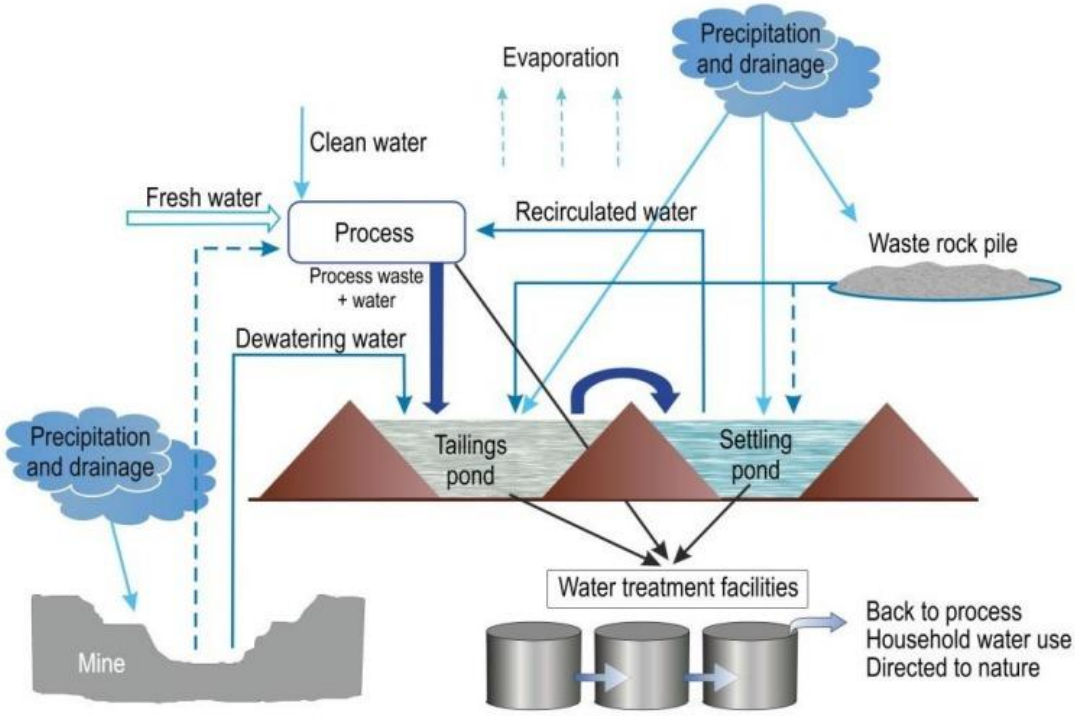

Figure 1.2 Examples of various mine water sources and streams (from Punkkinen et al., 2016).

Temperature, snow conditions, water system freezing, rapid melting periods, and ice depth are closely linked to mines' water balances (Punkkinen et al., 2016). Temporal variations

in precipitation, melting periods, and cold temperatures can complicate mining operations (Punkkinen et al., 2016). In cold climates, freezing condition can make water resources unusable for mining and processing operations. Additionally, seasonal changes can impact the water balance and should be considered (Department of Water Affairs and Forestry 2006b). Thus ensuring the long-term sustainability of mining processes necessitates responsible mine water management. This is currently one of the most critical challenges of the mining industry. Authorities worldwide are also striving to enhance the effectiveness of existing management practices.

In the mining industry, water balance and water management are crucial but distinct. The water balance involves accounting for all water inflows and outflows within a mining site over a specific period, including precipitation, evaporation, infiltration, and runoff (Kunz, 2016). This helps assess water availability and predict shortages or surpluses (Kunz, 2016). Water management, on the other hand, involves the strategic planning, development, distribution, and regulation of water resources to meet operational needs like ore processing, dust suppression, and environmental protection (Kunz, 2016). It aims for sustainable and efficient water use, addressing issues like scarcity and quality. Practices include water recycling, treatment of contaminated water, infrastructure development, policy-making, and stakeholder engagement (Kunz, 2016). While water balance helps understand water dynamics, water management encompasses broader strategies to utilize and protect water resources effectively (Kunz, 2016).

1.2 Impact of climate change on the components of the water balance

The global climate is undergoing changes. Since the start of the century, global temperatures have increased by approximately 0.5°C, with some regions in Canada (e.g., British Columbia) experiencing up to a 1°C rise (Pollock, 2009). A notable rise in the average annual air temperature from 1900 to 2010 is observed across the East Coast region (Savard et al., 2016). The data indicate a general warming trend with significant year-to-year and decade-to-decade variability (Savard et al., 2016). Over the 110-year period, the East Coast region experienced an average temperature increase of 0.90 ±0.37°C (Savard et al., 2016). Stations along the Atlantic Ocean saw a rise of 0.75 ±0.34°C, while those along the Gulf of St. Lawrence coast experienced a warming of 1.12 ±0.43°C. Other research

(Galbraith and Larouche, 2013) also highlights an increasing temperature change from the southeast to the northwest across the region. These temperature increases are comparable to or exceed the global average warming during the same period (e.g., IPCC, 2013).

If atmospheric greenhouse gas concentrations continue to rise unchecked, we can expect more rapid climate change in the coming generations. This increase, driven by a growing global population consuming vast amounts of energy and altering natural carbon cycles, traps heat in the atmosphere, leading to climate change. Canada will not be exempt from these changes, which are anticipated to result in a warming rate unprecedented in the last 10,000 years. Flooding has been the most prevalent disaster in the East Coast region, followed by hurricanes and winter storms (Public Safety Canada, 2014). The region is expected to face increasing catastrophic losses due to rising water levels and weather events, such as more frequent rain-on-snow flooding and winter thaws, which are likely to impact ice-jam flooding and river/estuarine drainage (Savard et al., 2016). These changes, combined with current development pressures and practices, could lead to greater damage to infrastructure and services (e.g., PIEVC, 2008), including mining infrastructures.

Snow cover plays a crucial role in the meteorological system, being highly responsive to shifts in climate and ecological conditions. It serves as a vital source of water for glacier runoff, particularly in arid regions (Immerzeel et al., 2010). Among various environmental factors, snow cover is the most reactive to intricate climate changes (Zhang, 2005).

In addition to its role in hydrology, the snow cover significantly influences local and global weather patterns. It affects albedo, which is the reflection of solar radiation, thereby impacting temperature regulation. Changes in snow cover can also alter the timing and volume of water availability, affecting agriculture, water resources, and ecosystems (Robinson et Frei, 2000). Understanding and monitoring snow cover is essential for predicting and mitigating the impacts of climate change (Che et al., 2008; Takala et al., 2011).

1.3 Mine water management methods

There are several methods that can be used to manage water in TSFs (Cacciuttolo et al., 2023). One method involves using flumes, which are engineered structures designed to

measure and control water flow (Cacciuttolo et al., 2023). Flumes ensure accurate monitoring and help prevent erosion by handling peak flow conditions (Vanani and Ostad-Ali-Askari, 2022). By accurately measuring water flow, flumes help maintain the water balance within the TSF, detecting any changes in flow rates early, which is crucial for preventing erosion and managing sediment transport effectively (Cacciuttolo et al., 2023).

Another method is the use of ditches, which are essential for drainage within TSFs (Cacciuttolo and Tabra, 2015). Ditches are designed to collect and divert surface water away from the tailings area, reducing the risk of water accumulation and erosion (Cacciuttolo and Tabra, 2015). The slope and gradient of the ditches are calculated to ensure efficient water flow without causing erosion. To maintain their structural integrity, ditches may be lined with materials like riprap or geotextiles, which help reduce erosion and ensure the ditches remain effective over time (Cacciuttolo and Tabra, 2015).

Spillways are also critical for managing water in TSFs (Cacciuttolo and Tabra, 2015). They are designed to safely discharge excess water, particularly during heavy rainfall or storm events. The capacity of spillways must be sufficient to handle the maximum expected flow, including extreme weather conditions (Cacciuttolo and Tabra, 2015). To prevent downstream erosion, spillways often include features like stilling basins or stepped chutes that dissipate the energy of the flowing water. This controlled release reduces the risk of structural failure and environmental damage (Cacciuttolo and Tabra, 2015).

The design of these components involves careful consideration of factors such as flow rates, material durability, slope gradients, and capacity to handle extreme weather events. Effective water management in TSFs combines these structures to ensure safe and efficient water handling, thereby enhancing the facility's stability and environmental safety (Trevelyan, 2021).

During high flow periods, mining operations can implement practices to manage water effectively and prevent flooding, erosion, and contamination. Diversion channels and ditches are used to redirect surface water away from storage areas, thus reducing the risk of water accumulation. Retention ponds capture and store excess water, allowing for controlled release and sediment settling (Spitz and Trudinger, 2019). Pumping systems are deployed to remove excess water, often automated to respond to rising levels (Cacciuttolo

and Marinovic, 2022). Integrated Drainage Systems (IDS) combine pumps, valves, monitoring devices, and drainage pipes to control water flow comprehensively (Anderson and Tinkler, 2021). Water treatment facilities ensure that discharged water meets regulatory standards by removing contaminants (Punkkinen et al., 2016, Hermassi et al., 2016). Advanced monitoring and early warning systems track water levels and flow rates in real-time, providing early alerts to enable proactive measures. These combined practices ensure operational stability and minimize environmental impact during high flow periods (Punkkinen et al., 2016).

1.4 Challenges in mine water management

Managing water in mining operations during periods of snowmelt and precipitation presents several challenges and unknowns, particularly in the context of climate change. For example, certain conditions such as a large snowpack combined with a warm and rainy spring could be critical to the performance and integrity of mine water management infrastructures.

Climate change is causing shifts in snowfall patterns and melting rates, making it difficult to predict when and how much snow will melt. This unpredictability can lead to sudden and unexpected increases in water flow, which can overwhelm existing water management systems (Ryberg, 2024).

Variability in precipitation is another significant challenge (Tang et al., 2024). Climate change is expected to increase the frequency and intensity of extreme weather events, including heavy rainfall (Trottier et al., 2023). This can result in rapid water accumulation and potential flooding, which can be difficult to manage without robust infrastructure (Trottier et al., 2023). Additionally, the seasonal distribution of precipitation is changing, with some regions experiencing more intense wet seasons and prolonged dry periods (Bulovic et al., 2024). This variability complicates the planning and management of water resources.

Temperature fluctuations also play a critical role. Warmer temperatures can lead to earlier snowmelt, which may not coincide with the peak water demand periods (Shockley, 2021). This mismatch can create challenges in storing and utilizing the available water efficiently.

Furthermore, higher temperatures can increase evaporation rates, reducing the overall availability of water for mining operations (Shockley, 2021). The interaction between groundwater and surface water during snowmelt and heavy precipitation events is another area of uncertainty (Shockley, 2021). Understanding how these interactions affect water availability and quality requires extensive monitoring and modeling, which can be complex and resource intensive (Shockley, 2021).

Lastly, long-term climate projections are inherently uncertain (Clemente and Huntsman, 2019). While models can provide general trends, the specific impacts on local water resources can be difficult to predict accurately (Clemente and Huntsman, 2019). This uncertainty makes it challenging to design and implement effective water management strategies that are resilient to future climate conditions (Clemente and Huntsman, 2019). Addressing these challenges requires adaptive management strategies, advanced monitoring technologies, and flexible infrastructure that can respond to changing conditions.

1.5 Snow management practices to help control spring runoff

The above information indicated that it is vital for mining operators to control water flows better to minimize the geotechnical and environmental risks associated with snowmelt. In some cases, mine water management systems can struggle to effectively deal with the volume of water generated during snowmelt on TSFs. Therefore, gaining control over spring water flows is particularly relevant in climate change, where accurately predicting climatic conditions is difficult. In this context, snow management practices such as snow management piles (SMPs) could contribute to the control of snowmelt and significantly decrease peak flows, providing enhanced control over mine water management and treatment during this critical time (Boulanger-Martel et al., 2022).

These piles could play a crucial role in regulating the water generated from melting snow and ice, thereby mitigating geotechnical risks. SMPs work by strategically storing snow in designated areas, allowing for a controlled and gradual release of meltwater. This method could help to prevent sudden and important influxes of water into TSFs water management and treatment systems, thus reducing the main risks associated with spring runoff. Additionally, incorporating snow management piles into the overall mine water

management strategy requires careful planning and coordination. It involves assessing the specific climatic conditions, snow accumulation patterns, and the hydrological characteristics of the mine site.

By reshaping the snow that naturally builds up at the TSFs' surface, these structures are created. SMP construction remolds and densifies snow in a way that maximizes the storage of the winter water inventory as a snow pile. Therefore, the use of SMPs for snow and meltwater management in TSFs could aid in extending the duration of spring runoff, reducing melting rates, and lowering maximum meltwater flows (Boulanger-Martel, 2022).

Figure 1.3 shows that many factors can affect the physical structure and properties of the snow. Snow grooming increases the density of snow due to compaction and yields to snow metamorphism. Such changes will modify the snow thermal properties, and most importantly the amount of latent heat that is contained within a given volume. As a result of the sun's radiation to the earth's surface, some of the snow melts on the surface of the block and flows to the lower layers. This will decrease the density at the surface of the layer and increase the density at the bottom of the snow block (due to the freezing of the runoff). Also, some amount of the snow mass evaporates due to the sun's radiation. The wind can change the surface of the snow block. Other factors that can change the heat transfer in snow are freezing rain and the falling of snow on the surface of the earth. Non-atmospheric factors such as the ground thermal regime can affect the temperature of the interface between the snow and the ground and affect snowmelt.

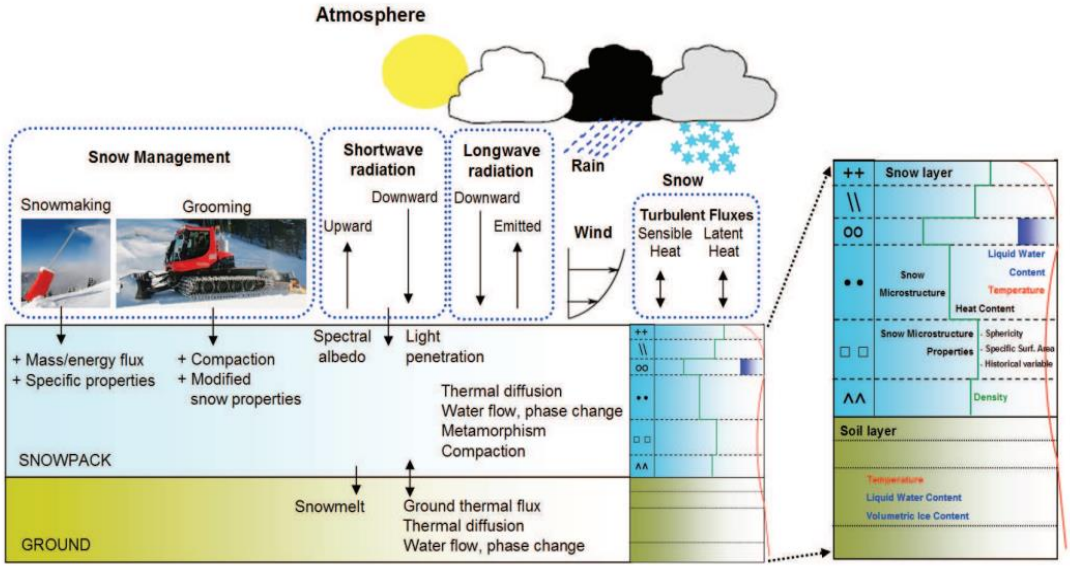

Figure 1.3 The SAFRAN-SURFEX/ISBA-Crocus scheme including grooming and snowmaking effects on snowpack physics, (adapted from Vionnet et al., 2012).

1.6 Research objectives

Preliminary field trials have demonstrated the efficacy and feasibility of engineered SMPs as a tool for proactively managing the winter water inventory of TSFs (Boulanger-Martel et al., 2022). However, more work needs to be done to further optimize the configuration and construction of snow management piles. As such, the main objective of this research project is to optimize the configuration and construction of SMPs to better control spring runoff on TSFs using pilot-scale field tests and numerical modeling. This study is structured around four specific objectives (SOs):

- SO1: Assess the performance of snow management piles constructed with conventional civil equipment and specialized groom equipment;
- SO2: Develop a simplified numerical model able to represent the observed SMPs' snowmelt-behaviour;
- SO3: Use the obtained field and numerical results to optimize the design and operation of SMPs within a spring runoff water management scheme on TSFs;

By achieving these specific objectives, this study is to investigate how different configurations of SMPs can control snowmelt and assess the main parameters affecting

their performance. Guideline for implementing SMPs in mining operations are also provided. Ultimately, the project aims to enhance the stability and safety of tailings storage facilities, contributing to the overall sustainability and efficiency of mining operations.

Using these results, this study aims to identify technically and cost-effective pile configuration for controlling snowmelt. Numerical modelling is used to better understand the parameters of influence and widen the application of the results.

1.7 Organization of the dissertation

This dissertation is organized into six comprehensive chapters, each addressing a specific aspect of the research:

- Chapter 1: Introduction

  This chapter sets the stage for the dissertation by introducing the research context, outlining the central problem, and stating the primary objectives of the project. It provides a foundational understanding of the study's significance and scope.
- Chapter 2: Literature Review

  The second chapter offers an in-depth review of existing literature related to snow structure, its physical properties, and the numerical modeling of snow behavior. This chapter synthesizes current knowledge and identifies gaps that this research aims to fill.
- Chapter 3: Materials and methods

  This chapter outlines the key materials and methods used in pilot-scale field tests, detailing the fieldwork conducted at mine sites in 2022 and 2023. Although the author did not take part in data collection in 2022, data have been utilized for in this study. Additionally, the chapter discusses the numerical modeling method.
- Chapter 4: Field results and Numerical Modeling

  This chapter present the field results and explores the concept of numerical modeling and its validation. It addresses SO1 and SO2, examining the melting of snow piles in 2022 and 2023.
- Chapter 5: General Discussion

  This chapter offers a comprehensive discussion that contextualizes the results obtained from the research. It explores the practical charts and snow pile structures,

providing insights into their potential uses and benefits. This chapter addresses SO3.

- Chapter 6: Conclusion and Recommendations

  The final chapter summarizes the key findings of the dissertation and presents the main conclusions. It also offers recommendations for future research and practical applications, highlighting the contributions of this study to the field.

CHAPTER 2 LITERATURE REVIEW

This chapter embarks on a comprehensive journey into the intricate world of snow, starting with a detailed exploration of its structural characteristics. It then transitions into an in-depth analysis of the various types of snow and into the fundamental physical properties of snow.

In addition, the chapter delves into the mechanisms of heat transfer within snow and discusses the various parameters that significantly influence heat transfer processes.

This chapter wraps up with an insightful discussion on the numerical modeling of snowmelt, as explored in the literature.

Overall, this chapter provides a holistic view of snow, covering its basic structure and types. It delves into the intricate physical properties and dynamic processes that govern snow's behavior in natural environments. Additionally, it reviews previous works on snowmelt numerical modeling.

2.1 Composition and types of snow

Snow is a multiphase system made up of three phases: solid, liquid, and gas (Figure 2.1). A snow cover is subjected to shifting temperature gradients in real-world conditions, and it also experiences significant mass flux from snowfalls, melting, etc. Pressure changes in different snow layers are also caused by changes in snow cover thickness. Due to these ever-changing circumstances, snow is a particularly dynamic substance. Snow is a granular material with a microstructure constantly undergoing metamorphism (Rahimi 2016). This makes it challenging to examine the phase changes that take place in snow because, in addition to the heat and mass transport, geometric issues also need to be considered (Domine et al., 2008). Snow's mechanical behavior is greatly influenced by its microstructure. The way the snow is packed depends on the size and form of the snowflakes (Gururajan, 2015).

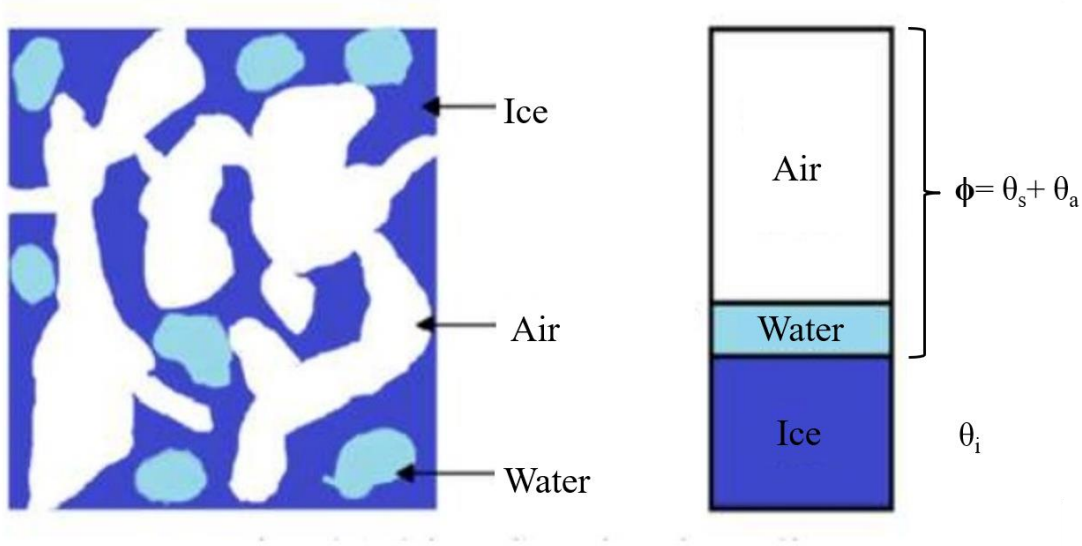

Figure 2.1 Schematic of a control volume (Rahimi 2016)

A detailed characterization of snow particles is essential to understanding snow settling behavior and modeling ground snow accumulation for various purposes, such as preventing avalanches and flooding caused by snowmelt (Li et al., 2022). Fierz et al. (2009) provides a comprehensive guide on classifying seasonal snow, including snow grain types and characteristics. It standardizes symbols for snow properties, offers multilingual terms, and includes historical perspectives on snow classification systems. This international standard aids consistent communication and data exchange among snow researchers worldwide. The nine main classes of grain shape are detailed in Table 2.1.

If different classes of grain shapes are present in a layer, they may be characterised individually, putting either symbol or abbreviation code of theminority class in round brackets. However, symbols and abbreviations should notbe used together (Fierz et al., 2009) (ICSSG).

Table 2.2 presents the qualifiers given by the ICSSG for the different average grain sizes. Several methods are used to determine the size of snow grains such as stereology, sieving and image analysis, the results obtained by each of the methods being however different (Riche et al., 2012). Therefore, a grain size analysis is a measurement with a large uncertainty (Fierz et al., 2009).

Table 2.1 Class of grain forms and description of the (ICSSG) (Fierz et al., 2009).

Code ICSSG	**Classes**	**Description**
PP	Precipitation Particles (Fresh snow)	Grains of snow resulting from a recent precipitation having preserved the fine structure of the flakes (new snow)
MM	Machine made snow (Artificial snow)	Grains produced mechanically, either by production of droplets (spherical particles), or by passage of ice (flat particles)
DF	Decomposing and Fragmented precipitation particles (fresh snow in transition)	Grains partially retaining the structure of precipitation particles, but in the process of becoming a fine, spherical particle
RG	Rounded Grains (spherical grain snow)	Spherical-grained snow (as a result of structure decomposition by sublimation and metamorphism)
FC	Faceted Crystals	Crystals formed by an excess of vapor inside the layer of snow which solidifies when the temperature change
DH	Depth Hoar (Inner frost inside the snow cover)	Crystals formed by large temperature gradients resulting in excess water vapor solidifying within the layer of snow (frost)
SH	Surface Hoar (Surface Frost)	Crystals formed on the surface due to the rapid transfer of water vapor from the atmosphere to the surface (surface hoar)
MF	Melt Forms (Ice pieces)	Ice particles formed using snow containing a lot of water (which is refrozen) or during a freeze-thaw cycle
IF	Ice Formations (ice layer)	Layer of ice formed during the freezing of a layer of water on the surface (rain), at the base or inside the layer of snow

Table 2.2 ICSSG's snow grain size classification (Fierz et al., 2009).

Term	**Dimensions (mm)**
Very fine	<0.2
Fine	0.2 to 0.5
Medium	0.5 to 1.0
Coarse	1.0 to 2.0
Very Coarse	2.0 to 5.0
Extreme	>5.0

2.2 Evolution of the snow cover

According to Fierz et al. (2009), the snow cover area is the geographic extent of the snow cover on the land surface and is an important variable in numerous research on hydrology, climatology, and ecology. The following aims to present the main mechanisms involved in the evolution of a snow cover.

2.2.1 Accumulation of snow

Multiple temporal and spatial scales reveal strong variability in snow accumulation. Inter-annual variability in weather and climate change impact snow melt timing and magnitude (Pedersen et al., 2013). Temperature increase reduces snowfall and snow cover duration (Bavay et al., 2013) and earlier melt of snow (López-Moreno et al., 2013). The lifespan of a snow cover depends on the geographical location and weather conditions (Edwards et al, 2007). If a snow cover melts after a few days, it is an intermittent snow cover such as snow that fell at low altitude or at high altitude but early in the fall or late in the spring (Laternser and Schneebeli, 2003). If the snow cover remains all winter due to climatic conditions, it represents a seasonal snow cover (Edwards et al, 2007). If the snow cover persists during the summer and its thickness increases during the accumulation period, then it is a permanent snow cover.

During the period of snow accumulation, the energy balance in a snow cover is negative, in other words the temperature drops by releasing energy (Anderson, 1976). However, during the melting period, the energy balance is positive (Anderson, 1976). In addition, sublimation and vaporization can also produce energy mass loss (Mott et al, 2018). In Figure 2.2, energy exchange activities over a continuous snow cover (a) and additional processes over a patchy snow cover (b) are schematically described. Present for the continuous snow cover are turbulent sensible and latent heat fluxes (Q_h, Q_e), incoming and outgoing longwave radiation (Q_{Lin}, Q_{Lout}), incoming and reflected shortwave radiation (Q_{Sin}, Q_{Sout}), and terrain radiation. The snowpack energy balance can be written as (Armstrong and Brun, 2008):

$$-\frac{dH}{dt} = Q_S + Q_L + Q_h + Q_e + Q_a + Q_G \tag{2.1}$$

Where $-\frac{dH}{dt}$ is the net change rate of the snowpack internal energy per unit area. Q_S is net shortwave radiation (incoming minus reflected shortwave radiation); Q_L is the net longwave radiation (downward and upward component of longwave radiation); Q_h is the turbulent flux of sensible heat exchanged at the surface due to the temperature gradient between snow surface and atmosphere; Q_a is the flux of energy advected via precipitation or blowing snow; Q_G is the ground heat flux due to conduction.

Additionally, typical profiles of wind, air temperature, and turbulence development over snow under stable atmospheric conditions are shown. The boundary layer evolution (air temperature, turbulence, and sensible heat fluxes) over snow caused by local heat advection from the snow-free area towards the snow-covered area is shown for the scenario of patchy snow cover (Mott et al, 2018). The latter two occur during periods of accumulation or melting. The mass lost by evaporation is small compared to that caused by sublimation, which is why it is often overlooked (Lundberg and Halldin, 1994). This type of snow cover is present in the north and gradually turns into a glacier (Singh, 2001). A snow cover has a stratified structure because it is deposited gradually and in several layers after each precipitation event. Each of the layers has different physical properties depending on the meteorological conditions during the precipitation (Mellor, 1964). In other words, the snowflake can form differently depending on the temperature and wind speed during its

formation in the clouds and after precipitation. For example, the wind compresses the snowflake and causes the density of the snowflake to increase. According to the study by McKay (1970), the density of fresh snow can then vary between 4 and 340 kg m^{-3}.

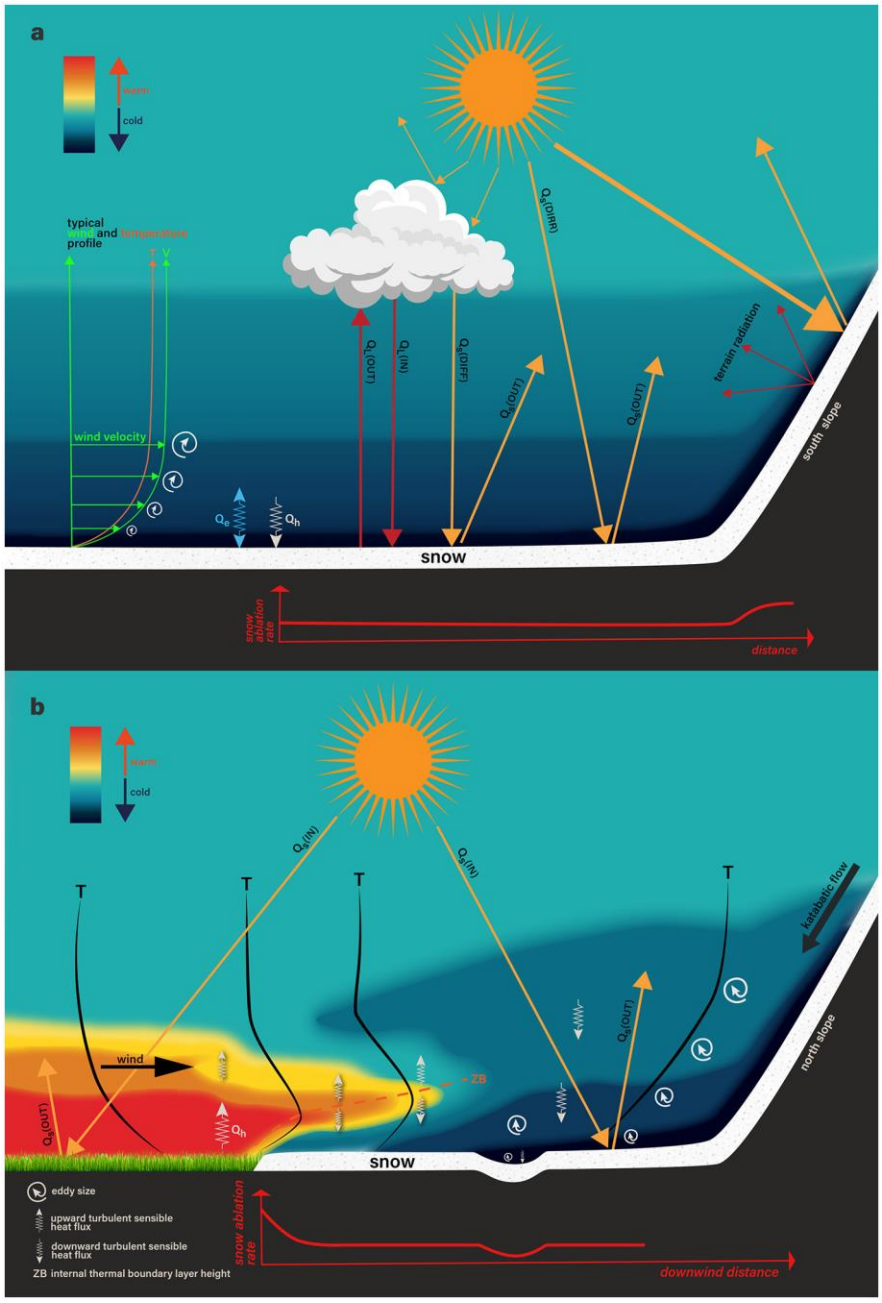

Figure 2.2 Energy exchange activities over a continuous snow cover (a) and additional processes over a patchy snow cover (b) are schematically described (Mott et al, 2018).

The complexity of snow processes across multiple scales is primarily responsible for the high variability in snow accumulation and ablation at smaller spatial and temporal scales (Clark et al., 2011). For capturing the timing and magnitude of hydrological responses in alpine catchments, the final snow cover variability at the end of the snow accumulation season is critical (Winstral et al., 2013). When the snow depth is heterogeneous at the beginning of a melting period, it produces a higher differential melt rate over time and space, faster runoff generation at the beginning of melting, and a longer melting season as more snow accumulation areas delay melting (Brauchli et al., 2017).

The evolution of a snow cover is not often homogeneous, particularly for places where the snow cover is thick, where there is wind and rain. For example, the lower part of a snow cover is often transformed into ice (depth hoar) due to the heat given off by the ground and the overload pressure imposed by its own weight. The presence of heat transferred by the ground and the presence of water vapor in the snow initiate a structural change under overload pressure, which can increase the density of the snow and change the connection between the grains. Morin et al. (2010) studied the evolution of a snow cover located in the Argentière glacier (France) and measured the density and temperature (Figure 2.3). Their results show that the density is higher in the lower part of the snow cover and lower at the surface. However, it is possible to observe an equivalent density value between 250 and 350 [kg m^{-3}] for this snow cover.

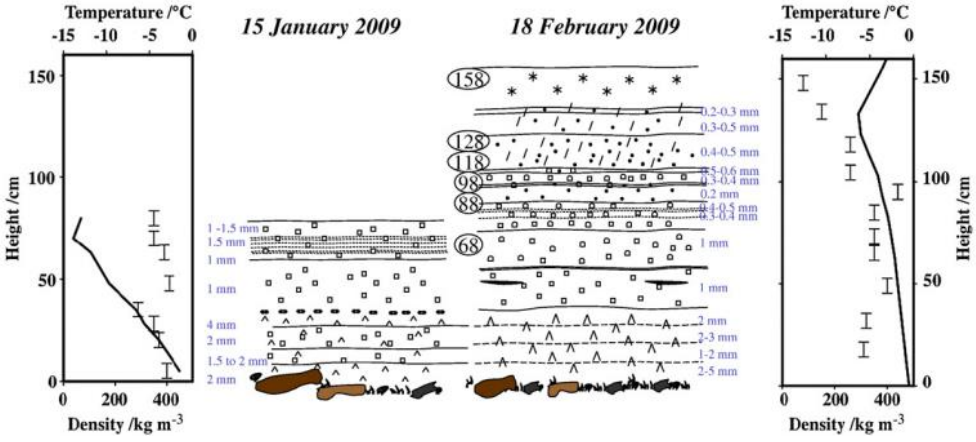

Figure 2.3 Stratification, density and temperature determined in situ on January 15, 2009 (left) and February 18, 2009 (right). (Morin et al. 2010)

Mass and energy fluxes between the snow cover and the overlying atmosphere drive spatial variability of snow at catchment and smaller scales. Pre- and post-depositional snow transport processes are determined by the interaction between the wind field, snowfall, and snow surface. Through sensible and latent heat exchange as well as blowing snow sublimation, the wind further plays an important role in the mass and energy balance of the snow cover. Furthermore, complex boundary layer flows over heterogeneous land-covers in spring strongly affect snow melt patterns (Mott et al., 2017).

2.2.2 Snow metamorphism

When snow is deposited on a surface and is immobile at the macroscopic scale, we are interested in phenomena occurring at the microscopic scale. Snow supports its own weight, which leads to densification, as well as a change in skeletal structure due to the presence of water vapor and a high thermal gradient between the ground and the snow surface. Under these conditions, the connection between snow crystals becomes different from that of fresh snow. Water vapor pressure gradients induce sublimation and/or condensation of snow crystals. This results in physical transformations of the snow crystals: the size, shape and arrangement evolve and modify the physical properties of the snow. These phenomena are known as snow metamorphism. Four mechanisms are responsible for this process: (1) destructive metamorphism, (2) constructive metamorphism, (3) melt metamorphism, and (4) pressure metamorphism (Alford, 1974).

Domine et al. (2003) and Legagneux et al. (2003) conducted several tests on snow samples stored in a cold room under isothermal conditions. They observed the morphological changes in these samples by scanning electron microscopy (SEM). Their results reveal that the structure of the snow has a visible tendency to round and is gradually evolving towards a larger and larger structure, not to mention that the connections between the grains have become larger and larger.

Metamorphism has consequences on the physical properties of the snow cover. Density tends to increase under overload pressure and due to thermodynamic grain transformations (Dibb and Fahnestock 2004). However, relating transfer properties to metamorphism is complex, as its evolution is a function of time and is related to several factors that are

difficult to estimate. This is why transfer properties have often been established as a function of density, despite the decrease in the quality of the estimate.

2.2.3 Snowmelt

Determining snow melt is crucial for various purposes, including seasonal volume estimation, stream flow predictions, designing flood control structures, and more. Snowmelt's thermodynamics are well known and have been extensively discussed in several publications. The early descriptions by (Clyde, 1931), (Light, 1941), and (Wilson, 1941) are among the lists. The U.S. Army Corps of Engineers' (COE, 1956) study, which is still frequently mentioned and recognized as a seminal work about snowmelt dynamics. The most important single indicator of melting conditions is air temperature. It is common to express snow-melt rates as functions of air temperature expressed in degree-days above freezing. But expressing snow-melt rates as a function of degree-days implies that other impacts are either insignificant, constant, or are straightforward temperature functions (Wilson, 1941).

The wind speed, latent heat released by moisture condensation on the cold snow surface, and the net effect of incoming and outgoing radiation are a few of these factors. A radiation-related example of a minimal effect is when, with a lot of cloud cover, the incoming and outgoing radiation may balance. The existence of relatively uniform wind speed over a certain basin at a given time is an illustration of a constant effect. As a result, the turbulent exchange produces little variation other than with changes in temperature and humidity. The air temperature reflects the overall impact of both incoming and outgoing radiation, and under some circumstances, the radiation effect can be represented as a straightforward function of air temperature (Wilson, 1941).

In a flat, prairie-like landscape, an ideal snowfall might have the same initial depth and melt rate everywhere (Figure 2.4.a). Any real-world landscape has hollows and stream valleys that tend to hold onto snow better than other places. Since the thinnest sections of the snowpack melt off first and the deepest parts last, even a spatially equal rate of melting will result in a gradual decrease in the snow-covered area (SCA) rather than a dramatic disappearance (Figure 2.4.b). Because the initial snowpack tends to be deeper at higher elevations and the heat supply for melting tends to be lower, snow persists for a long period

in the higher sections of mountain basins, where snow cover depletion is even more gradual (Figure 2.4.c).

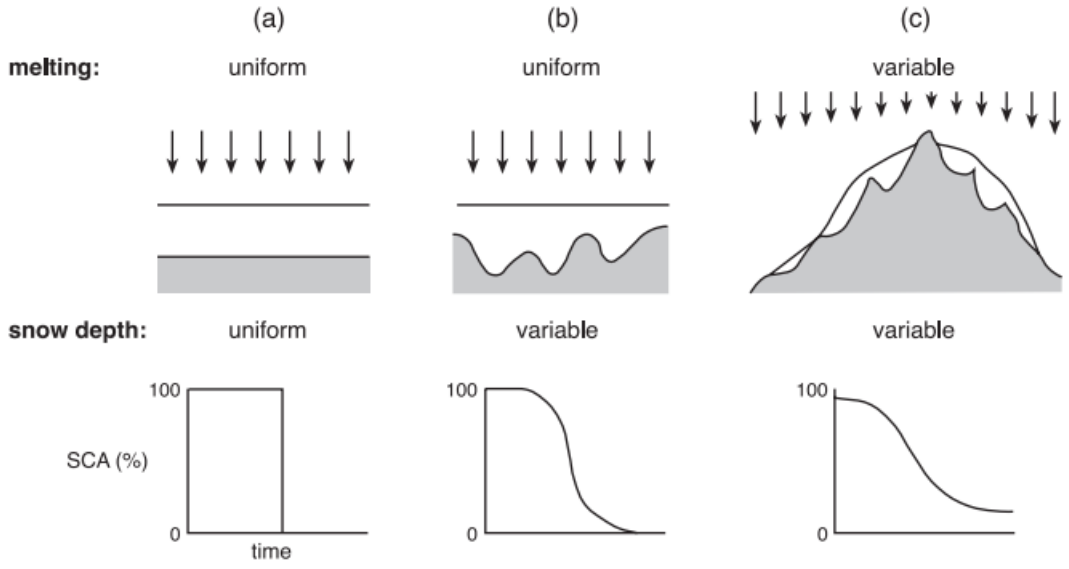

Figure 2.4 Relationship between temporal decline in a snow-covered area (lower diagrams) and spatial heterogeneity in snow depth and melt rate (upper diagrams) (Rahimi 2016).

Snowmelt is often conceptualized as an energy balance problem which can be expressed as follow (Van Mullem et al., 2004):

$$\Delta S = S_{net,sol} + S_{net,lw} + s_{sen} + S_l + S_g + Q_p \quad (2.2)$$

Where $S_{net,sol}$ (W m^{-2}) is the net solar radiation, $S_{net,lw}$ is the net thermal radiation (W m^{-2}), s_{sen} is the sensible heat transfer from air (W m^{-2}), S_l is the latent heat of vaporization from condensation or evaporation per sublimation (J kg^{-1}), S_g is the conducted heat from underlying ground (W m^{-2}), and Q_p is the advected heat from precipitation (W m^{-2}). Table 2.3 summarizes each of the terms in the energy balance equation and their relative importance.

Table 2.3 Relative importance of energy balance terms, Van Mullem et al., (2004)

Term	% **ΔH**	**comments**
H_{rs}, H_{rt}	60-90 %	Controlled by terrain, season, cloud cover, shading, air temperature, humidity. H_{rs} and H_{rt} are generally of about the same magnitude, but different sign. H_{rt} is usually negative and dominates in winter. H_{rs} is positive and dominates in spring. During a crossover period in early spring before the onset of melt, H_{rs} and H_{rt} cancel each other, and the net is near zero.
H_s, H_l	5-40 %	Controlled by temperature and humidity gradients and wind speed. H_s and H_l are usually of opposite sign, so they tend to cancel. That is, it is usually either warm (H_s +) and dry (H_l -) or cold (H_s -) and humid (H_l +). Sometimes H_s and H_l are of the same sign, but the magnitude is small (e.g., cold and dry). Occasionally both are positive and large (i.e., warm and humid), usually during high winds, such as during rain-on-snow events.
H_g	2-5 %	Usually small because the temperature of the ground is generally about the same as the temperature of the snow. During melt, both ground and snow are at 0 °C, so H_g= 0.
H_p	0-1 %	Heat content of precipitation is relatively small compared to latent heat required to melt snow, unless precipitation volume is very large and precipitation temperature is significantly greater than 0 °C.

2.3 Key physical attributes of snow

Among the key physical characteristics of snow, the density, porosity, snow-water equivalent, and specific surface area (SSA) area will be described further in this document. These are the mains physical properties relevant to snowmelt analyses.

2.3.1 Density

When it comes to mass transport and heat transfer, the mass and volume characteristics of a porous material is a crucial factor (Meinicke et al., 2020). A layer of snow has a density

between that of air, which is approximately 1.204 kg m^{-3} at 101.325 KPa and 20°C (Cavcar, 2000), and that of ice, which is 918.9 kg m^{-3} at -10°C (Ghormley and Hochanadel, 1971). On a spatial scale of the order of a centimeter, the medium is continuous, and its apparent density (ρ_0) is usually expressed as a function of the mass of snow per unit volume (Morris, 1987; Morland et al., 1990). The volume fraction Θ_k [-] and the density ρ_k [kg m^{-3}] are directly related to the apparent density:

$$\rho_0 = \sum \Theta_K \rho_K \tag{2.3}$$

Where k can be a, w, and i for air, water, and ice respectively. The sum of its volumetric fractions for all components equals one, where:

$$\sum \Theta_K = 1 \tag{2.4}$$

Snow density is defined as the weighted average of the density of each of the components. As the mass of the gaseous components is less than 1% of the total mass, the snow density can be defined as follows (Morland et al., 1990):

$$\rho_s = \Theta_i \rho_i + \Theta_w \rho_w \tag{2.5}$$

Where ρ_s is the density of snow, ρ_i is the density of ice (918.9 kg m^{-3}), ρ_w is the density of water (1000 kg m^{-3}), Θ_i and Θ_w are the volumetric ice, and water contents, respectively.

Snow density is often required in snow hydrology (Pulliainen and Hallikainen, 2001) and climatology (Derksen and Brown, 2012). Density is related to snow mechanical parameters (Schneebeli and Johnson, 1998; Wang and Baker, 2013), and vertical density fluctuations affect snowpack stability (Schweizer et al., 2011). Most of all, it describes the amount of water contained within it, which is very important in any hydrological application. Table 2.4 provides typical density values for different types of snow (Glen, 1997).

Table 2.4 Typical snow density values for different types of snow (Glen, 1997).

Type of Snow	**ρ_s (kg m^{-3})**
New snow (immediately after falling)	50-70
Damp new snow	100-200
Settled snow	200-300
Depth hoar	100-300
Wind packed snow	350-400
Firn	400-830
Very wet snow and firn	700-800
Glacier ice	830-917
Pure ice	917

2.3.2 Porosity

Snow can also be characterized by its porosity (n), which is the volume ratio of all voids (pores) to the total volume. When considering dry snow, it is appropriate to describe in terms of porosity because there is only a solid phase present (Ignoring the amount of unfrozen water, which can be large for temperatures near 0°C.) (Dozier et al, 1987):

$$n_s = 1 - \frac{\rho_s}{\rho_i} \tag{2.6}$$

Equation 2.6 connects the ice mass per unit sample volume plus the liquid mass per unit sample volume to the snow density. Therefore, using known values for S_W (liquid water saturation) and n, it is also possible to directly compute the snow density (Colbeck, 1978);

$$\rho_s = \rho_i(1 - n) + \rho_w n\, S_w \tag{2.7}$$

The literature provides measured values of porosity for different types of snow, some of which are summarized in Table 2.5.

Table 2.5 Porosity for different types of snow (Clifton et al, 2008)

Type of snow	Porosity (%)	Refrence
New snow, wind blown	83–85	Sommerfeld and Rocchio, (1993)
Wind-packed snow	77	Albert et al., (2000)
Melt-freeze surface	63	Albert and Perron, (2000)
Melt-freeze crystals	62	Albert and Perron, (2000)

2.3.3 Snow water equivalent

The snow water equivalent (SWE) is another important parameter, especially used in watershed management (Langlois et al., 2009). The SWE essentially represents the amount of water contained in the snowpack. It is an important parameter in hydrology to calculate the amount of water entering a basin at the end of winter (Langlois et al., 2009).

$$SWE = \frac{\rho_s}{\rho_w} H_s \tag{2.8}$$

where H_s is the snow depth.

2.4 Mechanisms of heat transfer in a snow cover

Heat transfer in snow arises mainly from four processes (Bishop et al., 2011): (1) conduction through the network of interconnected ice crystals, (2) conduction through interstitial air, (3) latent heat transfers due to sublimation-condensation cycles resulting from metamorphism, and (4) airflow within the snow, either in the form of convection caused by high-temperature gradients or advection caused by wind blowing over a rough snow surface. Airflow is typically less significant, latent heat transfer plays a major role only in depth hoar, and the thermal conductivity of ice (λ_{ice} = 2.3 W m^{-1} K^{-1} at -10°C) is much higher than that of air (λ_{air} = 0.023 W m^{-1} K^{-1} at -10°C) (Bishop et al., 2011). Consequently, the primary heat flow in snow mainly occurs through conduction within the interconnected network of snow crystals, resulting in wind packs having considerably higher thermal conductivity than depth hoar (Bishop et al., 2011). This section presents an analysis of snow's thermal properties and their implications for snowpack stability and

snowmelt. Understanding the dominant heat transfer mechanisms makes it possible to better predict snowmelt rates.

2.4.1 Conduction

The process of heat conduction in ice and snow encompasses various mechanisms outlined in Figure 2.5, which includes conduction through snow crystals and interstitial air. As the thermal conductivity of ice (λ_{ice}) is significantly higher than that of air (λ_{air}), the primary heat transfer process in snow is often through the network of interconnected snow grains (Sturm et al., 1997). It is logical to anticipate that snow with higher thermal conductivity values would generally be the hardest type of snow (Bishop et al., 2011). Nevertheless, Sturm et al. (1997) demonstrated a significant positive correlation between snow density and thermal conductivity.

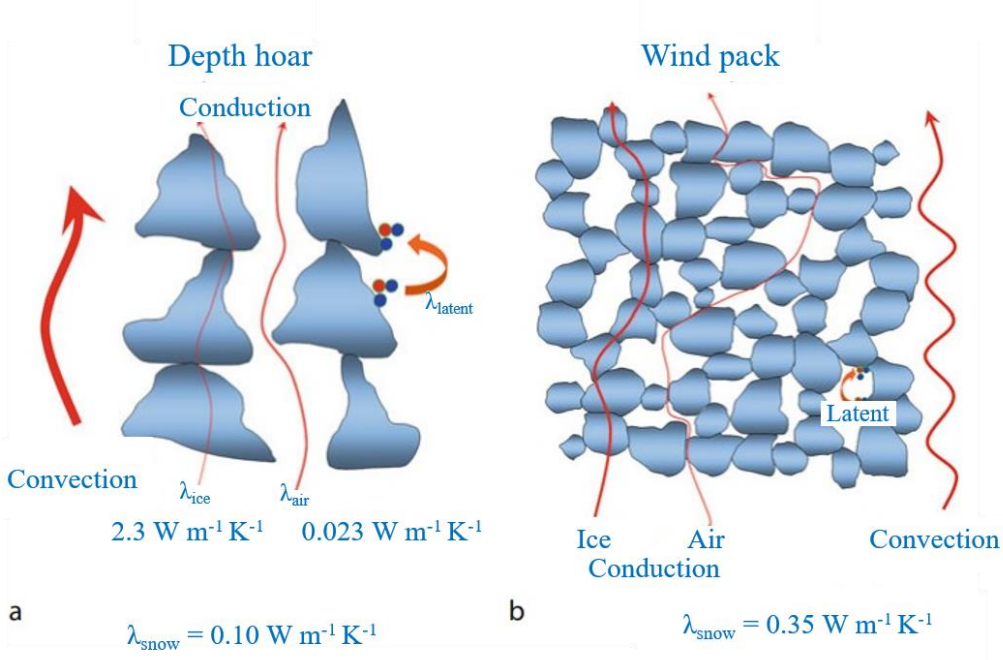

Figure 2.5 Main processes involved in heat transfer though (a) depth hoar and (b) wind-packed snow (Bishop et al., 2011).

Heat conduction in the snow cover can be described by a one-dimensional equation (Ashton, 2011):

$$\rho_s C_s \frac{\partial}{\partial t} T_s = \frac{\partial}{\partial z} (\lambda_s \frac{\partial}{\partial z} T_s + \varphi) \quad (2.9)$$

Where T_s is the temperature in the snow ($T_s \leq 0°C$), ρ_s is the density of the snow, C_s is the specific heat capacity of the snow, λ_s is the thermal conductivity of the snow, and φ is an internal heat source term due to solar radiation absorption.

2.4.2 Convection

For more than 30 years, the concept of air convection in the snow has been a subject of debate (Johnson et al., 1987; Brun and Touvier, 1987). Only limited conditions have been accepted for convection at the laboratory scale (Sturm and Johnson, 1991). Akitaya (1974) failed to induce convection in natural snow samples despite applying strong temperature gradients but was able to induce convection in artificial snow samples. According to Klever (1985), convection is common in new snow, but unlikely in rounded snow. Based on Rayleigh number calculations, Brun and Touvier (1987) concluded that convection was unlikely, although none of the snow samples they tested were of high permeability.

2.4.3 Radiation

In most studies, radiation at the surface is divided into two streams: shortwave radiation from the sun, which falls between 0.3 and 2.2 µm in wavelength, and longwave radiation from the sky and surrounding terrain, which falls between 6.8 and 100 µm in wavelength (Male and Granger, 1981). Almost 5% of the total radiation occurs between 2.2 µm and 6.8 µm (Geiger, 1966). Radiation is often taken as a boundary condition, including both solar (Marks and Dozier, 1992) and thermal radiation (Marks and Dozier, 1992).

2.4.4 Sensible and Latent heat

Figure 2.6 illustrates the concept of latent and sensible heat (Skovajsa et al., 2017). Also, it shows the conversion from sensible heat to latent heat occurs during the snow-to-water phase change. During this process, the temperature of the snowpack remains constant while the thermal energy of the solid phase is transformed into the liquid phase. The latent heat of fusion for water is 334 kJ kg^{-1}.

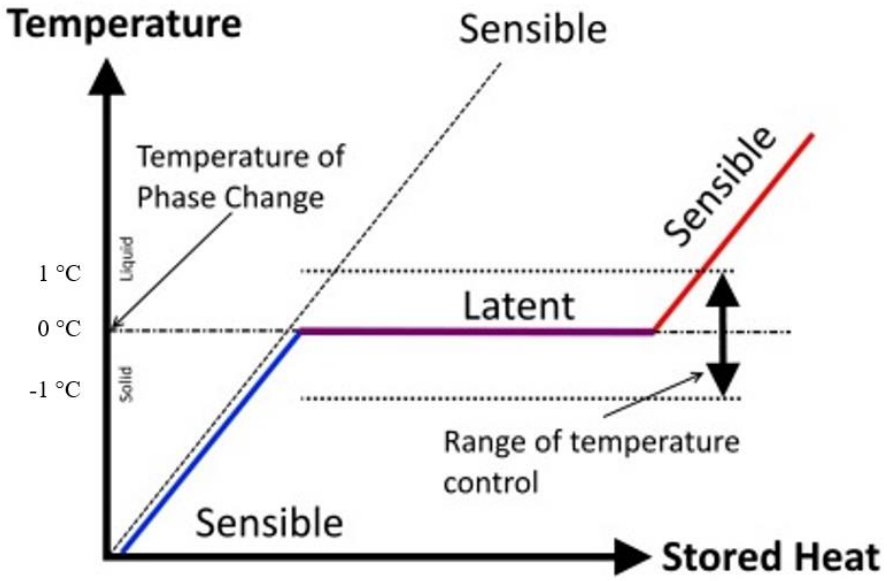

Figure 2.6 Temperature control during phase changes and a comparison of sensible heat and latent heat (adapted from Skovajsa et al., 2017).

By adopting the convention that energy influx into the snowpack is considered positive, the amount of energy accessible for snow melting, denoted as Q_m, relies on various factors including net radiation (R_n, which represents the difference between incoming and outgoing shortwave and longwave radiation), sensible heat flux (S_{sen}), latent heat flux (L), ground heat flux (G_h), and any energy flux caused by precipitation (Marks and Dozier, 1992; Burns et al., 2014).

$$Q_m + Q_{cc} = R_n + S_{sen} + L + G_h + P = R_n + F_T + G_h + P \qquad (2.10)$$

Qcc refers to the amount of energy necessary to raise the temperature of snow to its melting point, often referred to as the "cold content." The net turbulent flux, F_T, is the combined value of S_{sen} and L, with the latter being particularly significant in the realm of snow science as it represents sublimation, evaporation, condensation, and their connection to the overall mass balance of the snowpack. Although S_{sen} and L typically make up only a small portion of Q_m, they are still noteworthy contributors (Boon, 2009; Fitzpatrick et al., 2017).

2.5 Key thermal properties of snow

In this section, the thermal properties of snow are investigated. First, the thermal conductivity and the factors affecting it, such as density, porosity, and contact size between grains, are presented. Understanding these properties is crucial for predicting snow behavior in various environmental and engineering applications.

2.5.1 Thermal conductivity and factors of influence

The following aims to explain how snow density and porosity largely determines its thermal conductivity. However, several factors, including the relative humidity, the size and form of the grains, as well as the microstructure, affect the thermal conductivity value (Côté et al, 2012). Appendix A provides more information about available methods for computing the thermal conductivity of snow.

2.5.1.1 Effect of density and stratification on thermal conductivity

Sturm et al. (2002) conducted an in-depth study on the thermal conductivity and stratification of snow cover on the Beaufort Sea ice sheet. They measured the thermal conductivity of snow using a heated needle probe, finding values ranging from 0.078 W m^{-1} K^{-1} for fresh snow to 0.574 W m^{-1} K^{-1} for a snow-ice mixture. The study identified three major types of snow (Figure 2.7): depth hoar, wind slab, and recent snow. These types were observed in ten distinct layers at the Surface Heat Budget of the Arctic Ocean (SHEBA) site. The thermal conductivity of the snow was found to increase with density and could be estimated based on the snow's metamorphic state. Thermal conductivity measurements were made on approximately 10% of all layers measured for density, hardness, and type by Sturm et al. (2002). the thermal conductivity of snow layers measured by using a heated needle probe. This method involves inserting a thin needle into the snow layer and heating it. The rate at which the needle heats up is used to determine the thermal conductivity of the snow. The needle probe method is effective because it provides direct measurements of thermal conductivity and can be used in various types of snow, from fresh snow to snow-ice mixtures. Compared to the full set (Table 2.6), this thermal subset was slightly denser and harder, reflecting a natural bias toward layers. In Table 2.6, five of the ten layers of snow (“a”, “b”, “d”, “g”, and “j”) were under sampled,

while two layers (“c” and “f”) were oversampled. However, this bias is unimportant since (later) they derive a bulk value for the whole snowpack using layer-weighted averaging. Furthermore, Sturm et al. (1997) measured the thermal conductivity of 488 snow samples of known crystal type and density. They demonstrated that the thermal conductivity of snow composed of rounded grains correlates with their density. From these results, to demonstrate the relationship between the latter two, they established an empirical equation. Heat conduction has been shown to be less density dependent for snow subject to intense metamorphism, such as depth hoar. This happened due to the change in the connections between the grains due to metamorphism. The effect of metamorphism on thermal conductivity is not negligible, but it is not always easy to predict the variation of thermal conductivity by metamorphism. This is the reason why models of thermal conductivity are often a function of density.

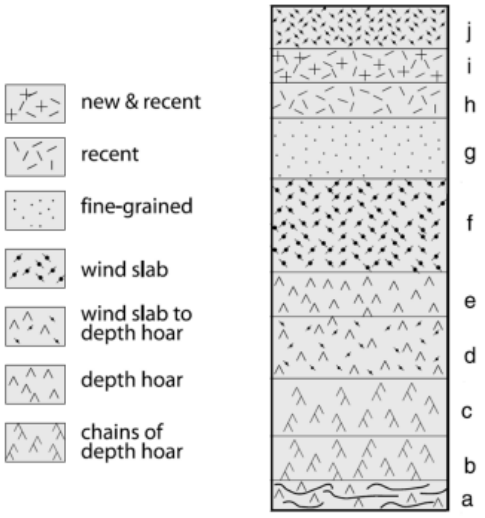

Figure 2.7 Stratification of a studied snow cover (Sturm et al., 2002)

Table 2.6 Average thermal conductivity of snow layers. (Sturm et al. 2002)

Layer	**ρ (Kg m^3)**	**λ (W m^{-1} K^{-1})**
J	390	0.203
H & I	200	0.078
G	360	0.197
F	420	0.290
E	280	0.157
D	360	0.164
C	270	0.081
B	270	0.087
A	600	0.574

2.5.1.2 Heat capacity of snow

The heat capacity is the amount of heat needed for a unit of mass to increase its temperature by one unit, either under constant pressure (c_p (J kg^{-1} K^{-1})) or constant volume (c_v (J kg^{-1} K^{-1})) conditions. Overall heat capacity is a function of the mass or volume of snow (i.s. density or porosity), calculated from that of ice. Mathematically, it is expressed as (Yen, 1981):

$$C_p = (\frac{\partial H}{\partial T})_p \; or \; C_v = (\frac{\partial U}{\partial T})_v \tag{2.11}$$

Where H and U are enthalpy and internal energy per unit mass, respectively.

As the heat required to warm up the air and vapor in the gaps is negligible, the heat capacity of dry snow and ice is practically the same. The value of C_v can be derived from C_p using the following relationship (Yen, 1981):

$$C_p - C_v = \frac{K_V^2 V_i T}{\omega_T} \tag{2.12}$$

Where V_i is the volume of ice, K_V is the coefficient of volumetric expansion, and ω_T is the compressibility. At the melting point, the value of C_v is approximately 3% lower than C_p, and as the temperature decreases, the difference between C_p and C_v diminishes.

Dickinson and Osborne (1915) and Dorsey (1940) conducted a comprehensive review and compilation of the heat capacity values for ice established during the early twentieth century. In an extensive investigation, Giauque, and Stout (1936) provided C_p values for hexagonal ice across a temperature range of 15 to 273 K. Flubacher et al. (1960) determined cp values for hexagonal ice within the range of 2 to 27 K. Additionally, Sugisaki et al. (1968) conducted comprehensive measurements of C_p for amorphous, cubic, and hexagonal ice at temperatures spanning from 20 to 250 K. Anderson (1976) presents a formulation for C_i (J kg^{-1} K^{-1}) as follows:

$$C_i = 1.6738 + 0.1327\,T \tag{2.13}$$

where C_i is the specific heat of ice.

Ding et al. (2021) provide an equation for the heat capacity of snow, which is a function of the heat capacities of ice and air:

$$C_s = C_i \frac{\rho_s}{\rho_i} + C_a\left(1 - \frac{\rho_s}{\rho_i}\right) \tag{2.14}$$

2.6 Snowmelt numerical models

Snowmelt hydrological models simulate snow accumulation, melting, and convergence. In comparison to rainfall runoff, the snowmelt process involves more complex energy transfer and water transfer processes between the atmosphere and snow, between different snow layers, and between snow layers and soil (Marks et al., 1998). Because of the mixture of rain and snow, it is extremely difficult to simulate runoff generated by rainfall on snow. Modeling plays a critical role in forecasting snowmelt floods (Zhou et al., 2021).

2.6.1 Evolution of snowmelt models

Snowmelt models have been around for a long time. In the beginning, people estimated how much water flowed from melting snow by finding a statistical link between observed variables (like how much snow there was, how much water it contained, etc.) and snowmelt runoff (DeWalle and Rango, 2008). This period also makes frequent use of empirical equations. Air temperature and snowmelt are assumed to be linearly related by empirical equations, also called degree-day factors (Martinec, 1975). In 1975, Martinec developed the Snow Runoff Model (SRM), which is the most classic model of snowmelt based on the

degree-day method. The International Meteorological Organization recommends the SRM model, which is the most widely used model of snowmelt based on the degree-day method in more than 100 watersheds worldwide (Rango, 1995). Due to its simplicity and accuracy, the degree-day model has been widely used. Its disadvantage is that it cannot simulate snow melting physically (Zhou et al., 2021).

The US Army Corps of Engineers was the first to estimate how much snow melted based on the energy transfer process between the snow and its surroundings in the 1950s (Dunkle et al., 1956). The energy balance model is based on two fundamental concepts: the conservation of energy and water in the system. The model has been applied and improved in various studies (Anderson, 1976; Jordan, 1991), and has become more refined over time. However, the model still only represents a single point in space and does not account for spatial variability. The advancement of computer technology in the 1970s enabled the creation of more sophisticated and detailed physical hydrological models that could account for spatial variation. The first such model, called the European Hydrological System (SHE), was developed in 1986 (Abbott et al., 1986). The model divides the watershed into grid cells to capture the spatial variation of model parameters, rainfall input and hydrological outputs. The model also splits the vertical dimension into several layers to simulate the movement of soil water in different depths. The model then uses the energy balance method to estimate the snowmelt amount for each grid cell separately (Abbott et al., 1986).

There have been several distributed snowmelt models developed since the 1990s, such as SNOBAL (Marks and Dozier, 1992), Utah Energy Balance (UEB) (Tarboton and Luce, 1996), Hydrological Simulation Program - HFORTAN (HSPF) (Johanson et al., 1984), etc. The Distributed Hydrology Soil Vegetation Model (DHSVM) (Wigmosta et al., 1994), Variable Infiltration Capacity (VIC) (Liang et al., 1994), and Soil and Water Assessment Tool (SWAT) (Arnold et al., 1998) all include snowmelt modules (degree-day snowmelt algorithm and energy balance algorithm). In addition, snowmelt models based on energy balance models, such as Snow Thermal Model (SNTHERM89) (Jordan, 1991) and SNOWPACK (Bartelt and Lehning, 2002), have been developed. Snow engineering now uses these models to consider more detailed vertical distributions. Machine learning is a

powerful and flexible technique that has transformed various fields and industries and enabled new possibilities for scientific exploration and model building. It is widely used for hydrological modeling and forecasting, becoming a new approach for hydrological research. Machine learning is evolving rapidly and creating more opportunities for snowmelt modeling, or what is also known as data-driven modeling (Zhou et al., 2021).

2.6.2 Types of Snowmelt Models

Snowmelt models can be grouped into four types based on the different methods they use to calculate the snowmelt rate: statistical, conceptual, physical, and data-driven (the green categories in Figure 2.8) (Zhou et al., 2021). Statistical snowmelt models use statistical techniques or black box modules to find the relationship between a specific snow hydrological parameter (such as snow area) and runoff, and use it to predict runoff (Zhou et al., 2021). The relationship between snowmelt and temperature is usually empirical in conceptual snowmelt models (Zhou et al., 2021). Several of these models are mature and widely used, such as SRM and HBV (Bergström, 1995). Based on the energy balance of snow cover, physical snowmelt models such as SNTHERM and SNOWPACK calculate snowmelt (Zhou et al., 2021). They have a strict physical meaning and are widely used in snowmelt modelling. Massive data and rapid computational power have enabled data-driven models to emerge (Zhou et al., 2021). Machine learning algorithms are used to select appropriate parameters from different data sources (e.g., daily rainfall, temperature, solar radiation, snow area, snow water equivalent) for these models, such as ANN (Vafakhah et al., 2014) and LSTM (Thapa et al., 2020).

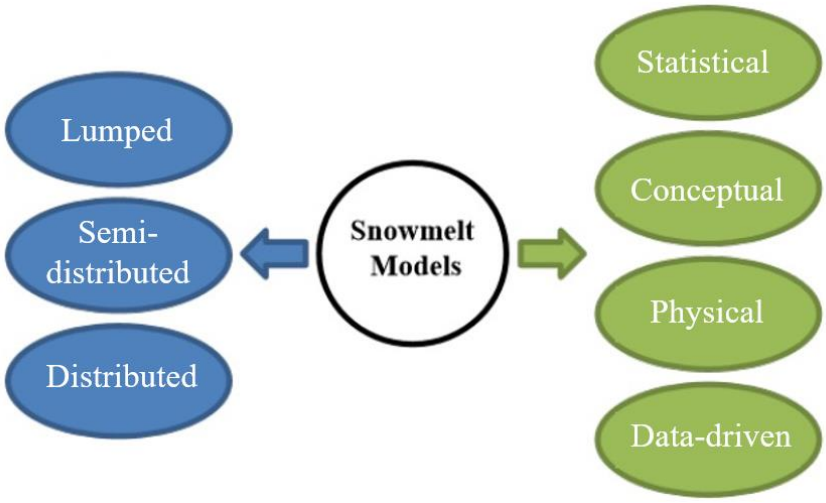

Figure 2.8 models of snowmelt categories. The models' spatial distribution features are used to produce the blue categories. Green ones are produced using various ablation algorithms (Thapa et al., 2020).

Snowmelt models can be categorized into lumped, semi-distributed, and distributed models based on the distribution features of models (Zhou et al., 2021). HBV, SWAT, and the Precipitation Runoff Modelling System (PRMS) (Leavesley and Stannard, 1995) are examples of semi-distributed models that divide the watershed into sub-watersheds or hydrological response units in accordance with a specific watershed characteristic (e.g., elevation, vegetation coverage, land use types, and topographic factors). Distributed models like SHE, DHSVM, and VIC segment the watershed into grid units, assigning distinct parameter values to each grid. These models subsequently incorporate processes involving wind, snow, and soil freezing within each grid entity (Zhou et al., 2021). Lately, driven by substantial advancements in computational capabilities, there has been a surge in the emergence of multi-layer hybrid and nested models. An example of such a model is the Water and Energy Budget-based Distributed Hydrological Model (WEB-DHM) (Wang et al., 2009). Nested calculations involving sub-catchments, grids, and slopes are employed to enhance the capacity for effectively depicting the snowmelt process (Wang et al., 2009).

2.6.3 Statistical Snowmelt Models

The prevalent statistical approach to predicting snowmelt runoff involves correlating the maximum SWE during the spring thaw with the total runoff volume, using regression

analysis to determine coefficients. SWE can be measured manually or via automated snow pillows. Another method uses runoff characteristic curves, relating spring snow cover ratio to basin runoff, which can be forecasted using remote sensing data. While these models can be accurate with sufficient observations, they may not perform well in unprecedented situations and are challenging to transfer between different watersheds due to varying hydrological characteristics (Zhou et al., 2021).

$$Q = a + b\,SWE \tag{2.15}$$

Where Q represents the complete runoff quantity. SWE can be derived either through manual measurement of snow depth along a designated survey line or via automated snow pillow measurements (Zhou et al., 2021). The values for coefficients 'a' and 'b' are derived through regression analysis performed on collected data.

2.6.4 Conceptual Snowmelt Models

The conceptual snowmelt model is commonly constructed using the degree-day factor approach, often termed the degree-day factor model (Zhou et al., 2021). Its fundamental premise postulates a linear correlation between alterations in the snowmelt rate and the daily average temperature surpassing a specific threshold. The typical formulation of the degree-day factor ablation algorithm is represented by Equation (2.16) (Zhou et al., 2021):

$$M_{mel} = DDF\ (T_{avg} - T_b) \tag{2.16}$$

In this equation, M_{mel} (cm day^{-1}) represents the quantity of melted snow, T_{avg} (°C) stands for the average temperature of the day, and T_b (°C) denotes the temperature threshold. Typically, the threshold temperature T_b (°C) is set at 0 °C, although alternative values might be employed in specific circumstances. DDF (cm °C^{-1} day^{-1}) represents the degree-day factor for snowmelt. Research has indicated substantial variability in DDF values across various areas, spanning from 0.1 to 1 (cm °C^{-1} day^{-1}). DDF can be ascertained through measured data or empirical formulas (Zhou et al., 2021):

$$DDF = 1.1\ \frac{\rho_s}{\rho_w} \tag{2.17}$$

Most conventional snowmelt models based on degree-day factors ignore the spatial variability of ablation in the watershed and use lumped or semi-distributed approaches

(Zhou et al., 2021). This leads to large uncertainties in the spatial distribution of snow melting simulation. Moreover, the degree-day factor is fixed on a daily scale and cannot reflect the intra-day variation of snowmelt rate, especially the contrast between day and night in temperature and snow energy supply. The enhanced spatial distribution degree model considers the time and space differences and incorporates energy exchange terms. This allows it to simulate the changes in snowmelt runoff on a daily scale and obtain reasonable results (Zhou et al., 2021).

2.6.5 Physical Snowmelt Models

The energy balance of the snow surface consists of the components shown in Figure 2.9 (Zhou et al., 2021). Several snow models have been developed over the years, including Anderson's multi-layer model (1976), Marks et al.'s SNOBAL (2015), and Bartelt et al.'s SNOWPACK (2002). These models simulate snow characteristics like depth, density, and temperature, and can forecast avalanche risks.

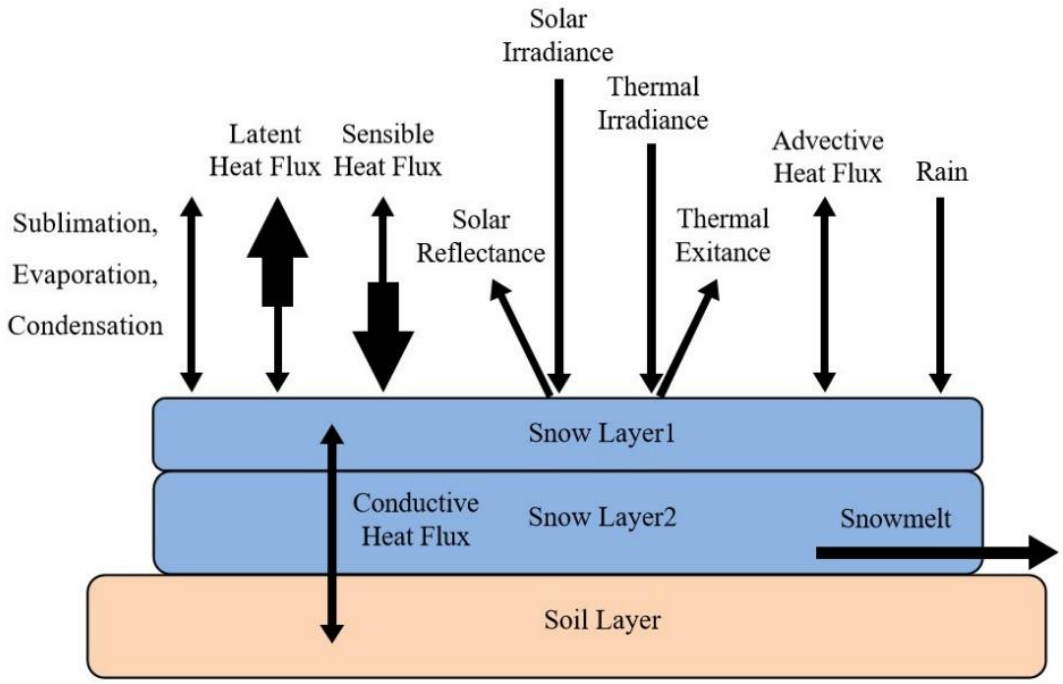

Figure 2.9 Diagram illustrating the process of exchanging energy in snow (Zhou et al., 2021).

Simulating snow ablation based on energy balance can be precise for small areas, but challenges arise for large watersheds due to data extrapolation issues and sparse monitoring stations (Zhou et al., 2021). Empirical methods are often used to estimate energy fluxes. Physically distributed snowmelt models, like SHE, DHSVM, VIC, and UEB, offer high-resolution simulations and follow strict physical principles (Zhou et al., 2021).

2.6.6 Models based on data

The development of data-driven models, enabled by data availability and machine learning advancements, focuses on enhancing prediction accuracy (Zhou et al., 2021). These models handle complex problems and identify essential inputs. Unlike physical models, data-driven models learn relationships between inputs and outputs without prior process knowledge (Zhou et al., 2021). Machine learning has been widely used for predicting snowmelt runoff and other hydrological applications. Combining data-driven and physical models can improve hydrological modeling by maintaining energy and water balance and determining model parameters. Despite challenges like unbalanced observations and limited training data, integrating machine learning with hydrological knowledge can enhance snowmelt modeling (Zhou et al., 2021).

2.6.7 Snowmelt modeling issues

Blowing snow, snow on frozen ground, and rain on snow are some of the key issues that need attention in the snowmelt model.

2.6.7.1 Blowing Snow

Snow melting varies spatially due to blowing snow, which creates uneven snow cover and impacts the snow water cycle (Zhou et al., 2021). MacDonald et al. (2010) found that 17–19% of yearly precipitation in the Rocky Mountains was due to wind-blown snow evaporation. Zhou et al. (2014) reported that blowing snow sublimation accounted for 24% of annual snowfall in western China's mountains. Hydrological studies use conceptual models based on terrain drift factors and physical models relying on wind fields. Key models include PBSM (Pomeroy et al., 1993), Snowtran-3D (Linston et al., 1998), Alpine3D (Lehning et al., 2006), and SnowDrift-3D (Schneiderbauer and Prokop, 2011). Challenges include identifying critical conditions for blowing snow, obtaining accurate

wind field data in complex terrain, and parameterizing data for widespread blowing snow (Zhou et al., 2021). Terrain significantly impacts blowing snow models, with terrain parameters crucial for snow depth estimation (Winstral et al., 2002). Integrating blowing snow models with snowmelt models remains a scientific challenge (Zhou et al., 2021).

2.6.7.2 Snow on Frozen Ground

Phase changes in soil water affect heat and water balance near the surface, impacting runoff and infiltration (Zhou et al., 2021). Frozen ground prevents infiltration, increasing surface runoff, while unfrozen soil allows high infiltration and water storage (Zhou et al., 2021). Various models, like SHAW and VIC, simulate these processes, considering factors like frost depth and snowmelt infiltration (Cherkauer and Lettenmaier, 1999). Advanced models, such as DWHC and SHAW-DHM, integrate these processes with climate models for accurate simulations in cold regions (Chen et al., 2006; Zhang et al., 2016).

Explicitly considering soil freezing and thawing enhances land surface and hydrological models (He et al., 2015). These processes adjust soil liquid water content and hydraulic conductivity, affecting evaporation, infiltration, and runoff (Zhou et al., 2021). Without a frozen ground module, models underestimate snowmelt runoff peaks in basins with strong frozen soil (Pohl et al., 2005). Accurately simulating frozen ground's influence remains challenging, requiring attention to different time scales and regional environments. Adding a frozen ground module to snowmelt models is essential for studying runoff dynamics in cold regions (Zhou et al., 2021).

2.6.7.3 Rain-on-Snow

Rain-on-Snow (ROS) events in mountainous areas cause severe mixed rain and snow floods, contributing to high flow peaks (Kattelmann, 1985). Studies show ROS events caused significant floods in regions like the Willamette River, Austria, and the western U.S. (Li et al., 2019). Climate change affects ROS frequency and peak flows, increasing risks in high altitudes (Zhou et al., 2021). Ignoring ROS conditions can lead to underestimating runoff and peak flow, highlighting the need for accurate ROS-based runoff models (Zhou et al., 2021). Many factors influence ROS event runoff, including rainfall, snow temperature, and moisture conditions (Singh et al., 1997). Physics-based models are

needed to simulate snow cover development and internal processes (Kattelmann, 2007). ROS enhances snowmelt runoff by reducing albedo and increasing snow energy, leading to faster melting (Ocampo Melgar and Meza, 2020). Improved hydrological models incorporating lateral flow could enhance predictions, but the mechanism of ROS-based runoff generation needs further study (Zhou et al., 2021).

2.7 Current snow management practices in mining operations and research needs

The current snow management practices during mining activities involve plowing roads and clearing access to specific parts of the operations for mining, construction or operation purposes. Some operations have snow storage facilities, that are used to keep snowmelt waters within the mine site's controlled waters. Operations dealing with filtered tailings can also adapt some snow management practices, essentially aiming to avoid the entrapment of snow in between tailings layers during deposition and provide optimal compaction conditions. However, there is not current practice aiming to manage snow as a spring runoff control strategy. The literature review has shown that the physics of snowmelt and the thermal and physical properties of snow are well known. Several snowmelt modeling approaches are available, but none is adapted to model the snowmelt of remoulded or piled snow. Based on the knowledge acquired through snow science, more research is required on snow management practices in mining operations.

CHAPTER 3 MATERIALS AND METHODS

3.1 General approach

First, the fieldwork has been completed. Using the data collected, numerical modeling was implemented. Initially, the impact of temperature variations on the melting process of SMPs will be investigated by conducting simulations with temperature data from different years. A detailed description includes the construction techniques used for creating SMPs, the climate monitoring methods employed for accurate data collection, and the specific parameters and conditions applied in the numerical modeling process.

The approach involves a comprehensive examination of the Goldex and Holt mine sites, providing site descriptions and climate monitoring data to contextualize the study. The construction and monitoring sections detail the techniques used in SMP construction, as well as the methods for monitoring snowmelt, internal and snow-surface temperatures, and snow density. Furthermore, the numerical modeling section delves into the selection of the model, the modeling approach, and the various parameters that influence the simulations, such as geometry, mesh, reference temperature, and porous medium type.

Additionally, this section outlines the calibration of a snow-surface temperature function based on measured air temperatures, which is crucial for establishing realistic surface boundary conditions in the model. The overall goal is to provide a comprehensive understanding of the materials and methods used in the study, ensuring that the approach is clearly articulated and that the results can be accurately interpreted and validated. This detailed explanation aims to provide a robust framework for analyzing the thermal dynamics and melting patterns of SMPs under varying temperature conditions.

Ultimately, this section is designed to comprehensively describe the materials and methods utilized in the study, setting the stage for the subsequent analysis and discussion of the results.

3.2 Site description and climate monitoring

The following sections will present descriptions of the Goldex and Holt mine sites, along with climate monitoring data for 2022 and 2023.

3.2.1 Goldex mine

The Goldex Mine is an underground gold mine operated by Agnico Eagle Mines Limited, and is located about 4 km west of Val d'Or, Québec. This mine produces conventional pulp tailings that were initially deposited in a TSF approximately 4 km south of the site. However, since 2008, most of these Goldex tailings have been redirected to the Manitou legacy site, which is owned by the government of Québec. While the Goldex tailings are currently mainly being used as construction material to reclaim the Manitou site (Ethier et al. 2014 b) the Goldex TSF is still used as an auxiliary TSF. Covering about 75 ha, the Goldex TSF is linked to a polishing pond capable of holding roughly 500,000 m^3 of water and used for settling particles from the TSF's seepage waters and storing surface drainage waters.

The Val-d'Or region experiences a humid continental climate characterized by significant seasonal temperature variations. According to Environment and Climate Change Canada (ECCC) data recorded from 1971-2000 (www.climate.weather.gc.ca), the mean annual temperature in this area is approximately 1.2°C. The coldest months are January and February, with average temperatures typically hovering around -17°C. Val-d'Or experiences an average total precipitation of 935 mm, with approximately 635 mm rainfall and 300 mm snowfall. (MSC ID 7098603; www.climate.weather.gc.ca). The snow cover typically spans from mid-November to early May, with the majority of snowmelt occurring in April. On average, there are about 121 days each year when the snow depth is 20 cm or more (MSC ID 7098603; www.climate.weather.gc.ca). Most of snowmelt typically occurs in two weeks in the region. It is important to note that while the author did not participate in the data collection at the Goldex mine, the data from this site was used and further interpreted to achieve the study's objectives.

3.2.2 Holt mine

The Holt Mine Complex is in the Kirkland-Matheson region of Ontario, approximately 68 km by road west of Matheson and 53 km east of Kirkland Lake. The complex consists of the Holt, Holloway, and Taylor Mines. The Holt Mine was built in the late 1980s, the Holloway Mine began operations in 1996, and the Taylor Mine was commissioned in 2015.

The complex includes two TSFs with a combined capacity to handle the tailings generated by the mining operations. In this mine, the tailings facilities consist of 18 individual dam structures, covering a total watershed area of 465.4 ha and a tailings area of 212 ha (116 ha for the North TSF and 96 ha for the South TSF). The Holt TSF is connected to a polishing pond with a capacity of approximately 1,400,000 m^3 of water. The Holt Mine began operations in 1988 when it was developed by Barrick Gold. Over the years, it has seen various phases of activity and ownership changes, including its acquisition by Kirkland Lake Gold in 2016 and later by Agnico Eagle Mines Limited in 2022.

The Kirkland Lake region has a humid continental climate with seasonal climatic variations similar to that of Val d'Or. According to ECCC data recorded from 1971-2000, the mean annual temperature in this area was approximately 2.7 °C. The coldest months are January and February, with average temperatures typically hovering around -17.9 °C. Precipitation in Kirkland Lake reach an average total of 970 mm, with approximately 741 mm rainfall and 229 mm snowfall (MSC ID 6074209; www.climate.weather.gc.ca). The snow-covered period and snowmelt in this area are similar to those in the Val d'Or region. On average, there are about 90 days each year when the snow depth is 20 cm or more.

3.2.3 Climate monitoring

For both sites, daily temperature, precipitation, and snow thickness data were retrieved from the nearest ECCC weather station. Climate data from the Val d'Or ECCC station (MSC ID 7098603; www.climate.weather.gc.ca) was used for the Goldex mine and covered a period spanning from February 25 to May 27, 2022. Due to the station's proximity (<4 km) to the Goldex TSF, the temperature and precipitation data were representative of in situ conditions (Boulanger-Martel et al., 2022). Climate data from the Kirkland Lake ECC station (MSC ID 6074209; www.climate.weather.gc.ca) was used for the Holt mine. For that site, retrieved data covered a period spanning from February 29 to May 29, 2023. This weather station is the closest and is located at about 40 km south-west of the Holt mine. For that case, the representativeness of snow thickness measurements at the Kirkland Lake ECCC weather station was assessed by comparing the daily thickness of snow on the ground recorded at the ECCC weather station data with manual, on-site measurements as well as LiDAR surveys. The Val d'Or ECC station (about 150 km west

from Holt mine) data were also recovered for the 2023 monitoring period for comparison purposes.

3.3 Construction and monitoring

The following section will outline the construction methods of SMPs and the techniques for monitoring snowmelt.

3.3.1 SMPs construction techniques

To assess the efficacy of SMPs at controlling snowmelt, six experimental SMPs were constructed within the TSFs of Canadian mine sites over two field seasons.

During the first field season (2022), three experimental SMP configurations were built at the Goldex TSF using common civil construction heavy equipment. Cubical, conical and ridge-shaped SMPs were selected and constructed to assess the effects of configuration on the melting behaviour. The construction occurred from mid-February to March 2022. The first step in the construction of the tested SMPs involved a pre-compaction of the natural snow accumulated at the surface of the TSFs using a snowmobile. Such approach was necessary to compact existing snow and promote the freezing of surface of the TSF. The construction of SMPs started once the surface of the TSF was frozen enough to withstand the traffic of heavy equipment. The SMPs were constructed at the beginning of March 2022 using two Caterpillar 938H wheel loaders (Figure 1a), a Caterpillar D6N LGP crawler dozer (Figure 3.1.a), and a Caterpillar 320E hydraulic excavator equipped with a long-reach boom-stick (Figure 1b). SMPs were built in a single lift mostly using a push-only approach, meaning that the snow was groomed by only pushing snow towards the SMPs (Figure 3.2.a). Footprints of 33×30 m, and 50×25 m were targeted for the cubic and ridge-shaped SMPs and snow was groomed to the maximum achievable height by the equipment (about 3.5m). For the conic SMP configuration, a conical base was first groomed to the height capacity of the dozer and loaders. Then, the hydraulic excavator was used to build a higher structure from snow that was brought by the loaders. Approximately 12,000 m^2 of snow was cleared to build the SMPs at this site (Figure 3.2.a). Considering that a snow depth of about 70 cm was observed at the site during construction, a volume of snow of about 8,400 m^3 was stored by the grooming operations. After construction the height of the

tested SMPs was of 7.3 m, 3.5 m, and 3.5 m for the conic, cubic and ridge-shaped SMPs, respectively. The initial footprint of the SMPs were of 665, 965, and 1150 m², respectively. The ridge-shaped SMP contained the most snow, and the conic SMP was about twice the height of the cubic and ridge-shaped SMPs, but contained the least snow (Table 3.1).

Figure 3.1 (a) Crawler dozer and wheel loaders used for the construction of SMPs in 2022; (b) hydraulic excavator lifting the conic SMP in 2022 and (c) final profile of the cubic SMP in 2022; (d) snow groomer used for the construction of SMP in 2023; (e) final profile of conic SMPs as well as groomer track on the snow in 2023; and (f) final profile of the ramp-shaped SMP in 2023.

The results of the first field season were used to determine promising SMP configurations. Monitoring results (presented later in this manuscript) and operational experience resulted in conical and ramp-shaped SMPs being the two optimal SMP shapes to test further. Thus, two cones and a ramp-shaped SMPs were designed and constructed at the Holt TSF during

winter 2023. Such configurations aimed to examine the impact of diverse sizes and shapes on snowmelt dynamics. Construction of all SMPs was achieved in two lifts performed mid- and at end of March. Snow was groomed with a Prinoth Bison-X snow groomer (Figure 3.1.d) equipped with a 4.5 m wide blade. The conic SMPs were constructed by creating concentric windrows that were systematically pushed toward the pile as soon as the blade was full of snow (Figure 3.1.e; 3.2.b). Such approach allowed maximizing the proportion of time the machinery was pushing snow. SMPs were grown by piling, compacting and shaping the snow with the snow groomer. The largest cone was 7.3 m high whereas the smallest was 5.5 m high (Table 3.1). The two conic SMPs were designed to directly assess the impact of height on snowmelt. In addition, the 2022 and largest 2023 conic SMPs had the same height and will be used as a reference to assess the impact of climate and volume on the performance of SMPs to control snowmelt. The ramp-shaped SMP was groomed using a push only approach. Snow was gradually pushed and piled along a ramp that grew in height with the increasing volume of snow being groomed. Such construction approach was selected for its ease of construction. This pile had a final height (5.6 m; Table 3.1) like that of the smallest conic SMP to allow for comparison. The largest cone held the most snow (Table 3.1). The smallest conic SMP held 1050 m^2 less snow than the ramp-shaped SMP despite being approximately the same height (Table 3.1). At the end of construction, around 55,000 m^2 of snow was cleared to build the three SMPs (Table 3.1). Overall, the SMP metrics presented in Table 1 indicate that the 2023 field tests involved clearing a larger surface (5.5 hectares) than 2022 (1.2 hectares). This resulted in more important snow volumes being stored in the 2023 SMPs. Considering that there was 60 cm of snow on the ground on average prior to constructions, this resulted in an approximate volume of groomed snow of 33 000 m^3.

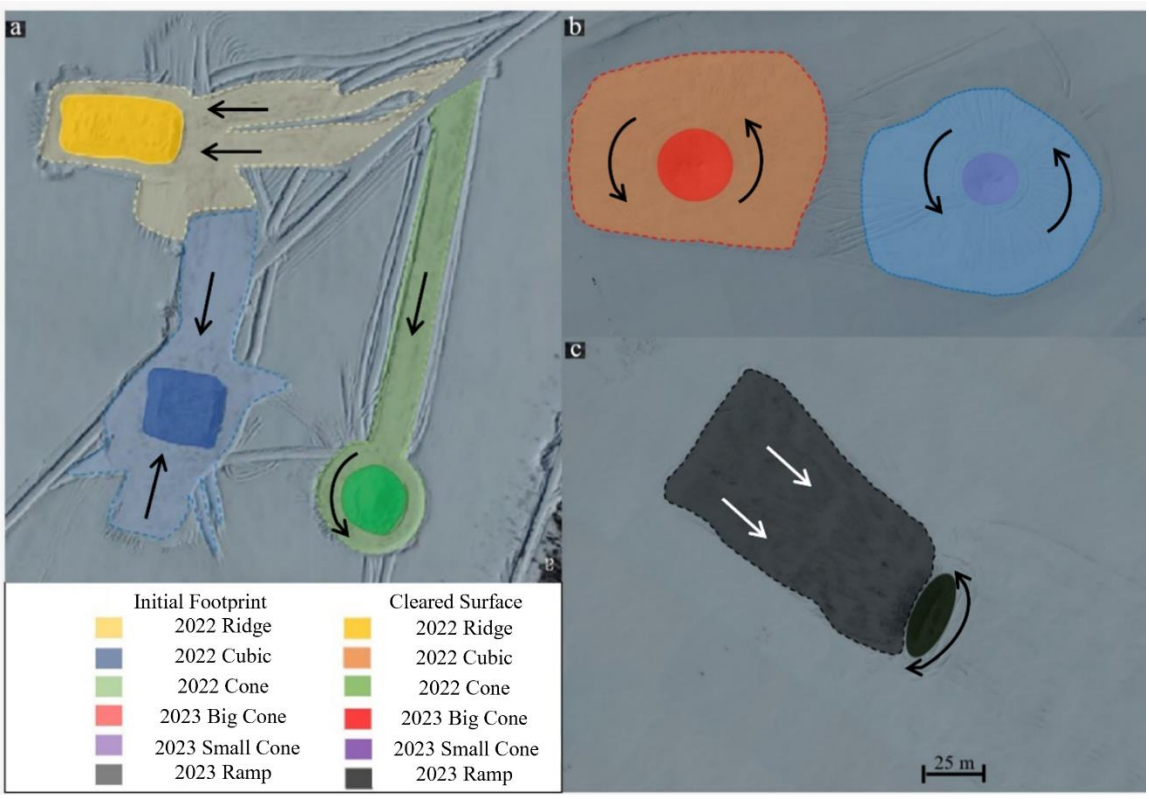

Figure 3.2 (a) Initial footprint, snow-cleared surface, and configuration of the SMPs in Goldex with arrows indicating the equipment movement for SMP construction; (b) and (c) Initial footprint, snow-cleared surface, and configuration of the SMPs in Holt with arrows indicating the equipment movement for SMP construction.

Table 3.1 Configuration, metrics and cleared surface of the tested SMPs.

Year	**Shape**	**Cleared surface (m^2)**	**Initial height (m)**	**Initial footprint (m^2)**	**Initial volume (m^3)**
2022	Cone	3000	7.3	665	1135
	Cubic	4260	3.5	965	2275
	Ridge-shaped	4700	3.5	1150	2565
2023	Big cone	24940	7.33	1950	4130
	Ramp-shaped	21420	5.5	1343	2650
	Small cone	9440	5.6	946	1600

3.3.2 Monitoring snowmelt

The effectiveness of the SMPs at controlling melting rates and delaying the snowmelt period was assessed through periodic measurements of the volume of snow contained in each SMP. The volume of the SMPs was measured through aerial LiDAR and SfM photogrammetry surveys acquired using an unmanned aerial vehicle (UAV). Such remote sensing tools have frequently been used to monitor snowpacks (e.g., Walker et al., 2020; Bash et al., 2020). Aerial surveys were performed with a DJI Matrice 300 RTK UAV equipped, with a DJI Zenmuse L1 Livox Lidar module installed in a single, downward gimbal configuration. The Matrice 300 RTK can operate at temperature as low as -20 °C, and in relatively high-wind conditions (15 m s^{-1}). The selection of such UAV helped to minimize the no-fly conditions often encountered during winter and spring in Canada. The Zenmuse L1 LiDAR sensor has a high-precision inertial measurement unit (IMU) and boasts a ranging accuracy of 3cm at 100m. The Zenmuse L1 LiDAR module supports up to three returns. This sensor also has an RGB mechanical shutter and 1-inch complementary metal oxide semiconductor (CMOS) camera that is suitable for photogrammetry surveys. A DJI-D RTK 2 Mobile Station was connected to the UAV and served as a base station to provide real-time kinematic (RTK) position corrections during data collection. The RTK positioning accuracy was about 1 cm horizontally and 1.5 cm vertically. The automatic survey functions were used to pre-program and fly all LiDAR and SfM photogrammetry surveys performed in this study. The IMU was calibrated before each flight.

In 2022, surveys were performed eighteen times from March 11 to May 27 over an area of approximately 98,500 m^2 (Table 3.2). The surveys performed in 2022 were configured to provide high-resolution acquisitions that were used to confirm the ability of each monitoring technique to accurately monitor the snowpack of small catchments such as TSFs and SMPs in a snowmelt scheme (see Boulanger-Martel et al., 2022). LiDAR scans were performed with a 70% lateral overlap and a three-return repetitive scanning pattern at a rate of 160 kHz. SfM photogrammetry surveys utilized 80% lateral and 70% frontal overlaps. Five to eight ground control points were surveyed to validate georeferencing and assess the accuracy of the surveys. Flights were conducted at an altitude of 50 meters to

obtain high-resolution data that yielded a point cloud density of 787 points m^{-2} and a ground sampling distance (GSD) of 1.26 cm $pixel^{-1}$ (Table 3.2). All surveys were carried out on sunny to partly cloudy days, at roughly the same time of day, to ensure consistent lighting conditions.

In 2023, flight parameters were optimized to balance spatial resolution, acquisition, and reconstruction time. In this case, eight to ten surveys per TSF section were performed between March 23 and May 26, depending on SMP configuration. The surveyed areas were of about 277,000 and 362,000 m^2 for the conic and ramp-shaped SMP sites (Table 3.2). Flights were conducted at an altitude of 100 m to capture high-enough data over these larger areas. This resulted in an average point cloud density of 488 points m^{-2} and a GSD of 2.73 cm $pixel^{-1}$ (Table 3.2). LiDAR and SfM acquisitions were performed using the same settings as in 2022 (Table 3.2).

DJI Terra Pro (v3.4.4) was used to do three-dimensional reconstructions and data analysis. This software uses reconstruction algorithms based on CUDA. A computer with an Intel Core i9-10900 CPU, NVIDIA GeForce RTX 3070 GPU, and 64 GB RAM was used to do the reconstructions in a standalone computation mode. The highest resolution was used for the reconstructions. The mean plane of the TSF surface was used as a reference to calculate the volume for both LiDAR and SfM photogrammetry analyses.

Table 3.2 Overview of Flight, LiDAR, and SfM Photogrammetry Survey Specifications.

Site	Survey parameter	LiDAR	SfM
2022- all SMPs	Flight altitude (m)	50	50
	Total flight distance (m)	7888	5130
	Mapping area (m^2)	98753	98143
	Lateral overlap (%)	70	80
	Frontal overlap (%)	-	70
	Number of optical images	358	560
	GSD* (cm $pixel^{-1}$)	1.26	1.26
	Point cloud density (points m^{-2})	787	-
2023- conic SMPs	Flight altitude (m)	100	100
	Total flight distance (m)	13694	6761
	Mapping area (m^2)	276675	276675
	Lateral overlap (%)	80	80
	Frontal overlap (%)	-	70
	Number of optical images	-	353
	GSD* (cm $pixel^{-1}$)	-	2.73
	Point cloud density (points m^{-2})	489	-
2023- ramp-shaped SMP	Flight altitude (m)	100	100
	Total flight distance (m)	17434	8938
	Mapping area (m^{-2})	361963	361963
	Lateral overlap (%)	80	80
	Frontal overlap (%)	-	70
	Number of optical images	-	472
	GSD* (cm $pixel^{-1}$)	-	2.73
	Point cloud density (points m^{-2})	487	-

3.3.3 Internal and snow-surface temperature monitoring

The temperature at the SMP-tailings interface was measured during the 2022 monitoring period for all SMPs. To do so, three custom made buried thermal monitoring setup were constructed. Such setup involved housing a ZL6 data logger (METER Group) within a waterproof protective case. Four RT-1 (METER Group) soil temperature sensors we then connected to the data logger and ran through the protective case via waterproof wire connectors. All connections were also sealed with silicon-based adhesive. The three thermal monitoring setups were started and buried at the SMP-tailings interface during construction. Data was recorded every 6 hours throughout snowmelt. In addition, the temperature of the snow-surface was also measured on the top as well as north-, south-, east- and west-facing slopes of the ridge-shaped pile using RT-1 sensors connected to ZL6 data loggers. For each station, four temperature sensors were connected to a data logger recording hourly. The temperature of the snow-surface was monitored by installing each RT-1 sensor just beneath the surface of the snow (<5-7 cm) at each site visit. Because of snowmelt, sensors were rapidly exposed to the sun, yielding in abnormally warm temperatures. Thus, a clean up of the obtained data was done to record only actual snow-surface temperature measurements. Such snow-surface temperature measurements were only performed in 2022 because the accessibility of the SMPs was very limited in 2023. However, in 2023 the internal temperatures of the ramp-shaped SMP were monitored at selected heights. Accordingly, the three buried thermal monitoring setups used in 2023 were installed within the ridge-shaped SMP during construction. Sensors were positioned at depths of 1.0, 2.5 and 3.5 m from the surface.

3.3.4 Monitoring snow density

To obtain the volume-mass relationship of the snow contained in the natural ground and within SMPs, several snow density measurements were performed throughout the two field trials (March 11 to May 12 in 2022 and March 22 to May 22 in 2023). All density measurements were taken using a large (100 × 15 cm), custom-made Adirondack-type snow sampler, was used. Made from reinforced PVC pipe with a toothed cutter at the base, the sampler could obtain samples between 15 and 55 cm in length. The mass of each snow sample was then measured using a portable electronic scale. During construction, 38

natural snow density measurements were also performed on undisturbed snow around the SMPs. During snowmelt, 105 snow density measurements (40 in 2022 and 65 in 2023) were taken at various depths, ranging from the surface to the interface between the SMP and the tailings with the SMPs.

3.4 Numerical modeling

The complexity of modeling snowmelt arises from the need to accurately simulate various interacting factors such as temperature fluctuations, solar radiation, and ground conditions, etc. Snowmelt is also a highly coupled phenomena involving several heat transfer mechanisms. In this study, a numerical code was selected to develop a simplified thermal model capable of representing the snowmelt of the tested SMPs. This section aims to present the methodological developments that were made to model the snowmelt of SMPs as well as presenting the calibration results.

3.4.1 Model selection

COMSOL Multiphysics is a comprehensive software suite designed for conducting finite element analysis, solving complex simulations, and facilitating a wide range of physics and engineering applications. Its primary focus is on addressing coupled phenomena and Multiphysics challenges. The software is used to solve conventional physics and enables the handling of interconnected systems involving partial differential equations (PDEs). COMSOL is a versatile simulation software that models various physics and engineering phenomena, including heat transfer, fluid flow, and phase change. Appendix C present General description of equations governing heat transfer in porous media in COMSOL Multiphysics.

3.4.2 Modeling approach

Snow transitions to water when it reaches a temperature close to 0°C. Due to gravity, this water flows through the spaces between snow particles and either exits the pile or refreezes if the air temperature drops during this process. Modeling this phase change and subsequent water movement within the SMP is highly complex. It requires defining the velocity of water particles, modeling the cooling process, and accounting for the refreezing of water within the pile. Additionally, as snow melts and water exit the model, the geometry of the

pile changes due to the reduction in volume. This necessitates updating the model with new geometry and boundary conditions at each step, further complicating the simulation. In this study, the aim was first to model the snowmelt process by integrating various heat transfer mechanisms. The complexity of this task stems from the need to simulate the interactions between temperature fluctuations, solar radiation, ground conditions, and phase changes. Given these challenges, a simplified modeling approach was selected. Thus, the modeling of the melting process of SMPs was simplified to a phase change and conduction problem. In order to avoid the complexity of moving boundary conditions and mass balance issues, the melting problem was simplified to a phase change from snow to a thermal diffusivity material. This approach eliminates the need to solve complex equations related to the movement and exit of water from the model. This material also simplifies the model by avoiding the complications associated with the phase change from snow to water and a downward moving boundary condition. There is no need to model the movement or exit of water, nor to update the geometry and boundary conditions of the pile continuously. By using this high thermal diffusivity material, the model remained manageable while still capturing the essential heat transfer dynamics. Figure 3.3 illustrates the process modeling involved in this project. Although highly simplified, the obtained results are expected to represent well enough the snowmelt of SMPs. Results will be used to further interpret field results and discuss future applications, keeping in mind the main limitations brought by the simpliciations that were made.

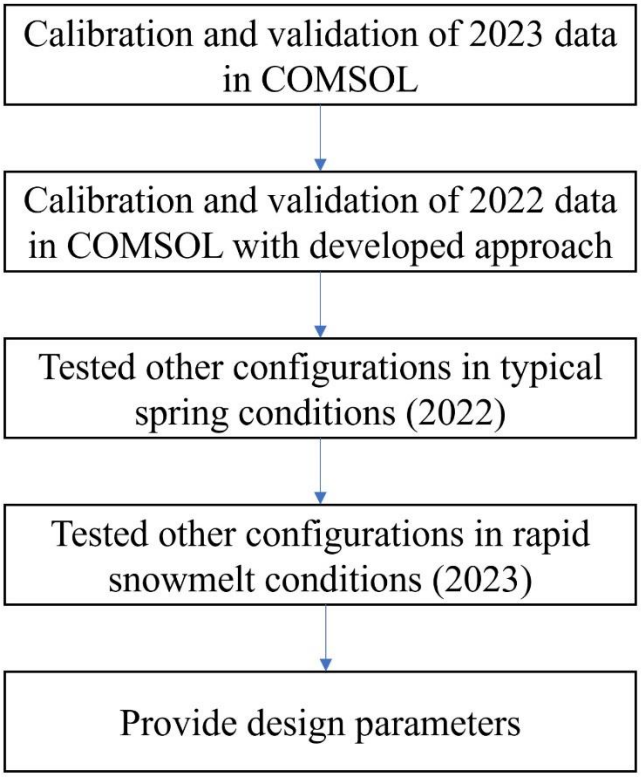

Figure 3.3 The process modeling of the project.

3.4.3 Modeling approach

In the following section, the model parameters will be presented.

3.4.3.1 Geometry

The shapes modeled in the software have approximately the same volume as those created in the field. However, the modeled piles have smooth surfaces without irregularities, whereas the field piles have surfaces with holes. Each SMP is developed and examined from multiple perspectives, with comprehensive details available in Table 3.4. Furthermore, Figure 3.4 depicts the geometry of SMPs within the COMOL software. Figures 3.4.a, 3.4.b, and 3.4.c illustrate cone, cubic, and ridge-shaped SMPs in 2022. Similarly, Figures 3.4.d, 3.4.e, and 3.4.f display the big cone, small cone, and ramp-shaped SMPs in 2023.

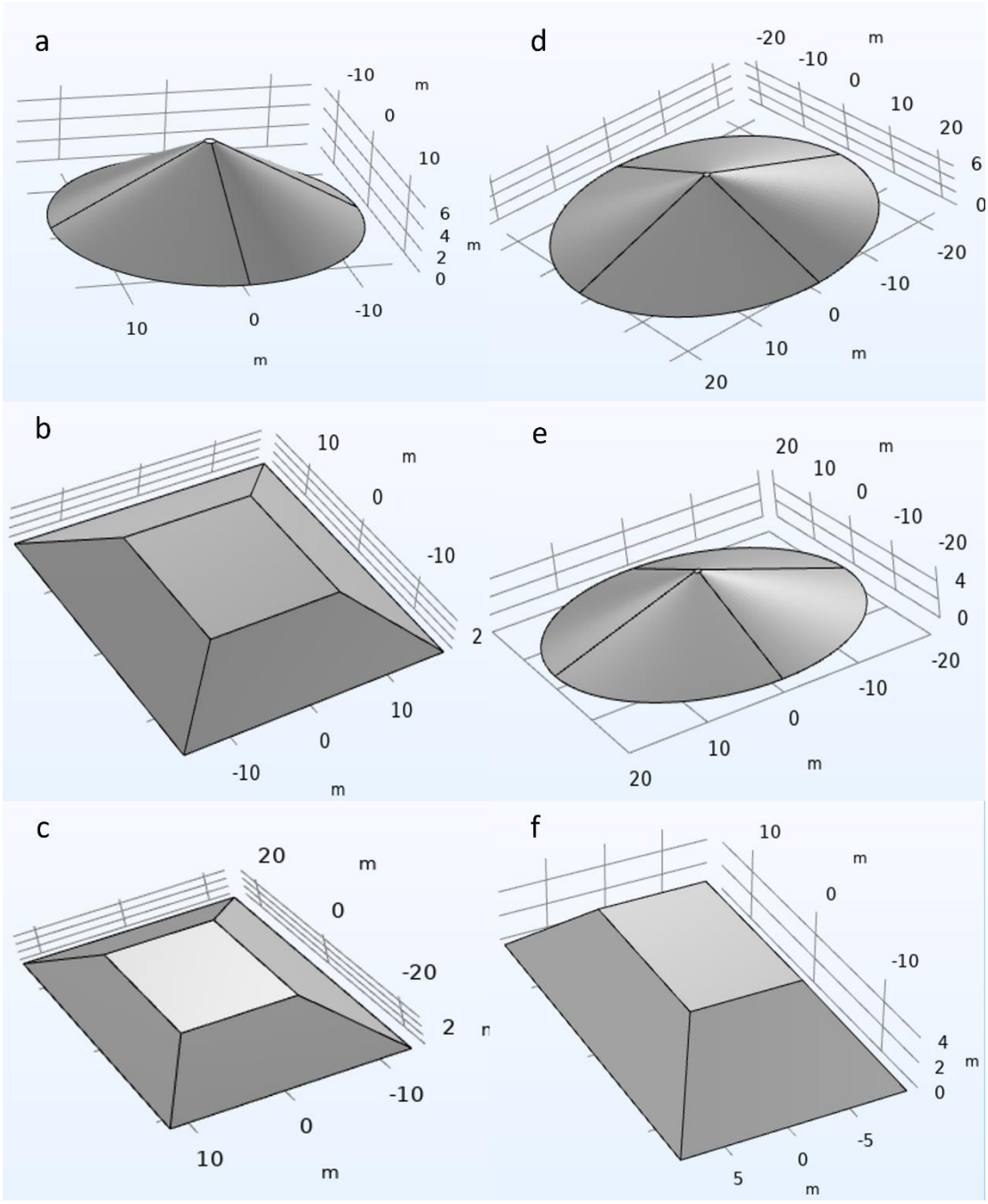

Figure 3.4 Shapes of the SMPs as defined in COMSOL (a) cone SMP, (b) cubic SMP, (c) ridge-shaped SMP in 2022, (d) big cone SMP, (e) small cone SMP, and (f) ramp-shaped SMP in 2023.

Table 3.3. Metrics of the SMPs specified in COMSOL Multiphysics.

Parametre	**Cone (2022)**	**Cubic (2022)**	**Ridge-shaped (2022)**	**Big cone (2023)**	**Small cone (2023)**	**Ramp-shaped (2023)**
Initial length (m)	-	33	50	-	-	30
Initial width (m)	-	33	25	-	-	18
Initial radius (m)	14	-	-	23	20	-
Initial height (m)	7.3	3.5	3.5	7.3	5.6	5.8
Initial footprint (m^2)	615	1089	750	1661	1256	480

3.4.3.2 Mesh

Meshing is a critical component in SMP simulation, influencing both the precision of the results and the efficiency of the computational process. Mesh size is pivotal in determining the stability and accuracy of the simulation. As the mesh becomes finer, the solution converges towards a more accurate representation of the physical phenomena, resulting in more stable numerical results.

While finer meshes enhance accuracy and stablity, they also demand more computational resources, resulting in longer simulation times. For several modeling purposes, medium dimension meshes are often used to ensure that the simulations remain both accurate enough and computationally feasible, avoiding excessively long run times (Hyun et al., 2024). Overall, an optimization of the mesh size is favourable to ensure numerical stability and minimize computation time. In this study, the mesh size was optimized to balance numerical.

Figure 3.5.a illustrates the average error of numerical modeling results for SMPs in 2022 and 2023 using COMSOL, along with the total solution time depending on mesh size. According to this figure, a medium-mesh size (0.2-2m) results in an average error of 5% and a total solution time of 10 minute. Although finer mesh sizes yield slightly lower error rates, the significantly higher total solution times make the medium mesh size a more practical choice.

Figure 3.5.b shows the average error of numerical modeling results for SMPs in 2022 and 2023 using COMSOL, along with the total solution time depending on time step. According to this figure, time step of 1 hour results in an average error of 5% and a total solution time of 10 minute. Although finer time steps (30 minutes or 1 minute) yield lower error rates, the significantly higher total computation times make the time step of 1 hour a more practical choice.

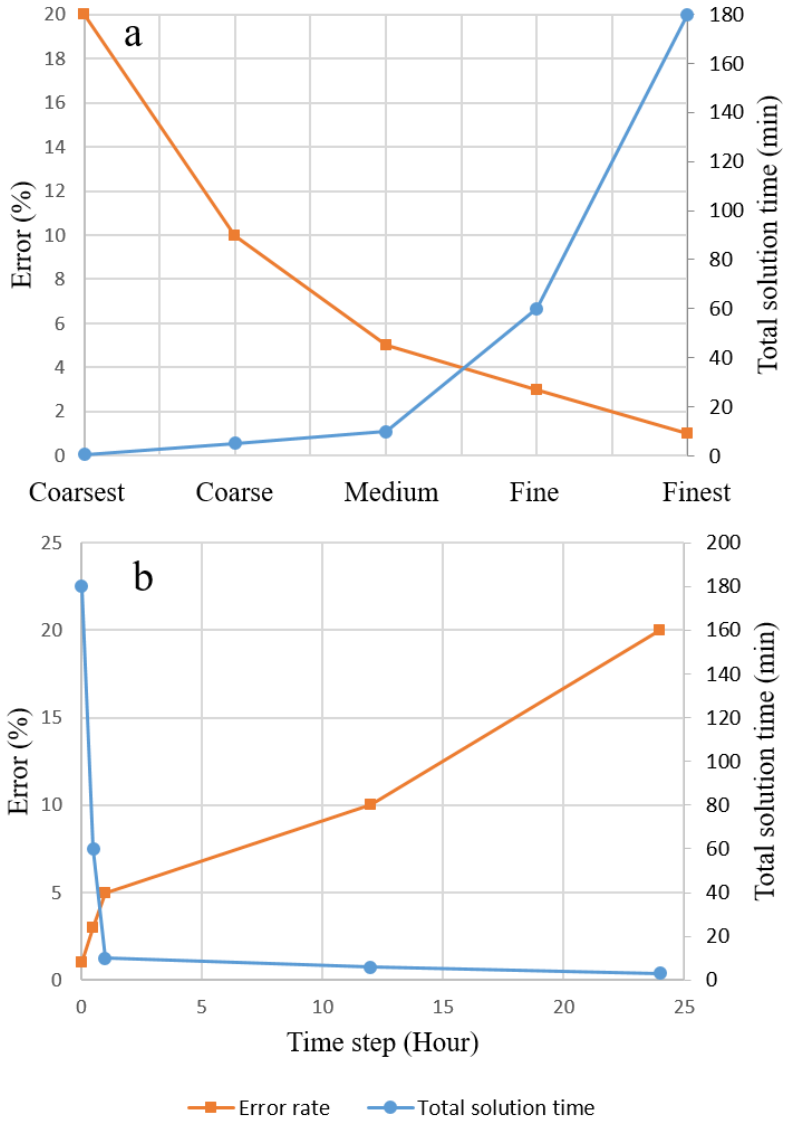

Figure 3.5 (a) Average error of numerical modeing of SMPs in 2022 and 2023 in COMSOL and total solution time depending on the mesh density, and (b) on the time step.

Given the substantial size of the snow piles, a medium-dimension mesh is employed to balance accuracy in the modeling process with manageable run times. This approach ensures that the simulations are both precise enough and efficient. The mesh sizes were set with a maximum dimension of 2 m and a minimum of 0.2 m for all the piles (Figure 3.6). In this project, time step considered in this numerical modeling is 1 hour to balance enough accuracy in the modeling process with manageable run times.

COMSOL also has features that increase numerical stability and accuracy:

- Fine Mesh Near the Surface and Coarser Deeper: COMSOL uses boundary layer meshing to create finer meshes near the surface of the snow piles and coarser meshes deeper within. This method captures important gradients more accurately close to the surface and favour convergence.
- Convergence Criteria: Convergence criteria are imposed to ensure the accuracy of the solution. This involves setting tolerances for residuals or errors in the solution, ensuring that the simulation results are reliable and accurate.

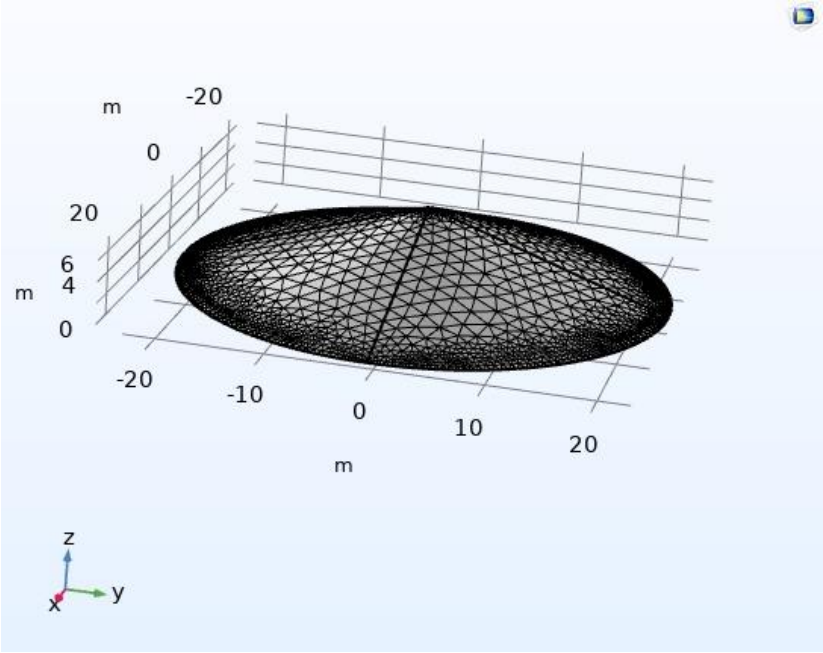

Figure 3.6 Mesh size on a SMP model.

3.4.3.3 Reference temperature, T_{ref}

When materials demonstrate temperature-dependent characteristics, such as thermal conductivity, specific heat, or material density, the reference temperature (T_{ref}) serves as a fundamental point of reference to describe how these properties change with temperature (COMSOL, 2008). As temperature influences material properties, T_{ref} enables the establishment of a standardized temperature value at which the material's properties are well-established and measured (COMSOL, 2008). The thermal strain ($\in_{th}$) due to temperature change is given by:

$$\in_{th} = \alpha(T - T_{ref}) \tag{3.1}$$

Where α is the coefficient of thermal expansion.

In this project, T_{ref} is set to 0°C. By establishing T_{ref} at 0°C, mathematical models and calculations become more straightforward. This simplification allows for easier comparison of temperature-dependent properties without the need to adjust for a non-zero reference point. Setting T_{ref} to zero makes it easier to interpret changes in material properties. For instance, if the temperature is 5°C, it is immediately clear that it is 5 degrees above the reference temperature, simplifying the analysis and interpretation of results. In snow management, 0°C is particularly significant because it is the melting point of ice. Aligning your reference temperature with this critical physical property makes it easier to understand and predict the melting behavior of snow piles.

3.4.3.4 Discretization type of temperature

The PDE and weak form interfaces offer various shape functions with associated element orders, directly impacting the solution's accuracy and the number of degrees of freedom. Increasing the element order corresponds to refining the mesh uniformly. Most physics interfaces employ Lagrange elements, typically of order 1 to 5 (or 1 to 7 for the PDE and weak form interfaces), with 2 being the default order in many cases (COMSOL, 2008). In certain situations, where serendipity elements are available (e.g., in mathematics interfaces and Solid Mechanics interfaces for element orders 2, 3, and sometimes 4), they can be more efficient than Lagrange elements of the same order in terms of the number of elements and solution time, particularly for hexahedral meshes. However, they might also be more

sensitive to distorted mesh elements (COMSOL, 2008). In this case, the software automatically adjusts the numerical integration order based on the element orders specific to the physics involved in the model. Some physics interfaces utilize element types or lower element orders for specific field variables. Users can usually choose Shape function types and Element orders as Linear, Quadratic, Cubic, Quartic, or Quintic (corresponding to orders 1–5, respectively) (COMSOL, 2008).

In this project, a linear function was chosen as the shape function. Linear elements, characterized by linear shape functions, simplify the mathematical formulation and computational process. This leads to faster solution times because the calculations are less complex compared to higher-order elements (Zohdi, 2015). Linear elements require fewer degrees of freedom and less memory, making them more efficient in terms of computational resources. This is particularly beneficial when dealing with large-scale problems or limited computational power (COMSOL, 2008). For problems where the solution does not involve significant curvature or bending, linear elements can provide sufficient accuracy. They are often adequate for problems involving simple geometries and boundary conditions (COMSOL, 2008). Linear elements also simplify the mesh generation process, especially for complex geometries. This can save time and reduce potential errors in the meshing stage (COMSOL, 2008). In this project linear elements are used in this project.

3.4.3.5 Porous medium type

In this project, the local thermal equilibrium (LTE) model has been chosen over other models. (see appendix C for more details) The LTE model assumes that the solid and fluid phases within the porous matrix are at the same temperature (Bansal and Suthar, 2024). This allows for a single unified heat transfer equation, simplifying the mathematical formulation and reducing computational complexity (Bansal and Suthar, 2024). Since the LTE model involves solving only one heat transfer equation, it requires fewer computational resources compared to the local thermal nonequilibrium (LTNE) model, which necessitates solving separate equations for the solid and fluid phases. This can lead to faster simulation times and lower memory usage (Bansal and Suthar, 2024).

3.4.3.6 Materials

In the snow melting process model, the software defines two distinct materials: one representing snow and another with high thermal conductivity to simulate the downward-moving boundary condition. The high thermal conductivity ensures a minimal temperature difference between the boundary condition and the actual value slightly below it. This material represents melting water and is replaced with air in the model. Essentially, the high thermal conductivity material allows the air function to be applied to the snow surface at each step while maintaining the shape and dimensions of the snow pile. This approach helps create a satisfactory simulation of the snow melting process by effectively modeling heat transfer and the interaction with air. Table 3.4 shows the properties of the materials for snow and the high thermal conductivity material as specified in the software. Snow density was determined using the average values from field measurements. The porosity, heat capacity, and thermal conductivity of the snow were estimated using equations 2.6, 2.14, and A.5. For high thermal conductivity materials, natural options were considered. Copper, one of the most thermally conductive natural materials, can transfer heat quickly. Therefore, the high thermal conductivity material in question has properties similar to copper, and these values are predefined in the COMSOL software.

Table 3.4 Material properties used for snow and the high thermal conductivity material as specified in COMSOL Multiphysics.

Parametre	**Snow**	**High thermal conductivity material**
Heat Capacity	1714 (J Kg^{-1} K^{-1})	390 (J Kg^{-1} K^{-1})
Density	600 (Kg m^{-3})	8900 (Kg m^{-3})
Thermal Conductivity	0.867 (W m^{-1} K^{-1})	390 (W m^{-1} K^{-1})
Porosity	0.35	0.1

3.4.3.7 Phase change temperature and latent heat

The Phase change temperature between phase 1 and phase 2 $T_{pc,\,1\rightarrow 2}$ should be set to define the center of the first transition interval. In this project, the following function is used to

change the phase of the materials. In this function, the phase change between snow and the high thermal conductivity material begins at -1°C and completes at 0°C (equation 3.2). This transition occurs continuously and smoothly, closely mimicking the natural phenomenon. Figure 3.7 shown the shape of thishe phase change function that was used to describe the phase change between snow and the high thermal conductivity model. The value of latent heat of phase change from water to ice is 333 kJ kg^{-1}.

$$\alpha_{\mathbf{1\rightarrow 2}} = exp\left(-\left(\frac{T-0}{0.5}\right)^2\right) * (T < 0) + 1 * (T \geq 0) \quad (3.2)$$

Where $\alpha_{\mathbf{1\rightarrow 2}}$ is the phase transition between phase 1 (snow) and phase 2 (high conductive material), and T is the temperature (°C).

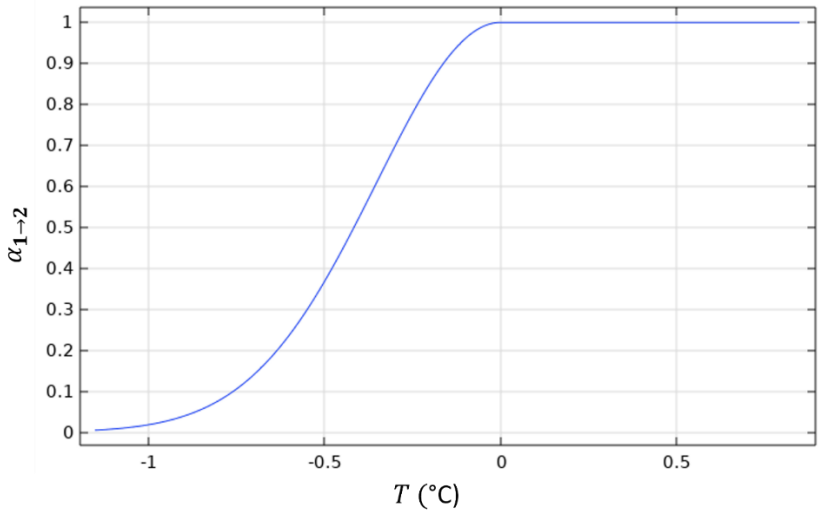

Figure 3.7 Phase change temperature function. The x-axis indicates the temperature inside the pile and the y-axis indicates the phase transition.

3.4.3.8 Ground temperature, initial temperature and bottom boundary condition of SMPs

Figure 3.8 illustrates the typical evolution of temperature at the interface between SMPs and the ground at the beginning of the melting process, which occurs from the end of March to mid-May (further discussed in Chapter 4). According to the figure, the initial temperature of the SMPs was approximately -4.5°C, which rose to -0.1°C after six days.

The blue line in the diagram represents the regression used to define the equation in the software. The defined equation is used as bottom boundary condition:

$$\begin{cases} D \leq 6: T = 0.6357 * D - 4.5 \\ D > 6: T = -0.1 \end{cases} \quad (3.3)$$

According to field data, the initial internal temperature of the SMPs was set to -5°C.

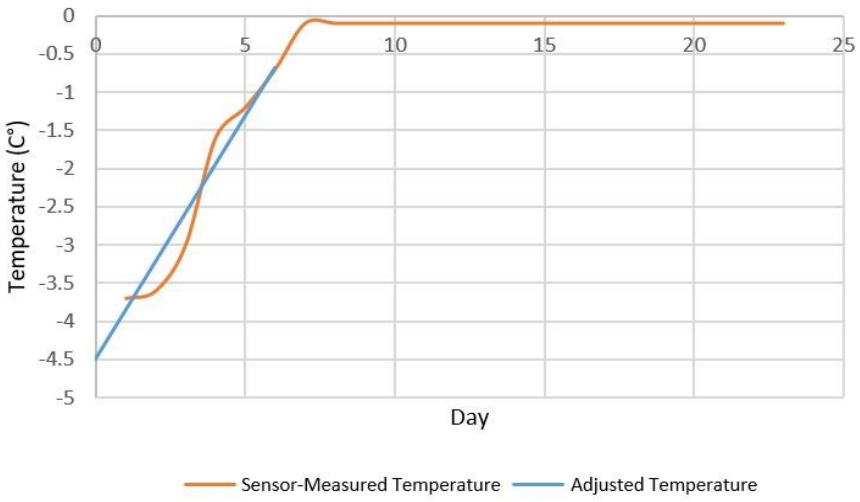

Figure 3.8 Evolution of the temperature at the SMP-ground interface in 2023.

3.4.3.9 Calibration of a snow-surface temperature function based on measured air temperature and establishment of the SMP surface boundary condition

Because air temperature fluctuates significantly from hour-to-hour and day-to-day during snowmelt, a calibrated surface boundary condition had to be developed to ensure numerical stability and convergence. The data from 2023 at Kirkland ECC station were first used to assess the best potential option to establish such boundary conditions. Such an approach came down to fit a polynomial curve representing the 100 days of snowmelt (more details in Chapter 4). Doing so resulted in the development of a site- and time-specific boundary condition that represented well the melting behavior of the tested SMPs and that could also be used to test different SMP sizes and configurations exposed to the 2023 Kirkland Lake climatic conditions. The same approach was then applied to the 2022 tested SMPs, using the Val D'Or station air temperature data (more details in Chapter 4). The 2022 climatic

conditions were used as ‘typical spring conditions’ in the modeling work that was done to extend the understanding of the melting behavior of SMPs in general (other sizes and configurations) whereas the 2023 climatic conditions were deemed representative of a rapid snowmelt.

CHAPTER 4 FIELD RESULTS AND MODEL CALIBRATION

4.1 General approach

This section presents the comprehensive field results gathered from the study, covering various aspects including temperature, precipitation, snow thickness, and their impact on SMPs. The data on temperature, precipitation, and snow thickness is analyzed to understand their effects on the study sites, including seasonal variations and their implications for the SMPs' performance. The observed snowmelt patterns of the SMPs are highlighted, showing differences in melting rates under various conditions. An assessment of snow density and its impact on the melting process is conducted, including measurements during different periods and their correlation with temperature changes. The effect of the slope on the performance of SMPs is examined. A comparison of the size parameters of SMPs is presented, detailing how size variations affect their performance. The efficiency of various sizes and shapes of SMPs is evaluated, providing a clear picture of which configurations yield the best results in terms of melting efficiency and stability. The relationship between temperature variations and the melting behavior of SMPs is explored, analyzing how different temperature profiles impact the rate and extent of snowmelt. The numerical modeling results are presented, showcasing the calibration and validation of the models used in the study. The results from field-tested SMPs are analyzed and compared with the numerical model predictions, helping to validate the accuracy of the models and providing insights into any discrepancies. Finally, a detailed comparison of the numerical modeling results and actual field results is provided, highlighting the strengths and limitations of the models and offering a comprehensive understanding of their reliability and accuracy in predicting the behavior of SMPs under various conditions.

4.2 Field results

The following sections will present the field results data.

4.2.1 Temperature, precipitation, and snow height

The temporal evolution of the average air temperature, precipitation and the thickness of the snow on the ground is provided at Figure 4.1 for 2022 (ECC-MSC VAL D’OR station)

and at Figure 4.2 for 2023 (ECCC KIRKLAND LAKE and ECCC-MSC VAL D'OR stations).

In 2022, the average daily temperatures during the monitoring period ranged from -22°C to 23°C. The average air temperature fluctuated above and below 0°C. Notably, on February 26, 2022, the average temperature rose above 0°C for the first time. During this time, the thickness of natural snow on the ground varied slightly until April 23. Initially, the snow depth decreased until March 25, then increased until March 30. After March 30, the snow depth began to decline, and by April 24, all-natural snow had melted. During this melting period, the air temperature rose from -15 to 6°C. This indicates that natural snow was present from the start of the monitoring period until April 24. Ultimately snowmelt occurred for 2 weeks. Figure 4.1 shows that rising air temperatures significantly influenced snow melting. Conversely, when temperatures were below zero, snow melting slowed or halted. Additionally, increased rainfall contributed to snow melting. For instance, snowfall on March 24 increased the snow depth, while up to 15 mm of rain at the end of April accelerated the melting process.

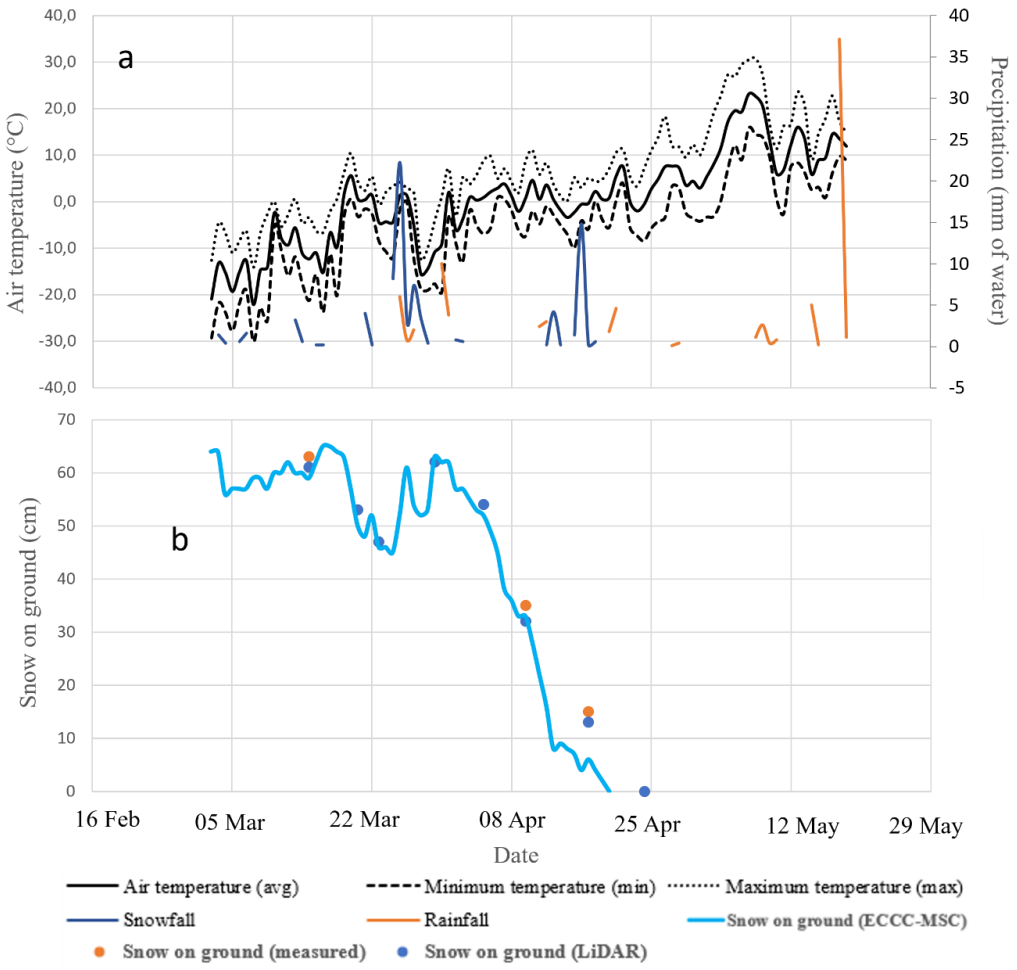

Figure 4.1 (a) Daily climatic parameters recorded at the ECCC Val d'Or weather station, and (b) comparison of the snow on the ground measured at the ECCC-MSC Val d'Or with field measurements and LiDAR surveys.

In 2023, the average temperatures during the monitoring period ranged from a high of 12°C to a low of -12°C. The average air temperature has been above 0°C from 6 April. Unlike 2022, the average air temperature in 2023 did not fluctuate above and below 0°C. Notably, on April 6, 2023, the average temperature rose above 0°C for the first time. During this time, the thickness of natural snow on the ground varied. Initially, the snow depth decreased to 60cm until March 31, then increased to 70cm until April 5. After April 6, the snow depth began to decline, and by April 14, all-natural snow had melted. The duration of snowmelt was 5 days. In 2023, one of the significant observations was the rapid snowmelt. Temperatures soared to over 20°C, causing the snow to melt almost entirely and very quickly. This indicates that natural snow was present from the start of the monitoring

period until April 14. Figure 4.1 and 4.2 show that rising air temperatures significantly influenced snow melting. Conversely, when temperatures were below zero, snow melting slowed or halted. Snowfall at the end of March increased the snow depth. Since mid-April, the snowfall has transitioned to rain due to rising temperatures.

The evolution of snow thickness over time, as monitored by the ECCC weather station, manual measurement techniques, and LiDAR surveys at both 2022 and 2023, is depicted in Figure 4.1b and 4.2b. Notably, all measurement methods yielded comparable results for snow thickness, suggesting their reliability and consistency. Consequently, the ECCC's snow-on-ground curve can serve as an effective representation of site conditions.

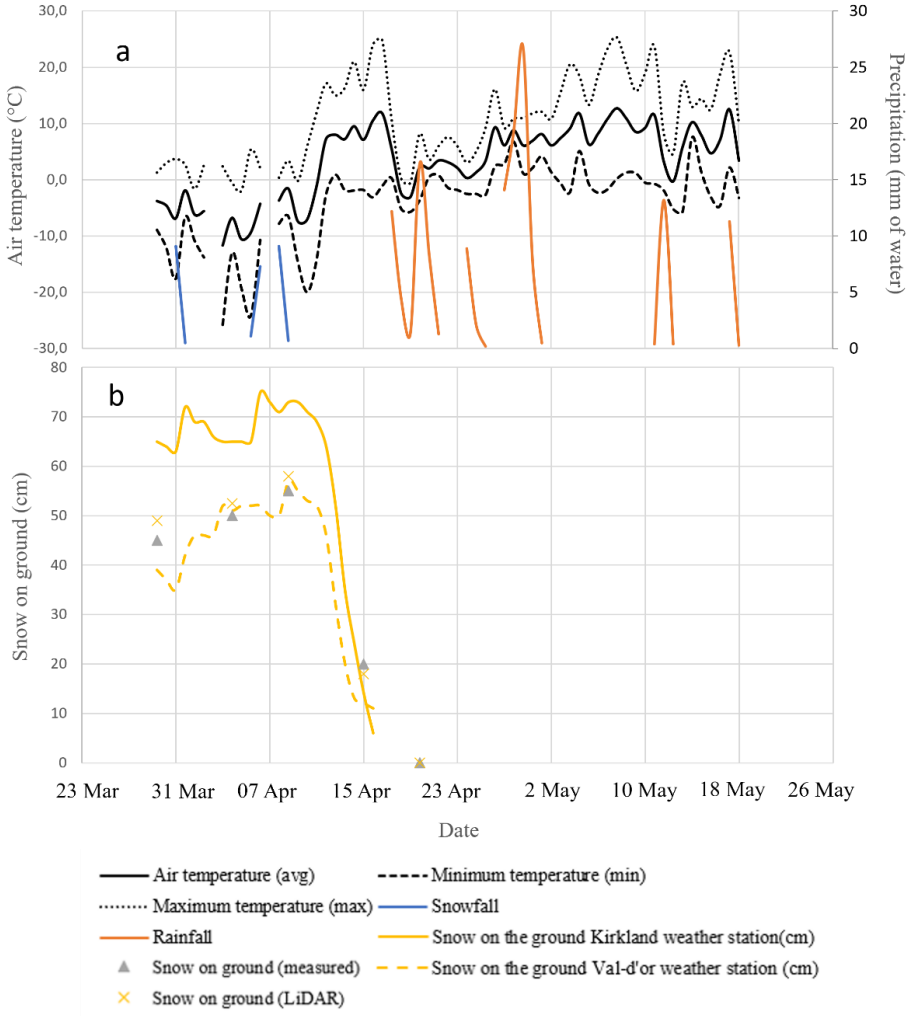

Figure 4.2 (a) Daily climatic parameters recorded at the ECCC Kirkland weather station, and (b) comparison of the snow on the ground measured at the ECCC-MSC Kirkland and Val d'Or weather station with field measurements and LiDAR surveys.

4.2.2 Snowmelt of SMPs

Figure 4.3a depicts the volume changes for each of the SMP constructed in 2022 using both Lidar and SfM photogrammetry. The SMPs were constructed by March 11, 2022. The initial average volumes for the ridge-shaped, cubic, and cone SMPs were 2565 m^3, 2275 m^3, and 1355 m^3, respectively. Despite its smaller volume, the cone SMP took the longest to melt. In general, the reduction of pile volumes follows a same pattern. As mid-May approaches, the reduction rate of ridge-shaped and cubic piles accelerates, diverging from the behavior of the cone pile. On May 15, the cone pile's volume, previously lower than the others, surpasses theirs. The cubic pile volume reaches 0 m^3 first on May 15, followed by the ridge-shaped pile, with the cone pile reaching 0 m^3 on May 24. The discrepancy between LiDAR and SfM data measurements for the cone pile was smaller compared to the other two piles. The difference ranged from 50 to 100 m^3 for the cone pile, whereas for the cubic and Ridge piles, the minimum difference was 350 m^3, with the minimum error at the end of the period being 60 m^3.

Figure 4.3b illustrates the changes in footprint size for each SMP in 2022. Initially, the footprints for the ridge-shaped SMP, cubic SMP, and cone SMP were 1150 m^2, 965 m^2, and 665 m^2, respectively. Initially, the ridge-shaped pile had a larger footprint compared to the other piles. However, over time, the volume reduction rate of the ridge-shaped pile accelerated. By May 9, the footprint of the two ridge-shaped and cubic piles reached 600m^2, after which they followed the same decreasing trend. The footprint of these two piles continued to diminish after May 9. Meanwhile, the cone pile experienced a consistent reduction in footprint without fluctuations. Although it started with a smaller footprint, by May 15, the footprint of the cone pile exceeded that of the other piles.

Figure 4.3c shows the heights of each SMP. The initial heights for the cone SMP, ridge-shaped SMP, and cubic SMP were 7.32 m, 3.52 m, and 3.49 m, respectively. Initially, the cone pile was taller than the other piles. The height reduction process follows a consistent pattern. The height changes of the cubic and ridge-shaped piles were almost identical. On May 15, the heights of both the ridge-shaped and cubic piles reached 0m, while this occurred for the cone pile on May 24. The height reduction of the cone pile showed an increase on May 9.

The green line in Figure 4.3 illustrates that all-natural snow on the ground had melted by April 25th. This suggests that the creation of SMPs postponed the snowmelt by 2 to 5 weeks.

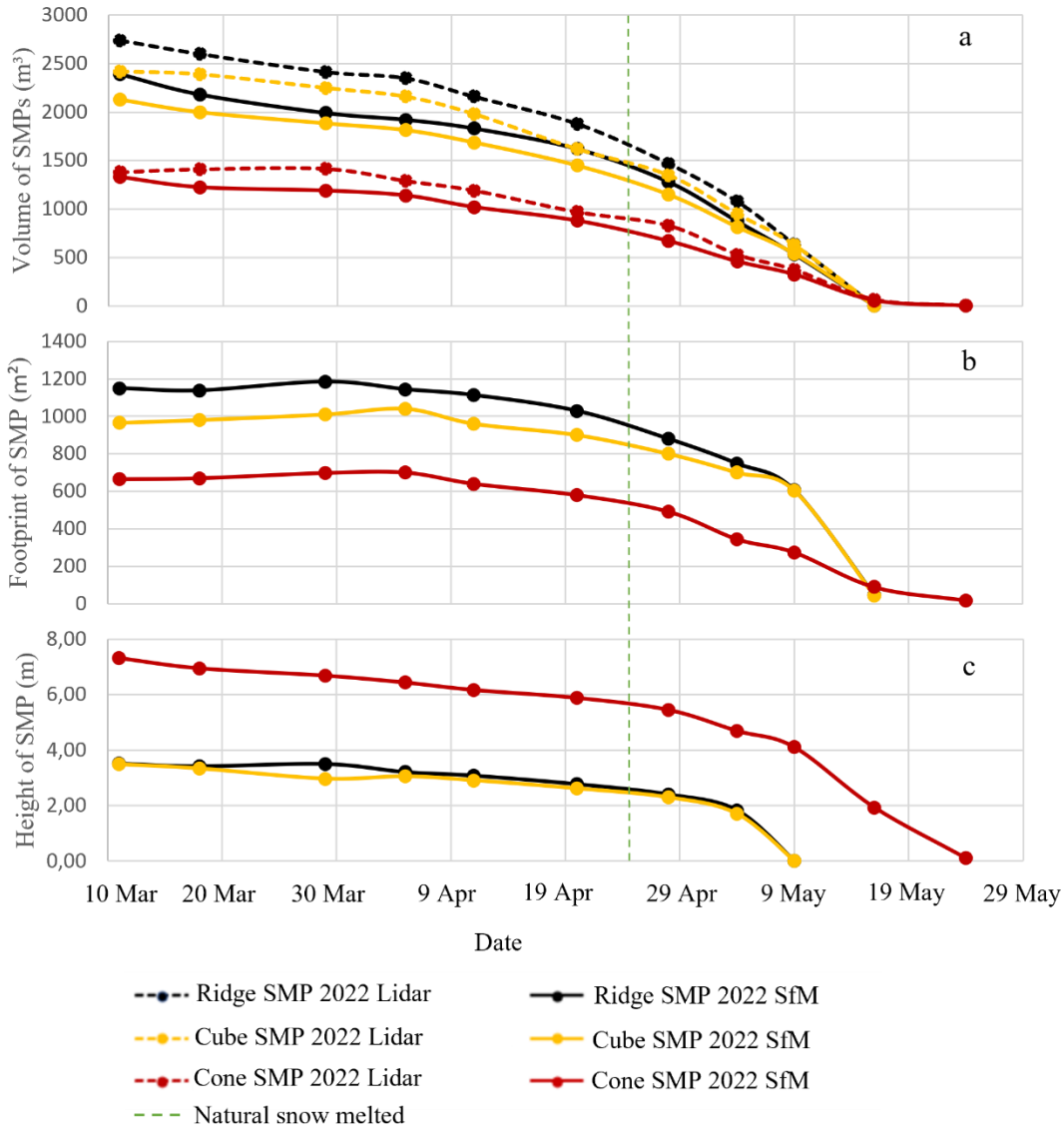

Figure 4.3 (a) Volume, (b) footprint, and (c) height measured for the SMPs throughout the monitoring period as determined by LiDAR and SfM photogrammetry in 2022.

Boulanger-Martel et al. (2022) noted that the absolute volume obtained for each SMP at any given time varied slightly depending on the measurement method. While the measured heights and footprints of SMPs were similar, the overall volumes measured by LiDAR

were generally greater than those computed using SfM photogrammetry. These discrepancies are likely due to the limitations of LiDAR and SfM photogrammetry in capturing and representing all features and snow conditions associated with snowmelt. For instance, LiDAR may have poor signal returns when water is present, and SfM photogrammetry may struggle with over-saturated snow-covered zones (Boulanger-Martel et al., 2022). Despite these differences, the trends in the volumetric decreases of SMPs were consistent.

In 2023, the construction of the SMPs was completed on March 23. The average initial volumes for the big cone, small cone, and ramped-shaped SMPs were 3628 m^3, 2213 m^3, and 1608 m^3, respectively. Notably, the big cone SMP melted later than the other SMPs (Figure 4.4a). The volume discrepancy measured by LiDAR and SfM for the ramp-shaped pile started at 500 $m^3$and decreased to 50 m^3over time. This trend was similar for both the big cone and small cone piles. For the big cone and small cone piles, the maximum difference was 450 m^3, while the minimum difference was 15 m^3. The melting process of all three piles follows a consistent pattern, with fluctuations occurring on April 25. The volume of the ramp-shaped pile reached 0 m^3 on May 4, followed by the small cone pile on May 11 and the big cone pile on May 19.

Figure 4.4b illustrates the initial footprints for the big cone, small cone, and ramped-shaped SMPs were 1950 m^2, 1343 m^2, and 946 m^2, respectively. Like the volume change, the footprint change for all three piles follows a consistent pattern. The footprint of the ramp-shaped pile reached 0 m^2 on May 4. The small cone's footprint dropped to 0 m^2 on May 11, followed by the big cone on May 19.

Figure 4.4c illustrates the height of each SMP, with the initial heights being 7.6 m for the big cone, 5.80 m for the ramped-shaped, and 5.58 m for the small cone. The height reduction process for all three piles follows a similar pattern. Interestingly, the small cone pile initially had a lower height compared to the other piles, but after April 9, its height decreased more slowly than the ramp pile. This indicates that the ramp-shaped pile's height decreased at a faster rate. Ultimately, the height of the ramp-shaped pile reached 0 m on May 4, the small cone on May 11, and the big cone on May 19.

The green line in Figure 4.4 illustrates that all-natural snow on the ground had melted by April 20th. This suggests that the creation of SMPs postponed the snowmelt by 4 to 8 weeks.

Differences in absolute volume measurements between SfM and Lidar similar to that of 2022 were observed in 2023. Because the trends are similar, an average of both measurement methods will be used from now on to push the interpretation further.

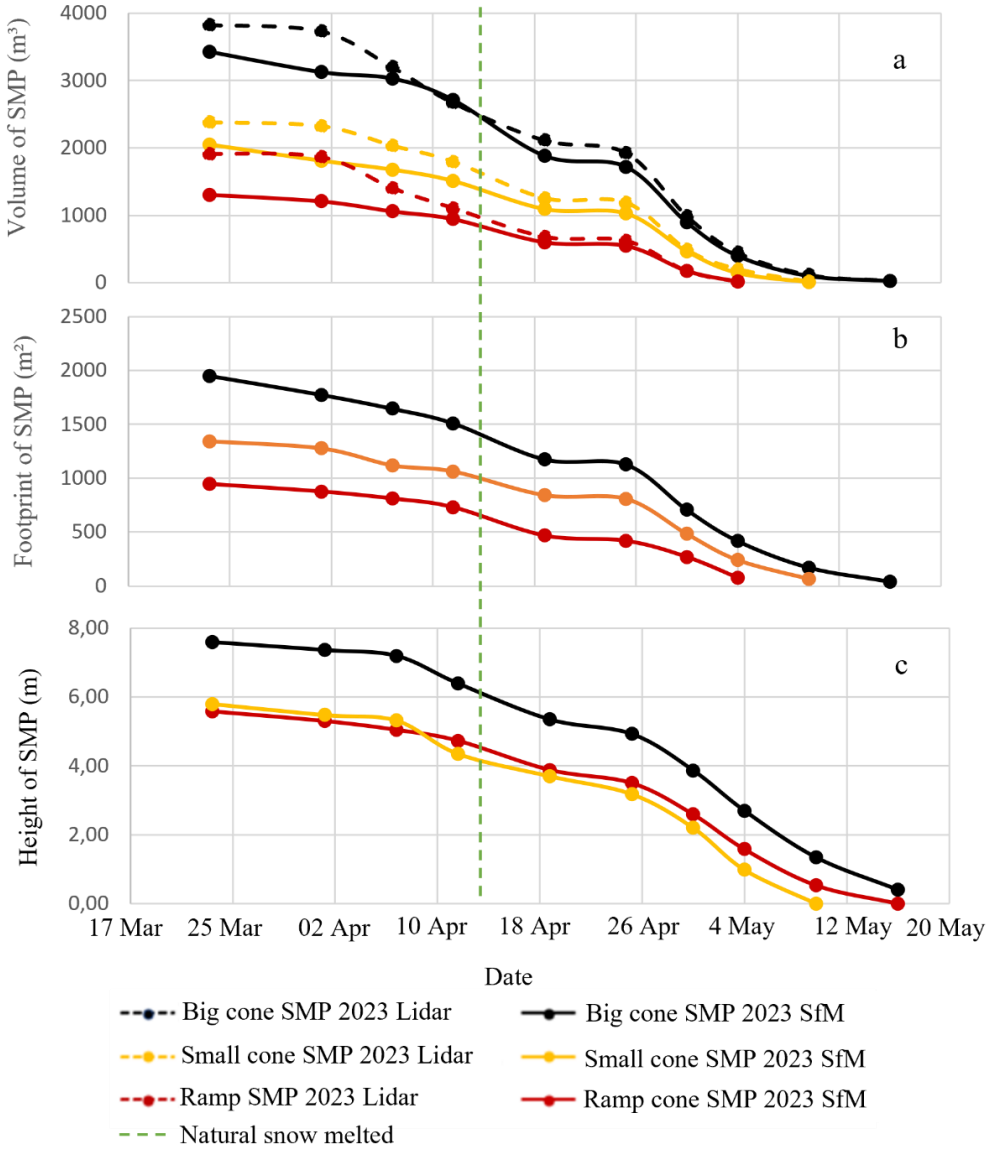

Figure 4.4 (a) Volume, (b) footprint, and (c) height measured for the SMPs throughout the monitoring period as determined by LiDAR and SfM photogrammetry in 2023.

4.2.3 Assessment of snow density

Throughout the entire duration spanning from the initiation of SMP construction until its eventual melting, there are fluctuations in the density of the snow. Figure 8c is segmented into three parts to illustrate distinct phases of snow density changes. In Part A, 23 snow density samples are presented from undisturbed ground conditions. Part B showcases density samples collected during SMP construction, while Part C depicts density measurements post-construction up to the onset of melting. Notably, there's a discernible increase in snow density from 250 kg m^{-3} to 600 kg m^{-3}, indicating that SMP construction led to densification by reducing air voids within the snow structure through compaction.

Further analysis in Part C reveals a subsequent rise in snow density, climbing from 600 kg m^{-3} to approximately 700 kg m^{-3} between late March and May, attributed to rising temperatures, and finally reached to 900 kg m^{-3} at the end of May. This heightened density is attributed to snowmelt and the consequent formation of water within the SMP.

As spring arrived, SMPs contained a mixture of snow, ice, and liquid water (Figure 4.5b). Meltwater and rainwater percolated to the bottom, increasing the snow's density, and creating more distinct layers. At the base, where the SMP met the tailings, there was an ice layer 10 to 20 cm thick with a density of approximately 910 kg m^{-3}. Above this ice layer, a 10 cm thick capillary fringe had an average density of 850 kg m^{-3}. The density decreased with height, averaging 600 kg m^{-3} at heights of 50 cm or more. Figure 4.5a illustrates this depth profile. The black-highlighted area indicates samples taken during the spring, while samples outside this area were collected in winter. These observations also show that a 20 cm thick ice layer forms within the SMP after the melting process.

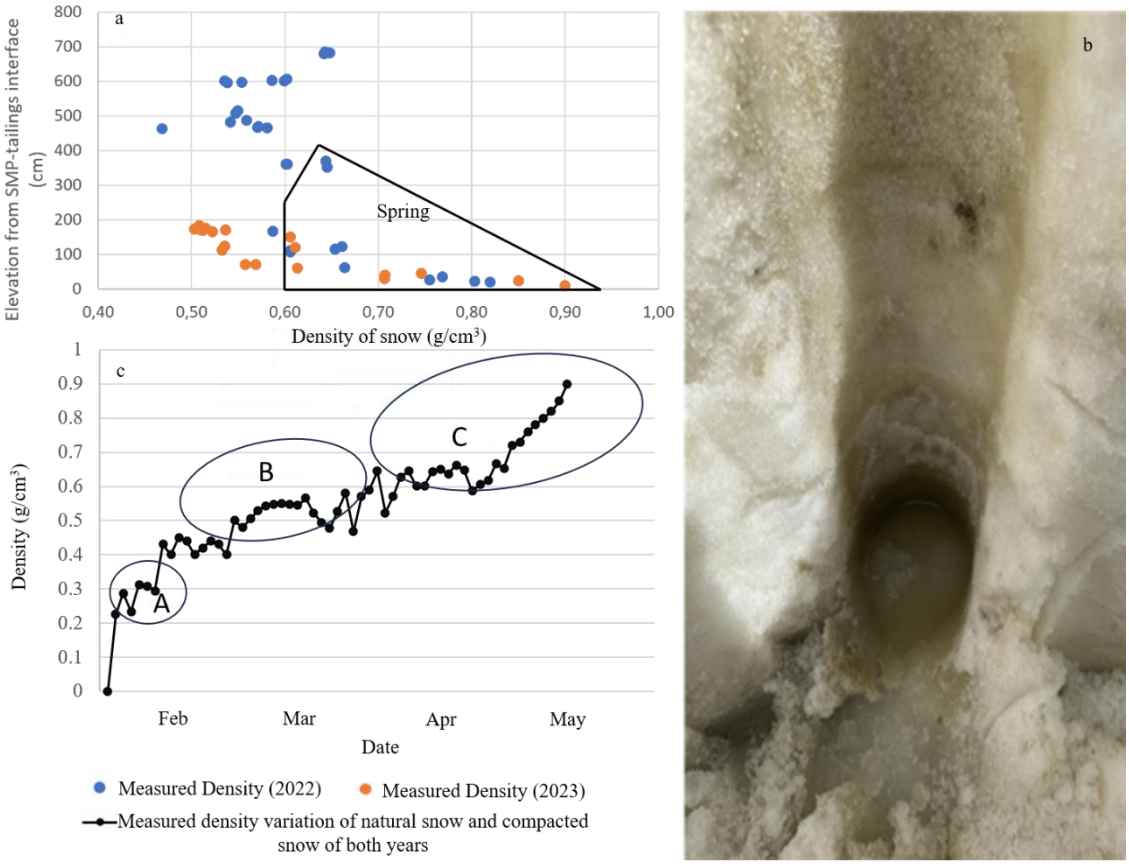

Figure 4.5 (a) The relationship between snow specific gravity at various elevations from the interface of SMP-tailings in 2022 and 2023, (b) The system involving snow, liquid water, and ice that formed within the SMP, and (c) Measured density variation of natural snow and compacted snow of both years

4.2.4 Effect of SMP's slope angle

Utilizing varying equipment during the construction of SMPs results in different side slopes. Illustrated in Figure 4.6 are the slopes of six distinct SMPs erected in 2023 (Figure 4.6b) and 2022 (Figure 4.6a). Notably, the slopes of SMPs in 2023 are softer compared to those built in 2022. This is essentially attributed to the construction methods; Utilizing a groomer yields to slopes much softer sloped than when loaders and bulldozers are used. Additionally, the variations in slope could be influenced by the contrasting sizes of the SMPs between the 2022 and 2023. Enlarging the SMP footprint may contribute to mitigating slope steepness.

Among the six SMPs constructed, the conical SMPs in 2022, exhibited the steepest slope while the most gradual incline was observed in the small cone in 2023.

Furthermore, it is important to note that a minimal slope on the SMPs can facilitate uniform melting of snow across all its sections. For instance, in 2023, SMPs have gradually attained slopes of less than 3 degrees over time, indicating a consistent decrease in SMP height corresponding to the reduction in footprint. This uniform slope contributes to an even melting process, ensuring that all sections of the piles melt at a similar rate.

Conversely, in 2022, the slope of the SMPs remained steep for a longer period, not decreasing to less than ten degrees until the final stages of melting. This suggests that the rate of height reduction was not uniform, with steeper sections of the piles storing more snow per footprint unit, thereby melting at a different rate compared to flatter sections. The gradual decrease in slope angle throughout 2022 led to an uneven melting process, with sections of the piles melting at different rates.

In contrast, the more drastic drop in slope observed in 2023 allowed for a more consistent melting pattern. The SMPs started with a steeper slope but quickly transitioned to a flatter angle, promoting uniformity in the melting process, and reducing the disparity in height reduction rates. This indicates that managing the slope of SMPs can significantly influence the melting behavior, with steeper slopes initially storing more snow per footprint unit but requiring more time to reach a uniform melting state.

Thus, the management of slope angles in snow piles is crucial for ensuring an efficient and uniform melting process. The observed patterns in 2022 and 2023 illustrate how changes in slope can impact the melting dynamics and the overall reduction in snow pile volume and height.

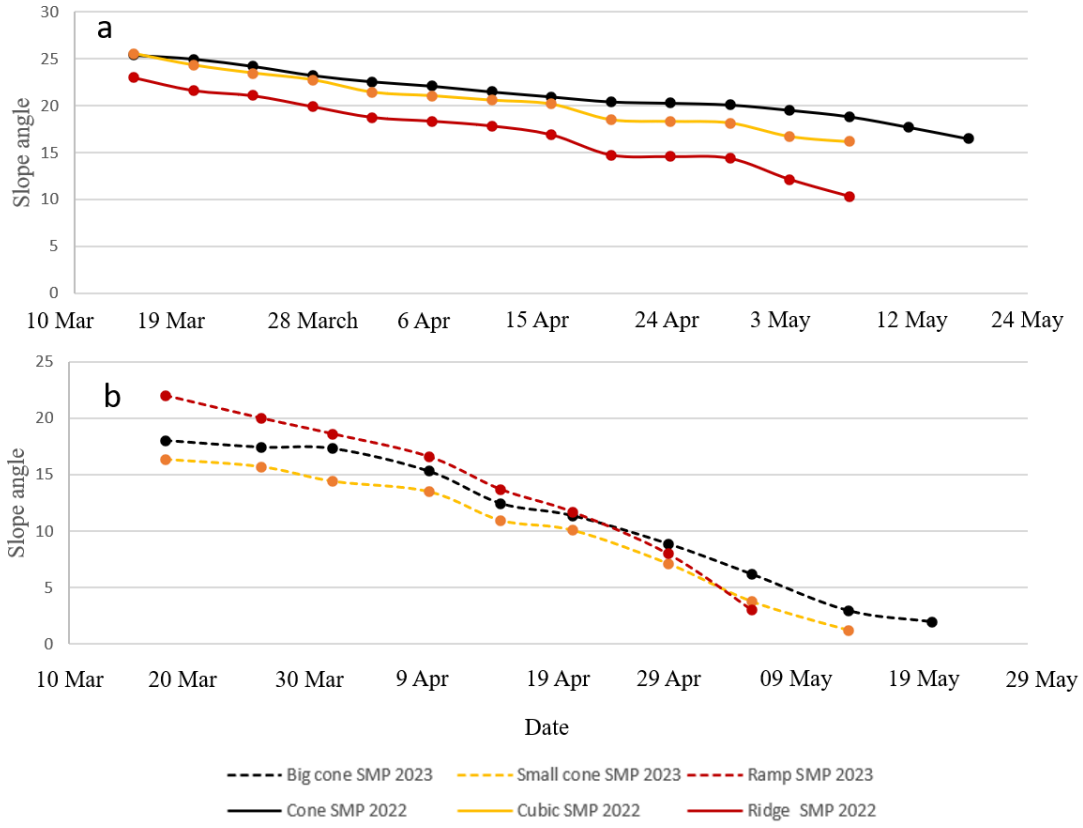

Figure 4.6 Slope of SMPs built in (a) 2022 and (b) 2023.

4.2.5 Effect of configuration and climate on melting behaviour

To enable comparison of SMP effectiveness in managing snowmelt in the two different climatic contexts (of 2022 and 2023), the evolution of the fraction of key SMP metrics is represented for the time from the beginning of the snowmelt (Figure 4.7). In Figure 4.7a, it is evident that volume reduction in SMPs in 2022 exhibits a consistent pattern, whereas, in 2023, this trend occurs in a staircase process. Notably, in early April, there is a notable observation that initially, the small cone SMP experiences a greater volume loss compared to the ramped-shaped SMP, but by the third week of April, this pattern reverses, with the ramped-shaped SMP melting earlier than the cone SMP.

Figure 4.7b illustrates that the reduction in footprint in both years. In 2023, SMPs follows a similar trend until mid-April, after which the rate of reduction accelerates notably for the ramped-shape SMP. Conversely, in 2022, the cone SMP exhibits a faster decrease in

footprint area compared to the ridge shaped and cubic SMPs. Notably, the ratio of SMP footprint changes in 2023 consistently surpasses that in 2022.

Examining Figure 4.7c reveals that the rate of height change in all SMPs follows a similar trajectory. Ramped-shaped SMP in 2023 and cubic SMP in 2022 reach zero height earlier than other SMPs. Despite the ramped-shape of the SMP in 2023 having greater height compared to the small cone SMP in 2023, the ridge shape SMP and cubic SMP in 2022, its dimensional changes diminish more rapidly, leading to an earlier melting. This underscores that height isn't the sole determinant influencing SMP melting; other factors such as volume play crucial roles as well.

To explore how air temperature influences SMP temperature, thermal sensors were positioned within the ridge SMP at a 4.3 m height. Figure 4.7 illustrates the month-long fluctuations in both air temperature and SMP temperature in 2023. Throughout the month, air temperature displayed significant variation, predominantly below freezing, with sporadic periods above zero. The lowest recorded air temperature was approximately -12°C, while the highest reached around 11°C. In contrast, SMP temperature remained relatively stable, consistently above freezing. However, it exhibited slight fluctuations correlating with changes in air temperature. The snow cover provided an insulating layer, which helped to buffer the SMP temperature against the more extreme fluctuations in air temperature. This insulation effect means that the SMP temperature did not drop as low as the air temperature during cold periods. The SMP exhibited a degree of thermal inertia, meaning it responded more slowly to changes in air temperature. This delayed response helped maintain a more stable temperature within the SMP. When the air temperature decreased, the SMP temperature also decreased but to a lesser extent. Similarly, when the air temperature increased, the SMP temperature rose, but not as dramatically.

The lowest SMP temperature recorded was around -1°C and the highest was approximately 1°C. The data suggests a relationship between air temperature and SMP temperature, although not identical. When air temperature decreased, SMP temperature followed suit but to a lesser extent. Conversely, when air temperature increased, so did SMP temperature, albeit less dramatically. This indicates some insulation effect, likely due to snow cover or water depth, and a degree of thermal inertia, resulting in delayed heating or cooling. The

important key is that in 2022, natural snow melted 46 days after the start of the monitoring period, whereas in 2023, it melted much faster, taking only 29 days.

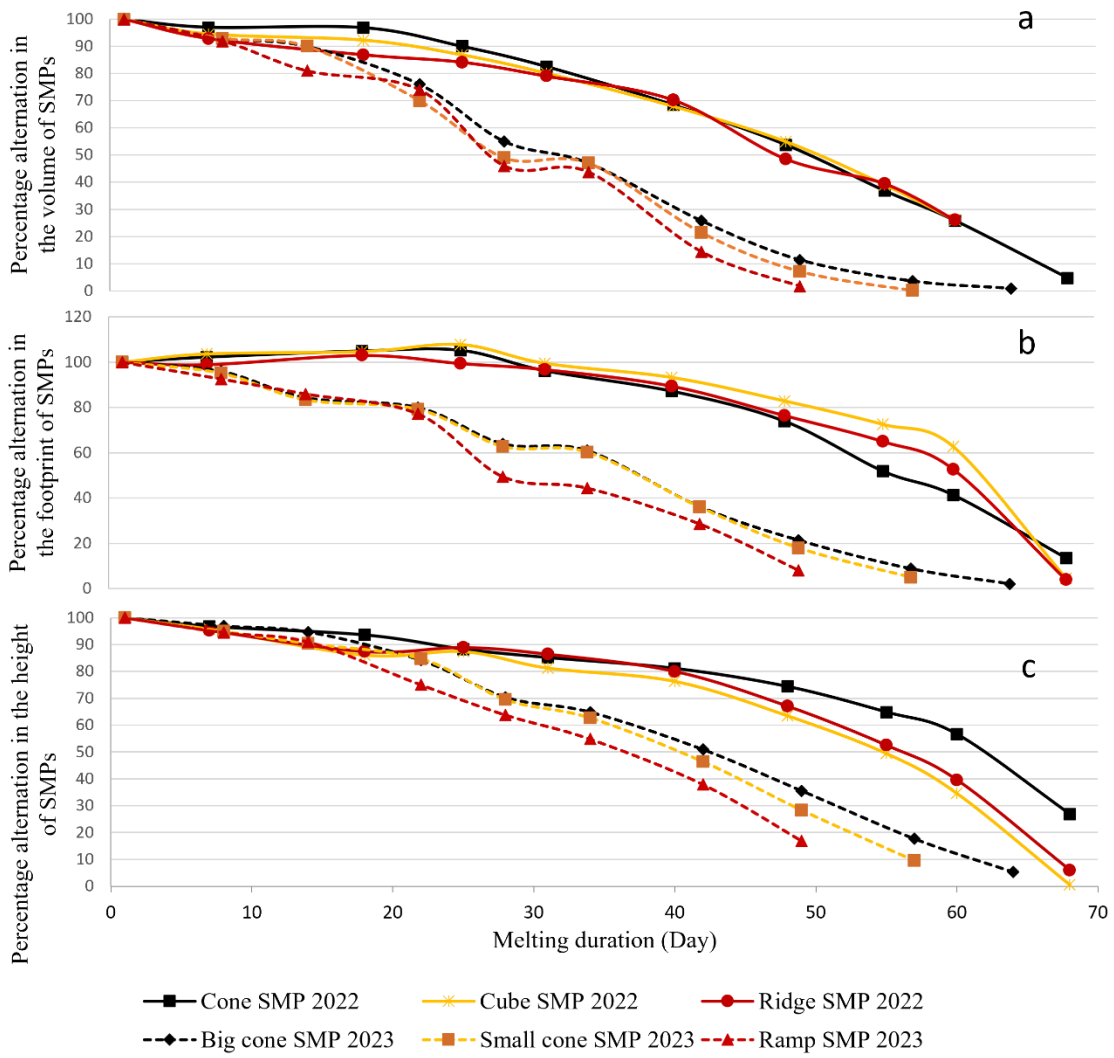

Figure 4.7 Assessment of changes in the percentage of (a) volume, (b) footprint, and (c) height of SMPs.

To further examine the impact of size and shape, we plotted the average volume of melted snow (measured in m^3) per m^2 of SMP footprint per day (Figure 4.8). The data was then converted to density to represent the snowmelt as meltwater. The data reveals a noteworthy disparity in that the amount of melted snow in 2023 SMPs surpasses that in 2022 SMPs. This discrepancy suggests that air temperature variations in 2023 were more pronounced,

exerting a substantial impact on snow melting dynamics. Particularly, the largest volume of melted snow is attributed to the big cone in 2023.

In 2022, the air temperature in the region showed less variation compared to 2023. This conclusion is based on the observation that the volume of melted snow in the fluctuated only twice in 2022, whereas in 2023, the volume of melted snow fluctuated four times. Essentially, the more frequent fluctuations in 2023 indicate greater variability in air temperature, leading to more frequent changes in the amount of snow melting.

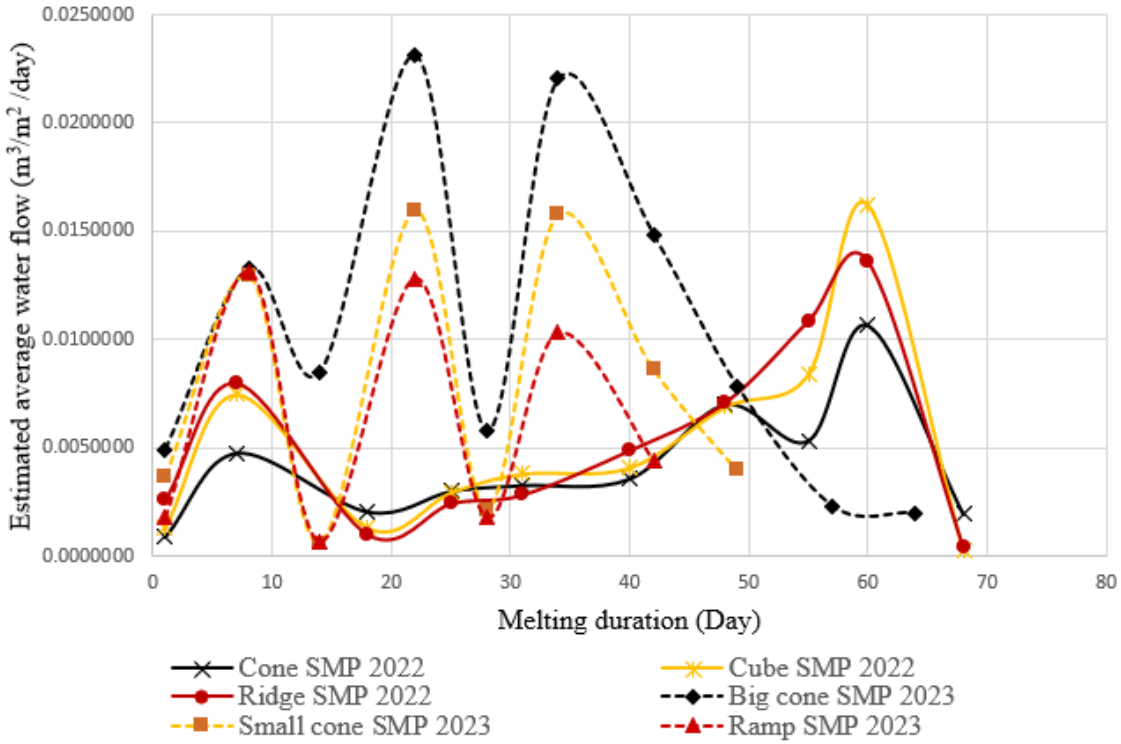

Figure 4.8 Variations of melted volume of snow between two consecutive surveys for the 2022 and 2023 SMPs.

To further explore the influence of air temperature on SMP melting, the degree-days of melting (DD) over the entire melting period (M) for each SMP has been calculated (Figure 4.9a). DD is calculated according to the ICCC and represents the total average daily air temperature above 0°C. During the 64-day melting period, the big cone SMP recorded the highest DD value at 304°C-days, while the ramped-shaped SMP had the lowest DD value at 189.6°C-days. Among the 2022 SMPs, the highest DD value during the 70-day melting

period was observed in the cone SMP at 278.3°C-days, whereas the ridge-shaped SMP had the lowest DD value at 240.3°C-days over a 66-day melting period.

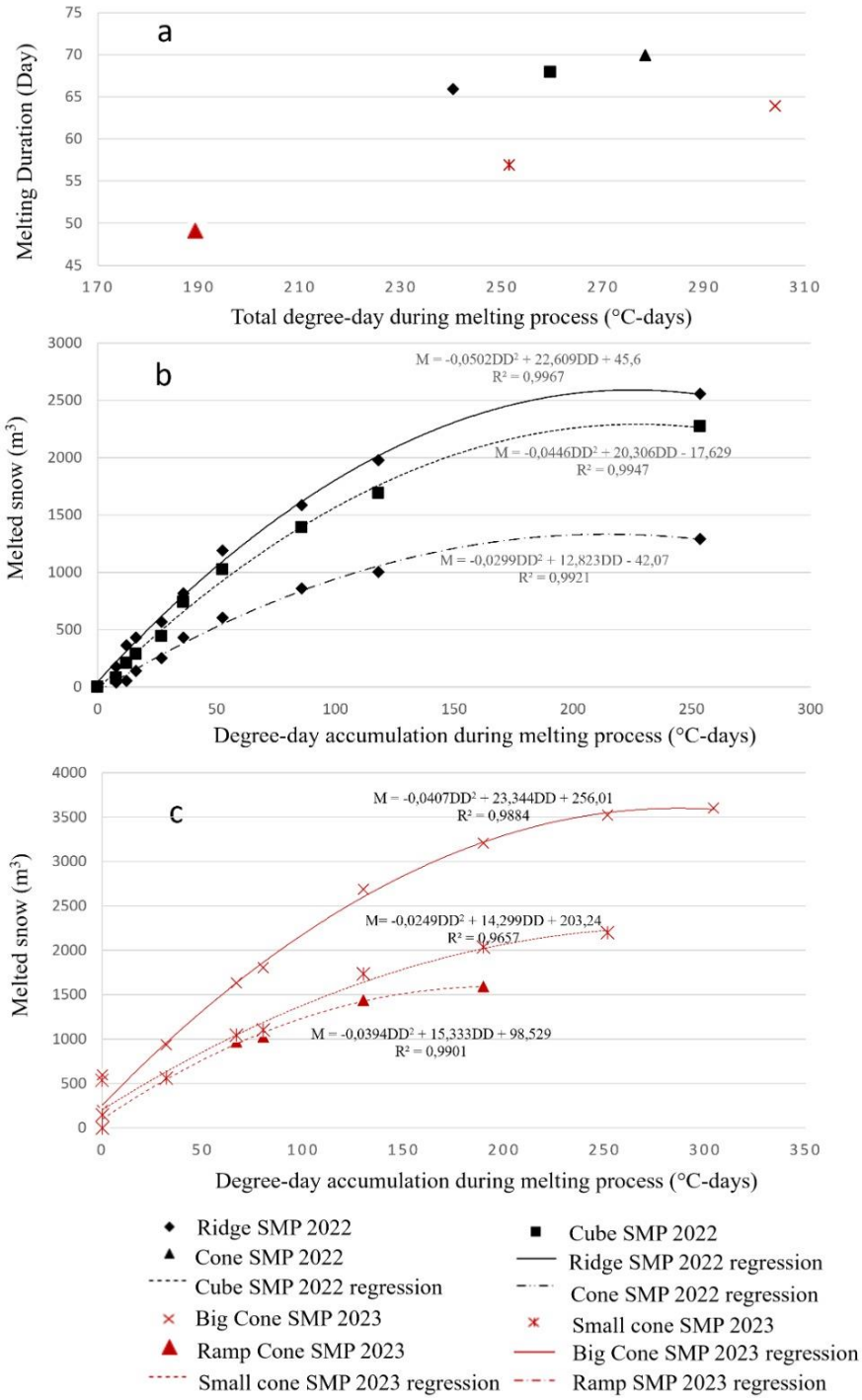

Figure 4.9 (a) Total degree- day during melting process for each SMP, (b) comparation of cumulative degree- day and melting period in 2022, and (c) 2023.

Figure 4.9b illustrates the cumulative DD for the melted snow in 2022. Additionally, this figure presents the behavioral regression equation for each snow SMP, demonstrating the relationship between the amount of melted snow and DD. By rearranging the equation, equations 4.1, 4.2, and 4.3 can be derived for the cone, cubic, and ridge-shaped SMPs in 2022.

$$M = -0{,}0502DD^2 + 22{,}609DD + 45{,}6 \quad (4.1)$$

$$M = -0{,}0446DD^2 + 20{,}306DD - 17{,}629 \quad (4.2)$$

$$M = -0{,}0299DD^2 + 12{,}823DD - 42{,}07 \quad (4.3)$$

Figure 4.9C also illustrates the cumulative DD for the melted snow in 2023. Additionally, this figure presents the behavioral regression equation for each SMP, demonstrating the relationship between the amount of melted snow and DD. By rearranging the equation, equations 4.4, 4.5, and 4.6 can be derived for the ramped-shaped, small cone, and big cone in 2023.

$$M = -0{,}0407DD^2 + 23{,}344DD + 256{,}01 \quad (4.4)$$

$$M = -0{,}0249DD^2 + 14{,}299DD + 203{,}24 \quad (4.5)$$

$$M = -0{,}0394DD^2 + 15{,}333DD + 98{,}529 \quad (4.6)$$

Utilizing the provided equations allows for the prediction of SMP melting based on DD, facilitating effective runoff management planning.

The robustness of these equations in space and time can be assessed based on their ability to predict the melting of snow in different shapes and conditions over multiple years. Here are some key points:

The equations are derived for different shapes of SMPs (cone, cubic, ridge, ramped-shaped, small cone, and big cone) in both 2022 and 2023. This indicates that the equations are adaptable to various geometries, suggesting spatial robustness. The ability to apply these equations to different shapes means they can be used in diverse physical settings.

The equations are based on data from two different years. The consistency in the form of the equations across these years suggests that they can reliably predict snow melting over

time. The equations account for the cumulative degree days, which is a measure of accumulated temperature over time, further supporting their temporal robustness.

The equations demonstrate a clear relationship between the amount of melted snow and the cumulative degree days. This relationship is captured through behavioral regression equations, which have been validated by the data from two consecutive years. The ability to rearrange and derive specific equations for different SMP shapes and years indicates a strong predictive capability.

These equations' use for predicting SMP melting based on degree days facilitates effective runoff management planning. This practical application underscores their robustness, as they provide actionable insights for managing snowmelt and associated water resources.

Overall, the equations appear to be robust both spatially and temporally, given their adaptability to different shapes and consistent performance over multiple years. They provide a reliable tool for predicting snow melting and effectively managing runoff.

4.3 Numerical modeling results

In the following sections, the numerical modeling results and their validation will be discussed.

4.3.1 Calibration of air temperature function

Figure 4.10 displays the adapted air temperature functions derived from Val d'Or and Kirkland station weather data. Both graphs illustrate the construction of two different functions from meteorological data. In 2022, equation 4-7 covers the melting period;

$$(\mathrm{T} = -5\mathrm{E}-05 * \mathrm{D}^3 + 0.0091 * \mathrm{D}^2 - 0.1673 * \mathrm{D} - 7) \quad (4.7)$$

The purpose of having a temperature function is first to analyze the melting behavior of the pile and compare it with actual samples, and then to predict the melting of piles with different dimensions throughout 70 to 100 days. This last aspect will be discussed in Chapter 5. Similarly, for the 2023, equation 4-8 covers the melting period;

$$(\mathrm{T} = 6\mathrm{E}-07 * \mathrm{D}^4 - 0.0001 * \mathrm{D}^3 + 0.0059 * \mathrm{D}^2 + 0.1956 * \mathrm{D} - 5) \quad (4.8)$$

This approach aims to reduce errors in predicting the long-term melting of snow piles.

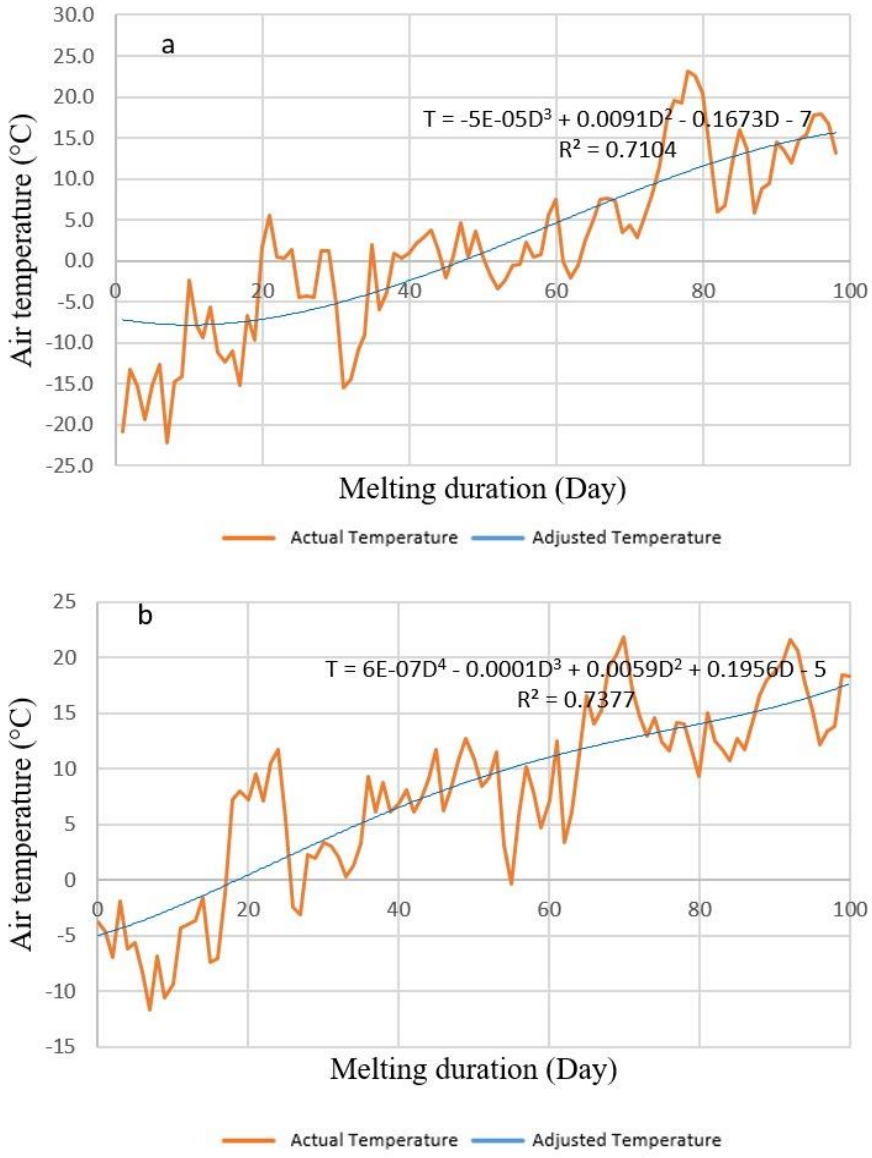

Figure 4.10 (a) The adapted air temperature functions derived from Val d'Or, and (b) Kirkland station weather data.

4.3.2 Numerical modelling of field-tested SMPs

Figure 4.10 illustrates that the Ridge-shaped SMP in 2022 and Big cone SMP in 2023 have significantly more snow than other SMPs. Initially, the snow volumes in 2022 were 1547.4 m^3 for the cone SMP, 2223.4 m^3 for the cubic SMP, and 2552.1 m^3 for the ridge-shaped SMP (Figure 4.11a). In 2023, the initial volumes were 1827 m^3 for the ramp-shaped SMP, 2400.3 m^3 for the small cone SMP, and 4142.7 m^3 for the big cone SMP (Figure 4.11b).

During the snowmelt period in 2022, the ridge-shaped and cubic SMP volumes decreased more rapidly than the cone SMP. The melting durations were 76 days for the cone SMP, 65 days for the cubic SMP, and 70 days for the ridge-shaped SMP. Notably, the initial volume of the ridge-Shaped SMP was about 1.7 times that of the cone SMP.

In 2023, the small cone SMP melted faster than the ramp-shaped SMP after 30 days. The melting periods were 58 days for the ramp-shaped SMP, 53 days for the small cone SMP, and 70 days for the big cone SMP. Interestingly, although the small cone SMP had a larger initial volume than the ridge-shaped SMP, its height was lower.

An additional crucial factor to consider is the impact of air temperature on SMP melting. Despite the two cone SMPs in 2022 and 2023 having identical heights, the snow volume in the 2022 cone SMP is roughly one-third of that of the 2023 cone SMP. Interestingly, the melting duration for in the 2022 cone SMP is five days longer than that in 2023. This observation underscores the importance of forecasting the air temperature when designing an optimal snow pile for a mining operation.

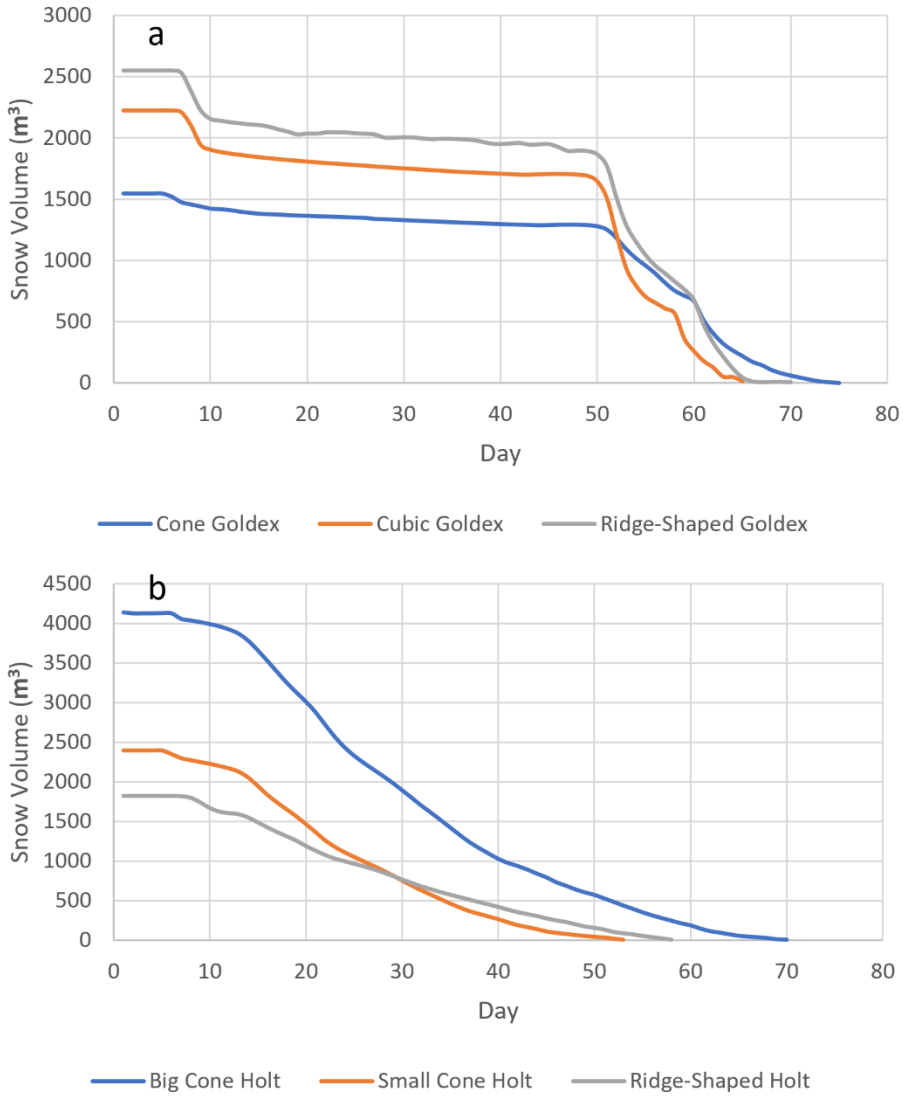

Figure 4.11 (a) Numerical Modeling of SMPs in 2022, and (b) in 2023.

4.3.3 Calibration of numerical modeling results and actual results

Figure 4.12 presents the results of numerical modeling alongside actual data for various SMPs in 2022 and 2023. Figure 4.12a shows the cone SMP in 2022. This will be further investigated by comparing the measured and modeled SMP snowmelt behaviours. The melting duration was 73 days, while the model predicted 76 days, resulting in a 3-day overestimation and a 3.94% error. The average error for predicting the melting process was 7.6%. Also, Figure 4.12b illustrates the cubic SMP in 2022. The actual melting duration

was 66 days, compared to the model's 65 days, leading to a 1-day underestimation and a 1.5% error. The average error for the melting process of that SMP was 7.2%. In Figure 4.12c, the ridge-shaped SMP in 2022 is depicted. The actual melting duration was 70 days, while the model predicted 69 days, resulting in a 1-day underestimation and a 1.42% error. The average error for the melting process was 4.64%. Figure 4.12d shows the big cone SMP in 2023. The actual melting duration was 67 days, compared to the model's 70 days, leading to a 3-day overestimation and a 4.47% error. The average error for the melting process was 4.86%. Figure 4.12e presents the small cone SMP in 2023. The actual melting duration was 59 days, while the model predicted 58 days, resulting in a 1-day underestimation and a 1.69% error. The average error for the melting process was 11.5%. Finally, Figure 4.12f illustrates the ramp-shaped SMP in 2023. The actual melting duration was 53 days, compared to the model's 58 days, leading to a 5-day overestimation and a 9.4% error. The average error for the melting process was 4.73%.

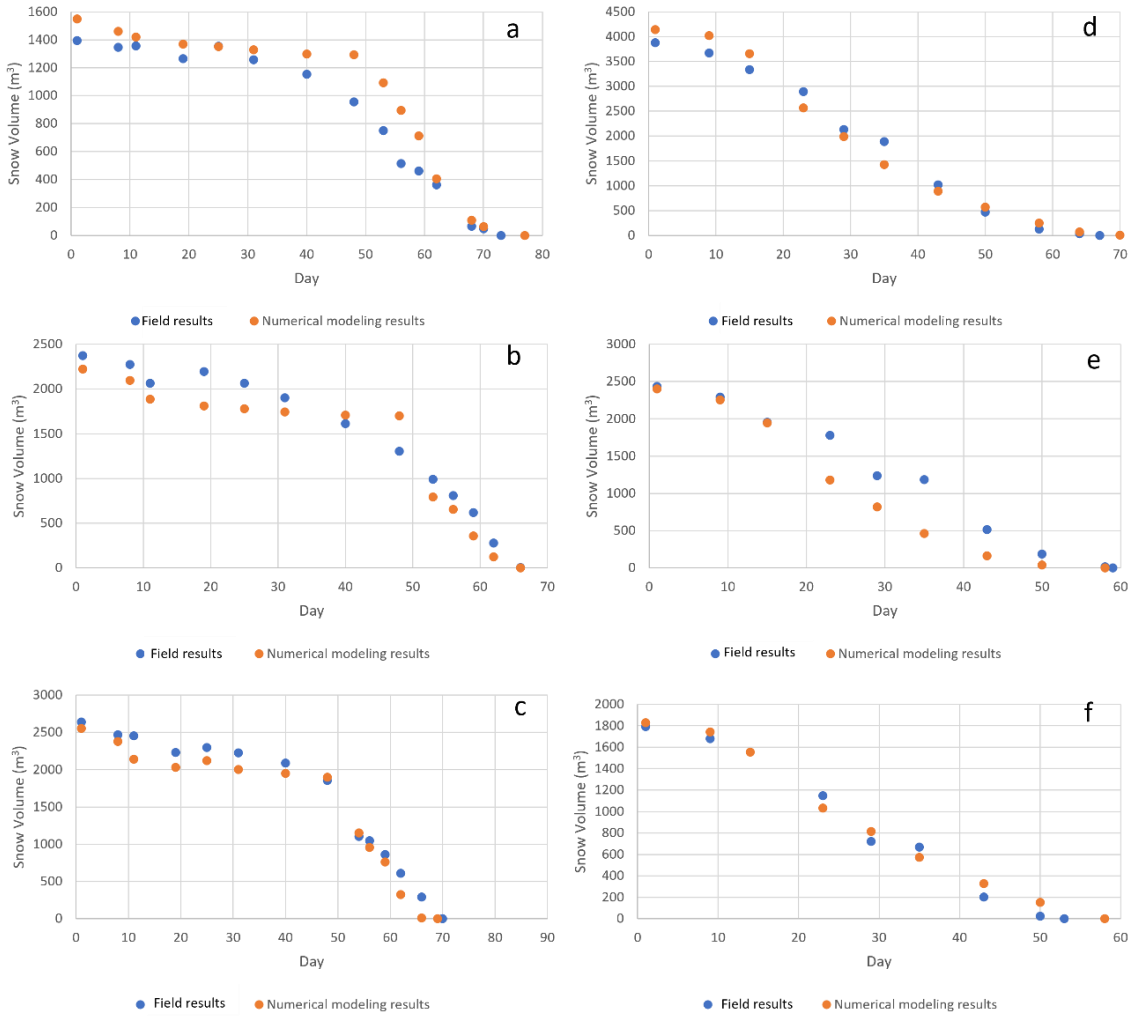

Figure 4.12 (a), (b), and (c) numerical modeling VS actual results of cone, cubic, and ridge-shaped SMPS in 2022, and (d), (e), and (f) numerical modeling VS actual results of big cone, small cone, and ramp-shaped SMPs in 2023.

Overall, the numerical modeling showed an average error of 3.73% for predicting the melting duration and 6.75% for the melting process. It should be noted that the error range for predicting the melting process of piles varies between 2% and 25%, with the maximum error typically occurring in the middle of the melting process. The reasons for this error in the melting process are discussed below. These results demonstrate accuracy for predicting the SMP melting behaviour. This approach will be used in Chapter 5 to further optimize SMPs at controlling snowmelt in TSFs.

The discrepancies observed between numerical modeling and fieldwork can be attributed to several factors:

- Temperature Variability: The numerical model uses average daily temperatures to simulate snow melting. However, air temperatures fluctuate throughout the day, impacting the melting process in ways that the model does not account for.

- Precipitation Effects: In the real world, snowfall and rain affect the snow pile's volume and influence its melting rate like the phenomenan in 2023. this phenomenon is often excluded from the numerical model, leading to inaccuracies.

- Water Movement: The presence and movement of water within the snow pile significantly affect the melting process. The numerical model ignores these dynamics, resulting in errors.

- Measurement Techniques: Errors can also stem from the methods used to measure the snow pile's volume, such as Lidar scanning and photogrammetry. These techniques, while advanced, can introduce inaccuracies that affect the overall modeling results.

Considering these factors helps to better understand the limitations of numerical modeling and work towards improving the accuracy of predictions in future studies.

CHAPTER 5 GENERAL DISCUSSION

In the earlier sections, a comprehensive description of the field data was provided, followed by the presentation of modeling results and their validation. The study modeled snow under three-dimensional conditions of varying dimensions using two distinct temperature functions. This section aims to further assess the impact of climate on the capacity of SMPs to control snowmelt. Thus, the snowmelt behavior of different SMP configurations under the climatic conditions of 2022 and 2023 were analysed by performing additional numerical analyses assessing the impact of height, volume, and air temperature functions on the melting duration. By comparing these factors, a comprehensive understanding of the snowmelt process for different SMP configurations is achieved. The relationship between the height of SMPs and their melting duration is examined further, revealing insights into how height affects snowmelt behavior under different climatic conditions. The impact of SMP volume on melting duration is also explored, highlighting significant correlations between volume, and melting rates. The effects of the two different air temperature functions on the melting duration of SMPs are analyzed, showcasing the sensitivity of SMPs to temperature variations. Additionally, the optimization of construction methods is discussed, providing recommendations for improving efficiency and effectiveness in real-world applications. Finally, the key findings and lessons learned from this study are summarized, offering valuable insights for future research and practical applications.

5.1 Prediction of the snowmelt behavior of SMP configurations under the 2022 and 2023 climatic conditions

This section presents the comprehensive modeling results of 70 distinct combinations of SMPs configurations and climatic conditions. The analysis covers several key aspects:

- Height and Melting Duration: The relationship between the height of the SMPs and the duration of their melting periods is explored, providing insights into how these two variables interact. The height of the piles for the cone SMP ranges from 3 to 10 m; for the ramp-shaped SMP, from 3 to 10 m; for the ridge-shaped SMP, from 3.5 to 9.5 m; and for the cube SMP, from 3.5 to 9.5 m.

- Volume and Melting Duration: The correlation between the volume of the SMPs and the time it takes for them to melt completely is examined. The volume of the piles for the cone SMP ranges from 509 to 5618 m^3; for the ramp-shaped SMP, from 330 to 7350 m^3; for the ridge-shaped SMP, from 2552 to 16204 m^3; and for the cube SMP, from 2223 to 14985 m^3.
- Temperature function: The impact of varying the temperature function considered as a boundary condition for melting SMPs with identical shapes and dimensions is studied to provide a detailed understanding of how temperature influences the melting process. The 2022 temperature function is considered representative of typical snowmelt, while the 2023 temperature function represents rapid snowmelt.

Empirical equations are presented to calculate both the height and the volume of SMPs based on their melting duration. This information is particularly useful for predicting and managing snow pile behavior in various conditions. Appendix D presents the geometric properties of the 70 modeled SMPs. Additionally, Appendix E provides detailed results for each SMP.

5.1.1 Impact of height and volume on the duration of SMP snowmelt within their respective climatic conditions

Generally, Figure 5.1 illustrates the relationship between the height of SMPs and the duration of their melting periods. The figure includes equations derived from the regression analysis of the modeling results, providing a clear visual representation of this relationship. To better identify the piles built in 2022 and 2023 (field-tested configuration), red circles are drawn around the respective piles in Figure 5.1.

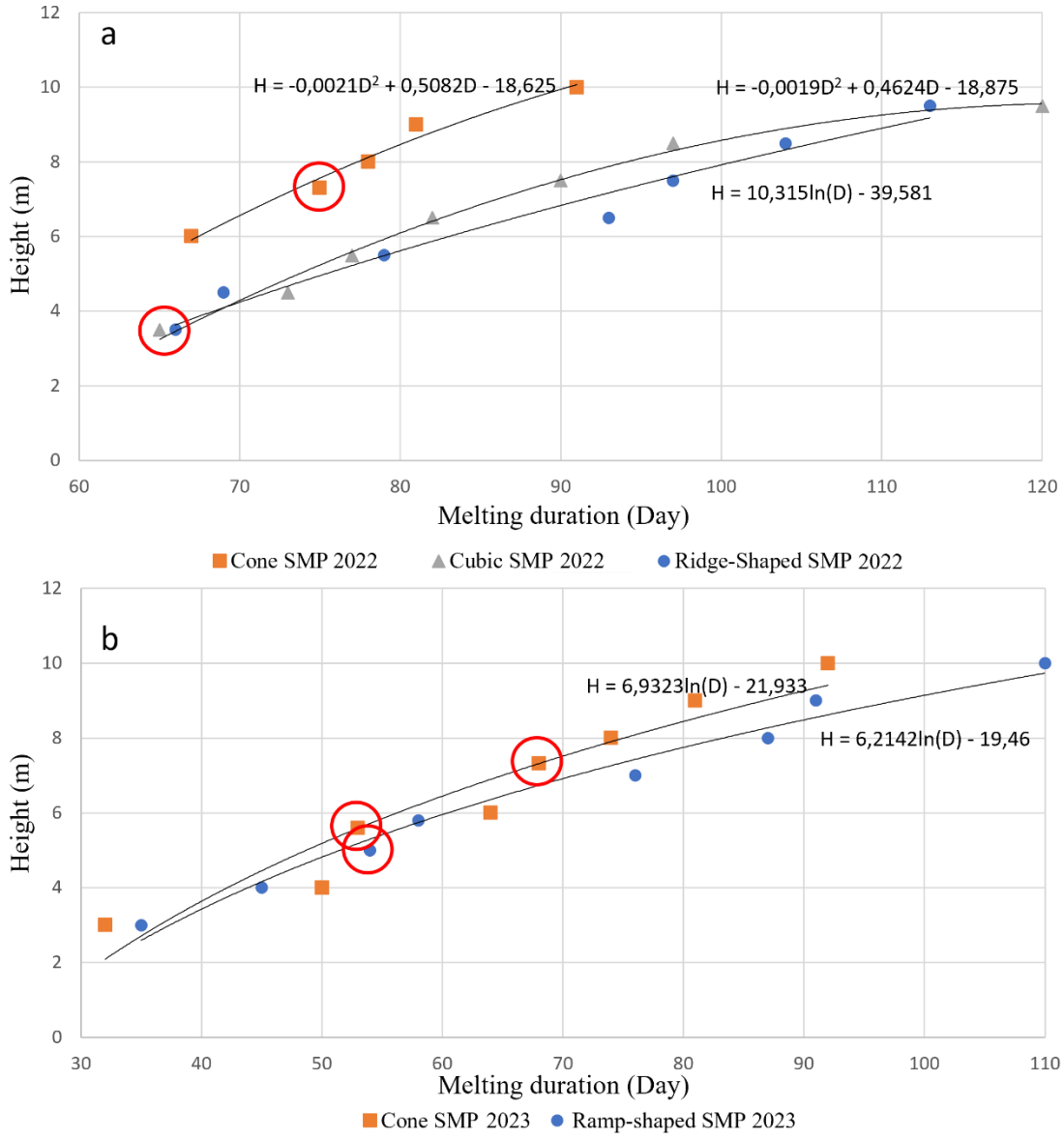

Figure 5.1 (a) Relationship between height and melting duration in 2022, and (b) in 2023.

Figure 5.1 reveals that the cone SMP, despite its greater height than other piles, experienced a shorter melting period. This anomaly can likely be attributed to its smaller volume, a factor that will be examined in more detail in the subsequent section. The cubic and ridge-shaped SMPs demonstrated nearly identical melting behaviors up to a height of 5.5 meters. Beyond this height, up to 9 meters, the ridge-shaped SMP exhibited a longer melting period

than the cubic SMP. Interestingly, this trend reversed beyond the 9-meter mark, with the cubic SMP taking longer to melt than the ridge-shaped SMP.

Equations 5.1, 5.2, and 5.3 illustrate the relationships between the height and melting period for cone, cubic, and ridge-shaped SMPs in 2022. Additionally, equations 5.4 and 5.5 depict the relationships between height and melting period specifically for cone-and ramp-shaped SMPs. These equations provide a mathematical framework for understanding how the height of different SMP geometries influences their melting durations, offering valuable insights for managing snow accumulation and melt in mining operations.

$$H = -0{,}0021D^2 + 0{,}5082D - 18{,}625 \quad (5.1)$$

$$H = -0{,}0019D^2 + 0{,}4624D - 18{,}875 \quad (5.2)$$

$$H = 10{,}315\ln(D) - 39{,}581 \quad (5.3)$$

$$H = 6{,}9323\ln(D) - 21{,}933 \quad (5.4)$$

$$H = 6{,}2142\ln(D) - 19{,}46 \quad (5.5)$$

Where H (m) is the height of SMP, and D (Day) is the melting duration.

These observations suggest that the melting dynamics of SMPs are influenced by their height, volume, and shape, highlighting the complex interplay of these factors. The forthcoming sections will delve deeper into these relationships, comprehensively analyzing the melting behaviors of different snow pile geometries.

Similary to Figure 5.1, Figure 5.2 illustrates the relationship between the volume of SMPs and the duration of their melting periods. The figure includes equations derived from the regression analysis of the modeling results, providing a clear visual representation of this relationship.

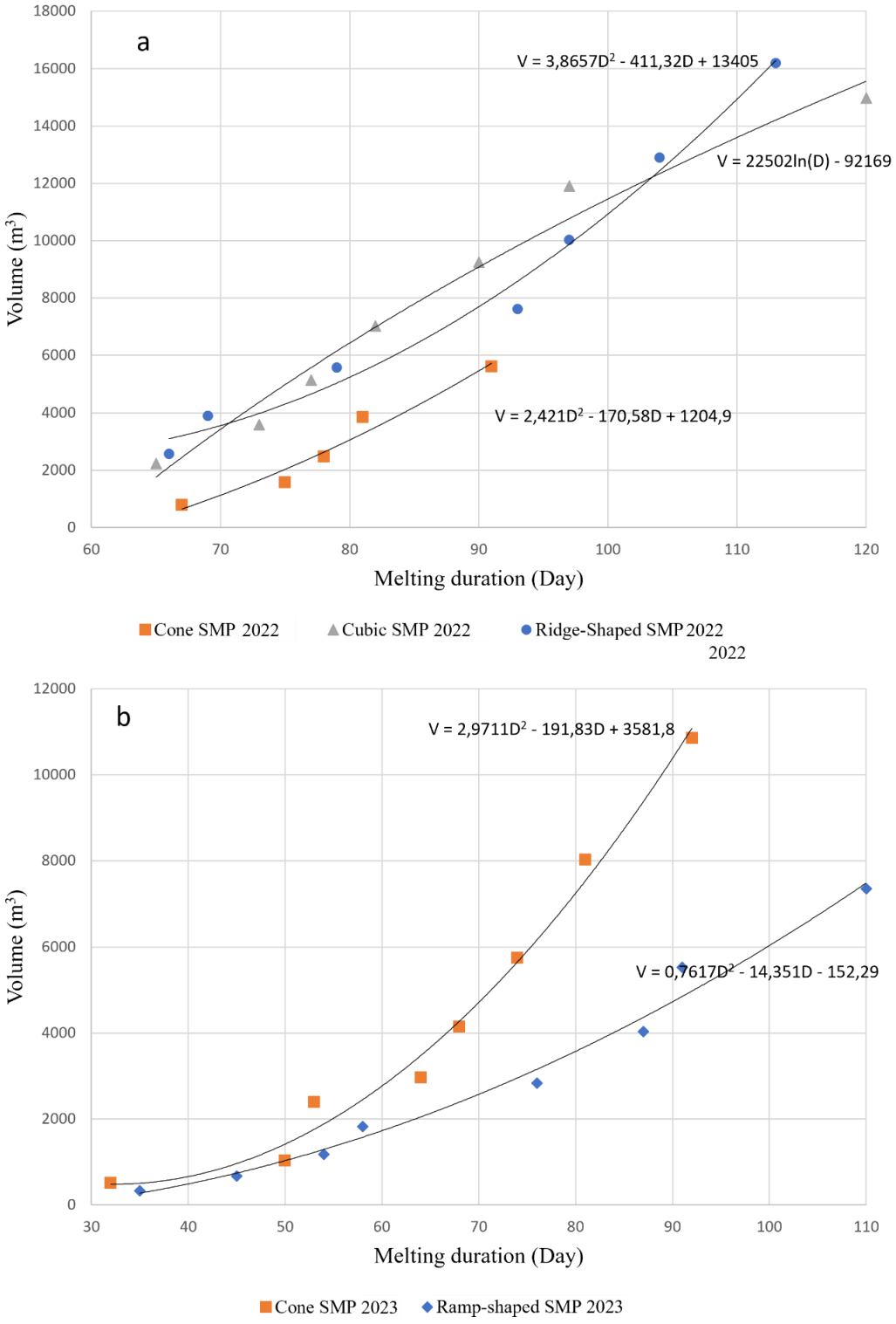

Figure 5.2 (a) Relationship between volume and melting duration in 2022, and (b) In 2023.

The shorter melting period of the cone SMP in 2022 is attributed to its smaller volume. Figure 5.2a illustrates that, despite the nearly equal volumes of all three SMPs in 2022, the cone SMP exhibits a longer melting period compared to the other shapes when volumes are considered. For instance, within the volume range of 2000 to 6000 m^3, the cone SMP has a longer melting period than both the cubic and ridge-shaped SMPs.

Furthermore, assuming a volume of 15,000 m^3 for the cone SMP, the melting period is calculated to be 119 days based on the derived equation. This duration is almost equivalent to the melting period of a cubic SMP with the same volume and exceeds the melting period of a ridge-shaped SMP with a larger volume.

Figure 5.2b depicts the relationship between volume and melting duration in 2023. The figure reveals an interesting phenomenon: despite having a larger volume than the ramp-shaped SMP, the cone SMP has a shorter melting period. Specifically, for volumes of 4000 m^3 and above, the melting period of the cone-shaped pile is shorter than that of the ridge-shaped pile, whereas, for volumes below this threshold, the cone SMP had a longer melting period.

Equations 5.6, 5.7, and 5.8 illustrate the relationships between the volume and melting period for cone, cubic, and ridge-shaped SMPs in 2022. Additionally, equations 5.9 and 5.10 depict the relationships between volume and melting period specifically for cone and ramp-shaped SMPs in 2023. These equations provide a mathematical framework for understanding how the volume of different SMP geometries influences their melting durations, offering valuable insights for managing snow accumulation and melt in mining operations.

$$V = 2{,}421D^2 - 170{,}58D + 1204{,}9 \quad (5.6)$$

$$V = 22502\ln(D) - 92169 \quad (5.7)$$

$$V = 3{,}8657D^2 - 411{,}32D + 13405 \quad (5.8)$$

$$V = 2{,}9711D^2 - 191{,}83D + 3581{,}8 \quad (5.9)$$

$$V = 0{,}7617D^2 - 14{,}351D - 152{,}29 \quad (5.10)$$

Observations indicate that cone SMPs exhibited different melting behaviors in 2022 and 2023. In 2022, the cone SMP, despite its smaller volume, had a longer melting period compared to other SMPs. Conversely, in 2023, the cone SMP, even with a larger volume, had a shorter melting period than the ramp-shaped SMP.

This suggests that when air temperatures are moderate, the cone shape is the optimal form for extended melting periods, as shown in Figure 5.2a. However, under higher temperatures, the cone shape is less effective, resulting in a shorter melting period, as illustrated in Figure 5.2b. This difference in melting behavior could be attributed to the shape's surface area exposure and heat absorption dynamics, which vary under different temperature conditions.

5.1.2 Impact of height and volume on the duration of SMP snowmelt with in typical and rapid snowmelt conditions

To thoroughly examine the impact of temperature variations on the melting process of SMPs, a detailed study has been conducted. This study involves re-modeling SMPs with the two temperature functions defined earlier. SMPs originally modeled using the 2022 temperature function were re-modeled using the 2023 temperature function, and vice-versa. This was done to test the melting behaviour of the SMP configurations in typical (2022) and rapid (2023) snowmelt conditions.

This comprehensive approach will generate five sets of outputs, as shown in Figure 5.3, enabling a comparative analysis of how the two distinct temperature functions influence the melting behavior of the SMPs volume. Similar to Figure 5.3, Figure 5.4 shows a comparative analysis of how the two distinct temperature functions influence the melting behavior of the SMPs volume height.

This investigation aims to provide deeper insights into the thermal dynamics and melting patterns under varying temperature conditions.

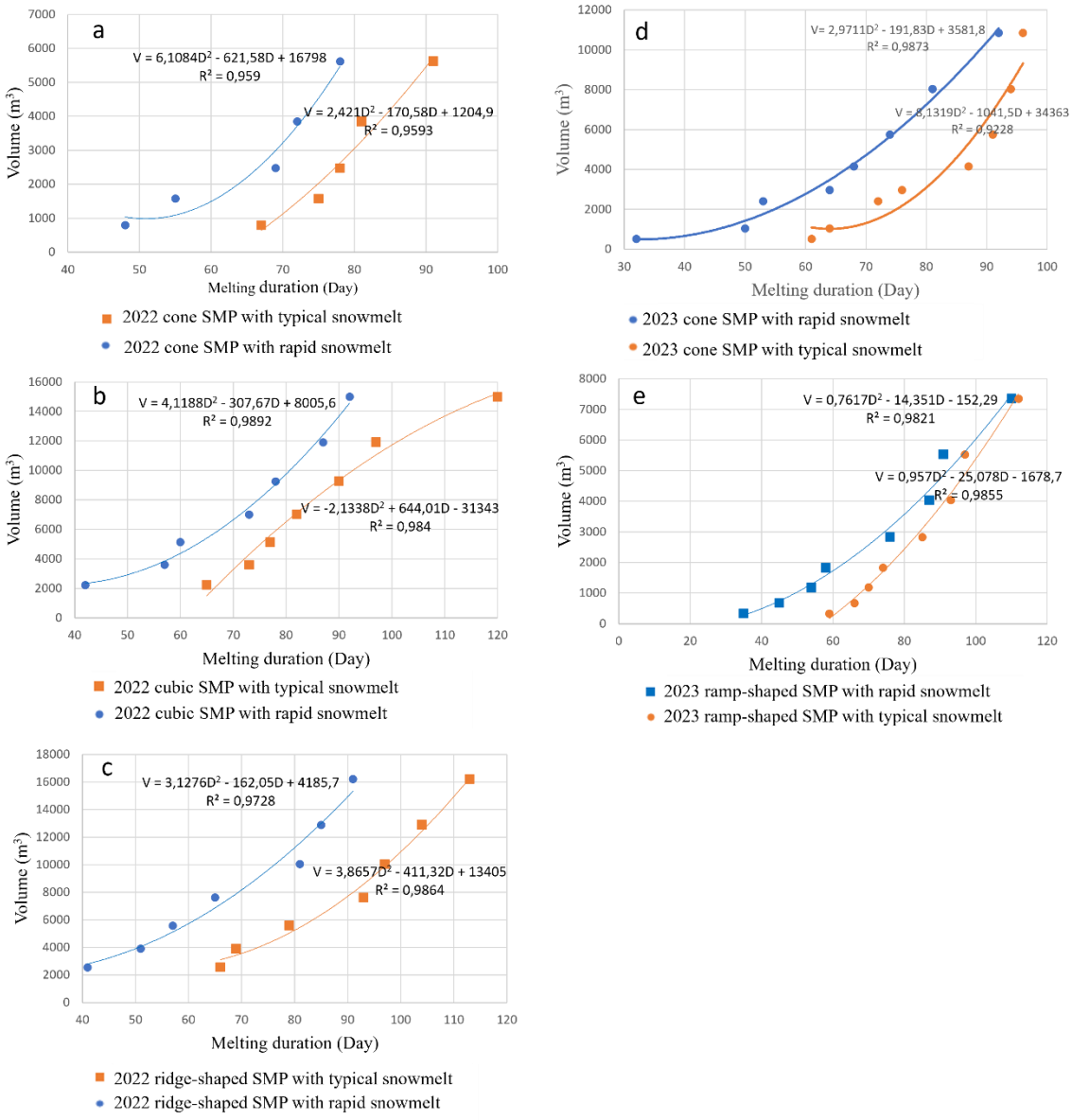

Figure 5.3 Impact of two temperature functions on volume change of (a) 2022 cone SMPs, (b) 2022 cubic SMPs, (c) 2022 ridge-shaped SMPs, (d) 2023 cone SMPs, and (e) 2023 ramp-shaped SMPs volume.

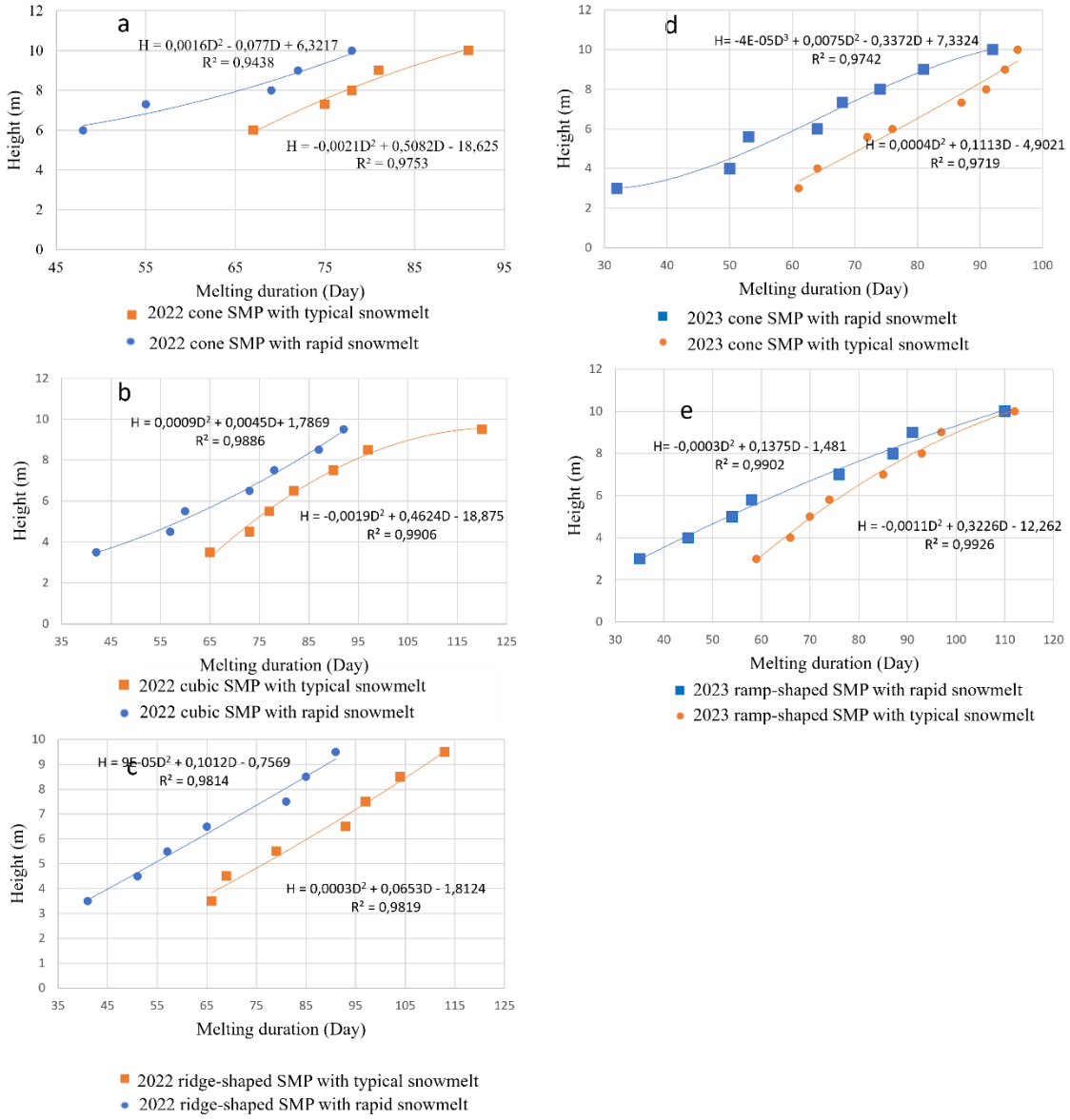

Figure 5.4 Impact of two temperature functions on height change of (a) 2022 cone SMPs, (b) 2022 cubic SMPs, (c) 2022 ridge-shaped SMPs, (d) 2023 cone SMPs, and (e) 2023 ramp-shaped SMPs volume.

Overall, the modeling results using the 2022 temperature data show a delay in the melting of SMPs, ranging from 30 days to 3 days. This underscores the crucial role of accurately predicting air temperatures in the proper design of SMPs. Figure 5.3a and 5.4a present the modeling results for the cone SMPs at Goldex mine, using the temperature functions of 2022 and 2023. The variation in these temperature functions indicates that the melting period of the pile decreases from 30 days to 20 days as the air temperature rises. Figure

5.3b and 5.4b present the modeling results for the cubic SMPs at Goldex mine, using the temperature functions of 2022 and 2023. The variation in these temperature functions indicates that the melting period of the pile decreases from 25 days to 10 days as the air temperature rises. Finally Figure 5.3c and 5.4c present the modeling results for the ridge-shaped SMPs at Goldex mine, using the temperature functions of 2022 and 2023. The variation in these temperature functions indicates that the melting period of the pile decreases from 25 days to 20 days as the air temperature rises. Figure 5.3d and 5.4d illustrates the modeling results for the cone SMP at Holt mine, modeled under the temperature functions of 2022 and 2023. The variation in temperature functions reveals that the melting period of the pile shortens from 30 days to 5 days as the air temperature increases. Figure 5.3e and 5.4e presents the modeling results for the ramp-shaped SMP at Holt mine, using the temperature functions of 2022 and 2023. The variation in these temperature functions indicates that the melting period of the pile decreases from 25 days to 3 days as the air temperature rises. This figure is less sensitive to changes in air temperature compared to other SMP shapes.

In summary, for a typical winter with an average temperature between 0 and 1°C during the SMP melting period, the cone SMP's estimated volume and height can be calculated using equations 5.1 and 5.6. By inputting the desired melting duration into these equations, the estimated height and volume values can be obtained. Similarly, for cubic or ridge-shaped SMPs under the same conditions, equations 5.2 and 5.7, as well as 5.3 and 5.8, are useful for determining height and volume.

In contrast, during winters with higher average temperatures (between 3 and 4°C) during the melting period, equations 5.4 and 5.9 for cone SMP, and equations 5.5 and 5.10 for ramp-shaped SMP, are effective for calculating the height and volume. These equations allow for predictions and management of SMP behavior under varying temperature conditions.

5.2 Optimisation of Construction Methods

The goal of this section is to compare the advantages and disadvantages of civil and specialized equipment. When evaluating these types of equipment for snow management,

several key differences and advantages emerge, each influencing their suitability for various tasks.

Civil equipment is characterized by its lower efficiency and relatively high ground pressure. This type of equipment is easily accessible and versatile, making it suitable for a wide range of applications beyond snow management. However, the lower efficiency means that it takes longer to cover a given area, which can be a significant drawback in time-sensitive operations. The higher ground pressure can also be a concern, particularly in environments where soil compaction or damage to underlying surfaces is an issue (Table 5.1).

In contrast, specialized equipment demonstrates significantly higher efficiency. This high efficiency makes it ideal for large-scale snow management tasks where speed and productivity are critical. Specialized equipment also exerts low ground pressure, reducing the risk of soil compaction and damage to surfaces, which is particularly beneficial in sensitive environments. However, this equipment is dedicated to specific tasks, meaning it may not be as versatile as civil equipment. Additionally, while the cost analysis is still in progress, specialized equipment typically involves higher initial investment and maintenance costs (Table 5.1).

The primary advantage of civil equipment lies in its accessibility and versatility. It can be used for various tasks, making it a practical choice for operations that require flexibility. However, its lower efficiency and higher ground pressure can limit its effectiveness in large-scale or sensitive projects.

On the other hand, specialized equipment excels in efficiency and minimal ground impact. Its ability to cover large areas quickly and with less environmental disturbance makes it ideal for extensive snow management operations. A detailed cost and operation analysis could provide further insights into the financial implications of using specialized equipment, but it is believed that the higher efficiency and lower ground pressure can justify the initial costs in many scenarios.

The choice between civil and specialized equipment depends largely on the specific requirements of the project. For tasks requiring versatility and accessibility, civil

equipment is advantageous. However, for large-scale operations where efficiency and minimal ground impact are paramount, specialized equipment is the superior choice.

Table 5.1 Optimization of construction methods.

Civil equipment	**Specialized equipment**
Lower efficiency	High efficiency
Relatively high ground pressure	Low ground pressure
Easily accessible	Dedicated equipment
Various uses	Cost analysis in progress

5.3 Lessons learned

At the outset of the project, it was assumed that modeling snow in the software would be a straightforward task. The initial plan was to utilize the physics of water flow in COMSOL software, along with the physics of phase change and heat transfer in porous media, to simulate snow melting. The project began with one-dimensional modeling, and the promising results suggested that an accurate model of snow pile melting could indeed be developed in COMSOL.

Upon completing the one-dimensional phase, the project progressed to two-dimensional modeling, which was intended to be the final goal. Initially, the physics of heat transfer in a porous medium, phase change, and Richard's equations were employed. However, contrary to expectations, the software failed to accurately predict snow melting. Specifically, it could not correctly simulate the movement of water within the model. This issue became apparent when the model was unable to effectively transfer water from the SMP to the lower sections and eventually remove it from the system. Consequently, water retention within the SMP hindered the proper transfer of thermal energy to the lower snow layers, leaving the bottom layers unchanged and trapping water inside the pile. This problem ultimately caused the software to halt the modeling process.

In response, the physics used in the water transfer section was modified. Darcy's law was introduced to simplify the water movement in the model. Although this change resulted in

slight improvements, the software still could not accurately model water movement, and the initial problem persisted.

Further investigation suggested that improper meshing dimensions might be causing the error and preventing the model from effectively moving and expelling water. Consequently, a thorough review of meshing was undertaken. Despite testing over 30 different meshing configurations, the software error continued. Additionally, fine meshing (with dimensions smaller than 0.2 m) significantly prolonged the modeling process.

Ultimately, it was decided to simplify the approach further. Instead of modeling the phase change from snow to water and its subsequent removal from the model, a material with high thermal conductivity was used to simulate water movement. This entire process was the start of SMPs behavior numerical modeling which is useful to predict the volume of snowmelt and meltwater. The starting simple can still provide insight full results despite the downfalls.

Preliminary 2D modeling brought-up the challenges of comparing modeling and field results. As a result, it was decided to proceed with three-dimensional modeling to enable a more accurate comparison of snow volume changes between the model and reality.

During the initial phase of three-dimensional modeling, it was assumed that the average air temperature over the entire period could be used as a constant boundary condition. This assumption led to an average error of about 30% in predicting snowmelt between real data and the model. To address this, the temperature functions presented in this chapter were defined based on real meteorological data, significantly improve numerical results.

Next, the effect of solar radiation was investigated using the physics of an external radiation source. This attempt aimed to measure the impact of sunlight on the walls of snow piles and determine the optimal slope for each shape. Despite extensive efforts, this modeling process was unsuccessful, leading to the removal of this part of the work from the project.

Additionally, an attempt was made to model the impact of rainfall using the Physics of Transport of Diluted Species Module. This was done before the secondary water change. Like the previous issue, water was not correctly added to the model, only causing a decrease in ambient temperature on the pile's surface and being used for heating the water.

Due to the complexity and lack of success, this process was also removed from the modeling.

In conclusion, the project faced numerous challenges and required several adjustments to the initial approach. The experience highlighted the importance of flexibility and the willingness to simplify models when necessary to achieve accurate and practical results.

CHAPTER 6 CONCLUSIONS AND RECOMMENDATIONS

6.1 Conclusions

A comprehensive review of studies on snow properties and heat transfer in snow provides valuable insights into the challenges and management strategies for snowmelt. This review evaluates various approaches to modeling heat transfer in snow, comparing the advantages and disadvantages of different models. It discusses the challenges associated with snow modeling and provides an overview of the current state of snow heat transfer modeling. Additionally, the review highlights the use of COMSOL software to model heat transfer in snow, explaining the necessary physics and key parameters that must be defined in the software.

The main objective of this research was to evaluate the effectiveness of SMPs in regulating the winter water balance of TSFs. Specifically, the study aimed to assess how SMPs can moderate snowmelt rates, reduce peak meltwater flows, and stagger spring runoff. To achieve this, three pilot-scale SMPs were constructed at the Holt mine in Kirkland, Ontario, 2023 using a Prinoth groomer, and another three at the Goldex mine in Val d'Or, Quebec, 2022 using a loader and bulldozer.

In 2022, the SMPs were designed in three shapes: a cone with an initial volume of 1135 m^3, a footprint of 665 m^2, and a height of 7.3 m; a cube with an initial volume of 2275 m^3, a footprint of 965 m^2, and a height of 3.5 m; and a ridge shape with an initial volume of 2565 m^3, a footprint of 1150 m^2, and a height of 3.5 m. The cone SMP melted in 70 days, the cubic SMP in 68 days, and the ridge-shaped SMP also in 68 days. In contrast, natural snow melted in 46 days from the start of the monitoring period, indicating that the SMPs delayed snowmelt by 3 to 4 weeks.

In 2023, the SMPs were redesigned with different shapes and sizes: a large cone with an initial volume of 4130 m^3, a footprint of 1950 m^2, and a height of 7.33 m; a ramp shape with an initial volume of 2650 m^3, a footprint of 1343 m^2, and a height of 5.5 m; and a small cone with an initial volume of 1600 m^3, a footprint of 946 m^2, and a height of 5.6 m. The large cone SMP melted in 64 days, the ramp-shaped SMP in 49 days, and the small cone in 57 days. Natural snow melted in 29 days from the start of the monitoring period,

showing that the SMPs delayed snowmelt by 3 to 5 weeks. These designs were used to investigate the impact of size and shape on snowmelt dynamics.

Changes in the SMPs, including volume, height, and footprint, were monitored using LiDAR and SfM photogrammetry techniques over ten weeks, with data collected between eight and eighteen times. Meteorological data revealed two distinct patterns of behavior in 2022 and 2023. In 2022, winter conditions were typical, resulting in natural snow melting over 46 days. Conversely, in 2023, warmer temperatures led to a much quicker snowmelt, taking only 29 days. Snow density measurements were also obtained through core sampling at different intervals during the observation period. The results indicated that SMPs effectively increased the duration of snowmelt, prolonging the process by approximately four to six weeks. The volume and height of SMPs emerged as critical factors influencing their ability to stagger snowmelt.

The modeling efforts, including both the unsuccessful attempts and the final successful model, were discussed in detail. These efforts aimed to simplify the process and reduce model error. The results showed that the prediction of snow melting behavior during the melting period had an average error of 6.75%, while the error rate for predicting the entire length of the snow melting period was less than 4%. Based on these modeling results, snow melting prediction charts were developed, considering the dimensions, shape, and cost of snow pile construction. These charts assist miners in reducing the geotechnical hazards of tailings dams by managing spring snowmelt.

To derive equations for the height and volume of SMPs with the required melting period, 70 piles were modeled, and the relevant equations were determined. It was found that cone-shaped SMPs are highly sensitive to temperature changes, while ridge-shaped SMPs are less sensitive and exhibit consistent performance across different temperatures. In another section, a comparison was made between the use of construction and specialized equipment, detailing the benefits and drawbacks of each. Furthermore, the study concluded that SMPs can help mitigate environmental and geotechnical risks associated with rapid snowmelt, potentially reducing the need for additional storage and treatment facilities during extreme events. This is particularly important in the context of climate change, where predicting future weather patterns is becoming increasingly challenging.

6.2 Recommendations

Here are some recommendations for future snow management and modeling projects:

- SMPs can be highly effective in mitigating the impacts of freshet on tailings dams and water management infrastructures. Implementing these practices helps manage the sudden influx of water during snowmelt periods, reducing potential damage and improving overall water management.

- There is a need for more research to develop and refine adaptive and autonomous monitoring tools. These tools can provide real-time data, enhancing the accuracy and responsiveness of snow management systems.

- Advancement in Snowmelt Process Modeling: Further research is essential to advance the modeling of snowmelt processes (SMP melting). This includes developing more accurate physics-based models that can better predict the dynamics of snowmelt, leading to improved management strategies.

- Utilize Real-Time Meteorological Data: Incorporate current meteorological data into your models to ensure that simulations reflect real-world conditions accurately.

By following these recommendations, future projects can achieve more precise and reliable results in snow management and modeling.

REFERENCES

Abbott, M. B., Bathurst, J. C., Cunge, J. A., O'connell, P. E., & Rasmussen, J. (1986). An introduction to the European Hydrological System—Systeme Hydrologique Europeen, "SHE", 2: Structure of a physically-based, distributed modelling system. Journal of hydrology, 87(1-2), 61-77.

Abegg, B., Agrawala, S., Crick, F., and de Montfalcon, A. (2007). "Climate change impacts and adaptation in winter tourism," in Climate Change in the European Alps: Adapting Winter Tourism and Natural Hazards Management, ed S. Agrawala (Paris: OECD Publishing), 25–60.

Abele, G., & Gow, A. J. (1975). Compressibility characteristics of undisturbed snow (Vol. 336). US Army Cold Regions Research and Engineering Laboratory.

Abels, H. F. (1892). Beobachtungen der täglichen Periode der Temperatur im Schnee und Bestimmung des Wärmeleistungsvermögens des Schnees als Function seiner Dichtigkeit.

Acar, R., Elik, S., Enocak, S. (2015). Modelling Snowmelt Runoff Using an Artificial Neural Network ANN Approach. In Proceedings of the 3rd International Conference on Advances in Civil, Structural and Mechanical Engineering (ACSM), Bangkok, Thailand, 28–29.

Akitaya, E. (1974). Studies on depth hoar. Contributions from the Institute of Low Temperature Science, 26, 1-67.

Albert M, Perron F (2000) Ice layer and surface crust permeabilty in a seasonal snowpack. Hydrol Process14:3207–3214

Albert M, Schultz E, Perron F (2000) Snow and firn permeability at Siple Dome, Antarctica. Ann Glaciol 31:353–356

Albert, M. R., & Perron Jr, F. E. (2000). Ice layer and surface crust permeability in a seasonal snowpack. Hydrological Processes, 14(18), 3207-3214.

Albert, M. R., Shultz, E. F., & Perron, F. E. (2000). Snow and firn permeability at Siple Dome, Antarctica. Annals of Glaciology, 31, 353-356.

Alford, D. L. (1974). Snow: Methuen & Company, Limited

Alizadeh, O. (2022). Advances and challenges in climate modeling. Climatic Change, 170(1), 18.

Allan, J. D., and Castillo, M. M. (2007). Stream Ecology: Structure and Function of Running Waters, 2nd Edn. New York, NY: Chapman and Hall.

Alley, R. B. (1987). Firn densification by grain-boundary sliding: a first model. Le Journal de Physique Colloques, 48(C1), C1-249.

Alley, R. B. (1987). Texture of polar firn for remote sensing. Annals of Glaciology, 9, 1-4.

Amiri, A., & Vafai, K. (1998). Transient analysis of incompressible flow through a packed bed. International Journal of Heat and Mass Transfer, 41(24), 4259-4279.

Andersland, O., & Anderson, D. (1978). Geotechnical engineering for cold regions

Anderson, E. A. (1973). National Weather Service River forecast system: Snow accumulation and ablation model (Vol. 17). US Department of Commerce, National Oceanic and Atmospheric Administration, National Weather Service.

Anderson, E. A. (1976). A point energy and mass balance model of a snow cover. Stanford University.

Anderson, S., & Tinkler, T. (2021). Developing Integrated Water Management Models to Address Water Related Risks and Provide Resilience in the Mining Industry.

Aoki, T., Hachikubo, A. & Hori, M. (2003) Effects of snow physical parameters on shortwave broadband albedos, J. Geophys.Res. 108(D19), 4616.

Arakawa, H., Izumi, K., Kawashima, K., & Kawamura, T. (2009). Study on quantitative classification of seasonal snow using specific surface area and intrinsic permeability. Cold Regions Science and Technology, 59(2), 163-168.

Araya, S. N., & Ghezzehei, T. A. (2019). Using machine learning for prediction of saturated hydraulic conductivity and its sensitivity to soil structural perturbations. Water Resources Research, 55(7), 5715-5737.

Arnaud, L., Gay, M., Barnola, J. M., & Duval, P. (1998). Imaging of firn and bubbly ice in coaxial reflected light: a new technique for the characterization of these porous media. Journal of Glaciology, 44(147), 326-332.

Arnold, J. G., Srinivasan, R., Muttiah, R. S., & Williams, J. R. (1998). Large area hydrologic modeling and assessment part I: model development 1. JAWRA Journal of the American Water Resources Association, 34(1), 73-89.

Arriagada, P., Karelovic, B., & Link, O. (2021). Automatic gap-filling of daily streamflow time series in data-scarce regions using a machine learning algorithm. Journal of Hydrology, 598, 126454.

Ashton, G. D. (2011). River and lake ice thickening, thinning, and snow ice formation. Cold Regions Science and Technology, 68(1-2), 3-19.

Aufdemberge, T. P. (1971). Energy balance studies over glacier and tundra surfaces, summer, 1969. University of Michigan.

Azam, S. & Li, Q. (2010). Tailings Dam Failures: A Review of the Last 100 Years, Waste Geotechnics. Geotechnical News: 50-53.

Baba, M. W., Gascoin, S., & Hanich, L. (2018). Assimilation of Sentinel-2 data into a snowpack model in the High Atlas of Morocco. Remote Sensing, 10(12), 1982.

Bader, H. (1939). Der schnee und seine metamorphose. Kommissionsverlag Kummerly & Frey, Druck von Aschmann & Scheller a.-g., Zurich.

Bader, H. (1939). Mineralogishe und Strukturelle Charakterisierung des Schnees und seiner Metamorphose. Beitrage zur Geologie der Schweiz, Geotechn. Ser. Hydrol, 3(1)

Bair, E. H., Abreu Calfa, A., Rittger, K., & Dozier, J. (2018). Using machine learning for real-time estimates of snow water equivalent in the watersheds of Afghanistan. The Cryosphere, 12(5), 1579-1594.

Bales, R. C., Molotch, N. P., Painter, T. H., Dettinger, M. D., Rice, R., & Dozier, J. (2006). Mountain hydrology of the western United States. Water Resources Research, 42(8).

Balland, V., & Arp, P. A. (2005). Modeling soil thermal conductivities over a wide range of conditions. Journal of Environmental Engineering and Science, 4(6), 549-558.

Bansal, A., & Suthar, O. P. (2024). Temperature modulation effects on chaos and heat transfer in Darcy–Bénard convection using a local thermal non-equilibrium model. Nonlinear Dynamics, 1-19.

Barnett, T. P., Adam, J. C., and Lettenmaier, D. P. (2005). Potential impacts of a warming climate on water availability in snow-dominated regions. Nature 438, 303–309.

Bartelt, P., & Lehning, M. (2002). A physical SNOWPACK model for the Swiss avalanche warning: Part I: numerical model. Cold Regions Science and Technology, 35(3), 123-145.

Bavay, M., Grünewald, T., & Lehning, M. (2013). Response of snow cover and runoff to climate change in high Alpine catchments of Eastern Switzerland. Advances in water resources, 55, 4-16.

Bear, J. (2012). Hydraulics of groundwater. Courier Corporation.

Bear, J. (2013). Dynamics of fluids in porous media. Courier Corporation

Bear, J., & Braester, C. (1972). On the flow of two immscible fluids in fractured porous media. In Developments in soil science (Vol. 2, pp. 177-202). Elsevier.

Bejan, A. (2013). Convection heat transfer. John wiley & sons.

Bender, J. A. (1957). Air permeability of snow, SIPRE research report 37, U.S. Army corps of engineers, Snow Ice and Permafrost Research Establishment, November 1957, 27 pp.

Beniston, M. (2012). Is snow in the Alps receding or disappearing? WIRES Climate Change 3, 349–358.

Benson, C. (1962). Stratigraphic studies in the snow and firn of the Greenland Icesheet, Cold Regions Research and Engineering Laboratory–Research Report 70. US Army Snow, Ice, and Permafrost Research Establishment, Engineer Research and Development Center (US).

Bergström, S. (1995). The HBV models. Computer models of watershed hydrology., 443-476.

Bernhardt, M., Zängl, G., Liston, G. E., Strasser, U., & Mauser, W. (2009). Using wind fields from a high-resolution atmospheric model for simulating snow dynamics in mountainous terrain. Hydrological Processes: An International Journal, 23(7), 1064-1075.

Berris, S. N., & Harr, R. D. (1987). Comparative snow accumulation and melt during rainfall in forested and clear-cut plots in the western Cascades of Oregon. Water Resources Research, 23(1), 135-142.

Bieniek, P. A., Bhatt, U. S., Walsh, J. E., Lader, R., Griffith, B., Roach, J. K., & Thoman, R. L. (2018). Assessment of Alaska rain-on-snow events using dynamical downscaling. Journal of Applied Meteorology and Climatology, 57(8), 1847-1863.

Bishop, M. P., Björnsson, H., Haeberli, W., Oerlemans, J., Shroder, J. F., & Tranter, M. (2011). Encyclopedia of snow, ice, and glaciers. Springer Science & Business Media.

Blackwell, J. (1954). A transient-flow method for determination of thermal constants of insulating materials in bulk part I—Theory. Journal of applied physics, 25(2), 137-144.

Blöschl, G. (1999). Scaling issues in snow hydrology. Hydrological processes, 13(14-15), 2149-2175.

Bloschl, R. (1991). A spatially distributed snowmelt model for application in alpine terrain. Snow, Hydrology and Forests in High Alpine Areas.

Boon, S. (2009). Snow ablation energy balance in a dead forest stand. Hydrological Processes: An International Journal, 23(18), 2600-2610.

Bowling, L. C., Pomeroy, J. W., & Lettenmaier, D. P. (2004). Parameterization of blowing-snow sublimation in a macroscale hydrology model. Journal of Hydrometeorology, 5(5), 745-762.

Bracht, J. (1949). Über die Wärmeleitfähigkeit des Erdbodens und des Schnees und den Wärmeumsatz im Erdboden.

Braithwaite, R. J., Laternser, M., & Pfeffer, W. T. (1994). Variations of near-surface firn density in the lower accumulation area of the Greenland ice sheet, Pâkitsoq, West Greenland. Journal of Glaciology, 40(136), 477-485.

Brauchli, T., Trujillo, E., Huwald, H., & Lehning, M. (2017). Influence of slope-scale snowmelt on catchment response simulated with the Alpine3D model. Water Resources Research, 53(12), 10723-10739.

Brooks, R. H., & Corey, A. T. (1966). Properties of porous media affecting fluid flow. Journal of the irrigation and drainage division, 92(2), 61-90.

Brown, R. D., & Mote, P. W. (2009). The response of Northern Hemisphere snow cover to a changing climate. Journal of Climate, 22(8), 2124-2145.

Brubaker, K., Rango, A., & Kustas, W. (1996). Incorporating radiation inputs into the snowmelt runoff model. Hydrological processes, 10(10), 1329-1343.

Brucker, L., Picard, G., Arnaud, L., Barnola, J. M., Schneebeli, M., Brunjail, H., ... & Fily, M. (2011). Modeling time series of microwave brightness temperature at Dome C, Antarctica, using vertically resolved snow temperature and microstructure measurements. Journal of Glaciology, 57(201), 171-182.

Brun, E., & Touvier, F. (1987). Etude expérimentale de la convection thermique dans la neige. Le journal de physique colloques, 48(C1), C1-257.

Buckingham, D., Skalka, C., & Bongard, J. (2015). Inductive machine learning for improved estimation of catchment-scale snow water equivalent. Journal of Hydrology, 524, 311-325.

Bulovic, N., McIntyre, N., & Trancoso, R. (2024). Climate change risks to mine closure. Journal of Cleaner Production, 142697.

Burns, S. P., Molotch, N. P., Williams, M. W., Knowles, J. F., Seok, B., Monson, R. K., ... & Blanken, P. D. (2014). Snow temperature changes within a seasonal snowpack

and their relationship to turbulent fluxes of sensible and latent heat. Journal of Hydrometeorology, 15(1), 117-142.

Bussière, B. & Guitonny, M. (2020). Hard Rock Mine Reclamation: From Prediction to Management of Acid Mine Drainage. CRC Press, Taylor and Francis Group.

Cacciuttolo, C., & Marinovic Pulido, A. (2022). Sustainable management of thickened tailings in Chile and Peru: a review of practical experience and socio-environmental acceptance. Sustainability, 14(17), 10901.

Cacciuttolo, C., & Tabra, K. (2015). Water management in the closure of tailings storage facilities. Santiago: 10a ICARD IMWA.

Cacciuttolo, C., Pastor, A., Valderrama, P., & Atencio, E. (2023). Process water management and seepage control in tailings storage facilities: Engineered environmental solutions applied in Chile and Peru. Water, 15(1), 196.

Caldwell, J. (2017). Tailings History: 2006 and 2017. Proceedings of the Tailings and Mine Wastes Conference, Banff, AB.

Calonne, N., Geindreau, C., Flin, F., Morin, S., Lesaffre, B., Rolland du Roscoat, S., & Charrier, P. (2012). 3-D image-based numerical computations of snow permeability: links to specific surface area, density, and microstructural anisotropy. The Cryosphere, 6(5), 939-951.

Campbell, G. S., & Norman, J. M. (2000). An introduction to environmental biophysics. Springer Science & Business Media.

Carbonell, R. G., & Whitaker, S. (1984). Heat and mass transfer in porous media. In Fundamentals of transport phenomena in porous media (pp. 121-198). Dordrecht: Springer Netherlands.

Carman, P. C. (1937). Fluid flow through granular beds. Transactions-Institution of Chemical Engineers, 15, 150-166

Carman, P. C. (1956). Flow of gases through porous media: Academic press

Carroll, T. (1977). A comparison of the CRREL 500 cm3 tube and the ILTS 200 and 100 cm3 box cutters used for determining snow densities. Journal of Glaciology, 18(79), 334-337.

Carroll, T.: A comparison of the CRREL 500cm 3 tube and the ILTS 200 and 100cm3 box cutters used for determining snow densities, J. Glaciol., 18, 334–337, 1977.

Cavcar, M. (2000). The international standard atmosphere (ISA). Anadolu University, Turkey, 30(9), 1-6.

Cavcar, M. (2000). The international standard atmosphere (ISA). Anadolu University, Turkey, 30(9), 1-6.

Cazorzi, F., & Dalla Fontana, G. (1996). Snowmelt modelling by combining air temperature and a distributed radiation index. Journal of Hydrology, 181(1-4), 169-187.

Chakraborty, K., Mehrotra, K., Mohan, C. K., & Ranka, S. (1992). Forecasting the behavior of multivariate time series using neural networks. Neural networks, 5(6), 961-970.

CHANGE, O. C. (2007). Intergovernmental panel on climate change. World Meteorological Organization, 52, 1-43.

Che, T., Li, X., Jin, R., Armstrong, R., & Zhang, T. (2008). Snow depth derived from passive microwave remote-sensing data in China. Annals of glaciology, 49, 145-154.

Chen, R., Lü, S., Kang, E., Ji, X., Yang, Y., & Zhang, J. (2006). A distributed water-heat coupled (DWHC) model for mountainous watershed of an inland river basin (I): model structure and equations. Advances in Earth Science, 21(8), 806.

Chen, Y. N., Yang, Q., Luo, Y., Shen, Y., Pan, X. L., Li, L., & Li, Z. Q. (2012). Ponder on the issues of water resources in the arid region of northwest China. Arid Land Geography, 35(1), 1-9.

Cheng, B., & Titterington, D. M. (1994). Neural networks: A review from a statistical perspective. Statistical science, 2-30.

Cherkauer, K. A., & Lettenmaier, D. P. (1999). Hydrologic effects of frozen soils in the upper Mississippi River basin. Journal of Geophysical Research: Atmospheres, 104(D16), 19599-19610.

Cherkauer, K. A., & Lettenmaier, D. P. (2003). Simulation of spatial variability in snow and frozen soil. Journal of Geophysical Research: Atmospheres, 108(D22).

Chivers, B. D., Wallbank, J., Cole, S. J., Sebek, O., Stanley, S., Fry, M., & Leontidis, G. (2020). Imputation of missing sub-hourly precipitation data in a large sensor network: A machine learning approach. Journal of Hydrology, 588, 125126.

Clemente, J. S., & Huntsman, P. (2019). Potential climate change effects on the geochemical stability of waste and mobility of elements in receiving environments for Canadian metal mines south of 60° N. Environmental Reviews, 27(4), 478-518.

Clifton, A., Manes, C., Rüedi, J. D., Guala, M., & Lehning, M. (2008). On shear-driven ventilation of snow. Boundary-layer meteorology, 126, 249-261.

Cline, D. W. (1997). Snow surface energy exchanges and snowmelt at a continental, midlatitude Alpine site. Water Resources Research, 33(4), 689-701.

Clyde, G. (1931). Snow-melting characteristics. Tech. Bull. 231, Utah Agric. Exp. Sta., Logan, UT.

Cohen, J., Ye, H., & Jones, J. (2015). Trends and variability in rain-on-snow events. Geophysical Research Letters, 42(17), 7115-7122.

Colbeck, S. (1974). The capillary effects on water percolation in homogeneous snow. Journal of Glaciology, 13, 85-97

Colbeck, S. (1978). The Difficulties of Measuring the Water Saturation and Porosity of Snow. Journal of Glaciology, 20(82), 189-201.

Colbeck, S. C. (1975). A theory for water flow through a layered snowpack. Water Resources Research, 11(2), 261-266.

Colbeck, S. C., Akitaya, E., Armstrong, R. L., Gubler, H., Lafeuille, J., Lied, K., Mcclung, D. M., Morris, E. M. (1990). The International Classification for Seasonal Snow on

the Ground. International Commission on Snow and Ice (IAHS), World Data Center A for Glaciology, University of Colorado, Boulder, CO, USA

Combarnous, M. A., & Bories, S. A. (1975). Hydrothermal convection in saturated porous media. In Advances in hydroscience (Vol. 10, pp. 231-307). Elsevier.

COMSOL, A. (2018). Subsurface flow module user's guide. COMSOL Multiphysics, 5.

Conger, S. M., & McCLUNG, D. M. (2009). Comparison of density cutters for snow profile observations. Journal of Glaciology, 55(189), 163-169.

Conway, H., & Benedict, R. (1994). Infiltration of water into snow. Water Resources Research, 30(3), 641-649.

Côté, J., & Konrad, J. M. (2009). Assessment of structure effects on the thermal conductivity of two-phase porous geomaterials. International Journal of Heat and Mass Transfer, 52(3-4), 796-804.

Côté, J., Rahimi, M., Konrad, J.M. (2012). Thermal conductivity of compacted snow. 15th International Conference on Cold Regions Engineering, ed. Brian Morse, ASCE, Québec, Canada.

Daanen, R. P. (2004). Modeling liquid water flow in snow. University of Minnesota

Daanen, R. P., & Nieber, J. L. (2009). Model for coupled liquid water flow and heat transport with phase change in a snowpack. Journal of Cold Regions Engineering, 23(2), 43-68

Dadic, R., Mott, R., Lehning, M., & Burlando, P. (2010). Wind influence on snow depth distribution and accumulation over glaciers. Journal of Geophysical Research: Earth Surface, 115(F1).

Davies, J. A., & Idso, S. B. (1979). Estimating the surface radiation balance and its components.

De Oliveira, V. A., Rodrigues, A. F., Morais, M. A. V., Terra, M. D. C. N. S., Guo, L., & de Mello, C. R. (2021). Spatiotemporal modelling of soil moisture in an A tlantic forest through machine learning algorithms. european Journal of soil science, 72(5), 1969-1987.

De Quervain, M. (1956). Zur Wärmeleitung von Schnee. Eidg. Institut für Schnee-und Lawinenforschung, Weissfluhjoch/Davos.

De Quervain, M. R. (1973). Snow structure, heat, and mass flux through snow.

De Vries, D. A. (1963). Thermal properties of soil. Chapter 7 In: WR Van Wijk. Physics of Plant Environment.

Debye, P., Anderson Jr, H. R., & Brumberger, H. (1957). Scattering by an inhomogeneous solid. II. The correlation function and its application. Journal of applied Physics, 28(6), 679-683.

Dedieu, J. P., Carlson, B. Z., Bigot, S., Sirguey, P., Vionnet, V., & Choler, P. (2016). On the importance of high-resolution time series of optical imagery for quantifying the effects of snow cover duration on alpine plant habitat. Remote Sensing, 8(6), 481.

Denoth, A., Foglar, A., Weiland, P., Mätzler, C., Aebischer, H., Tiuri, M., & Sihvola, A. (1984). A comparative study of instruments for measuring the liquid water content of snow. Journal of Applied Physics, 56(7), 2154-2160.

Denoth, A., Foglar, A., Weiland, P., Mätzler, C., Aebischer, H., Tiuri, M., & Sihvola, A. (1984). A comparative study of instruments for measuring the liquid water content of snow. Journal of Applied Physics, 56(7), 2154-2160.Derksen, C., & Brown, R. (2012). Spring snow cover extent reductions in the 2008–2012 period exceeding climate model projections. Geophysical Research Letters, 39(19).

Desilets, D., Zreda, M., & Ferré, T. P. (2010). Nature's neutron probe: Land surface hydrology at an elusive scale with cosmic rays. Water Resources Research, 46(11).

Devaux, J. (1933). L'économie radio-thermique des champs de neige et des glaciers. In Annales de Physique (Vol. 10, No. 20, pp. 5-67). EDP Sciences.

DeWalle, D. R., & Rango, A. (2008). Principles of snow hydrology. Cambridge University Press.

DeWalle, D. R., Henderson, Z., & Rango, A. (2002, May). Spatial and temporal variations in snowmelt degree-day factors computed from SNOTEL data in the Upper Rio

Grande basin. In Proceedings of the Western Snow Conference (Vol. 70, p. 73). Colorado State University.

Dibb, J. E., & Fahnestock, M. (2004). Snow accumulation, surface height change, and firn densification at Summit, Greenland: Insights from 2 years of in situ observation. Journal of Geophysical Research: Atmospheres, 109(D24)

Dickinson, H. C., & Osborne, N. S. (1915). Specific heat and heat of fusion of ice (No. 248). US Government Printing Office.

Ding, J., & Cui, C. (2017). Simulation and validation of enhanced snowmelt runoff model with topographic factor. Transactions of the Chinese Society of Agricultural Engineering, 33(19), 179-186.

Ding, M., Zhang, T., Yang, D., Allison, I., Dou, T., & Xiao, C. (2021). Brief communication: Evaluation of multiple density-dependent empirical snow conductivity relationships in East Antarctica. The Cryosphere, 15(9), 4201-4206.

Dingman SL (1994) Physical hydrology. MacMillan Publishing Company, New York

Dominé, F., & Shepson, P. B. (2002). Air-snow interactions and atmospheric chemistry. Science, 297(5586), 1506-1510.

Domine, F., Albert, M., Huthwelker, T., Jacobi, H. W., Kokhanovsky, A. A., Lehning, M., & Simpson, W. R. (2008). Snow physics as relevant to snow photochemistry. Atmospheric chemistry and physics, 8(2), 171-208.

Domine, F., Lauzier, T., Cabanes, A., Legagneux, L., Kuhs, W. F., Techmer, K., & Heinrichs, T. (2003). Snow metamorphism as revealed by scanning electron microscopy. Microscopy research and technique, 62(1), 33-48

Domine, F., Salvatori, R., Legagneux, L., Salzano, R., Fily, M., & Casacchia, R. (2006). Correlation between the specific surface area and the short wave infrared (SWIR) reflectance of snow. Cold Regions Science and Technology, 46(1), 60-68.

Domine, F., Taillandier, A. S., & Simpson, W. R. (2007). A parameterization of the specific surface area of seasonal snow for field use and for models of snowpack evolution. Journal of Geophysical Research: Earth Surface, 112(F2).

Dorsey, N. E. (1940). Properties of ordinary water-substance in all its phases: water-vapor, water, and all the ices.

Dozier, J. (1980). A clear-sky spectral solar radiation model for snow-covered mountainous terrain. Water Resources Research, 16(4), 709-718.

Dozier, J., & Warren, S. G. (1982). Effect of viewing angle on the infrared brightness temperature of snow. Water resources research, 18(5), 1424-1434.

Dozier, J., Davis, R. E., & Perla, R. (1987). On the objective analysis of snow microstructure. Avalanche Formation, Movement and Effects, 162, 46-59.

Dunkle, Robert V., and J. T. Bevans. "An approximate analysis of the solar reflectance and transmittance of a snow cover." Journal of Atmospheric Sciences 13.2 (1956): 212-216.

East, D., & Fernandez, R. (2021). Managing water to minimize risk in tailings storage facility design, construction, and operation. Mine Water and the Environment, 40(1), 36-41.

Edwards, A. C., Scalenghe, R., & Freppaz, M. (2007). Changes in the seasonal snow cover of alpine regions and its effect on soil processes: a review. Quaternary international, 162, 172-181.

Eidsvik, K. J., Holstad, A., Lie, I., & Utnes, T. (2004). A prediction system for local wind variations in mountainous terrain. Boundary-Layer Meteorology, 112, 557-586.

Eiriksson, D., Whitson, M., Luce, C. H., Marshall, H. P., Bradford, J., Benner, S. G., ... & McNamara, J. P. (2013). An evaluation of the hydrologic relevance of lateral flow in snow at hillslope and catchment scales. Hydrological Processes, 27(5), 640-654.

Environnement Canada. (2009). Code de Pratiques Écologiques pour les Mines de Métaux.

ERMITE-Consortium, Younger, P. L., & Wolkersdorfer, C. (2004). Mining impacts on the freshwater environment: technical and managerial guidelines for catchment scale management. Mine water and the environment, 23(Suppl 1), s2-s80.

Essery, R., Li, L., & Pomeroy, J. (1999). A distributed model of blowing snow over complex terrain. Hydrological processes, 13(14-15), 2423-2438.

Fang, S. F., Pei, H., Liu, Z. H., Dai, W., & Zhao, Q. D. (2008). Study on the distributed snowmelt runoff process based on RS and GIS. J. Remote Sens, 12(4), 655-662.

Fausto, R. S., Box, J. E., Vandecrux, B., Van As, D., Steffen, K., MacFerrin, M. J., ... & Braithwaite, R. J. (2018). A snow density dataset for improving surface boundary conditions in Greenland ice sheet firn modeling. Frontiers in Earth Science, 6, 51.

Federer, C. A., & Lash, D. (1978). BROOK: A hydrologic simulation model for eastern forests.

Federer, C. A., Pierce, R. S., & Hornbeck, J. W. (1972). Snow management seems unlikely in the Northeast. Proceedings series.

Fedoseeva, V. I., & Fedoseev, N. F. (1988). Evaluation of the coefficient of diffusion of water vapour in snow cover. Meteorologiya i Gidrologiya, 2, 132-35.

Fernandes, C. G., Lee, O., & Wakabayashi, Y. (2009). Minimum cycle cover and Chinese postman problems on mixed graphs with bounded tree-width. Discrete Applied Mathematics, 157(2), 272-279.

Fierz, C. R. L. A., Armstrong, R. L., Durand, Y., Etchevers, P., Greene, E., McClung, D. M., ... & Sokratov, S. A. (2009). The international classification for seasonal snow on the ground. Fierz, C. & Baunach, T. (2000) Quantifying grain-shape changes in snow subjected to large temperature gradients. Ann. Glaciol. 31, 439–444.

Finsterwalder, S. (1887). Der suldenferner. Zeitschrift des Deutschen und Osterreichischen Alpenvereins, 18, 72-89.

Finnis, J. (2013). Projected impacts of climate change for the province of Newfoundland & Labrador.

Fitzpatrick, N., Radić, V., & Menounos, B. (2017). Surface energy balance closure and turbulent flux parameterization on a mid-latitude mountain glacier, Purcell Mountains, Canada. Frontiers in Earth Science, 5, 67.

Flanner, M. G., Shell, K. M., Barlage, M., Perovich, D. K., & Tschudi, M. A. (2011). Radiative forcing and albedo feedback from the Northern Hemisphere cryosphere between 1979 and 2008. Nature Geoscience, 4(3), 151-155.

Flerchinger, G. N., & Hanson, C. L. (1989). Modeling soil freezing and thawing on a rangeland watershed. Transactions of the ASAE, 32(5), 1551-1554.

Fletcher, C. G. (2005). Investigations into seasonal predictability of North Atlantic winter climate. University of London, University College London (United Kingdom).

Fletcher, C. G., Zhao, H., Kushner, P. J., & Fernandes, R. (2012). Using models and satellite observations to evaluate the strength of snow albedo feedback. Journal of Geophysical Research: Atmospheres, 117(D11).

Flin, F., Brzoska, J. B., Lesaffre, B., Coléou, C., & Pieritz, R. A. (2004). Three-dimensional geometric measurements of snow microstructural evolution under isothermal conditions. Annals of glaciology, 38, 39-44.

Flood, I., & Kartam, N. (1994). Neural networks in civil engineering. I: Principles and understanding. Journal of computing in civil engineering, 8(2), 131-148.

Freeze, R. A. (1971). Three-dimensional, transient, saturated-unsaturated flow in a groundwater basin. Water Resources Research, 7(2), 347-366.

Freudiger, D., Kohn, I., Seibert, J., Stahl, K., & Weiler, M. (2017). Snow redistribution for the hydrological modeling of alpine catchments. Wiley Interdisciplinary Reviews: Water, 4(5), e1232.

Freudiger, D., Kohn, I., Stahl, K., & Weiler, M. (2014). Large-scale analysis of changing frequencies of rain-on-snow events with flood-generation potential. Hydrology and Earth System Sciences, 18(7), 2695-2709.

Galbraith, P. S., & Larouche, P. (2013). Trends and variability in air and sea surface temperatures in eastern Canada. Aspects of Climate Change in the Northwest Atlantic off Canada. Canadian Technical Report of Fisheries and Aquatic Science, 3045, 1-18.

Gallet, J. C., Domine, F., Arnaud, L., Picard, G., & Savarino, J. (2010). Vertical profiles of the specific surface area of the snow at Dome C, Antarctica. Cryos. Discuss, 4(3), 1647-1708.

Gallet, J. C., Domine, F., Zender, C. S., & Picard, G. (2009). Measurement of the specific surface area of snow using infrared reflectance in an integrating sphere at 1310 and 1550 nm. The Cryosphere, 3(2), 167-182.

Geiger, R. (1966). The climate near the ground Harvard Univ. Press, Cambridge, Mass.

Gelfan, A. L. E. X. A. N. D. E. R. (2006). Physically based model of heat and water transfer in frozen soil and its parameterization by basic soil data. IAHS publication, 303, 293.

Gergely, M., Schneebeli, M., & Roth, K. (2010). First experiments to determine snow density from diffuse near-infrared transmittance. Cold regions science and technology, 64(2), 81-86.

Geris, J., Comte, J. C., Franchi, F., Petros, A. K., Tirivarombo, S., Selepeng, A. T., & Villholth, K. G. (2022). Surface water-groundwater interactions and local land use control water quality impacts of extreme rainfall and flooding in a vulnerable semi-arid region of Sub-Saharan Africa. Journal of Hydrology, 609, 127834.

Ghormley, J. A., & Hochanadel, C. J. (1971). Amorphous ice: Density and reflectivity. Science, 171(3966), 62-64.

Giauque, W. F., & Stout, J. W. (1936). The Entropy of Water and the Third Law of Thermodynamics. The Heat Capacity of Ice from 15 to 273° K. Journal of the American Chemical Society, 58(7), 1144-1150.

Giddings, J. C., & LaChapelle, E. (1962). The formation rate of depth hoar. Journal of Geophysical Research, 67(6), 2377-2383.

Glen, J. W. (1997). Paterson, WSB 1994. The physics of glaciers. Oxford, New York, Tokyo, Pergamon, ix, 480 pp. ISBN 0-08037945 1, HB. ISBN 0-08037944 3, Flexicover. Journal of Glaciology, 43(145), 594-594.

Goering, D. J. (2003). Passively cooled railway embankments for use in permafrost areas. Journal of Cold Regions Engineering, 17(3), 119-133

Gogoi, M. M., & Babu, S. S. (2016, May). Aerosol optical properties over the Svalbard region of Arctic: ground-based measurements and satellite remote sensing. In

Remote Sensing of the Atmosphere, Clouds, and Precipitation VI (Vol. 9876, pp. 194-200).

Golubev, V. N., & Frolov, A. D. (2000). Model of structure and mechanical properties of dry granular snow. Annals of Glaciology, 31, 434-438.

Gray DM, Male DH (1981) Handbook of snow, principles, processes, management, and use. Pergamon Press, New York

Gray, D. M., & Landine, P. G. (1988). An energy-budget snowmelt model for the Canadian Prairies. Canadian Journal of Earth Sciences, 25(8), 1292-1303.

Grell, G. A., Dudhia, J., & Stauffer, D. R. (1994). A description of the fifth-generation Penn State/NCAR Mesoscale Model (MM5).

Grenfell, T. C. & Warren, S. G. (1999) Representation of a nonspherical ice particle by a collection of independent spheres for scattering and absorption of radiation. J. Geophys. Res. 104(D24), 31 697– 31 709.

Grenier, C., Anbergen, H., Bense, V., Chanzy, Q., Coon, E., Collier, N., ... & Voss, C. (2018). Groundwater flow and heat transport for systems undergoing freeze-thaw: Intercomparison of numerical simulators for 2D test cases. Advances in water resources, 114, 196-218.

Grundstein, A. J., and Leathers, D. J. (1999). A spatial analysis of snow-surface energy exchanges over the northern Great Plains of the United States in relation to synoptic scale forcing mechanisms. Int. J. Climatol. 19, 489–511.

Grünewald, T., Wolfsperger, F., and Lehning, M. (2018). Snow farming: conserving snow over the summer season. Cryosphere 12, 385–400.

Guide, E. U., & Multiphysics, C. O. M. S. O. L. (2006). V6. 0. Lowell, MA, USA: Diagnosys LLC.

Guo, J., Li, Z., Li, F., & Zhang, S. (2021). Evaluation on snow coverage and snow depth simulated by VIC-CAS model based on multi-source remote sensing data in mountainous upper reach of the Shule River basin. J. Glaciol. Geocryol, 43, 650-661.

Gururajan, M. P. (2015). Dry Snow Metamorphism.

Gutmann, E. D., Larson, K. M., Williams, M. W., Nievinski, F. G., & Zavorotny, V. (2012). Snow measurement by GPS interferometric reflectometry: an evaluation at Niwot Ridge, Colorado. Hydrological Processes, 26(19), 2951-2961.

Guyomarc'h, G., & Mérindol, L. (1998). Validation of an application for forecasting blowing snow. Annals of Glaciology, 26, 138-143.

Hamlet, A. F., and Lettenmaier, D. P. (2007). Effects of 20th century warming and climate variability on flood risk in the western US. Water Resour. Res. 43: W06427.

Hansen, A. C., & Foslien, W. E. (2015). A macroscale mixture theory analysis of deposition and sublimation rates during heat and mass transfer in dry snow. The Cryosphere, 9(5), 1857-1878.

Harding, R. J., & Pomeroy, J. W. (1996). The energy balance of the winter boreal landscape. Journal of Climate, 9(11), 2778-2787.

Hardy, J., & Albert, D. (1993). The Permeability of Temperate Snow. Paper presented at the Proceedings of the Annual Meeting-Eastern Snow Conference

Harlan, R. L. (1973). Analysis of coupled heat-fluid transport in partially frozen soil. Water Resources Research, 9(5), 1314-1323.

Hermassi, M., Valderrama, C., Gibert, O., Moreno, N., Font, O., Querol, X., ... & Cortina, J. L. (2016). Integration of powdered Ca-activated zeolites in a hybrid sorption–membrane ultrafiltration process for phosphate recovery. Industrial & Engineering Chemistry Research, 55(21), 6204-6212.

Harr, R. D. (1981). Some characteristics and consequences of snowmelt during rainfall in western Oregon. Journal of Hydrology, 53(3-4), 277-304.

Hartman, M. D., Baron, J. S., Lammers, R. B., Cline, D. W., Band, L. E., Liston, G. E., & Tague, C. (1999). Simulations of snow distribution and hydrology in a mountain basin. Water Resources Research, 35(5), 1587-1603.

Hashin, Z., & Shtrikman, S. (1962). A variational approach to the theory of the effective magnetic permeability of multiphase materials. Journal of applied Physics, 33(10), 3125-3131.

Hashin, Z., Shtrikman, S. (1962). A variational approach on the theory of the effective magnetic permeability of multiphase materials. Journal of Applied Physic 33, 3125-3131.

He, S. W., Nan, Z. T., Zhang, L., & Yu, W. (2015). Spatial-temporal distribution of water and energy fluxes in the upper reaches of the Heihe River simulated with VIC model. J. Glaciol. Geocryol, 37, 211-225.

Hedstrom, N. R., & Pomeroy, J. W. (1998). Accumulation of intercepted snow in the boreal forest: measurements and modelling. Hydrological Processes, 12(1), 611-1.

Heusser, C. J. (1995). Late-Quaternary vegetation response to climatic-glacial forcing in North Pacific America. Physical Geography, 16(2), 118-149.

Hirashima, H., Yamaguchi, S., Sato, A., & Lehning, M. (2010). Numerical modeling of liquid water movement through layered snow based on new measurements of the water retention curve. Cold Regions Science and Technology, 64(2), 94-103.

Hock, R. (1999). A distributed temperature-index ice-and snowmelt model including potential direct solar radiation. Journal of glaciology, 45(149), 101-111.

Hori, M., Aoki, T., Tanikawa, T., Motoyoshi, H., Hachikubo, A., Sugiura, K., ... & Takahashi, F. (2006). In-situ measured spectral directional emissivity of snow and ice in the 8–14 μm atmospheric window. Remote Sensing of Environment, 100(4), 486-502.

Hu, X., Yang, J., Tu, Y., Su, Z., Guan, Q., & Ma, Z. (2024). Hydrogel-Based Interfacial Solar-Driven Evaporation: Essentials and Trails. Gels, 10(6), 371.

Hyun, S. W., Kim, S., Jeong, H., Ko, H. S., & Shin, D. H. (2024). Development of snow removal system using embedded piped inside road with solar thermal energy collector and packed bed latent heat thermal energy storage. Journal of Energy Storage, 83, 110737.

Il Jeong, D., & Sushama, L. (2018). Rain-on-snow events over North America based on two Canadian regional climate models. Climate Dynamics, 50, 303-316.

Illangasekare, T. H., Walter Jr, R. J., Meier, M. F., & Pfeffer, W. T. (1990). Modeling of meltwater infiltration in subfreezing snow. Water Resources Research, 26(5), 1001-1012.

Immerzeel, W. W., Van Beek, L. P., & Bierkens, M. F. (2010). Climate change will affect the Asian water towers. science, 328(5984), 1382-1385.

Izumi, K., & Huzioka, T. (1975). Studies of metamorphism and thermal conductivity of snow. I.

Jaafar, H., & Picot, J. J. C. (1970). Thermal conductivity of snow by a transient state probe method. Water Resources Research, 6(1), 333-335.

Jafari, M., Sharma, V., & Lehning, M. (2022). Convection of water vapour in snowpacks. Journal of Fluid Mechanics, 934, A38.

Jansson, M. (1901). Über die Warmeleitungsfahigkeit des Schnees. Ofversigt K. Vetenskapsakad. Forh., 58, 207-222.

Jansson, P. E., & Halldin, S. (1979). Model for annual water and energy flow in a layered soil. In Developments in Agricultural and Managed Forest Ecology (Vol. 9, pp. 145-163). Elsevier.

Jansson, P. E., & Moon, D. S. (2001). A coupled model of water, heat and mass transfer using object orientation to improve flexibility and functionality. Environmental Modelling & Software, 16(1), 37-46.

Jin, Z., Charlock, T. P., Yang, P., Xie, Y., & Miller, W. (2008). Snow optical properties for different particle shapes with application to snow grain size retrieval and MODIS/CERES radiance comparison over Antarctica. Remote Sensing of Environment, 112(9), 3563-3581.

Jóhannesson, T., Sigurdsson, O., Laumann, T., & Kennett, M. (1995). Degree-day glacier mass-balance modelling with applications to glaciers in Iceland, Norway, and Greenland. Journal of Glaciology, 41(138), 345-358.

Johanson, R. C., Imhoff, J. C., Kittle, J. L., & Donigan, A. S. (1984). Hydrological Simulation Program--FORTRAN(HSPF): User's Manual for Release 8. 0. EPA-600/3-84-006 June 1984. Environmental Protection Agency, Athens, GA. 767 p, 138 p, 49 Ref, 5 Append. Contract/Grant, (68-01).

Johnson, J. B., Sturm, M. A. T. T. H. E. W., Perovich, D. K., & Benson, C. S. (1987). Field observations of thermal convection in a subarctic snow cover. Intl Assoc. Hydrol. Sci. Publ, 162, 105-118.

Jordan, D. R. (1991). A new reading of a phylactery from Beirut. Zeitschrift für Papyrologie und Epigraphik, 61-69.

Jordan, R. E. (1991). A one-dimensional temperature model for a snow cover: Technical documentation for SNTHERM. 89.

Jordan, R. E., Andreas, E. L., & Makshtas, A. P. (1999). Heat budget of snow-covered sea ice at North Pole 4. Journal of Geophysical Research: Oceans, 104(C4), 7785-7806

Jost, G., Moore, R. D., Smith, R., & Gluns, D. R. (2012). Distributed temperature-index snowmelt modelling for forested catchments. Journal of Hydrology, 420, 87-101.

Juras, R., Pavlásek, J., Vitvar, T., Šanda, M., Holub, J., Jankovec, J., & Linda, M. (2016). Isotopic tracing of the outflow during artificial rain-on-snow event. Journal of Hydrology, 541, 1145-1154.

Kaimal, J. C., & Finnigan, J. J. (1994). Atmospheric boundary layer flows: their structure and measurement. Oxford university press.

Kane, H. S. (1969). A neutron probe for the determination of snow density and its use in Antarctica. Research Foundation and the Institute of Polar Studies, The Ohio State University.

Kargl, G., Zohrer, A., (2006). Reconstruction of grain size distributions in granular and regolith soil with ground penetrating instruments. Geophysical Research Abstracts, vol. 8, 04280.

Kattelmann, R. (1985). Macropores in snowpacks of Sierra Nevada. Annals of Glaciology, 6, 272-273.

Kattelmann, R. (1997). Flooding from rain-on-snow events in the Sierra Nevada. IAHS Publications-Series of Proceedings and Reports-Intern Assoc Hydrological Sciences, 239, 59-66.

Katto, Y., & Masuoka, T. (1967). Criterion for the onset of convective flow in a fluid in a porous medium. International Journal of Heat and Mass Transfer, 10(3), 297-309.

Keeler, C. M. (1964). Relationship between Climate, Ablation, and Run-Off on an Arctic Glacier. McGill University (Canada).

Kelly, R. E., & Pal, D. (1978). Thermal convection with spatially periodic boundary conditions: resonant wavelength excitation. Journal of Fluid Mechanics, 86(3), 433-456.

Kendra, J. R., Ulaby, F. T., & Sarabandi, K. (1994). Snow probe for in situ determination of wetness and density. IEEE Transactions on Geoscience and Remote Sensing, 32(6), 1152-1159.

Kerbrat, M., Pinzer, B., Huthwelker, T., Gäggeler, H. W., Ammann, M., & Schneebeli, M. (2008). Measuring the specific surface area of snow with X-ray tomography and gas adsorption: comparison and implications for surface smoothness. Atmospheric Chemistry and Physics, 8(5), 1261-1275.

Kersten, M. S. (1949). Thermal properties of soils.

Kiedrzyńska, E., Kiedrzyński, M., & Zalewski, M. (2015). Sustainable floodplain management for flood prevention and water quality improvement. Natural Hazards, 76, 955-977.

Klever, N. (1985). Air and water-vapour convection in snow. Annals of glaciology, 6, 39-42.

Klute, A. (1988). Methods of soil analysis 2d ed., pt. 1; physical and mineralogical methods. Soil Science, 146(2), 138.

Knox, S. H., Carey, S. K., & Humphreys, E. R. (2012). Snow surface energy exchanges and snowmelt in a shrub-covered bog in eastern Ontario, Canada. Hydrological Processes, 26(12), 1876-1890.

Kodaira, N., & Inada, M. (1955). Measurement of snowfall intensity by radar. Papers in Meteorology and Geophysics, 6(2), 126-129.

Kojima, K. (1954) Visco-elastic property of snow. Low Temp. Sci., Series A, 12.

Kojima, K. (1956). Viscous compression of natural snow-layer II. Low Temperature Science, 15, 117-135.

Kojima, K. (1957). Viscous compression of natural snow-layers III. Low Temperature Science, 16, 167-196.

Kojima, K. (1958). Sekisetsuso no nensei asshuku. IV [Viscous compression of natural snow layers. IV]. Low Temp. Sci, 53-64.

Kokhanovsky, A. A. and Zege, E., (2004): Scattering optics of snow, Appl. Optics, 43, 1589–1602.

Kokhanovsky, A., & Schreier, M. (2009). The determination of snow specific surface area, albedo and effective grain size using AATSR space-borne measurements. International Journal of Remote Sensing, 30(4), 919-933.

Kokhanovsky, A., Rozanov, V. V., Aoki, T., Odermatt, D., Brockmann, C., Krüger, O., ... & Hori, M. (2011). Sizing snow grains using backscattered solar light. International Journal of Remote Sensing, 32(22), 6975-7008.

Kolomyts, E. G. (1984) Kristallo-morfologicheskii atlas snega: posobie dlya snegolavinnykh stantsii. [Acrystallomorphological atlas of snow: a handbook for snow-avalanche stations]. Gidrometeoizdat, Leningrad, Russia (in Russian).

Kondrat'eva, A. S. (1954). Thermal conductivity of the snow cover and physical processes caused by the temperature gradient (p. 0012). Snow, Ice and Permafrost Research Establishment, Corps of Engineers, US Army.

Kozeny, J. (1927). Über kapillare Leitung des Wassers im Boden:(Aufstieg, Versickerung und Anwendung auf die Bewässerung): Hölder-Pichler-Tempsky.

Kratzert, F., Klotz, D., Brenner, C., Schulz, K., & Herrnegger, M. (2018). Rainfall–runoff modelling using long short-term memory (LSTM) networks. Hydrology and Earth System Sciences, 22(11), 6005-6022.

Kustas, W. P., Rango, A., & Uijlenhoet, R. (1994). A simple energy budget algorithm for the snowmelt runoff model. Water resources research, 30(5), 1515-1527.

Kuusisto, E. (1980). On the values and variability of degree-day melting factor in Finland. Hydrology Research, 11(5), 235-242.

Kuvaeva, G. M. (1975). Physical properties of snow cover of the Greater Caucasus.

Kuvaeva, G. M., Sulakvelidze, G. K., Chitadze, V. S., Chotorlishvili, L. S., & El'Mesov, A. M. (1975). Physical properties of snow cover of the Greater Caucasus.

Kuyucak, N. (2021). Water in Mining and Environment for Sustainability. Mine Water and the Environment, 40(4), 815-817.

Lachance, O. (2014). Conductivité thermique et perméabilité intrinsèque de la neige compactée. Université Laval

Lafleur PM, Hember RA, Admiral SW, Roulet NT. (2005). Annual and seasonal variability in evapotranspiration and water table at a shrub-covered bog in southern Ontario, Canada. Hydrological Processes 19(18): 3533– 3550.

Laliberte, G. E., Corey, A. T., & Brooks, R. H. (1966). Properties of unsaturated porous media (Doctoral dissertation, Colorado State University. Libraries).

Lange, M.A. (1985). Measurements of thermal parameters in Antartic snow and firn. Ann. Glaciol., 6, 100-104.

Langlois, A., Kohn, J., Royer, A., Cliche, P., Brucker, L., Picard, G., ... & Willemet, J. M. (2009). Simulation of snow water equivalent (SWE) using thermodynamic snow models in Québec, Canada. Journal of Hydrometeorology, 10(6), 1447-1463.

Lapwood, E. (1948, October). Convection of a fluid in a porous medium. In Mathematical Proceedings of the Cambridge Philosophical Society (Vol. 44, No. 4, pp. 508-521). Cambridge University Press.

Laternser, M., & Schneebeli, M. (2003). Long-term snow climate trends of the Swiss Alps (1931–99). International Journal of Climatology: A Journal of the Royal Meteorological Society, 23(7), 733-750.

Lazri, M., Labadi, K., Brucker, J. M., & Ameur, S. (2020). Improving satellite rainfall estimation from MSG data in Northern Algeria by using a multi-classifier model based on machine learning. Journal of Hydrology, 584, 124705.

Leavesley, G. H. (1984). Precipitation-runoff modeling system: User's manual (Vol. 83, No. 4238). US Department of the Interior.

Leavesley, G. H., & Stannard, L. G. (1995). The precipitation-runoff modeling system-PRMS. Computer models of watershed hydrology., 281-310.

Legagneux, L., Cabanes, A., & Dominé, F. (2002). Measurement of the specific surface area of 176 snow samples using methane adsorption at 77 K. Journal of Geophysical Research: Atmospheres, 107(D17), ACH-5.

Legagneux, L., Lauzier, T., Domin, F., Kuhs, W. F., Heinrichs, T., & Techmer, K. (2003). Rate of decay of specific surface area of snow during isothermal experiments and morphological changes studied by scanning electron microscopy. Canadian Journal of Physics, 81(1-2), 459-468

Lehning, M., Bartelt, P., Brown, B., Fierz, C., & Satyawali, P. (2002). A physical SNOWPACK model for the Swiss avalanche warning: Part II. Snow microstructure. Cold regions science and technology, 35(3), 147-167.

Lehning, M., Doorschot, J., & Bartelt, P. (2000). A snowdrift index based on SNOWPACK model calculations. Annals of Glaciology, 31, 382-386.

Lehning, M., Völksch, I., Gustafsson, D., Nguyen, T. A., Stähli, M., & Zappa, M. (2006). ALPINE3D: a detailed model of mountain surface processes and its application to snow hydrology. Hydrological Processes: An International Journal, 20(10), 2111-2128.

Lesaffre, B., Pougatch, E. & Martin, E. (1998) Objective determination of snow-grain characteristics from images. Ann. Glaciol. 26, 112–118.

Li, D., Lettenmaier, D. P., Margulis, S. A., & Andreadis, K. (2019). The role of rain-on-snow in flooding over the conterminous United States. Water Resources Research, 55(11), 8492-8513.

Li, J., Guala, M., & Hong, J. (2022). Snow particle analyzer for simultaneous measurements of snow density and morphology. arXiv preprint arXiv:2209.11129.

Li, P., Zha, Y., Shi, L., Tso, C. H. M., Zhang, Y., & Zeng, W. (2020). Comparison of the use of a physical-based model with data assimilation and machine learning methods for simulating soil water dynamics. Journal of Hydrology, 584, 124692.

Li, X., & Koike, T. (2003). Frozen soil parameterization in SiB2 and its validation with GAME-Tibet observations. Cold Regions Science and Technology, 36(1-3), 165-182.

Liang, X., Lettenmaier, D. P., Wood, E. F., & Burges, S. J. (1994). A simple hydrologically based model of land surface water and energy fluxes for general circulation models. Journal of Geophysical Research: Atmospheres, 99(D7), 14415-14428.

Light, P. (1941). Analysis of high rates of snow melting. Trans. AGU, 195-205.

Link, T., & Marks, D. (1999). Distributed simulation of snowcover mass-and energy-balance in the boreal forest. Hydrological Processes, 13(14-15), 2439-2452.

Lipiec, J., & Hatano, R. (2003). Quantification of compaction effects on soil physical properties and crop growth. Geoderma, 116(1-2), 107-136.

List, R. J. (1951). Smithsonian meteorological tables. Smithsonian miscellaneous collections.

Lister, H., & Taylor, P. F. (1961). Heat balance and ablation on an Arctic glacier. CA Reitzel.

Liston, G. E., & Sturm, M. (1998). A snow-transport model for complex terrain. Journal of Glaciology, 44(148), 498-516.

Liu, Q., & Hu, R. (2017). Simulation of Heat and Mass Transfer during Artificial Ground Freezing in Saturated Saline Groundwater. In Excerpt from the Proceedings of the 2017 COMSOL Conference in Rotterdam.

Liu, S., XIE, Z., Song, G., Ma, L., & Ageta, Y. (1996). Mass balance of Kangwure (flat-top) Glacier on the north side of Mt. Xixiabangma, China. Bulletin of glacier research, (14), 37-43.

Loescher, H. W., Hanson, C. V., & Ocheltree, T. W. (2009). The psychrometric constant is not constant: A novel approach to enhance the accuracy and precision of latent energy fluxes through automated water vapor calibrations. Journal of Hydrometeorology, 10(5), 1271-1284.

López-Moreno, J. I., Pomeroy, J., Revuelto, J., and Vicente-Serrano, S. M. (2013). Response of snow processes to climate change: spatial variability in a small basin in the Spanish Pyre- nees. Hydrol. Process. 27, 2637–2650.

Lougeay, R.L. (1969). Micro-climatological Studies Over the Seward Glacier Snowpack. Climatological Investigations in the Icefield Ranges, Summer 1965. Washington, D.C.: Research Paper No. 54, Arctic Institute of North America, pp. 51-102.

Lu, H., Wei, W. S., Liu, M., Han, X., & Hong, W. (2015). Energy budget over seasonal snow surface at an open site and beneath forest canopy openness during the snowmelt period in western Tianshan Mountains, China. Journal of Mountain Science, 12, 298-312.

Luce, C. H., Tarboton, D. G., & Cooley, K. R. (1998). The influence of the spatial distribution of snow on basin-averaged snowmelt. Hydrological Processes, 12(10-11), 1671-1683.

Lundberg, A., Granlund, N., & Gustafsson, D. (2010). Towards automated 'Ground truth'snow measurements—A review of operational and new measurement methods for Sweden, Norway, and Finland. Hydrological processes, 24(14), 1955-1970.

Lundy, C. C., Edens, M. Q., & Brown, R. L. (2002). Measurement of snow density and microstructure using computed tomography. Journal of Glaciology, 48(161), 312-316.

Luo, L., Robock, A., Vinnikov, K. Y., Schlosser, C. A., Slater, A. G., Boone, A., ... & Yang, Z. L. (2003). Effects of frozen soil on soil temperature, spring infiltration, and runoff: Results from the PILPS 2 (d) experiment at Valdai, Russia. Journal of Hydrometeorology, 4(2), 334-351.

Lyapustin, A., Tedesco, M., Wang, Y., Aoki, T., Hori, M., & Kokhanovsky, A. (2009). Retrieval of snow grain size over Greenland from MODIS. Remote Sensing of Environment, 113(9), 1976-1987.

MacDonald, M. K., Pomeroy, J. W., & Pietroniro, A. (2010). On the importance of sublimation to an alpine snow mass balance in the Canadian Rocky Mountains. Hydrology and Earth System Sciences, 14(7), 1401-1415.

Magnusson, J., Jonas, T., Lopez-Moreno, I., & Lehning, M. (2010). Snow cover response to climate change in a high alpine and half-glacierized basin in Switzerland. Hydrology research, 41(3-4), 230-240.

Maier, H. R., & Dandy, G. C. (2000). Neural networks for the prediction and forecasting of water resources variables: a review of modelling issues and applications. Environmental modelling & software, 15(1), 101-124.

Male, D. H., & Granger, R. J. (1979). Energy mass fluxes at the snow surface in a prairie environment.

Male, D. H., & Granger, R. J. (1981). Snow surface energy exchange. Water Resources Research, 17(3), 609-627.

Malnes, E., Buanes, A., Nagler, T., Bippus, G., Gustafsson, D., Schiller, C., & Wiesmann, A. (2015). User requirements for the snow and land ice services–CryoLand. The Cryosphere, 9(3), 1191-1202.

Marchenko, S., Cheng, G., Lötstedt, P., Pohjola, V., Pettersson, R., Van Pelt, W., & Reijmer, C. (2019). Thermal conductivity of firn at Lomonosovfonna, Svalbard, derived from subsurface temperature measurements. The Cryosphere, 13(7), 1843-1859.

Margulis, S. A., Cortés, G., Girotto, M., & Durand, M. (2016). A Landsat-era Sierra Nevada snow reanalysis (1985–2015). Journal of Hydrometeorology, 17(4), 1203-1221.

Marks D, Domingo J, Susong D, Link T, Garen D (1999) A spatially distributed energy balance snowmelt model for application in mountain basins. Hydrol Process 13:1935–1959

Marks, D. G. (1988). Climate, energy exchange, and snowmelt in Emerald Lake watershed, Sierra Nevada. University of California, Santa Barbara.

Marks, D., & Dozier, J. (1992). Climate and energy exchange at the snow surface in the alpine region of the Sierra Nevada: 2. Snow cover energy balance. Water Resources Research, 28(11), 3043-3054.

Marks, D., & Winstral, A. (2001). Comparison of snow deposition, the snow cover energy balance, and snowmelt at two sites in a semiarid mountain basin. Journal of Hydrometeorology, 2(3), 213-227.

Marks, D., Dozier, J. (1992). Climate and energy exchange at the snow surface in the alpine region of the Sierra Nevada: 2. Snow cover energy balance. Water Resources Research, 28(11), 3043-3054

Marks, D., Kimball, J., Tingey, D., & Link, T. (1998). The sensitivity of snowmelt processes to climate conditions and forest cover during rain-on-snow: A case study of the 1996 Pacific Northwest flood. Hydrological Processes, 12(10-11), 1569-1587.

Marks, D., Kimball, J., Tingey, D., & Link, T. (1998). The sensitivity of snowmelt processes to climate conditions and forest cover during rain-on-snow: A case study of the 1996 Pacific Northwest flood. Hydrological Processes, 12(10-11), 1569-1587.

Marks, D., Winstral, A., Flerchinger, G., Reba, M., Pomeroy, J., Link, T., & Elder, K. (2008). Comparing simulated and measured sensible and latent heat fluxes over snow under a pine canopy to improve an energy balance snowmelt model. Journal of Hydrometeorology, 9(6), 1506-1522.

Marsh, P. (1991). Water flux in melting snow covers. Advances in porous media, 1, 61-124

Marsh, P., & Pomeroy, J. W. (1996). Meltwater fluxes at an arctic forest-tundra site. Hydrological Processes, 10(10), 1383-1400.Marshall, S. E. (1987). Parameterization of snow albedo for climate models. IAHS Publ., 166, 43-50.

Marshall, H. P., Conway, H., & Rasmussen, L. A. (1999). Snow densification during rain. Cold Regions Science and Technology, 30(1-3), 35-41.

Martinec, J. (1975). Snowmelt-runoff model for stream flow forecasts. Hydrology Research, 6(3), 145-154.

Martinec, J., & Rango, A. (1986). Parameter values for snowmelt runoff modelling. Journal of hydrology, 84(3-4), 197-219.

Mary, A., Dumont, M., Dedieu, J. P., Durand, Y., Sirguey, P., Milhem, H., ... & Morin, S. (2013). Intercomparison of retrieval algorithms for the specific surface area of snow from near-infrared satellite data in mountainous terrain, and comparison with the output of a semi-distributed snowpack model. The Cryosphere, 7(2), 741-761.

Matson, M., & Wiesnet, D. R. (1981). New data base for climate studies. Nature, 289 (5797), 451-456.

Matzl, M., & Schneebeli, M. (2006). Measuring specific surface area of snow by near-infrared photography. Journal of Glaciology, 52(179), 558-564.

Matzl, M., & Schneebeli, M. (2010). Stereological measurement of the specific surface area of seasonal snow types: Comparison to other methods, and implications for mm-scale vertical profiling. Cold Regions Science and Technology, 64(1), 1-8.

Matzl, M., & Schneebeli, M. (2010). Stereological measurement of the specific surface area of seasonal snow types: Comparison to other methods, and implications for mm-scale vertical profiling. Cold Regions Science and Technology, 64(1), 1-8.

Mätzler, C. (2002) Relation between grain-size and correlation length of snow. J. Glaciol. 48(162), 461–466.

McCabe, G. J., Clark, M. P., & Hay, L. E. (2007). Rain-on-snow events in the western United States. Bulletin of the American Meteorological Society, 88(3), 319-328.

McKay, G. A. (1970). Precipitation. Handbook on the principles of hydrology. Edited by DM Gray. Secretariat, Canadian National Committee for the International Hydrological Decade, Saskatoon, Sask. pp. II

Meinicke, S., Dubil, K., Wetzel, T., & Dietrich, B. (2020). Characterization of heat transfer in consolidated, highly porous media using a hybrid-scale CFD approach. International Journal of Heat and Mass Transfer, 149, 119201.

Melloh, R. A., Hardy, J. P., Bailey, R. N., & Hall, T. J. (2002). An efficient snow albedo model for the open and sub-canopy. Hydrological Processes, 16(18), 3571-3584.

Mellor, M. (1964). Properties of snow: US Army Materiel Command, Cold Regions Research & Engineering Laboratory

Mellor, M. (1974). A review of basic snow mechanics (pp. 251-291). Hanover, NH: US Army Cold Regions Research and Engineering Laboratory.

Mendoza Zúñiga, P., Musselman, K. N., Revuelto, J., Deems, J. S., López Moreno, J. I., & McPhee, J. (2020). Interannual and seasonal variability of snow depth scaling behavior in a subalpine catchment.

Merz, R., & Blöschl, G. (2003). A process typology of regional floods. Water resources research, 39(12).

Minkowycz, W. J., Haji-Sheikh, A., & Vafai, K. F. (1999). On departure from local thermal equilibrium in porous media due to a rapidly changing heat source: the Sparrow number. International journal of heat and mass transfer, 42(18), 3373-3385.

Monteith, J. L. (1973). Principles of environmental physics.

Morid, S. (2000). Snowmelt-Runoff simulation for snowbound ungauged catchments (Doctoral dissertation, IIT Delhi).

Morid, S., Gosain, A. K., & Keshari, A. K. (2000, December). An algorithm for monitoring snow water equivalent in ungauged catchments using GIS. In Submitted to International Conference of Integrated Water Resource Management.

Morin, S., Domine, F., Arnaud, L., & Picard, G. (2010). In-situ monitoring of the time evolution of the effective thermal conductivity of snow. Cold Regions Science and Technology, 64(2), 73-80

Morin, S., Domine, F., Dufour, A., Lejeune, Y., Lesaffre, B., Willemet, J. M., ... & Jacobi, H. W. (2013). Measurements and modeling of the vertical profile of specific surface area of an alpine snowpack. Advances in water resources, 55, 111-120.

Morland, L., Kelly, R., & Morris, E. (1990). A mixture theory for a phase-changing snowpack. Cold Regions Science and Technology, 17(3), 271-285

Morris, E. (1987). Modelling of water flow through snowpacks Seasonal Snowcovers: Physics, Chemistry, Hydrology (pp. 179-208): Springer.

Morris, E. M., & Cooper, J. D. (2003). Density measurements in ice boreholes using neutron scattering. Journal of Glaciology, 49(167), 599-604.

Mosley-Thompson, E., McConnell, J. R., Bales, R. C., Li, Z., Lin, P. N., Steffen, K., ... & Bathke, D. (2001). Local to regional-scale variability of annual net accumulation on the Greenland ice sheet from PARCA cores. Journal of Geophysical Research: Atmospheres, 106(D24), 33839-33851.

Mote, P. W. (2006). Climate-driven variability and trends in mountain snowpack in Western North America. J. Clim. 19, 6209–6220.

Mott, R., & Lehning, M. (2010). Meteorological modeling of very high-resolution wind fields and snow deposition for mountains. Journal of Hydrometeorology, 11(4), 934-949.

Mott, R., Faure, F., Lehning, M., Henning, L. Ö. W. E., Hynek, B., Michlmayer, G., & Schöner, W. (2008). Simulation of seasonal snow-cover distribution for glacierized sites on Sonnblick, Austria, with the Alpine3D model. Annals of Glaciology, 49, 155-160.

Mott, R., Vionnet, V., & Grünewald, T. (2018). The seasonal snow cover dynamics: review on wind-driven coupling processes. Frontiers in Earth Science, 6, 197.

Mualem, Y. (1976). A new model for predicting the hydraulic conductivity of unsaturated porous media. Water Resources Research, 12(3), 513-522.

Mueller, S. (2015). What is Goldsim? Boliden Mining, Sweden. WaterSmart-Seminar on Management of water balance in mining areas, 28th of August 2015. Finnish Environment Institute, Helsinki.

Multiphysics, C. O. M. S. O. L. (2008). Variably Saturated Flow and Transport: Sorbing Solute. Earth Science Module Model Library.

Multiphysics, C. O. M. S. O. L. (2019). Frozen Inclusion. COMSOL Multiphysics, 6.1.

Munneke, P. K., Ligtenberg, S., Noel, B., Howat, I., Box, J. E., Mosley-Thompson, E., ... & van den Broeke, M. R. (2015, December). Taking the Firn into Account: Elevation Change of the Greenland Ice Sheet due to Surface Mass Balance and Firn Processes, 1960-2014. In 2015 AGU Fall Meeting. AGU.

Munro, D. S., & Young, G. J. (1982). An operational net shortwave radiation model for glacier basins. Water Resources Research, 18(2), 220-230.

Musselman, K. N., Clark, M. P., Liu, C., Ikeda, K., & Rasmussen, R. (2017). Slower snowmelt in a warmer world. Nature Climate Change, 7(3), 214-219.

Musselman, K. N., Lehner, F., Ikeda, K., Clark, M. P., Prein, A. F., Liu, C., ... & Rasmussen, R. (2018). Projected increases and shifts in rain-on-snow flood risk over western North America. Nature Climate Change, 8(9), 808-812.

Nakai, Y., Sakamoto, T., Terajima, T., Kitamura, K., & Shirai, T. (1999). Energy balance above a boreal coniferous forest: a difference in turbulent fluxes between snow-covered and snow-free canopies. Hydrological Processes, 13(4), 515-529.

Nakano, Y., & Froula, N. H. (1973, July). Sound and shock transmission in frozen soils. In Proceedings of the 2nd International Conference on Permafrost, North American Contribution, Yakutsk, USSR (pp. 359-369).

Nakaya, U., & Kuroiwa, D. (1970). Physical properties and internal structure of Greenland snow (Vol. 89). Corps of Engineers, US Army Cold Regions Research and Engineering Laboratory.

Narita, H. (1971). Specific surface of deposited snow II, Low Temp.

Negi, H. S., & Kokhanovsky, A. (2011). Retrieval of snow grain size and albedo of western Himalayan snow cover using satellite data. The Cryosphere, 5(4), 831-847.

Nelson, J. (1998). Sublimation of ice crystals. Journal of the atmospheric sciences, 55(5), 910-919.

Nield, D. A. (1968). Onset of thermohaline convection in a porous medium. Water Resources Research, 4(3), 553-560.

Nield, D. A. (1998). Effects of local thermal nonequilibrium in steady convective processes in a saturated porous medium: forced convection in a channel. Journal of porous media, 1(2), 181-186.

Niittynen, P., & Luoto, M. (2018). The importance of snow in species distribution models of arctic vegetation. Ecography, 41(6), 1024-1037.

Niu, G. Y., & Yang, Z. L. (2006). Effects of frozen soil on snowmelt runoff and soil water storage at a continental scale. Journal of Hydrometeorology, 7(5), 937-952.

Obled, C., & Harder, H. (1978). A review of snow melt in the mountain environment. Proceedings, Modeling of Snow Cover Runoff, 179-204.

Ocampo Melgar, D., & Meza, F. J. (2020). Exploring the fingerprints of past rain-on-snow events in a central Andean Mountain range basin using satellite imagery. Remote Sensing, 12(24), 4173.

Ochsner, T. E., Horton, R., & Ren, T. (2001). A new perspective on soil thermal properties. Soil science society of America Journal, 65(6), 1641-1647.

Oerlemans, J., Anderson, B., Hubbard, A., Huybrechts, P., Johannesson, T., Knap, W. H., ... & Zuo, Z. (1998). Modelling the response of glaciers to climate warming. Climate dynamics, 14, 267-274.

Olyphant, G. A. (1984). Insolation topoclimates and potential ablation in alpine snow accumulation basins: Front Range, Colorado. Water Resources Research, 20(4), 491-498.

Osborn, G. (1982). Handbook of snow: Principles, processes, management & use, edited by DM Gray and DH Male. Arctic, 35(2), 346-346.

Östin, R., & Andersson, S. (1991). Frost growth parameters in a forced air stream. International Journal of Heat and Mass Transfer, 34(4-5), 1009-1017.

Painter, T. H., Molotch, N. P., Cassidy, M., Flanner, M., & Steffen, K. (2007). Contact spectroscopy for determination of stratigraphy of snow optical grain size. Journal of Glaciology, 53(180), 121-127.

Pall, P., Tallaksen, L. M., & Stordal, F. (2019). A climatology of rain-on-snow events for Norway. Journal of Climate, 32(20), 6995-7016.

Palm, E., & Tveitereid, M. (1979). On heat and mass flux through dry snow. Journal of Geophysical Research: Oceans, 84(C2), 745-749.

Paltridge, G. W., & CMR, P. (1976). Radiative Processes in Meteorology and Climatology.

Pawlowski, M., Lipiec, J., & Debicki, R. (1996). Computer-aided penetrometer system for measuring soil strength. Polish Journal of Soil Science, 29(1), 1-7.

Pedersen, A., Speed, J. D. M., and Tombre, I. M. (2013). Prevalence of grubbing in the arctic tundra increases with the pink- footed goose population expansion. Polar Biol. 36, 1569–1575.

Pellicciotti, F., Brock, B., Strasser, U., Corripio, J., Burlando, P., & Funk, M. (2003, December). The Distributed Application of an Enhanced Temperature-Index Melt Model Including Albedo and Global Radiation. In AGU Fall Meeting Abstracts (Vol. 2003, pp. C22B-02).

Picard, G., Arnaud, L., Domine, F., & Fily, M. (2009). Determining snow specific surface area from near-infrared reflectance measurements: Numerical study of the influence of grain shape. Cold Regions Science and Technology, 56(1), 10-17.

PIEVC [Public Infrastructure Engineering Vulnerability Committee] (2008): Water resources public infrastructure vulnerability assessment for Placentia, Newfoundland; Appendix B-2 in Adapting to Climate Change: Canada's First

National Engineering Vulnerability Assessment of Public Infrastructure; Engineers Canada, 76 p.

Picard, G., Brucker, L., Fily, M., Gallée, H., & Krinner, G. (2009). Modeling time series of microwave brightness temperature in Antarctica. Journal of Glaciology, 55(191), 537-551.

Pitman, D., & Zuckerman, B. (1968). Effective Thermal Conductivity of Snow at-88 C, -27 C and-5 C. SAO Special Report, 267.

Pitman, D., & Zuckerman, B. (1968). Effective Thermal Conductivity of Snow at-88 C, -27 C and-5 C. SAO Special Report, 267

Pohl, S., Davison, B., Marsh, P., & Pietroniro, A. (2005). Modelling spatially distributed snowmelt and meltwater runoff in a small Arctic catchment with a hydrology land-surface scheme (WATCLASS). Atmosphere-Ocean, 43(3), 193-211.

Pollock, E. (2009). Glaciers of the Canadian Rockies and their response to global climate change.

Pomeroy, J. W., & Brun, E. (2001). Physical properties of snow. Snow ecology: An interdisciplinary examination of snow-covered ecosystems, 45, 118.

Pomeroy, J. W., & Essery, R. L. H. (1999). Turbulent fluxes during blowing snow: field tests of model sublimation predictions. Hydrological Processes, 13(18), 2963-2975.

Pomeroy, J. W., & Goodison, B. E. (1997). Winter and snow. The surface climates of Canada, 68-100.

Pomeroy, J. W., & Gray, D. M. (1995). Snowcover accumulation, relocation, and management. (No Title).

Pomeroy, J. W., Gray, D. M., & Landine, P. G. (1993). The prairie blowing snow model: characteristics, validation, operation. Journal of Hydrology, 144(1-4), 165-192.

Pool, S., Molnar, P., Hunkeler, D., Lienert, C., Peleg, N., Sinreich, M., ... & Hosi, S. 13 Hydrology and Hydrogeology.

Powers, D. J., Colbeck, S. C., & O'Neill, K. (1985). Thermal convection in snow. COLD REGIONS RESEARCH AND ENGINEERING LAB HANOVER NH.

Powers, D., O'Neill, K., & Colbeck, S. C. (1985). Theory of natural convection in snow. Journal of Geophysical Research: Atmospheres, 90(D6), 10641-10649.

Proksch, M., Löwe, H., & Schneebeli, M. (2015). Density, specific surface area, and correlation length of snow measured by high-resolution penetrometry. Journal of Geophysical Research: Earth Surface, 120(2), 346-362.

Proksch, M., Rutter, N., Fierz, C., & Schneebeli, M. (2016). Intercomparison of snow density measurements: bias, precision, and vertical resolution. The Cryosphere, 10(1), 371-384.

PSC, (2014). The Canadian disaster database, Public Safety Canada, Ottawa, Canada.

Pulliainen, J., & Hallikainen, M. (2001). Retrieval of regional snow water equivalent from space-borne passive microwave observations. Remote sensing of environment, 75(1), 76-85.

Punkkinen, H., Räsänen, L., Mroueh, U. M., Korkealaakso, J., Luoma, S., Kaipainen, T., ... & Krogerus, K. (2016). Guidelines for mine water management. VTT Technology, 266, 1-157.

Purves, R. S., Barton, J. S., Mackaness, W. A., & Sugden, D. E. (1998). The development of a rule-based spatial model of wind transport and deposition of snow. Annals of Glaciology, 26, 197-202.

Qu, S. M., Liu, H., Cui, Y. P., Shi, P., Bao, W. M., & Yu, Z. B. (2013). Test of newly developed conceptual hydrological model for simulation of rain-on-snow events in forested watershed. Water Science and Engineering, 6(1), 31-43.

Rahimi, M., & Côté, J. (2016). Modélisation de l'effet du couvert de neige sur les transferts thermiques sol-atmosphère, Ph.D. dissertation, Laval University, Canada

Rango, A. (1995). The Snowmelt Runoff Model (SRM). Computer models of watershed hydrology., 477-520.

Reeh, N., Fisher, D. A., Koerner, R. M., & Clausen, H. B. (2005). An empirical firn-densification model comprising ice lenses. Annals of Glaciology, 42, 101-106.

Rees, D. A. S., & Riley, D. S. (1986). Free convection in an undulating saturated porous layer: resonant wavelength excitation. Journal of Fluid Mechanics, 166, 503-530.

Rees, D. A. S., & Riley, D. S. (1989). The effects of boundary imperfections on convection in a saturated porous layer: near-resonant wavelength excitation. Journal of Fluid Mechanics, 199, 133-154.

Reimer, A. (1980). The effect of wind on heat transfer in snow. Cold Regions Science and Technology, 3(2), 129-137.

Ryberg, K. R. (2024). Why snow is crucial for water supply—and what will happen when it becomes scarce.

Riche, F., Schneebeli, M., & Tschanz, S. A. (2012). Design-based stereology to quantify structural properties of artificial and natural snow using thin sections. Cold regions science and technology, 79, 67-74.

Robinson, D. A., & Frei, A. (2000). Seasonal variability of Northern Hemisphere snow extent using visible satellite data. The Professional Geographer, 52(2), 307-315.

Saadat, S., Pandey, G., & Tharmavaram, M. (2020). Microscopy for forensic investigations. Technology in Forensic Science: Sampling, Analysis, Data and Regulations, 101-127.

Savard, J. P., Van Proosdij, D., & O'Carroll, S. (2016). Chapter 4: Perspectives on Canada's East Coast region; in canada's Marine Coasts in a Changing Climate, (ed,) D.S. Lemmen, F.J. Warren, T.S. James and C.S.L Mercer Clarke; Government of Canada, Ottawa, ON, p. 99-152.

Sawatsky, L. F., Beckstead, G., & Long, D. (1998). Integrated mine water management planning for environmental protection and mine profitability. International Journal of Surface Mining, Reclamation and Environment, 12(1), 37-39.

Schmidt, R. A., & Gluns, D. R. (1991). Snowfall interception on branches of three conifer species. Canadian Journal of Forest Research, 21(8), 1262-1269.

Schneebeli, M., & Johnson, J. B. (1998). A constant-speed penetrometer for high-resolution snow stratigraphy. Annals of Glaciology, 26, 107-111.

Schneebeli, M., & Sokratov, S. A. (2004). Tomography of temperature gradient metamorphism of snow and associated changes in heat conductivity. Hydrological Processes, 18(18), 3655-3665.

Schneiderbauer, S., & Prokop, A. (2011). The atmospheric snow-transport model: SnowDrift3D. Journal of Glaciology, 57(203), 526-542.

Schuh, W., & Cline, R. (1990). Effect of soil properties on unsaturated hydraulic conductivity pore-interaction factors. Soil science society of America journal, 54(6), 1509- 1519

Schweizer, J., van Herwijnen, A., & Reuter, B. (2011). Measurements of weak layer fracture energy. Cold Regions Science and Technology, 69(2-3), 139-144.

Seiferlin, K., Kargl, G., & Kömle, N. (2003). The effect of cementation on the thermal conductivity of porous media. In EGS-AGU-EUG Joint Assembly (p. 10748).

Seiferlin, K., Kömle, N. I., Kargl, G., & Spohn, T. (1996). Line heat-source measurements of the thermal conductivity of porous H2O ice, CO2 ice and mineral powders under space conditions. Planetary and Space Science, 44(7), 691-704.

SHAL, L. S. Atmospheric Environment Service Nownsview, Orntario.

Sharma, V., & Yuden, K. (2021). Imputing missing data in hydrology using machine learning models. Int. J. Eng. Res. Technol, 10(2021), 78-82.

Shen, C., Laloy, E., Elshorbagy, A., Albert, A., Bales, J., Chang, F. J., ... & Tsai, W. P. (2018). HESS Opinions: Incubating deep-learning-powered hydrologic science advances as a community. Hydrology and Earth System Sciences, 22(11), 5639-5656.

Shertzer, R. H., & Adams, E. E. (2011). Anisotropic thermal conductivity model for dry snow. Cold Regions Science and Technology, 69(2-3), 122-128.

Shimizu, H. (1970). Air permeability of deposited snow. Contributions from the Institute of Low Temperature Science, 22, 1-32

Shockley, J. C. (2021). Modeling watershed sensitivity to climate change in systems affected by discharge of mine tailings (Doctoral dissertation, The University of Nebraska-Lincoln).

Sihvola, A., & Tiuri, M. (1986). Snow fork for field determination of the density and wetness profiles of a snowpack. IEEE Transactions on Geoscience and Remote Sensing, (5), 717-721.

Singh, P., & Kumar, N. (1996). Determination of snowmelt factor in the Himalayan region. Hydrological sciences journal, 41(3), 301-310.

Singh, P., Spitzbart, G., Hübl, H., & Weinmeister, H. W. (1997). Hydrological response of snowpack under rain-on-snow events: a field study. Journal of Hydrology, 202(1-4), 1-20.

Sommerfeld, R. A., & Rocchio, J. E. (1993). Permeability measurements on new and equiseparated snow. Water resources research, 29(8), 2485-2490.

Sommerfeld, R., Rocchio, J. (1989). The Darcy permeability of finegrained compact snow. Paper presented at the Proceedings of the 46th Annual Eastern Snow Conference

Sommerfeld, R., Rocchio, J. (1993). Permeability measurements on new and equitemperature snow. Water Resources Research, 29(8), 2485-2490.

Spitz, K., & Trudinger, J. (2019). Tailings disposal: Concepts and practices. In Mining and the Environment (pp. 649-704). CRC Press.

Stadler, D., Flühler, H., & Jansson, P. E. (1997). Modelling vertical and lateral water flow in frozen and sloped forest soil plots. Cold Regions Science and Technology, 26(3), 181-194.

Steinacker, H. H. R. Hydrometeorological implications of the mass balance of Hintereisferner, 1952-53 to 1968-69.

Stoy, P. C., Peitzsch, E., Wood, D., Rottinghaus, D., Wohlfahrt, G., Goulden, M., & Ward, H. (2018). On the exchange of sensible and latent heat between the atmosphere and melting snow. Agricultural and Forest Meteorology, 252, 167-174.

Strachan, C. & Goodwin, S. (2015). The role of water management in tailings dam incidents. Proceedings of the Tailings and Mine Wastes Conference, Vancouver, BC, 26-28 October 2015.

Sturm, M., & Johnson, J. B. (1991). Natural convection in the subarctic snow cover. Journal of Geophysical Research: Solid Earth, 96(B7), 11657-11671.

Sturm, M., Benson, C. S. (1997). Vapor transport, grain growth and depth-hoar development in the subarctic snow. Journal of Glaciology, 43(143), 42-59.

Sturm, M., Goldstein, M. A., and Parr, C. (2017). Water and life from snow: a trillion-dollar science question. Water Resour. Res. 53, 3534–3544.

Sturm, M., Holmgren, J., König, M., & Morris, K. (1997). The thermal conductivity of seasonal snow. Journal of Glaciology, 43(143), 26-41.

Sturm, M., Perovich, D. K., & Holmgren, J. (2002). Thermal conductivity and heat transfer through the snow on the ice of the Beaufort Sea. Journal of Geophysical Research: Oceans, 107(C10).

Sugisaki, M., Suga, H., & Seki, S. (1968). Calorimetric study of the glassy state. IV. Heat capacities of glassy water and cubic ice. Bulletin of the Chemical Society of Japan, 41(11), 2591-2599.

Surdyk, S. (2002). Using microwave brightness temperature to detect short-term surface air temperature changes in Antarctica: An analytical approach. Remote Sensing of Environment, 80(2), 256-271.

Surfleet, C. G., & Tullos, D. (2013). Variability in effect of climate change on rain-on-snow peak flow events in a temperate climate. Journal of Hydrology, 479, 24-34.

Takala, M., Luojus, K., Pulliainen, J., Derksen, C., Lemmetyinen, J., Kärnä, J. P., ... & Bojkov, B. (2011). Estimating northern hemisphere snow water equivalent for climate research through assimilation of space-borne radiometer data and ground-based measurements. Remote Sensing of Environment, 115(12), 3517-3529.

Tang, M., Yu, S., You, S., & Jiang, P. (2024). The Characteristics and Application of Deuterium and Oxygen Isotopes to Karst Groundwater, Southwest China. Water, 16(13), 1812.

Tarboton D. G, Chowdhury T. G, Jackson T. H (1995) A spatially distributed energy balance snowmelt model. Proceedings of symposium on biogeochemistry of seasonally snow-covered catchments, Boulder, Colorado

Tarboton, D. G., & Luce, C. (1996). Utah Energy Balance Snow Accumulation and Melt Model (UEB)–Computer model technical description and user guide USDA Forest Service Research Technical Report.

Tarboton, D. G., Chowdhury, T. G., Jackson, T. H. (1994). A spatially distributed energy balance snowmelt model.

Taylor, B., & Taylor, E. M. (Eds.). (1997). Responding to global climate change in British Columbia and Yukon (Vol. 1). Environment Canada, Pacific and Yukon Region, Aquatic and Atmospheric Sciences Division.

Tedesco, M., & Kokhanovsky, A. A. (2007). The semi-analytical snow retrieval algorithm and its application to MODIS data. Remote Sensing of Environment, 111(2-3), 228-241.

Tedesco, M., Derksen, C., Deems, J. S., & Foster, J. L. (2015). Remote sensing of snow depth and snow water equivalent. Remote Sensing of the Cryosphere, 73-98.

Thapa, S., Zhao, Z., Li, B., Lu, L., Fu, D., Shi, X., ... & Qi, H. (2020). Snowmelt-driven streamflow prediction using machine learning techniques (LSTM, NARX, GPR, and SVR). Water, 12(6), 1734.

Tiuri, M. A. R. T. T. I., & Sihvola, A. (1985, August). Snow fork for field determination of the density and wetness profiles of a snowpack. In Hydrologic Applications of Space Technology, Proceedings of the Cocoa Beach Workshop, Florida (pp. 225-230).

Tiuri, M., Sihvola, A., Nyfors, E. G., & Hallikaiken, M. (1984). The complex dielectric constant of snow at microwave frequencies. IEEE Journal of oceanic Engineering, 9(5), 377-382.

Trabant, D., & Benson, C. (1972). Field experiments on the development of depth hoar. Geological Society of America Memoir, 135, 309-322.

Trevelyan, J. (2021). Learning engineering practice. CRC Press.

Trottier, M. O., Franklin, K., Portocarrero, J., Dufault, D., & Millar, R. (2023). The Impact of Climate Change on Extreme Events for Operation and Closure of Tailings Facilities.

Trujillo, E., Ramírez, J. A., & Elder, K. J. (2007). Topographic, meteorologic, and canopy controls on the scaling characteristics of the spatial distribution of snow depth fields. Water Resources Research, 43(7).

Turcotte, D. L. (1982). and G. Schubert, Geodynamics, 450 pp.

United States Army, Corps of Engineers. (1956). Snow hydrology. Portland, OR.

United States Army, Corps of Engineers. (1991). Streamflow synthesis and reservoir regulation (SSARR) model user manual. N. Pacific Div., Portland, OR.

US Army Corps of Engineers (1998) Runoff from snowmelt. (EM 1110-2-1406), Washington, DC, USA

Usowicz, B., Lipiec, J., & Usowicz, J. B. (2008). Thermal conductivity in relation to porosity and hardness of terrestrial porous media. Planetary and Space Science, 56(3-4), 438-447.

Usul N, Turan B (2006) Flood forecasting and analysis within the Ulus Basin, Turkey, using geographic information systems. Nat Hazards 39:213–229.

United Nations Economic Commission for Europe. Safety Guidelines and Good Practices for Tailings Management Facilities; United Nations Economic Commission for Europe: New York, NY, USA; Geneva, Switzerland, 2014.

Vafakhah, M., Sedighi, F., & Javadi, M. R. (2014). Modeling the rainfall-runoff data in snow-affected watershed. International Journal of Computer and Electrical Engineering, 6(1), 40.

Van Genuchten, M. T. (1980). A closed-form equation for predicting the hydraulic conductivity of unsaturated soils. Soil science society of America journal, 44(5), 892-898

Van Genuchten, M. T., & Nielsen, D. (1985). On describing and predicting the hydraulic properties of unsaturated soils. Ann. Geophys, 3(5), 615-628

Van Mullem, J. A., Garen, D., Woodward, D., & Mockus, V. (2004). Chapter 11: Snowmelt, part 630 hydrology national engineering handbook. Washington, DC: US Dept. of Agriculture Natural Resources Conservation Service.

Vanani, H. R., & Ostad-Ali-Askari, K. (2022). Correct path to use flumes in water resources management. Applied Water Science, 12(8), 187.

Vick, B., Özişik, M. N., & Bayazitoğlu, Y. (1980). A method of analysis of low Peclet number thermal entry region problems with axial conduction. Letters in Heat and Mass Transfer, 7(4), 235-248.

Vionnet, V., Brun, E., Morin, S., Boone, A., Martin, E., Faroux, S., Moigne, P.L., Willemet, J.M., (2012). The detailed snowpack scheme Crocus and its implementation in SURFEX v7.2. Geosci. Model. Dev. 5, 773–791. doi :10.5194/gmd-5-773-2012.

Vionnet, V., Martin, E., Masson, V., Guyomarc'h, G., Naaim-Bouvet, F., Prokop, A., ... & Lac, C. (2014). Simulation of wind-induced snow transport and sublimation in alpine terrain using a fully coupled snowpack/atmosphere model. The Cryosphere, 8(2), 395-415.

Wagener, T., Sivapalan, M., Troch, P. A., McGlynn, B. L., Harman, C. J., Gupta, H. V., ... & Wilson, J. S. (2010). The future of hydrology: An evolving science for a changing world. Water Resources Research, 46(5).

Wakao, N., Kaguei, S., & Funazkri, T. (1979). Effect of fluid dispersion coefficients on particle-to-fluid heat transfer coefficients in packed beds: correlation of Nusselt numbers. Chemical engineering science, 34(3), 325-336.

Walmsley, J. L., Salmon, J. R., & Taylor, P. A. (1982). On the application of a model of boundary-layer flow over low hills to real terrain. Boundary-Layer Meteorology, 23(1), 17-46.

Walter MT, Brooks ES, McCool DK, King LG, Molnau M, Boll J (2005) Process-based snowmelt modeling: does it require more input data than temperature-index modeling.

Wang, L., Koike, T., Yang, K., Jackson, T. J., Bindlish, R., & Yang, D. (2009). Development of a distributed biosphere hydrological model and its evaluation with the Southern Great Plains Experiments (SGP97 and SGP99). Journal of Geophysical Research: Atmospheres, 114(D8).

Wang, L., Koike, T., Yang, K., Jin, R., & Li, H. (2010). Frozen soil parameterization in a distributed biosphere hydrological model. Hydrology and Earth System Sciences, 14(3), 557-571.

Wang, X., & Baker, I. (2013). Observation of the microstructural evolution of snow under uniaxial compression using X-ray computed microtomography. Journal of Geophysical Research: Atmospheres, 118(22), 12-371.

Wang, Z.L.; Liu, C.X.; Jiang, Q.X.; Fu, Q.; Chen, W.J.; Ying, Y.M. (2019). Simulation of soil water-heat process in black soil region of Songnen Plain based on COUPMODEL. J. Northeast Agric. Univ. 50, 50–58.

Wankiewicz, A. (1978). A review of water movement in snow. Modeling of Snow Cover Runoff, 26-28

Warren, S. G. (1982). Optical properties of snow. Reviews of Geophysics, 20(1), 67-89.

Warscher, M., Strasser, U., Kraller, G., Marke, T., Franz, H., & Kunstmann, H. (2013). Performance of complex snow cover descriptions in a distributed hydrological

model system: A case study for the high Alpine terrain of the Berchtesgaden Alps. Water resources research, 49(5), 2619-2637.

Washburn, E. W. (1928). International critical tables of numerical data, physics, chemistry, and technology, vol III (p. 272). New York: McGraw-Hill.

Wei, C. A. O., Yu, S. H. E. N. G., Jichun, W. U., Shengting, W. A. N. G., & Shuai, M. A. (2018). Seasonal variation of soil hydrological processes of active layer in source region of the Yellow River. 水科学进展, 29(1), 1-10.

Weltzin, J. F., Betancourt, J. L., Cook, B. I., Crimmins, T. M., Enquist, C. A., Gerst, M. D., ... & Running, S. W. (2020). Seasonality of biological and physical systems as indicators of climatic variation and change. Climatic change, 163(4), 1755-1771.

Welch, C. M., Stoy, P. C., Rains, F. A., Johnson, A. V., & McGlynn, B. L. (2016). The impacts of mountain pine beetle disturbance on the energy balance of snow during the melt period. Hydrological Processes, 30(4), 588-602.

Whalley, W. R., Lipiec, J., Stępniewski, W., & Tardieu, F. (2000). Control and measurement of the physical environment in root growth experiments.

Wheeler, J. A., Cortés, A. J., Sedlacek, J.; Karrenberg, S., Van Kleunen, M., Wipf, S., et al. (2016). The snow and the willows: earlier spring snowmelt reduces performance in the low-lying alpine shrub Salix herbacea. J. Ecol. 104, 1041–1050.

Wiebe, H., Heygster, G., Zege, E., Aoki, T., & Hori, M. (2013). Snow grain size retrieval SGSP from optical satellite data: Validation with ground measurements and detection of snow fall events. Remote sensing of environment, 128, 11-20.

Wiesmann, A., Mätzler, C., & Weise, T. (1998). Radiometric and structural measurements of snow samples. Radio Science, 33(2), 273-289.

Wigmosta, M. S., Vail, L. W., & Lettenmaier, D. P. (1994). A distributed hydrology-vegetation model for complex terrain. Water resources research, 30(6), 1665-1679.

Wilson, W. T. (1941). An outline of the thermodynamics of snowmelt. Eos, Transactions American Geophysical Union, 22(1), 182-195.

Winstral, A., & Marks, D. (2002). Simulating wind fields and snow redistribution using terrain-based parameters to model snow accumulation and melt over a semi-arid mountain catchment. Hydrological Processes, 16(18), 3585-3603.

Winstral, A., Elder, K., & Davis, R. E. (2002). Spatial snow modeling of wind-redistributed snow using terrain-based parameters. Journal of hydrometeorology, 3(5), 524-538.

Winstral, A., Marks, D., & Gurney, R. (2013). Simulating wind-affected snow accumulations at catchment to basin scales. Advances in Water Resources, 55, 64-79.

Woodside, W. (1958). Calculation of the thermal conductivity of porous media. Canadian Journal of Physics, 36(7), 815-823

Wosten, J., & Van Genuchten, M. T. (1988). Using texture and other soil properties to predict the unsaturated soil hydraulic functions. Soil science society of America journal, 52(6), 1762-1770

WSB, Paterson. The physics of glaciers. Oxford: Pergamon, 1994

Xie, Z., Hu, Z., Ma, Y., Sun, G., Gu, L., Liu, S., ... & Ma, W. (2019). Modeling blowing snow over the Tibetan Plateau with the Community Land Model: Method and preliminary evaluation. Journal of Geophysical Research: Atmospheres, 124(16), 9332-9355.

Yamaguchi, S., Katsushima, T., Sato, A., & Kumakura, T. (2010). Water retention curve of snow with different grain sizes. Cold Regions Science and Technology, 64(2), 87-93

Yamazaki, Y., Kubota, J., Ohata, T., Vuglinsky, V., & Mizuyama, T. (2006). Seasonal changes in runoff characteristics on a permafrost watershed in the southern mountainous region of eastern Siberia. Hydrological Processes: An International Journal, 20(3), 453-467.

Yang, S., Yang, D., Chen, J., Santisirisomboon, J., Lu, W., & Zhao, B. (2020). A physical process and machine learning combined hydrological model for daily streamflow

simulations of large watersheds with limited observation data. Journal of Hydrology, 590, 125206.

Yang, Y., & Chen, R. (2011). Research Review on Hydrology in the Permafrost and Seasonal Frozen Regions. Advances in earth science, 26(7), 711.

Ye, H., Yang, D., & Robinson, D. (2008). Winter rain on snow and its association with air temperature in northern Eurasia. Hydrological Processes: An International Journal, 22(15), 2728-2736.

Yen, Y. C. (1963). Heat transfer by vapor transfer in ventilated snow. Journal of Geophysical Research, 68(4), 1093-1101.

Yen, Y. C. (1969). Recent studies on snow properties. Advances in Hydroscience, 5, 173-214.

Yen, Y. C. (1981). Review of thermal properties of snow, ice, and sea ice (Vol. 81, No. 10). US Army, Corps of Engineers, Cold Regions Research and Engineering Laboratory.

Yong, Y., Ren-sheng, C. H. E. N., Xi-bin, J. I., Wen-wu, Q. I. N. G., Jun-feng, L. I. U., & Chun-tan, H. A. N. (2010). Heat and water transfer processes on alpine meadow frozen grounds of Heihe mountainous in Northwest China, 21(1), 30-35.

Yosida, Z. (1955). Physical Studies on Deposited Snow. I.; Thermal Properties. Contributions from the Institute of Low Temperature Science, 7, 19-74.

Yosida, Z., Oura, H., Kuroiwa, D., Huzioka, T., Kojima, K., & Kinosita, S. (1958). Physical Studies on Deposited Snow. IV.; Mechanical Properties. (3). Contributions from the Institute of Low Temperature Science, 13, 55-100.

You J (2004) Snow hydrology: the parameterization of subgrid processes within a physically based snow energy and mass balance model. Ph.D. dissertation, Utah State University, USA.

Zahmatkesh, Z., Kumar Jha, S., Coulibaly, P., & Stadnyk, T. (2019). An overview of river flood forecasting procedures in Canadian watersheds. Canadian Water Resources Journal/Revue canadienne des ressources hydriques, 44(3), 213-229.

Zanotti F, Endorzzi S, Bertoldi G, Rigon R (2004) The GEOTOP snow model. 61st Eastern Snow Conference Portland, Maine, USA.

Zeiringer, B., Seliger, C., Greimel, F., & Schmutz, S. (2018). River hydrology, flow alteration, and environmental flow. Riverine ecosystem management: Science for governing towards a sustainable future, 67-89.

Zege, E. P., Katsev, I. L., Malinka, A. V., Prikhach, A. S., Heygster, G., & Wiebe, H. (2011). Algorithm for retrieval of the effective snow grain size and pollution amount from satellite measurements. Remote Sensing of Environment, 115(10), 2674-2685.

Zhang, L., Li, X., Zheng, D., Zhang, K., Ma, Q., Zhao, Y., & Ge, Y. (2021). Merging multiple satellite-based precipitation products and gauge observations using a novel double machine learning approach. Journal of Hydrology, 594, 125969.

Zhang, T. (2005). Influence of the seasonal snow cover on the ground thermal regime: An overview. Reviews of Geophysics, 43(4).

Zhang, Y., Chang, X., Liang, J., & He, R. X. (2016). Influence of frozen ground on hydrological processes in alpine regions: A case study in an upper reach of the Heihe River. J. Glaciol. Geocryol, 38, 1362-1372.

Zhang, Y., Liu, S., & Wang, X. (2019). A dataset of spatial distribution of degree-day factors for glaciers in High Mountain Asia. China Sci. Data, 4(3), 141-151.

Zhao, M., Srebric, J., Berghage, R. D., & Dressler, K. A. (2015). Accumulated snow layer influence on the heat transfer process through green roof assemblies. Building and Environment, 87, 82-91.

Zhou, G., Cui, M., Wan, J., & Zhang, S. (2021). A review on snowmelt models: progress and prospect. Sustainability, 13(20), 11485.

Zhou, J., Pomeroy, J. W., Zhang, W., Cheng, G., Wang, G., & Chen, C. (2014). Simulating cold regions hydrological processes using a modular model in the west of China. Journal of Hydrology, 509, 13-24.

Zhou, Y.L.; Mu, Z.X.; Peng, L.; Yin, Z.Y.; Tang, R. (2018). Change of snowmelt runoff in western Tianshan Mountains under future climate scenarios. J. China Hydrol. 38, 12–17.

Zohdi, T. I. (2015). A finite element primer for beginners: the basics. Springer International Publishing.

Zuzel, J. F., & Cox, L. M. (1975). Relative importance of meteorological variables in snowmelt. Water Resources Research, 11(1), 174-176.

Zuzel, J. F., Pikul Jr, J. L., & Rasmussen, P. E. (1990). Tillage and fertilizer effects on water infiltration. Soil Science Society of America Journal, 54(1), 205-208.

APPENDIX

APPENDIX A Computing the thermal conductivity of snow

A.1 Computing the thermal conductivity of snow

By using equation (2.10), the thermal conductivity of snow can be predicted using regression equation and based on index of hardness and porosity index (Usowicz et al, 2008):

$$\lambda = a.exp\,Hc + b.\emptyset + c \tag{A.1}$$

Where λ (W m^{-1} K^{-1}) is the thermal conductivity; a, b, c are the parameters indicated by B coefficients; ∅ (m^3 m^{-3}) is the volumetric snow water content; H_c is the index of hardness (Sturmet al., 2002).

After examining the influencing factors on the thermal conductivity of snow, the models presented by researchers in recent years are shown to estimate it.

In the literature, there are several thermal conductivity models for snow (Sturm et al., 1997; Ostin and Andersson, 1991; Lange, 1985; Reimer, 1980; Côté and al., 2012). Generally, they are obtained by logarithmic, exponential, or power regressions between the effective thermal conductivity (λ_{eff}) and the density, presented in Table 2.7. These models do not consider the effects of temperature and grain size, but they are easy to use. Figure A.1 shows the regression equations (thermal conductivity vs. density) by 15 different authors for the time 1892 to 2012. Abel's regression equation,1892 is an equation that is used as a reference to predict thermal conductivity. There are large (and mostly undocumented) differences in accuracy, temperature, and snow type in these datasets between 1892 and 1997. By dividing the steady-state heat flow by the steady-state temperature gradient, the thermal conductivity is determined. This method has been employed in three investigations (Jansson, 1901; De Quervain, 1956; Pitman and Zuckerman, 1967), but only the most recent study used a guarded form of heated plate, a method that is now acknowledged as crucial if correct results are to be obtained (Sturm et al., 1997).

Table A.1 Equations obtained by different types of regression (Sturm et al.1997)

Reference	**Temperature [˚c]**	**Regression equation**
Adel's, 1892	-10 to -30	$\lambda = 10^{2.846\,\rho^2}$
Jansson, 1901	-2 to -13	$\lambda = 0.02093 + 0.7953\,\rho + 2.512\,\rho^4$
VanDusen, 1929	-	$\lambda = 0.021 + 0.42\,\rho + 2.16\,\rho^3$
Devaux, 1933	-5 to -20	$\lambda = 0.0293 + 2.93\,\rho^2$
Bracht, 1949	-3 to -13.5	$\lambda = 2.051\,\rho^2$
Kondrat'eva, 1954	-2 to 13.5	$\lambda = 3.558\,\rho^2$
Sulakvelidze, 1955	-2 to -13	$\lambda = 0.5107\,\rho$
Yosida et al. 1955	-1 to -6	$\lambda = 10^{-1.378+2\rho}$
Lange, 1985	-4 to -20	$\lambda = 10^{-3+6.9\,\rho}$
Ostin and Andresson, 1991	-6.5 to -19.9	$\lambda = -0.0871 + 0.439\,\rho + 1.05\,\rho^2$
Sturm et al. 1997	-1 to -77	$\lambda = 0.138 - 1.01\,\rho + 3.233\,\rho^2,\ 0.156 \le \rho \le 0.6$ $\lambda = 0.023 + 0.234\,\rho,\ \rho \le 0.156$ $\lambda = 10^{-1.652+2.650\,\rho}$
Côté et al. 2012	-12	$\lambda = \frac{(\lambda_{glace} k_{2p} - \lambda_{air})(1-n) + \lambda_{air}}{1 + (k_{2p} - 1)(1-n)}$

Transient approaches involve heating a source that is initially isothermal and in steady state within a block of snow using a point, line, or plate (Sturm et al., 1997). The temperature of the snow at or close to the source is used to calculate the thermal conductivity. There have been utilised numerous heat source and temperature probe configurations. Cylindrical and spherical heat sources were used by Devaux (1933). Two parallel needles, one holding a heater and the other a temperature-measuring device, were utilised by Bracht (1949). Jaafar and Picot (1970) employed a single needle that had both a heater and a thermometer. A heated plate was put into a block of snow that had previously included thermocouples by Kuvaeva and colleagues (1975). A heated strip that was inserted in frost samples was utilised by Stin and Andersson in 1991.

As shown in Table 2.8, In 1997, Sturm et al. Presented an updated set of 488 measurements with known temperature, type, and measurement accuracy. In quadratic form:

$$\lambda = \begin{cases} 0.138 - 1.01\rho + 3.233\,\rho^2 & 0.156 \le \rho \le 0.6 \\ 0.023 + 0.234\,\rho & \rho \le 0.156 \end{cases} \quad \text{(A.2)}$$

A logarithmic expression can also be used.:

$$\lambda = 10^{-1.652+2.650\,\rho} \qquad \rho \le 0.6 \quad \text{(A.3)}$$

When estimating values that are outside the range of the data, the first regression performs better than the second when estimating values for low-density snow. Snow types produced by kinetic growth exhibit behavior irrespective of density within the data set. Strong density dependence can be seen in wind-blown snow and rounded grain. The mean density of the new data set is higher than that of the previous data set, although the mean thermal conductivity is lower. This shift is explained by variations in the types of snow and sample temperatures between the sets. We demonstrate that there are well-defined limits to the geometric forms that naturally occurring seasonal snow can adopt using both data sets (Sturm et al., 1997).

These equations, along with the rest of the equations in Table A.1, provide a satisfactory correlation for typical porosities but do not adhere to the theoretical bounds anticipated at low and high porosities.

By utilizing a relative thermal conductivity model for porous 2-phase materials created by Côté and Konrad (2009), Côté and al. (2012) aimed to solve this issue. The latter limits the solid's and fluid's respective solid and fluid thermal conductivity values:

$$\lambda_{rel} = \frac{\lambda_{eff} - \lambda_f}{\lambda_{solid} - \lambda_f} \qquad 0 \leq k_r \leq 1 \qquad \text{(A.4)}$$

Where λ_{rel} is the relative thermal conductivity, λ_{eff} (W m^{-1} $°C^{-1}$) is the effective thermal conductivity of the snow sample, λ_f (W m^{-1} $°C^{-1}$) and λ_{solid} (W m^{-1} $°C^{-1}$) are the thermal conductivities respectively fluid and solid.

Effectively, Equation A.4 produces a value of λ_{rel} of 0 for air and 1 for ice. By using an empirical parameter, Côté and Konrad (2009) were able to establish a connection between the relative thermal conductivity and the porosity of the porous material:

$$\lambda_{rel} = \frac{\kappa_{2p}(1-n)}{1+(\kappa_{2p}-1)(1-n)} \qquad \text{(A.5)}$$

Where κ_{2p} is the empirical parameter that considers the structure of materials, namely the size, shape, and organization of the grains in a granular material.

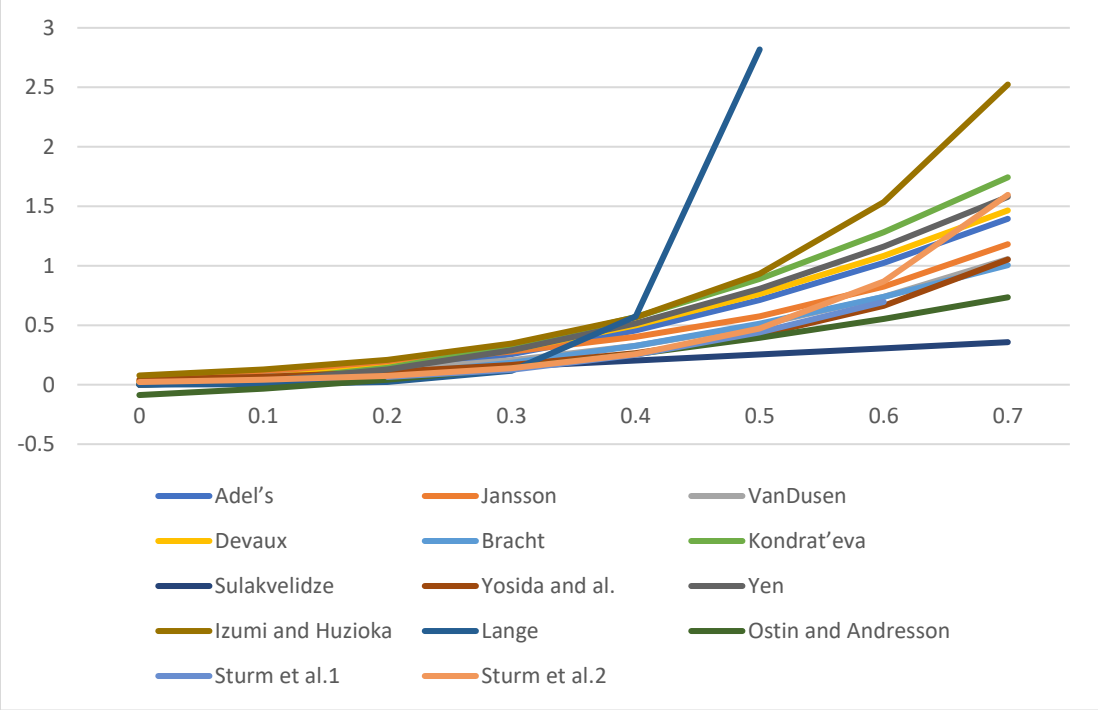

Figure A.1 Regressions developed are shown for comparison.

A.2 The range of potential values for κ2p

The range of potential values for κ_{2p} as a function of the ratio λ_f/λ_s is depicted in Figure A.2, which is taken from Côté and al. (2012) and is based on the restrictions of Hashin and Shtrikman (1962) that fall within the restrictions of Weiner (parallel and series thermal circuit). The higher and lower Hashin and Shtrikman limitations are represented by the HSH and HSB limits, whereas the upper and lower Weiner limits are represented by the WH and WB limits. The following equations are used to derive these limitations (Côté and Konrad, 2009):

$$\kappa_{2p,HSH} = \frac{\lambda_f}{3\lambda_s} + \frac{2}{3} \tag{A.6}$$

$$\kappa_{2p,HSB} = \frac{3(\lambda_f/\lambda_s)}{1+2(\lambda_f/\lambda_s)} \tag{A.7}$$

$$\kappa_{2p,WH} = 1 \tag{A.8}$$

$$\kappa_{2p,WB} = \frac{\lambda_f}{\lambda_s} \tag{A.9}$$

Pitman and Zuckerman (1968) data were used to determine the λ_f/λ_s ratio's variation range, which is 0.0054 to 0.019. This variation is mostly caused by how f and s change as a function of temperature (-5 to -88°C), as determined by Côté et al (2012). Therefore, for the lowest λ_f - λ_s and for the larger ratios, the value of κ_{2p} can change between 0.016 and 0.668 and between 0.055 and 0.673. The potential values of κ_{2p} are displayed in the shaded area of Figure A-2.

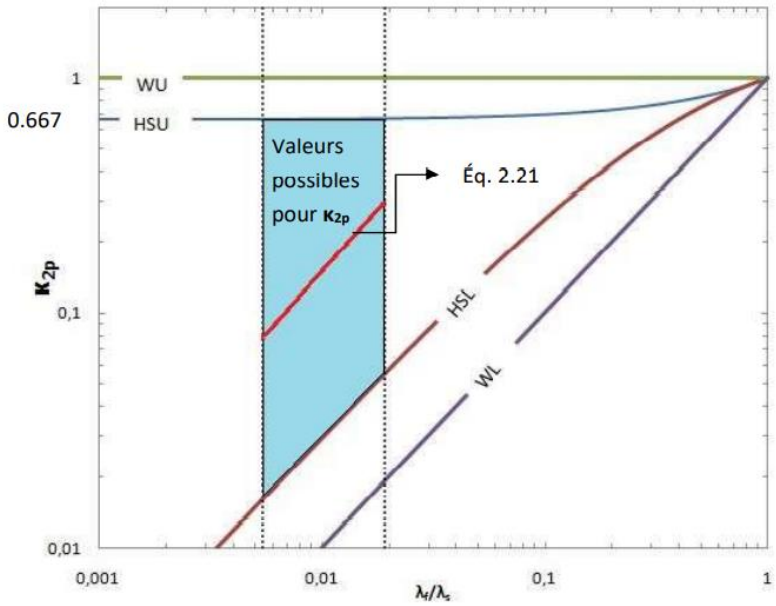

Figure A.2 Possible values and illustration of limits for κ2p (redrawn from Côté and al., (2012)).

The developed thermal conductivity model of Côté et al. (2009 and 2012)

By substituting the expression from equation 2.14 for the term in equation 2.13's λ_{rel}, one can derive a direct relationship for the conductivity of snow as a function of the parameter κ_{2p} and the conductivity values of ice and air. The equation that results is:

$$\lambda = \frac{(\lambda_{glace}\kappa_{2p} - \lambda_{air})(1-n) + \lambda_{air}}{1 + (\kappa_{2p} - 1)(1-n)} \quad \text{(A.10)}$$

Where λ_{ice} (W m^{-1} °C^{-1}) is the conductivity value of ice and λ_{air} (W m^{-1} °C^{-1}) is the thermal conductivity of air.

Regardless of the value of κ_{2p} falling within the acceptable ranges, this equation respects the theoretical bounds for the projected theoretical conductivity. As determined by Côté and al. based on the findings of Pitman and Zuckerman (1967), the value of ice can be estimated as a function of the temperature T (°C) as follows:

$$\lambda_{glace} = 2.22 - 0.011\,T \quad \text{(A.11)}$$

Côté et al. (2012) claim that the equation developed from the data put forth by Pitman and Zuckerman (1967) is how the thermal conductivity of the air in the sample is determined:

$$\lambda_{air} = 0.072(-T)^{-0.32} \quad \text{(A.12)}$$

Pitman and Zuckerman (1967) measured the thermal conductivity of snow samples at temperatures ranging from -5 to -88°C, and Côté and al. (2012) developed a helpful relation to determine κ2p as a function of the ratio λf/λs:

$$\kappa_{2p} = 18.7(\frac{\lambda_{air}}{\lambda_{glace}})^{1.05} \quad \text{(A.13)}$$

Figure A.3 is drawn from Equation A.13. The models from Sturm et al. (1992) and Côté et al. (2012) were utilized in comparison to this study. The first was a compilation of prior findings, while the second provided theoretical foundations and relied on the boundaries of the physical properties of air and ice.

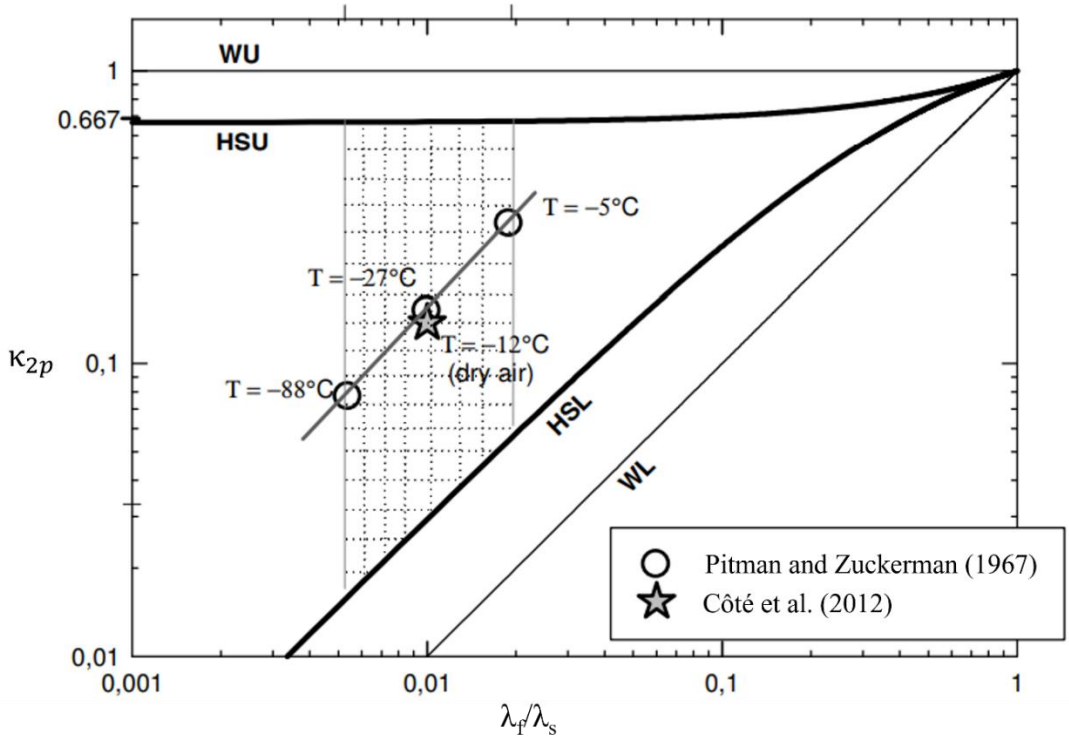

Figure A.3 κ_{2p} values for compacted snow at various temperatures (Côté et al., 2012).

APPENDIX B Effective thermal conductivity type in COMSOL Multiphysics

There are eight different types for effective thermal conductivity in COMSOL Multiphysics:

B.1 Plane layers parallel to heat flow

The default option of "Plane layers parallel to heat flow" computes the effective conductivity of the solid-fluid system by taking the weighted arithmetic mean, or volume average, of the conductivities of both the fluid and the porous matrix.

$$\lambda_{eff} = \theta_{solid}\lambda_{solid} + \varepsilon_p\lambda_f \tag{B.1}$$

B.2 Plane layers perpendicular to heat flow

The "Plane layers perpendicular to heat flow" option computes the effective conductivity of the solid-fluid system by taking the weighted harmonic mean, or reciprocal average, of the conductivities of both the fluid and the porous matrix.

$$\frac{1}{\lambda_{eff}} = \frac{\theta_{solid}}{\lambda_{solid}} + \frac{\varepsilon_p}{\lambda_f} \tag{B.2}$$

B.3 Power law

The "Power law" option computes the effective conductivity of the solid-fluid system by taking the weighted geometric mean of the conductivities of both the fluid and the porous matrix.

$$\lambda_{eff} = {\lambda_{solid}}^{\theta_{solid}}.{\lambda_f}^{\varepsilon_p} \tag{B.3}$$

B.4 Solid spherical inclusions

The "Solid spherical inclusions" option calculates the effective conductivity of the solid-fluid system using a specific method or formula.

$$\lambda_{eff} = \lambda_f \frac{2\lambda_f+\lambda_{solid}-2(\lambda_f-\lambda_{solid})\theta_{solid}}{2\lambda_f+\lambda_{solid}+(\lambda_f-\lambda_{solid})\theta_{solid}} \tag{B.4}$$

B.5 Fluid spherical inclusions

The "Fluid spherical inclusions" option calculates the effective conductivity of the solid-fluid system using a specific method or formula.

$$\lambda_{eff} = \lambda_{solid} \frac{2\lambda_{solid}+\lambda_f-2(\lambda_{solid}-\lambda_f)\varepsilon_p}{2\lambda_{solid}+\lambda_f+(\lambda_{solid}-\lambda_f)\varepsilon_p} \quad \text{(B.5)}$$

B.6 Wrapped screen

The "Wrapped screen" option computes the effective conductivity of the solid-fluid system using a specific method or formula.

$$\lambda_{eff} = \lambda_f \frac{\lambda_f+\lambda_{solid}-(\lambda_f-\lambda_{solid})\theta_{solid}}{\lambda_f+\lambda_{solid}+(\lambda_f-\lambda_{solid})\theta_{solid}} \quad \text{(B.6)}$$

B.7 Sintered metal fibers

The "Sintered metal fibers" option computes the effective conductivity of the solid-fluid system using a specific method or formula.

$$\lambda_{eff} = {\varepsilon_p}^2\lambda_f + {\theta_{solid}}^2\lambda_{solid} + \frac{4\varepsilon_p\theta_{solid}\lambda_f\lambda_{solid}}{\lambda_f+\lambda_{solid}} \quad \text{(B.7)}$$

B.8 Equivalent thermal conductivity

It is also feasible to directly define λ_{eff}. When choosing "Equivalent thermal conductivity" from the Effective thermal conductivity options, a specific value for λ_{eff} must be provided. The default λ_{eff} value is derived from the material properties. If a Porous Material node is activated, the property from the Homogenized Properties section is used.

APPENDIX C Heat Transfer Equations in Porous Media in COMSOL Multiphysic

Applying the mixture rule to the energies in the heat transfer equations of solid and fluid allows derivation of the equation for heat transfer in porous media, assuming no deformation or movement of solids (Bejan, 2013):

$$\rho_{solid} C_{p,solid} \frac{\partial T_{solid}}{\partial t} + \nabla . q_{solid} = Q_{solid} \quad \text{(C.1)}$$

Where ρ_{solid} is the density of solid (Kg m^{-3}), $C_{p,solid}$ is the solid heat capacity at constant pressure, T_{solid} is the temperature of solid phase, and q_{solid} is the conductive heat flux in solid phase (J m^{-2}). For the fluid domain, the equation simplifies by neglecting pressure work and viscous dissipation (COMSOL, 2008):

$$\rho_f C_{p,f} \frac{\partial T_f}{\partial t} + p_f C_{p,f} u_f . \nabla . q_f = Q_f \quad \text{(C.2)}$$

Multiplying equation C.1 by the solid volume fraction, and equation C.2 by the porosity, and then summing the results allows for the application of the mixture rule (COMSOL, 2008).

The hypothesis of local thermal equilibrium states that the temperature of both fluid and solid phases is the same (COMSOL, 2008):

$$T_f = T_{solid} = T \quad \text{(C.3)}$$

The section Local Thermal Equilibrium below explains the theory behind this hypothesis. The section Local Thermal Non-Equilibrium shows the theory for using two temperatures to model heat transfer in porous media (COMSOL, 2008).

As stated in Equation C.3, the classical local equilibrium hypothesis for heat transfer in porous media assumes that the solid and fluid temperatures are equal at each point (COMSOL, 2008). The derivation of the energy equation using this assumption, which is valid for many applications, is explained in the Local Thermal Equilibrium section below. Nield in 1998 demonstrates that the temperatures of solid and fluid are the same in steady conduction problems where only fixed temperature conditions are applied. Many problems

with slow motion can also assume that the phase temperatures are equal if there is no difference in volumetric internal heating between the two materials.

For conduction in porous plates, Minkowycz et al., 1998 gives criteria based on the dimensionless Sparrow number, S_p, to determine if temperature equilibrium is still valid or if a non-equilibrium point of view is better. Amiri and Vafai in 1998 studied how the Darcy number, Da, and the ratio of phase conductivities affect transient heat transfer in packed beds. The Sparrow and Darcy numbers are given by:

$$S_p = \frac{h_{sf} Ht^2}{\lambda p_{eff} r_h} \, , Da = \frac{K}{d^2} \tag{C.4}$$

Where h_{sf} the interstitial heat transfer coefficient between solid and fluid phases (W m^{-2} K^{-1})), H_t is the plate layer thickness (m), λp_{eff} is the equivalent thermal conductivity of the porous medium (W m^{-1} K^{-1}), r_h is the hydraulic radius (m), K is the permeability (m^2), and d is the average particle diameter (m).

Amiri and Vafai, 1998, and Minkowycz et al., 1999, indicate discrepancies in temperature between phases with low values of S_p (less than 100 or 500) and high values of Da (10^{-7}). However, assessing the validity of local thermal equilibrium is generally not straightforward (COMSOL, 2008). Instead of assuming that the two phases of the porous medium have the same temperature, the Local Thermal Non-Equilibrium approach, explained below, uses two separate energy equations to calculate two different temperature fields for each phase (COMSOL, 2008). This method increases the number of variables to solve, but it also offers a more general framework for heat transfer in porous media without having to check the validity of the equilibrium assumption (COMSOL, 2008).

C.1 Local Thermal Equilibrium

According to Equation C.5, the solid and fluid phases of the porous medium share the same temperature, T, under the local thermal equilibrium hypothesis. The Heat Transfer in Porous Media Interface uses a different form of the heat equation (Bear et al., 1990), which is based on T, to solve for heat transfer in porous media:

$$(\rho_f C_{pf})_{eff} \frac{\partial T}{\partial t} + \rho C_p u . \nabla T + \nabla . q = \varphi \tag{C.5}$$

$$q = -\lambda_{eff} \nabla T \tag{C.6}$$

Where ρ_f is the fluid density, C_{pf} is the fluid heat capacity at constant pressure, $(\rho_f C_{pf})_{eff}$ (J m^{-3} K^{-1}) is the effective volumetric heat capacity at constant pressure, defined by (Bear et al., 1990):

$$(\rho C_p)_{eff} = \theta_p \rho_p C_{\rho,p} + (1 - \theta_p) \rho C_\rho \tag{C.7}$$

λ_{eff} is the effective thermal conductivity (either a scalar or a tensor, based on the anisotropy of the thermal conductivity), q is the conductive heat flux, u (m s^{-1}) is the velocity field, which can be either an analytic expression or computed from a Fluid Flow interface. It represents the Darcy velocity, meaning the volume flow rate per unit cross sectional area. The average linear velocity (the velocity inside the pores) can be obtained as $u_f = u/(1-\theta_p)$, where $(1-\theta_p)$ is the fluid's volume fraction, or the same as the porosity, θ_p is volume fraction of solid material in porous media, φ is the heat source (or sink). Make one or more heat sources separate physics features.

The temperature is constant and does not vary with time for a steady-state problem, and the terms with time derivatives of Equation C.8 are eliminated (COMSOL, 2008). Solid-fluid thermal conductivity, $\lambda_{s,f\,eff}$, depends on the solid-fluid conductivity, $\lambda_{s,f}$, and the fluid conductivity, λ_f, and is complicated by the medium geometry. Three isotropic medium models are proposed by Bejan (2013):

- Heat conduction in solids and fluids occurs in parallel, so the effective thermal conductivity is the weighted arithmetic mean of λ_f and $\lambda_{s,f}$: (COMSOL, 2008):

  $$\lambda_{s,f\,eff} = \theta_{s,f} \lambda_{s,f} + \left(1 - \theta_p\right) \lambda_f \tag{C.8}$$

  $\lambda_{s,f\,eff}$, cannot be higher than the volume average model, which is based on the average of the heat transfer rates of the solid and the fluid (COMSOL, 2008).

- When the heat moves in a straight line through both fluid and solid, the heat flow rate depends on the combined effect of the conductivities λ_f and $\lambda_{s,f}$, which is calculated by the weighted harmonic mean (COMSOL, 2008).

  $$\frac{1}{\lambda_{s,f\,eff}} = \frac{\theta_{s,f}}{\lambda_{s,f}} + \frac{(1-\theta_p)}{\lambda_f} \tag{C.9}$$

The effective thermal conductivity cannot be lower than the value given by this model that uses the inverse average of the conductivities (COMSOL, 2008).

- The final approximation is obtained by the weighted geometric average of λ_f and $\lambda_{s,f}$ (COMSOL, 2008).

$$\lambda_{s,f\ eff} = \lambda_{s,f}^{\theta_{s,f}} . \lambda_f^{\ 1-\theta_p} \tag{C.10}$$

If the conductivities λ_f and $\lambda_{s,f}$ are similar, this model gives a reasonable approximation (COMSOL, 2008).

C.2 Local Thermal Non-Equilibrium

In porous media with a temperature difference between the fluid and the porous matrix, the Local Thermal Non-Equilibrium Interface facilitates heat transfer (COMSOL, 2008).

C.3 Equation for Local Non-Equilibrium Heat Transfer

The heat transfer in porous media for binary systems of fluid phase and rigid porous matrix that are not in thermal equilibrium is controlled by two equations. They are the standard heat equations for fluids and solids, with a factor of θ_p and $(1 - \theta_p)$ for each, and an extra term that measures the heat transfer between the two phases (Bejan, 2013)

$$\begin{cases} \theta_p \rho_{solid} C_{p,solid} \frac{\partial T_{solid}}{\partial t} + \nabla . q_{solid} = q_{sf}\left(T_f - T_{solid}\right) + \theta_p Q_{solid} \\ q_{solid} = -\theta_p \lambda_{solid} \nabla T_{solid} \\ (1-\theta_p)\rho_f C_{p,f} \frac{\partial T_f}{\partial t} + \left(1-\theta_p\right)\rho_f C_{p,f} u_f . \nabla T_f + \nabla . q_f = q_{sf}\left(T_{solid} - T_f\right) + \\ (1-\theta_p) Q_f \\ q_f = -(1-\theta_p)\lambda_f \nabla T_f \end{cases} \tag{C.11}$$

Where θ_p is the solid volume fraction, ρ_{solid} and ρ_f are the solid and fluid densities (Kg m^{-3}), $C_{p,s}$ and $C_{p,f}$ are the solid and fluid heat capacities at constant pressure (J Kg^{-1} K^{-1}), q_{solid} and q_f are the solid and fluid conductive heat fluxes (J m^{-2}), λ_{solid} and λ_f are the solid and fluid thermal conductivities (J m^{-1} K^{-1}), q_{sf} is the interstitial convective

heat transfer coefficient (J m^{-3} K^{-1}), Q_{solid} and Q_f are the solid and fluid heat sources (J m^{-3}), and u_f is the fluid velocity vector (m s^{-1}).

The porous velocity u_p (m s^{-1}), which can be obtained from Darcy's law or Brinkman equations, is frequently used to calculate the fluid velocity. The formula is (COMSOL, 2008):

$$u_f = \frac{u_p}{1-\theta_p} \tag{C.12}$$

These are the simplified forms of the heat equations in the fluid domain (COMSOL, 2008):

$$\begin{cases} (1-\theta_p)\rho_f C_{p,f}\frac{\partial T_f}{\partial t} + \rho_f C_{p,f} u_p . \nabla T_f + \nabla . q_f = q_{sf}\left(T_{solid} - T_f\right) + (1-\theta_p)Q_f \\ q_f = -(1-\theta_p)\lambda_f \nabla T_f \end{cases} \tag{C.13}$$

When the temperatures of the two phases are not the same, the Local Thermal Non-Equilibrium multiphysics coupling introduces the opposite heat sources q_{sf} ($T_f - T_s$) and q_{sf} ($T_s - T_f$) that each phase gets from or gives to the other. The temperature of the porous medium, T_p, is defined as follows (Carbonell and Whitaker, 1984):

$$T_p = \frac{\theta_p \rho_{solid} C_{p,s} T_{solid} + (1-\theta_p)\rho_f C_{p,f} T_f}{\theta_p \rho_s C_{p,s} + (1-\theta_p)\rho_f C_{p,f}} \tag{C.14}$$

C.4 Correlation for the interstitial convective heat transfer coefficient

The spherical pellet bed configuration has a built-in correlation for q_{sf} that can be used with the Local Thermal Non-Equilibrium Multiphysics feature (Bejan, 2013):

$$q_{sf} = SSA\, h_{sf} \tag{C.15}$$

For a bed of spherical particles with radius r_p, the specific surface area, a_{sf} (m^{-1}), is (Bejan, 2013):

$$a_{sf} = \frac{6\theta_p}{2r_p} \tag{C.16}$$

The relation for the interstitial heat transfer coefficient, h_{sf} (W m^{-2} K^{-1}), is (COMSOL, 2008):

$$\frac{1}{h_{sf}} = \frac{2r_p}{\lambda_f N_u} + \frac{2r_p}{\beta \lambda_{solid}} \tag{C.17}$$

The fluid-to-solid Nusselt number, Nu, is obtained from the following correlation, and β is equal to 10 for spherical particles (Wakao et al., 1979):

$$N_u = 2 + 1.1 p_r^{1/3} Re_p^{0.6} \tag{C.18}$$

The definitions of the Prandtl number, P_r, and the particle Reynolds number, R_{ep}, are (Wakao et al., 1979):

$$P_r = \frac{\mu C_{p,f}}{\lambda_f} \quad \text{and} \quad Re_p = \frac{2 r_p \rho_f \|u_f\|}{\mu} \tag{C.19}$$

C.5 Effective thermal conductivity type

In this project among the eight different types for effective thermal conductivity in the COMSOL Multiphysics (Appendix B), the "Plane layers parallel to heat flow" model was chosen. This model simplifies the mathematical formulation, allowing for easier and faster calculations. This is crucial when managing large snow piles where quick decision-making is essential. By using this model, computational resource requirements are reduced, which is beneficial when dealing with extensive simulations needed for predicting the melting behavior of large snow piles. Faster simulation times mean more timely and efficient snow management operations. The default option of "Plane layers parallel to heat flow" computes the effective conductivity of the solid-fluid system by taking the weighted arithmetic mean, or volume average, of the conductivities of both the fluid and the porous matrix. This approach ensures that the model remains computationally efficient while providing accurate predictions of thermal behavior in the system. The choice of the "Plane layers parallel to heat flow" model assumed that the porous media is considered uniform. This uniformity implies that there is no significant difference between using a perpendicular or parallel model for the heat flow. The parallel model was selected because it simplifies the calculations and reduces computational time, which is advantageous for large-scale simulations.

By choosing this model, the research benefits from a balance between computational efficiency and the accuracy of the thermal predictions, making it a suitable choice for the study of snowmelt in large piles.

C.6 Plane layers parallel to heat flow

The default option of "Plane layers parallel to heat flow" computes the effective conductivity of the solid-fluid system by taking the weighted arithmetic mean, or volume average, of the conductivities of both the fluid and the porous matrix.

$$\lambda_{eff} = \theta_{solid}\lambda_{solid} + \varepsilon_p\lambda_f \tag{C.20}$$

APPENDIX D Geometric Properties of the 70 Modeled SMPs

Table D.1 Geometric Properties of the 70 Modeled SMPs

Number of Pile	**Type of Pile**	**Weather Function (Holt or Goldex)**	**Height (m)**	**Width (m)**	**Radius (m)**	**Length (m)**	**Area (m^2)**	**Volume (m^3)**	**Melt Duration (D)**
1	Cone	2023	3	-	12.5	-	490.87	509.3	32
2	Cone	2023	4	-	15.5	-	754.76	1036.4	50
3	Cone	2023	5.6	-	20	-	1256.63	2400.3	53
4	Cone	2023	6	-	21.5	-	1451.46	2966.7	64
5	Cone	2023	7.33	-	23	-	1661.06	4142.7	68
6	Cone	2023	8	-	26	-	2123.71	5747	74
7	Cone	2023	9	-	29	-	2640.74	8028.6	81
8	Cone	2023	10	-	32	-	3216	10856	92
9	Cone	2022	6	-	11	-	380.13	792.19	67
10	Cone	2022	7.3	-	14	-	615.75	1547.4	75
11	Cone	2022	8	-	17	-	907.92	2474.1	78
12	Cone	2022	9	-	20	-	1256.63	3847	81
13	Cone	2022	10	-	23	-	1661.9	5618.2	91
14	Ramp	2023	3	9	-	21	189	330.75	35
15	Ramp	2023	4	12	-	24	288	672	45

Table D.1 Geometric Properties of the 70 Modeled SMPs (Continue)

16	Ramp	2023	5	15	-	27	405	1181.3	54
17	Ramp	2023	5.8	18	-	30	540	1827	58
18	Ramp	2023	7	21	-	33	693	2829.8	76
19	Ramp	2023	8	24	-	36	864	4032	87
20	Ramp	2023	9	27	-	39	1053	5528.2	91
21	Ramp	2023	10	30	-	42	1260	7350	110
22	Ridge	2022	3.5	25	-	50	1250	2552.1	66
23	Ridge	2022	4.5	28	-	53	1484	3895.5	69
24	Ridge	2022	5.5	31	-	56	1736	5569.7	79
25	Ridge	2022	6.5	34	-	59	2006	7606.1	93
26	Ridge	2022	7.5	37	-	62	2294	10036	97
27	Ridge	2022	8.5	40	-	65	2600	12892	104
28	Ridge	2022	9.5	43	-	68	2924	16204	113
29	Cubic	2022	3.5	33	-	33	1089	2223.4	65
30	Cubic	2022	4.5	37	-	37	1369	3593.6	73
31	Cubic	2022	5.5	40	-	40	1600	5133.3	77
32	Cubic	2022	6.5	43	-	43	1849	7010.8	82
33	Cubic	2022	7.5	46	-	46	2116	9257.5	90
34	Cubic	2022	8.5	49	-	49	2401	11905	97

Table D.1 Geometric Properties of the 70 Modeled SMPs (Continue)

35	Cubic	2022	9.5	52	-	52	2704	14985	120
36	Cone	2022	3	-	12.5	-	490.87	509.3	32
37	Cone	2022	4	-	15.5	-	754.76	1036.4	50
38	Cone	2022	5.6	-	20	-	1256.63	2400.3	53
39	Cone	2022	6	-	21.5	-	1451.46	2966.7	64
40	Cone	2022	7.33	-	23	-	1661.06	4142.7	68
41	Cone	2022	8	-	26	-	2123.71	5747	74
42	Cone	2022	9	-	29	-	2640.74	8028.6	81
43	Cone	2022	10	-	32	-	3216	10856	92
44	Ramp	2022	3	9	-	21	189	330.75	59
45	Ramp	2022	4	12	-	24	288	672	66
46	Ramp	2022	5	15	-	27	405	1181.3	70
47	Ramp	2022	5.8	18	-	30	540	1827	74
48	Ramp	2022	7	21	-	33	693	2829.8	85
49	Ramp	2022	8	24	-	36	864	4032	93
50	Ramp	2022	9	27	-	39	1053	5528.2	97
51	Ramp	2022	10	30	-	42	1260	7350	112
52	Cone	2023	6	-	11	-	380.13	792.19	48
53	Cone	2023	7.3	-	14	-	615.75	1547.4	55

Table D.1 Geometric Properties of the 70 Modeled SMPs (Continue)

54	Cone	2023	8	-	17	-	907.92	2474.1	69
55	Cone	2023	9	-	20	-	1256.63	3847	72
56	Cone	2023	10	-	23	-	1661.9	5618.2	78
57	Ridge	2023	3.5	25	-	50	1250	2552.1	41
58	Ridge	2023	4.5	28	-	53	1484	3895.5	51
59	Ridge	2023	5.5	31	-	56	1736	5569.7	57
60	Ridge	2023	6.5	34	-	59	2006	7606.1	65
61	Ridge	2023	7.5	37	-	62	2294	10036	81
62	Ridge	2023	8.5	40	-	65	2600	12892	85
63	Ridge	2023	9.5	43	-	68	2924	16204	91
64	Cubic	2023	3.5	33	-	33	1089	2223.4	42
65	Cubic	2023	4.5	37	-	37	1369	3593.6	57
66	Cubic	2023	5.5	40	-	40	1600	5133.3	60
67	Cubic	2023	6.5	43	-	43	1849	7010.8	73
68	Cubic	2023	7.5	46	-	46	2116	9257.5	78
69	Cubic	2023	8.5	49	-	49	2401	11905	87
70	Cubic	2023	9.5	52	-	52	2704	14985	92

APPENDIX E Detailed Results for Each SMP

Pile Number 1

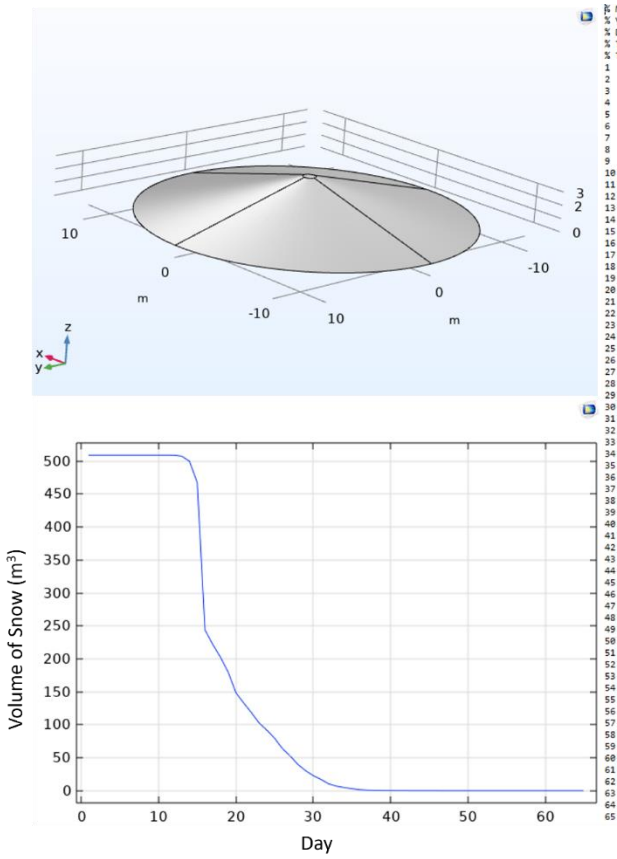

% Model:		3D big cone Holt 3mH 12.5mR- Success .mph
% Version:		COMSOL 6.1.0.252
% Date:		Oct 27 2024, 21:00
% Table:		Table 1 - Volume Integration 1
% Time (d)		Phase indicator, phase 1 (m^3)
1		509.03106544140746
2		509.03106544140746
3		509.03106544140746
4		509.03106544140746
5		509.03106544140746
6		509.03106544140746
7		509.03106544139365
8		509.0310654349611
9		509.0310640285457
10		509.0309444056152
11		509.02602846513525
12		508.9184970239192
13		507.4767206258532
14		499.73718107588587
15		467.3638543033177
16		244.00710617715794
17		222.06729026740473
18		202.5774307731484
19		179.88138657423315
20		148.73614705370056
21		133.11932231178875
22		118.4491884610907
23		102.8087952343611
24		91.9164222840759
25		79.67413582866678
26		63.909513805043645
27		52.98726175845797 6
28		40.01594684450531 5
29		30.479443955410453
30		22.890860970906154
31		17.109145431641686
32		10.382638303071582
33		6.915724250122156
34		4.799730326193847
35		3.063813928353406
36		1.5092403110930648
37		0.7238187565037834
38		0.46546429092403 77
39		0.3161342921979285 5
40		0.2285917466090996
41		0.18454830397374333
42		0.14944060935325493
43		0.11962020724609781
44		0.0943497609447111 6
45		0.0734275440703908 8
46		0.0565466976214017 3
47		0.0427092986148080 44
48		0.0323995355784115 5
49		0.0248350377263645 84
50		0.0193503830531857 88
51		0.0154750862482276 88
52		0.0125157249864327 2
53		0.0098914408626151 4
54		0.0078464559072739 13
55		0.0063216309080270285
56		0.0052018842714536 08
57		0.0042415369266689 65
58		0.003401276490997 53
59		0.0026649809253555 7
60		0.0019695114024478 77
61		0.0013682213844863696
62		8.7082781474087 14E-4
63		4.8720304923204 85E-4
64		2.2732948683143 169E-4
65		7.617079020140798E-5

Figure E.1 Numerical modeling results for the cone (3 m height, and 12.5 m radius) SMP with 2023 weather function

Pile Number 2

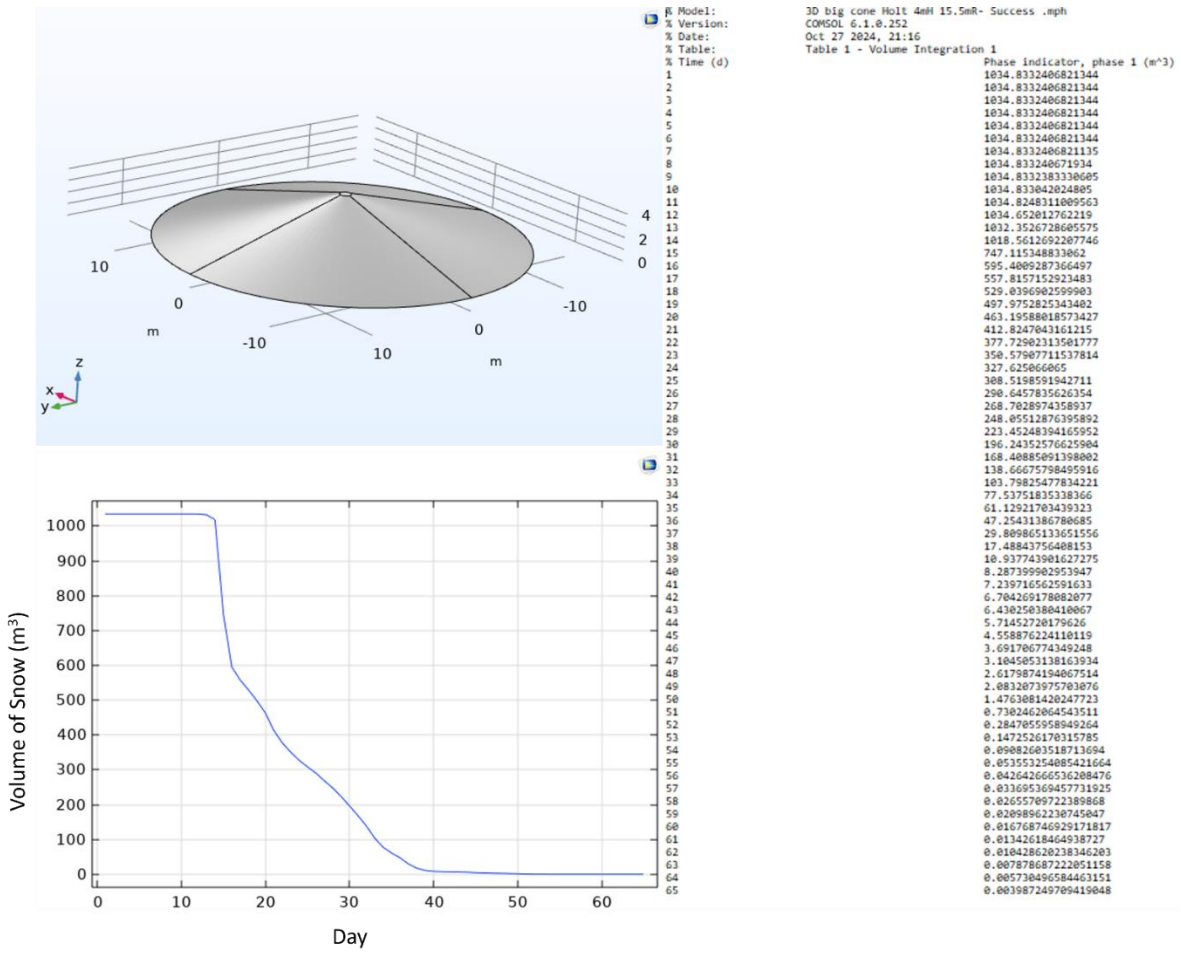

% Model:
% Version:
% Date:
% Table:
% Time (d)

3D big cone Holt 4mH 15.5mR- Success .mph
COMSOL 6.1.0.252
Oct 27 2024, 21:16
Table 1 - Volume Integration 1

	Phase indicator, phase 1 (m^3)
1	1034.8332406821344
2	1034.8332406821344
3	1034.8332406821344
4	1034.8332406821344
5	1034.8332406821344
6	1034.8332406821344
7	1034.8332406821135
8	1034.833240671934
9	1034.8332383330605
10	1034.833042024805
11	1034.824831109563
12	1034.652012762219
13	1032.3526728605575
14	1018.5612692207746
15	747.115348833062
16	595.4009287366497
17	557.8157152923483
18	529.0396902599903
19	497.9752825343402
20	463.19588018573427
21	412.8247043161215
22	377.729023113501777
23	350.57907711537814
24	327.625066065
25	308.5198591942711
26	290.6457835626354
27	268.7028974358937
28	248.05512876395892
29	223.45248394165952
30	196.243525766259504
31	168.40885091398002
32	138.666757984959116
33	103.79825477834221
34	77.53751835338366
35	61.12921703439323
36	47.25431386780685
37	29.809865133651556
38	17.48843756408153
39	10.937743901627275
40	8.287399902953947
41	7.239716562591633
42	6.704269178082077
43	6.430250380410067
44	5.71452720179626
45	4.558876224110119
46	3.691706774349248
47	3.1045053138163934
48	2.6179874194067514
49	2.08320739757030076
50	1.476308142024772 3
51	0.7302462064543511
52	0.28470559589492 64
53	0.1472526170315785
54	0.09082603518713694
55	0.053553254085421664
56	0.042642666536208476
57	0.013695369457731925
58	0.026557097223898 68
59	0.020989622307450 47
60	0.016768746929171817
61	0.013426184649387 27
62	0.010428620238346203
63	0.007878687222051158
64	0.005730496584463151
65	0.003987249709419048

Figure E.2 Numerical modeling results for the cone (4 m height, and 15.5 m radius) SMP with 2023 weather function

Pile Number 3

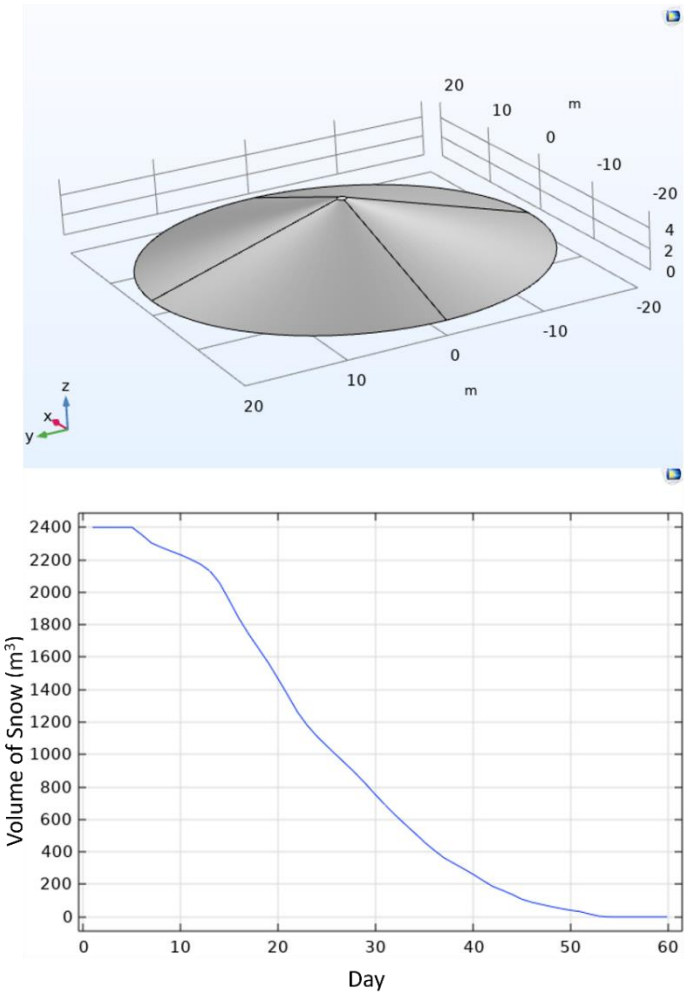

% Model:	3D small cone Holt- Success.mph
% Version:	COMSOL 6.1.0.252
% Date:	Oct 27 2024, 21:44
% Table:	Table 1 - Volume Integration 1
% Time (d)	Phase indicator, phase 1 (m^3)
1	2400.293062706985
2	2400.293062706985
3	2400.2930627069786
4	2400.293061558892
5	2400.2831481770936
6	2354.0670549138154
7	2303.089676068449
8	2276.797716865667
9	2252.7680639327805
10	2230.503821797739
11	2203.428405524794
12	2173.3138627325743
13	2130.8031357393616
14	2056.091076838584
15	1947.4039214625088
16	1836.1515713424574
17	1740.428954514826
18	1652.6472355478027
19	1564.7403770650938
20	1466.0740037800742
21	1364.7812063064982
22	1261.1026628729248
23	1179.1658678837964
24	1111.5678165665283
25	1052.9700684125391
26	995.7886015294456
27	939.3690416673965
28	881.6564995114975
29	819.1319817774519
30	752.3359170672729
31	689.0890849310196
32	629.126605602104
33	572.7242521336881
34	518.3365588444558
35	461.85119238442445
36	412.12530333542586
37	365.50468688453884
38	331.4078688036952
39	297.944138664517
40	263.69126764568534
41	225.30121513980015
42	189.02983309759446
43	164.89578651969822
44	138.96570165227698
45	109.88129550610066
46	91.09890675079414
47	77.52063357468005
48	64.05284979381652
49	51.844647612355985
50	41.20558649682568
51	32.97431776694101
52	17.516462934473108
53	4.311991851695753
54	0.3855256431165244
55	0.021095383974961992
56	0.0019283736332809135
57	2.262872106208012E-5
58	0
59	0
60	0

Figure E.3 Numerical modeling results for the cone (5.6 m height, and 20 m radius) SMP with 2023 weather function

Pile Number 4

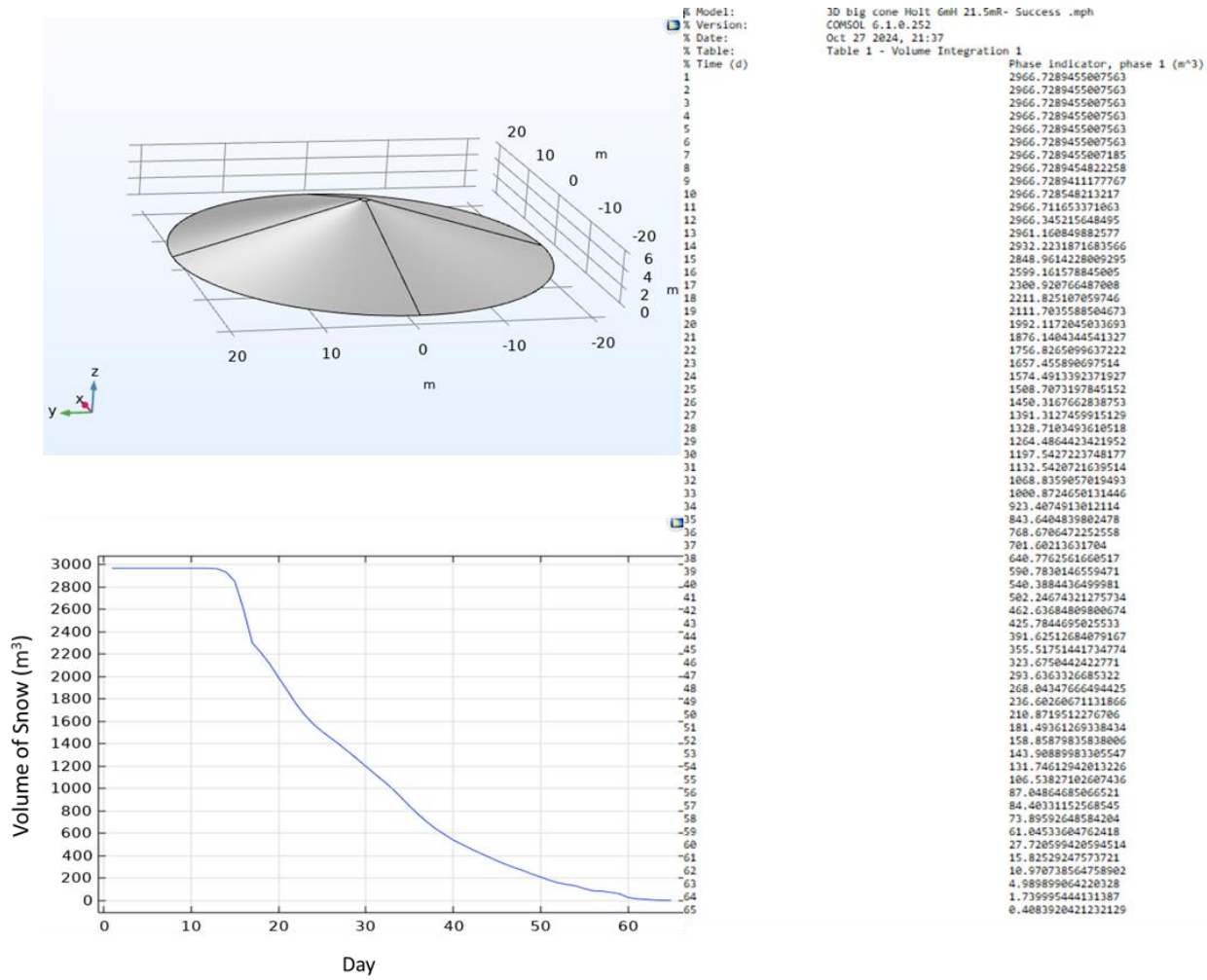

Figure E.4 Numerical modeling results for the cone (6 m height, and 21.5 m radius) SMP with 2023 weather function

Pile Number 5

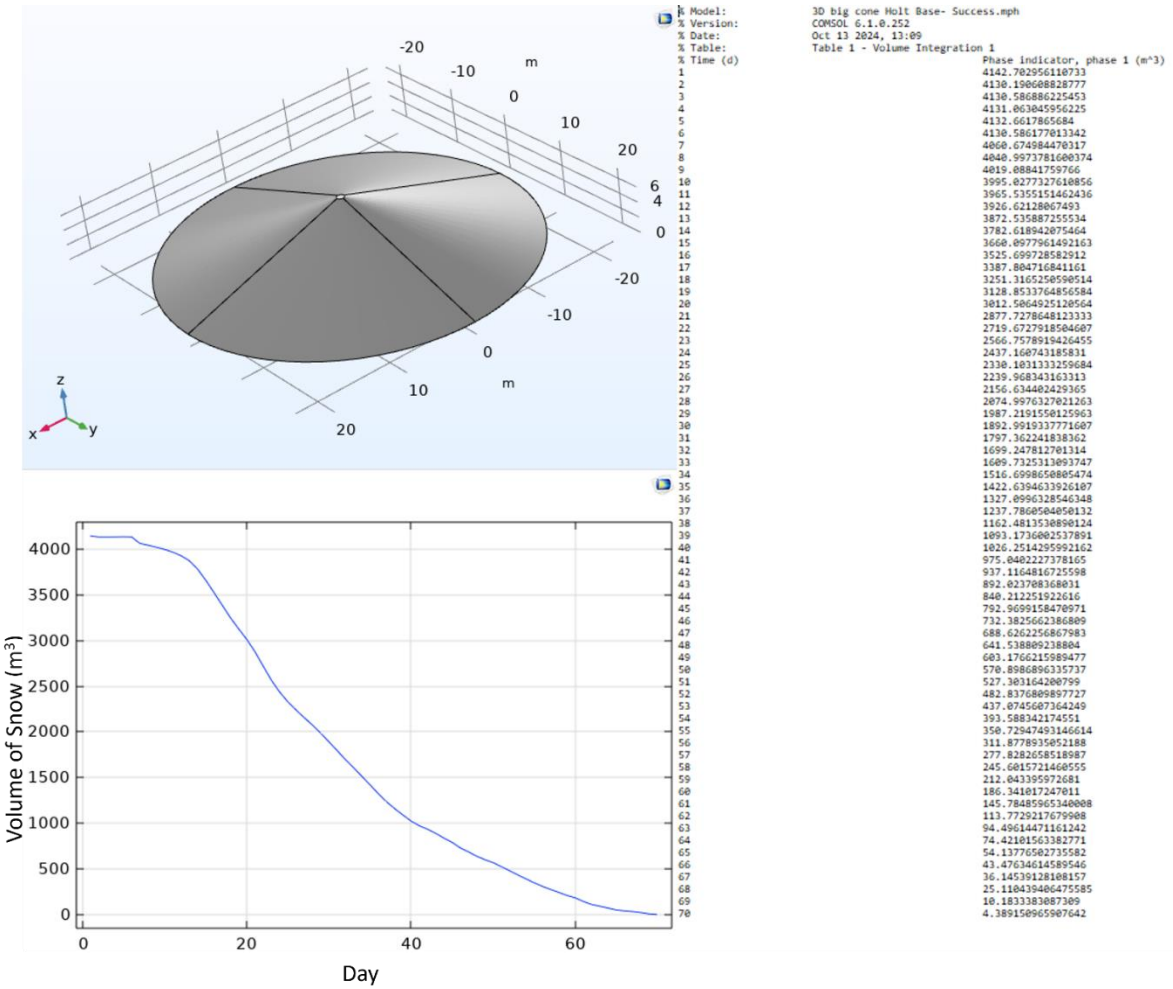


```
% Model:    3D big cone Holt Base- Success.mph
% Version:  COMSOL 6.1.0.252
% Date:     Oct 13 2024, 13:09
% Table:    Table 1 - Volume Integration 1
% Time (d)  Phase indicator, phase 1 (m^3)
1           4142.702956110733
2           4130.1906088828777
3           4130.586886225453
4           4131.0630459562225
5           4132.6617865684
6           4130.586177013342
7           4060.674984470317
8           4040.9973781600374
9           4019.08841759766
10          3995.0277127610856
11          3965.5355151462436
12          3926.62128067493
13          3872.535887255534
14          3782.618942075464
15          3660.0977961492163
16          3525.699728582912
17          3387.8047160841161
18          3251.3165250590514
19          3128.8533764856584
20          3012.5064925120564
21          2877.7278648123333
22          2719.6727918504607
23          2566.7578919426455
24          2437.160743185831
25          2330.1031333259684
26          2239.968343163313
27          2156.6344024229365
28          2074.9976327021263
29          1987.2191550125963
30          1892.9919337771607
31          1797.362241838362
32          1699.247812701314
33          1609.7325313093747
34          1516.6998650805474
35          1422.6394633926107
36          1327.0996328546348
37          1237.7860504050132
38          1162.4813530890124
39          1093.1736002537891
40          1026.2514295992162
41          975.0402227378165
42          937.1164816725598
43          892.023708368031
44          840.212251922616
45          792.9699158470971
46          732.3825662386809
47          688.6262256867983
48          641.538809238804
49          603.1766215989477
50          570.8986896335737
51          527.303164200799
52          482.8376809897727
53          437.07455073642249
54          393.588342174551
55          350.72947493146614
56          311.8778935052188
57          277.8282658518987
58          245.6015721460555
59          212.043395972681
60          186.341017247011
61          145.78485965340008
62          113.7729217679908
63          94.49614471161242
64          74.42101563382771
65          54.137765027355582
66          43.476346145895546
67          36.145391281081157
68          25.110439406475585
69          10.18333830873O9
70          4.3891509659O7642
```

Figure E.5 Numerical modeling results for the cone (7.33 m height, and 23 m radius) SMP with 2023 weather function

Pile Number 6

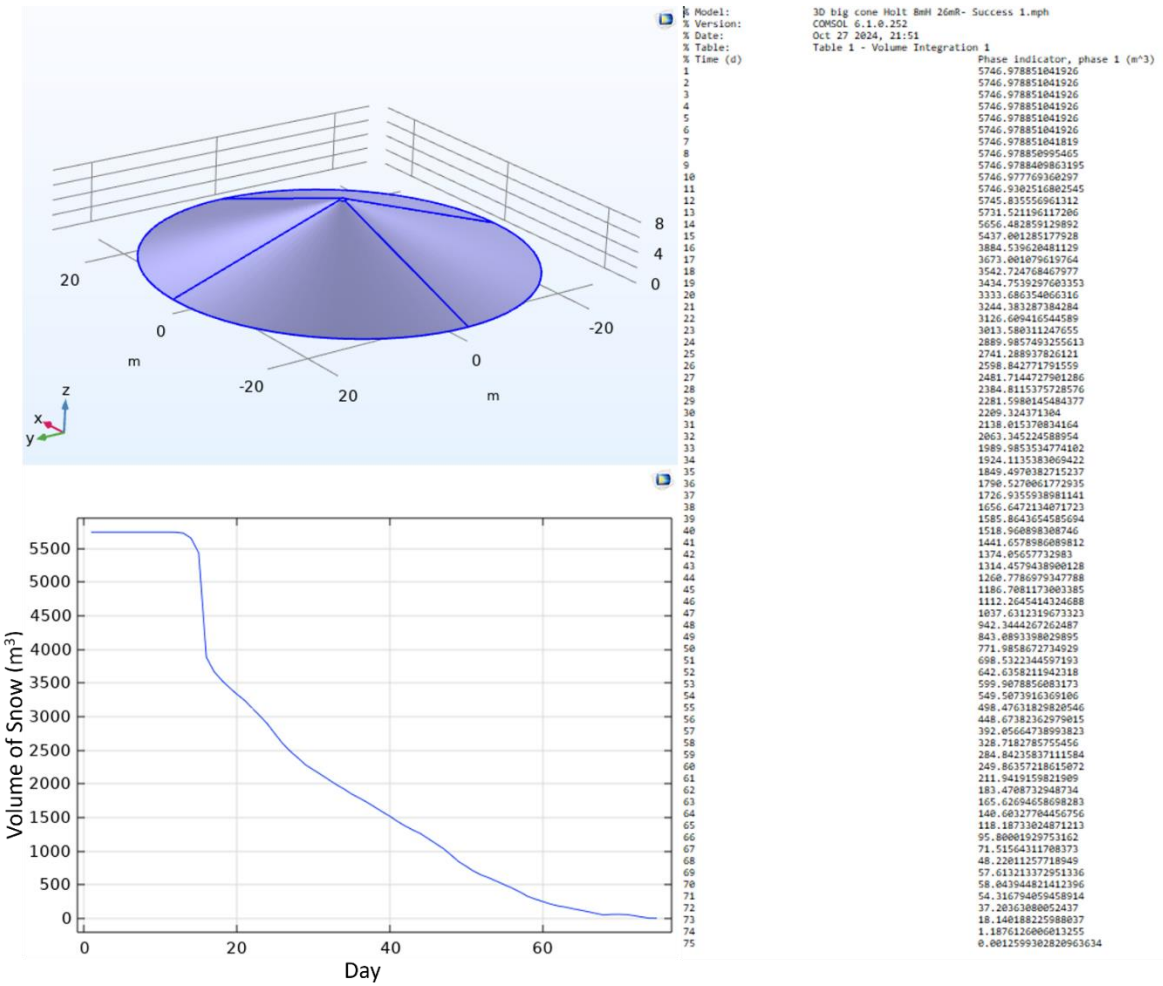

% Model:
% Version:
% Date:
% Table:
% Time (d)

3D big cone Holt 8mH 26mR- Success 1.mph
COMSOL 6.1.0.252
Oct 27 2024, 21:51
Table 1 - Volume Integration 1

	Phase indicator, phase 1 (m^3)
1	5746.978851041926
2	5746.978851041926
3	5746.978851041926
4	5746.978851041926
5	5746.978851041926
6	5746.978851041926
7	5746.978851041819
8	5746.978850995465
9	5746.978840863195
10	5746.977769360297
11	5746.9302516802545
12	5745.835556961312
13	5731.521196117206
14	5656.482859129892
15	5437.001285177928
16	3884.539620481129
17	3673.001079619764
18	3542.724768467977
19	3434.7539297603353
20	3333.686354066316
21	3244.383287384284
22	3126.609416544589
23	3013.580311247655
24	2889.9857493255613
25	2741.288937826121
26	2598.842771791559
27	2481.7144727901286
28	2384.8115375728576
29	2281.5980145484377
30	2209.324371304
31	2138.015370834164
32	2063.345224588954
33	1989.9853534774102
34	1924.1135383069422
35	1849.4970382715237
36	1790.5270061772935
37	1726.9355938981141
38	1656.6472134071723
39	1585.8643654585694
40	1518.960898308746
41	1441.6578986088912
42	1374.05657732983
43	1314.4579438900128
44	1260.7786979347788
45	1186.7081173003385
46	1112.2645414324688
47	1037.6312196073323
48	942.3444267262487
49	843.0893398029895
50	771.9858672734929
51	698.5322344597193
52	642.6358211942218
53	599.9078856083173
54	549.5073916369106
55	498.47631829820546
56	448.67382362979015
57	392.05664738993823
58	328.7182785755456
59	284.84235837111584
60	249.86357218615072
61	211.9419159821909
62	183.4708732948734
63	165.62694658698283
64	140.60327704456756
65	118.18733024871213
66	95.80001929751162
67	71.51564311708373
68	48.22011257718949
69	57.6132133729513336
70	58.043944821412396
71	54.316794059458914
72	37.203630005 2437
73	18.140188225988037
74	1.18761260006013255
75	0.0012599302820963634

Figure E.6 Numerical modeling results for the cone (8 m height, and 26 m radius) SMP with 2023 weather function

Pile Number 7

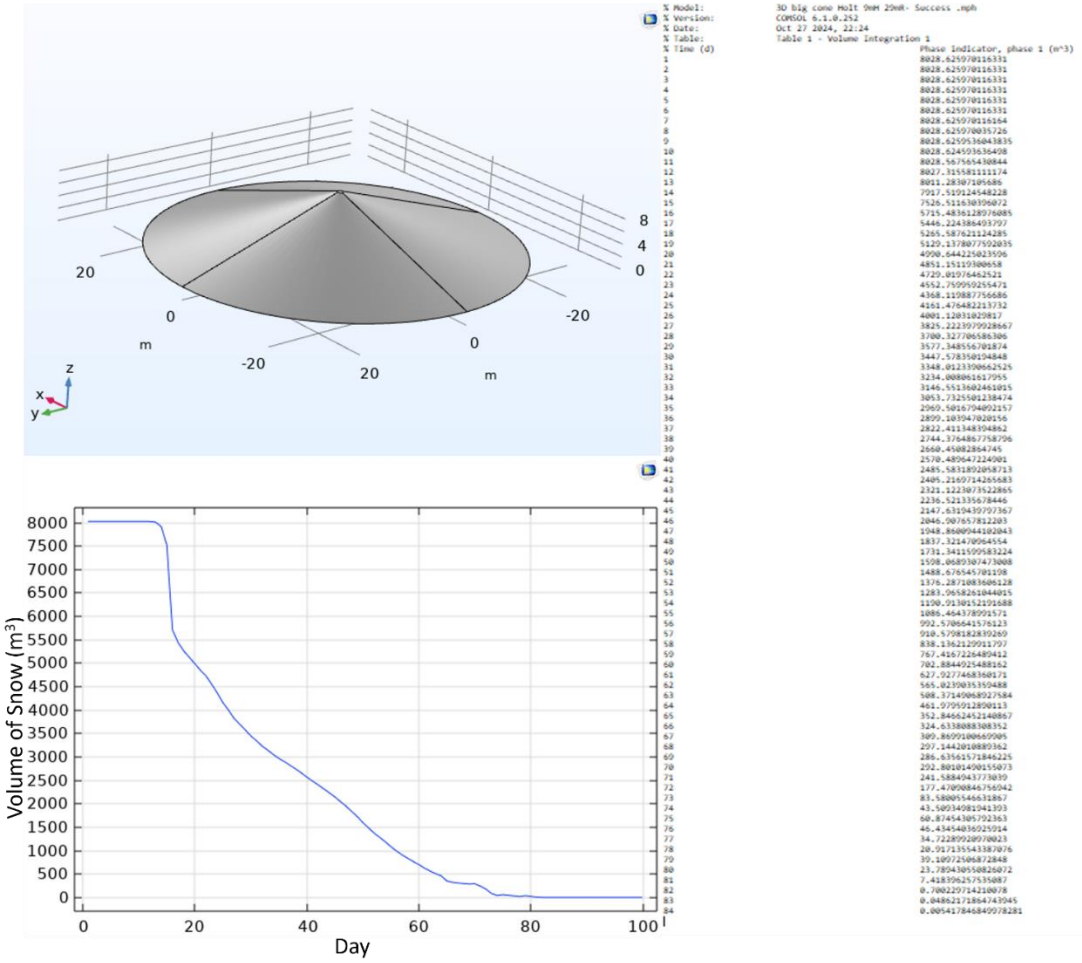

Figure E.7 Numerical modeling results for the cone (9 m height, and 29 m radius) SMP with 2023 weather function

Pile Number 8

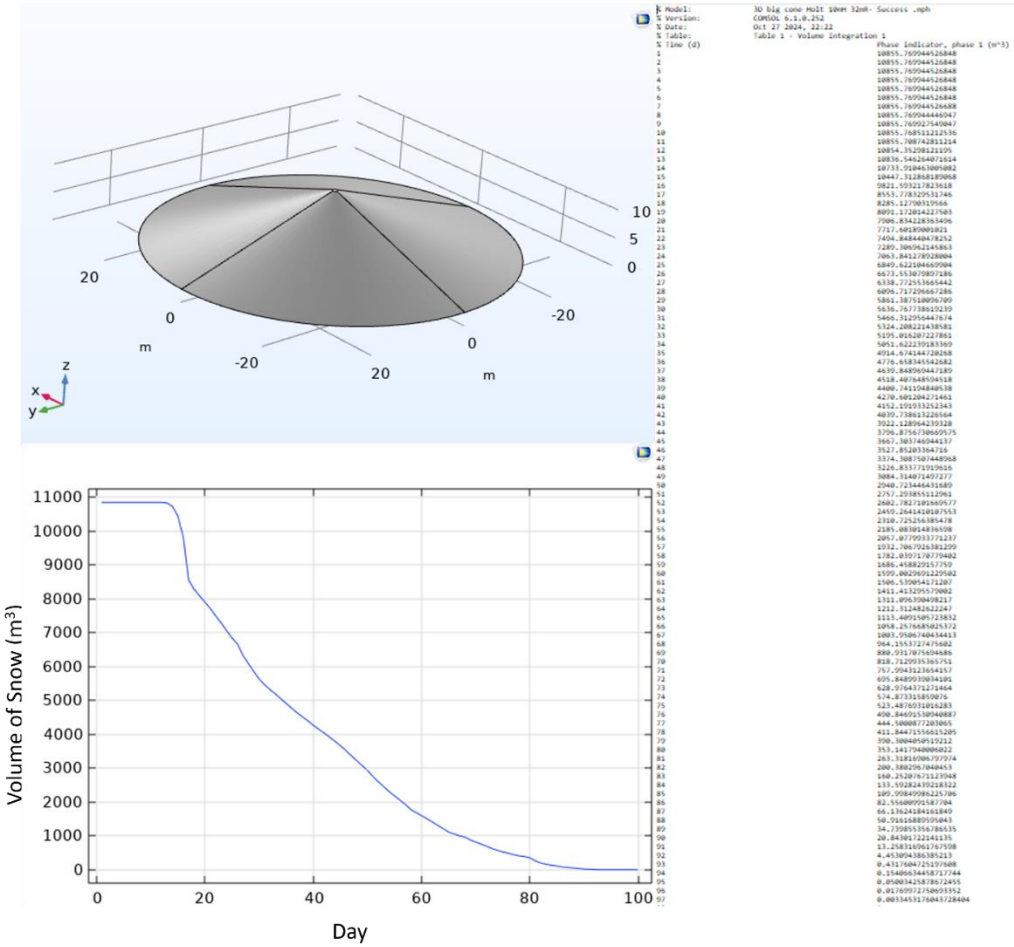

Figure E.8 Numerical modeling results for the cone (10 m height, and 32 m radius) SMP with 2023 weather function

Pile Number 9

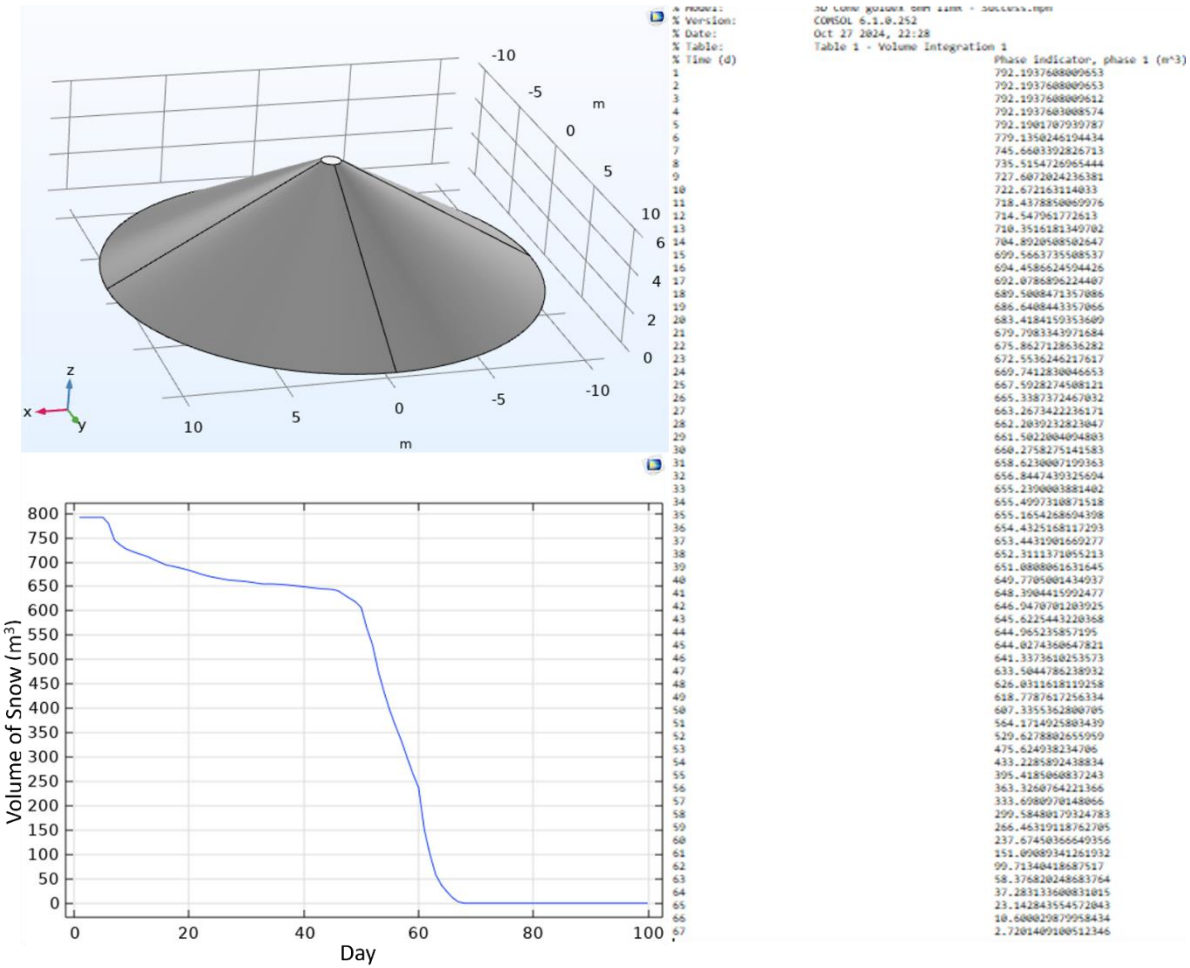

% Version: COMSOL 6.1.0.252
% Date: Oct 27 2024, 22:28
% Table: Table 1 - Volume Integration 1
% Time (d) Phase Indicator, phase 1 (m^3)
1 792.1937608009653
2 792.1937608009653
3 792.1937608009612
4 792.1937603008574
5 792.1901707939787
6 779.1350246194434
7 745.6603392826713
8 735.5154726965444
9 727.6072024236381
10 722.672163114033
11 718.4378850069976
12 714.547961772613
13 710.3516181349702
14 704.8920508502647
15 699.5663735508537
16 694.4586624594426
17 692.0786896224407
18 689.5008471357086
19 686.6408443357066
20 683.4184159353609
21 679.7983343971684
22 675.8627128636282
23 672.5536246217617
24 669.7412830046653
25 667.5928274508121
26 665.3387372467032
27 663.2673422236171
28 662.2039232823047
29 661.5022004094803
30 660.2758275141583
31 658.6230007199363
32 656.8447439325694
33 655.2390003881402
34 655.4997310871518
35 655.1654268694398
36 654.4325168117293
37 653.4431901669277
38 652.3111371055213
39 651.0808061631645
40 649.7705001434937
41 648.3904415992477
42 646.9470701203925
43 645.6225443220368
44 644.965235857195
45 644.0274360647821
46 641.3373610253573
47 633.5044786238932
48 626.0311618119258
49 618.7787617256334
50 607.3355362800705
51 564.1714925803439
52 529.6278802655959
53 475.624938234706
54 433.2285892438834
55 395.4185060837243
56 363.3260764221366
57 333.6080970148066
58 299.584801793247 83
59 266.4631911876270 5
60 237.6745036664035 6
61 151.0900893412610 32
62 99.71404186875170
63 58.37682024868376 4
64 37.28313360083101 5
65 23.14284355472084 3
66 10.60002987995843 4
67 2.720140910051234 6

Figure E.9 Numerical modeling results for the cone (6 m height, and 11 m radius) SMP with 2022 weather function

Pile Number 10

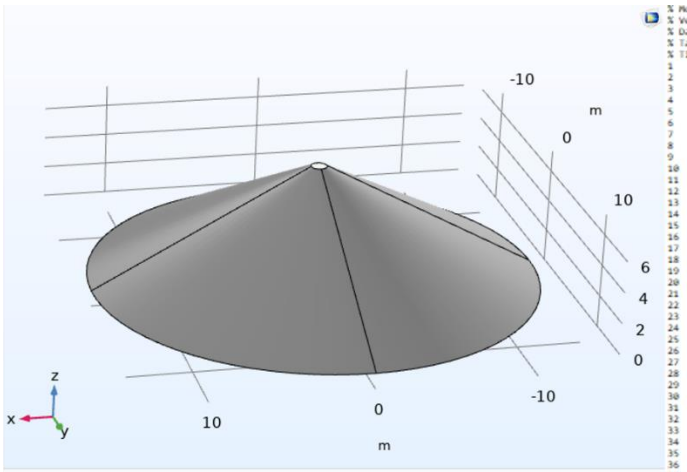

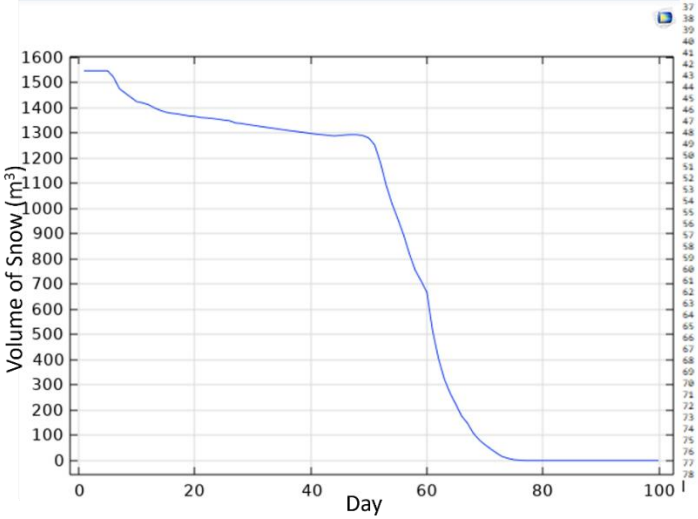


```
% Model:                 3D Cone goldex Base- Success.mph
% Version:               COMSOL 6.1.0.252
% Date:                  Oct 27 2024, 22:30
% Table:                 Table 1 - Volume Integration 1
% Time (d)               Phase Indicator, phase 1 (m^3)
1                        1547.3768423371853
2                        1547.3768423371853
3                        1547.3768423371785
4                        1547.3768415365687
5                        1547.3710853200892
6                        1521.6898765602475
7                        1476.3953786244226
8                        1458.768749140192
9                        1441.7633025490102
10                       1424.7543063842963
11                       1419.8088990259344
12                       1413.0709496379202
13                       1400.4827377049262
14                       1390.7508672030222
15                       1383.0011760952553
16                       1378.6255253029688
17                       1376.1601626095205
18                       1371.7229700483315
19                       1368.0560924883146
20                       1366.3261922259591
21                       1361.9547265357805
22                       1360.4235953973691
23                       1357.993824900613
24                       1354.9522126697352
25                       1351.5829563533777
26                       1348.7880757390265
27                       1340.5201094696724
28                       1338.259018041681
29                       1334.20873217307
30                       1330.7437327831694
31                       1327.3528074158903
32                       1323.9222689342687
33                       1320.7339207090886
34                       1317.4164072122337
35                       1313.971402330951
36                       1310.7300821445283
37                       1307.6422183787374
38                       1304.7284232334132
39                       1301.6982951692664
40                       1298.6756389270763
41                       1295.7466108957246
42                       1293.4298570140586
43                       1291.1141296680494
44                       1288.675074813174
45                       1290.4459639970728
46                       1292.6825460894242
47                       1293.8447476569925
48                       1293.315402593338
49                       1289.859101244648
50                       1280.4963064346455
51                       1253.1233847944402
52                       1182.6817439458772
53                       1092.5526828864229
54                       1019.4548525636928
55                       959.0716214593457
56                       895.4021578209643
57                       820.0284753278394
58                       755.3675257856666
59                       713.6320333816756
60                       668.3982282362446
61                       613.7746474623744
62                       486.6354270670628
63                       324.1543173081624
64                       267.9147822083077
65                       222.8236697172257
66                       176.418683235322
67                       148.1356498049911
68                       108.9838510758572
69                       82.26362285203894
70                       63.00406523185
71                       45.83616971324478
72                       29.82575560556358
73                       15.54581603680966
74                       8.378566833430519
75                       3.1490197243149085
76                       1.3770938280846767
77                       0.06850487780335597
78                       1.9993512009024766E-4
```


Figure E.10 Numerical modeling results for the cone (7.3 m height, and 14 m radius) SMP with 2022 weather function

Pile Number 11

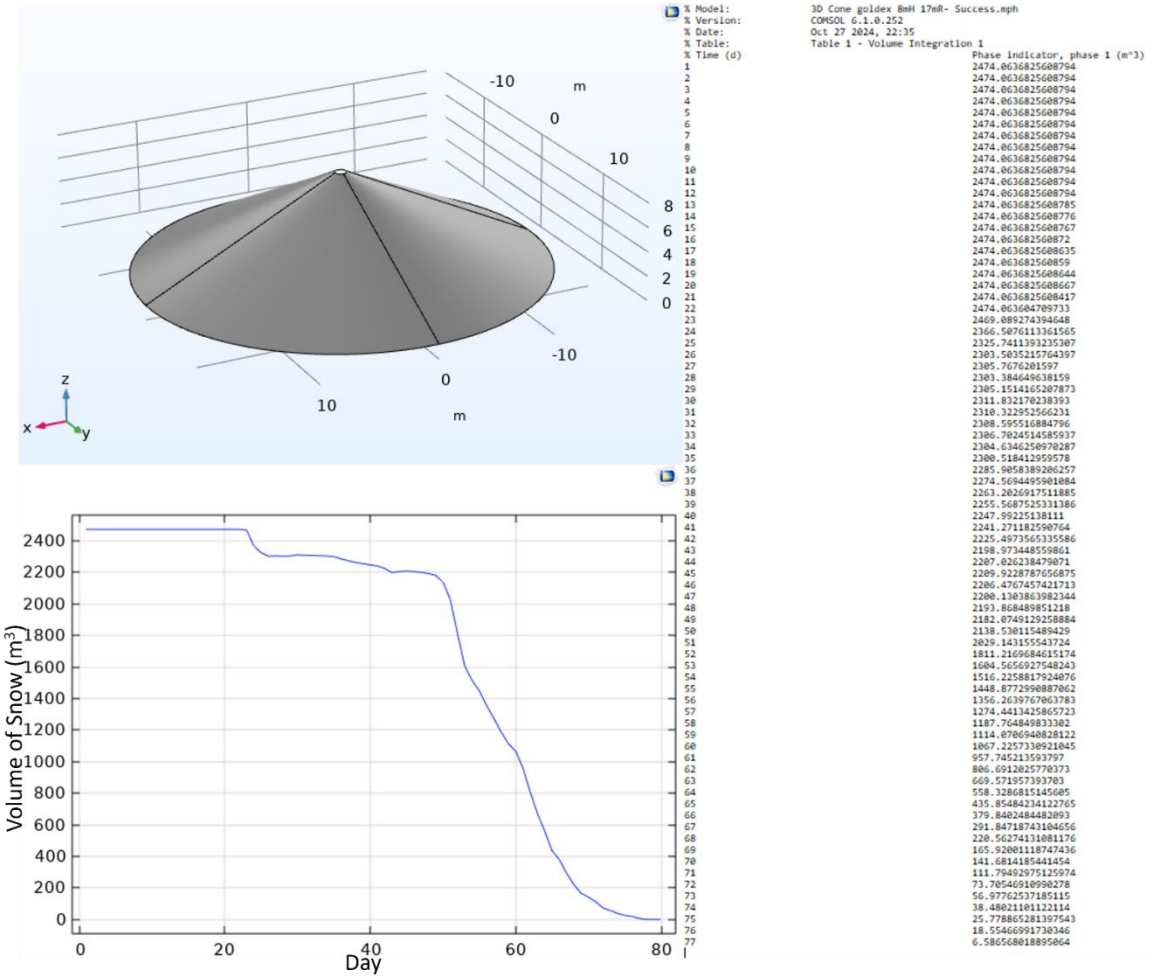

% Model:
% Version:
% Date:
% Table:
% Time (d)
3D Cone goldex BmH 17mR- Success.mph
COMSOL 6.1.0.252
Oct 27 2024, 22:35
Table 1 - Volume Integration 1
Phase Indicator, phase 1 (m^3)
2474.0636825608794
2474.0636825608794
2474.0636825608794
2474.0636825608794
2474.0636825608794
2474.0636825608794
2474.0636825608794
2474.0636825608794
2474.0636825608794
2474.0636825608794
2474.0636825608794
2474.0636825608794
2474.0636825608794
2474.0636825608785
2474.0636825608776
2474.0636825608767
2474.063682560872
2474.0636825608635
2474.063682560859
2474.0636825608644
2474.0636825608667
2474.0636825608417
2474.063604709733
2469.089274394648
2366.5076113361565
2325.7411393235307
2303.5035215764397
2305.7676201597
2303.384649638159
2305.1514165207873
2311.832170238393
2310.322952566231
2308.595516884796
2306.7024514585937
2304.6346250970287
2300.518412959578
2285.9058389206257
2274.5694495901884
2263.2026917511885
2255.5687525331386
2247.99225138111
2241.271182590764
2225.4971565335586
2198.973448559861
2207.026238479071
2209.9228787656875
2206.4767457421713
2200.1303863982344
2193.868489851218
2182.0749129258884
2138.530115489429
2029.143155543724
1811.2169684615174
1604.5656927548243
1516.2258817924076
1448.8772990887062
1356.2639767863783
1274.4413425865723
1187.7648489833302
1114.0706940828122
1067.2257330921045
957.745213593797
806.6912025770373
669.571957393703
558.3286815145605
435.85484234122765
379.8402484482093
291.84718743104656
220.56274131081176
165.92001118747436
141.68141854414454
111.79492975125974
73.70546910990278
56.977625371851115
38.48021101122114
25.778865281397543
18.554669917303 46
6.586568018895064

Figure E.11 Numerical modeling results for the cone (8 m height, and 17 m radius) SMP with 2022 weather function

Pile Number 12

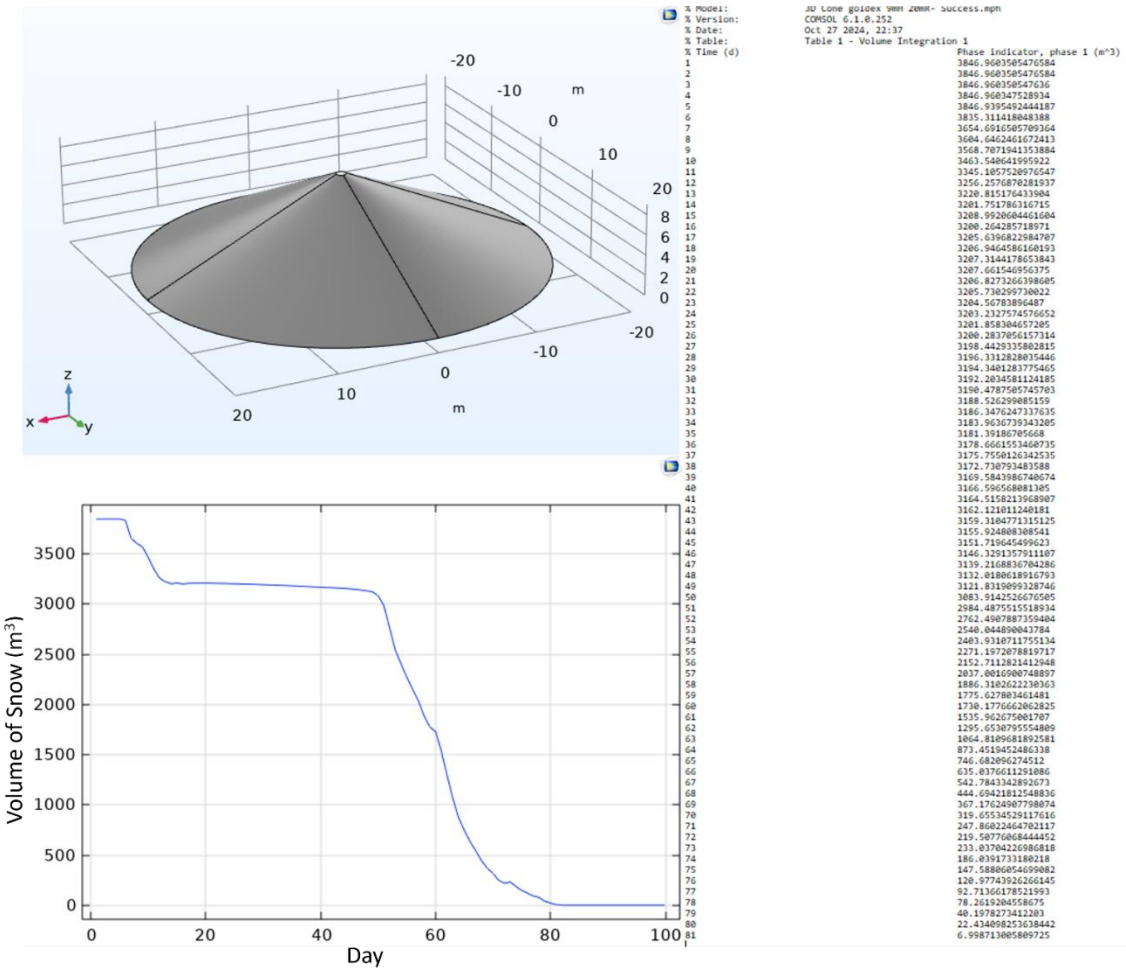

% Model:
% Version:
% Date:
% Table:
% Time (d)
COMSOL 6.1.0.252
Oct 27 2024, 22:37
Table 1 - Volume Integration 1
Phase Indicator, phase 1 (m^3)
3846.9603505476584
3846.9603505476584
3846.960350547636
3846.960347528934
3846.9395492444187
3835.311418048388
3654.6916505709364
3604.6462461672413
3568.707194135884
3463.540641995922
3345.1057520976547
3256.2576870281937
3220.8151764133984
3201.751786316715
3208.9920604461604
3200.264285718971
3205.6396822984707
3206.9464586160193
3207.3144178653843
3207.661546956375
3206.8273266398605
3205.730299730022
3204.56783896487
3203.2327574576652
3201.858304657205
3200.2837056157314
3198.4429335802815
3196.3312828035446
3194.3401283775465
3192.2034581124185
3190.4787505745703
3188.52629985159
3186.3476247337635
3183.9636739343205
3181.39186705668
3178.6661553460735
3175.7550126342535
3172.730793483588
3169.5843986740674
3166.5965680081305
3164.5158213968907
3162.121011240181
3159.3104771315125
3155.924808308541
3151.719645499623
3146.3291357911107
3139.2168836704286
3132.0180618916793
3121.8319099328746
3083.9142526676505
2984.4875515518934
2762.4907887359404
2540.044890043784
2403.9310711755134
2271.1972078819717
2152.7112821412948
2037.0016900748897
1886.3102622230363
1775.627803461481
1730.1776662062825
1535.962675001707
1295.6530795554809
1064.8109681892581
873.4519452486338
746.682096274512
635.0376611291086
542.7843342892673
444.69421812548836
367.17624907798074
319.65534529117616
247.86022464702117
219.58776068444452
233.03704226986818
186.0391733180218
147.58806054699082
120.97743926266145
92.71366178521993
78.2619204558675
40.19782734122003
22.434098253638442
6.998713005809725

Figure E.12 Numerical modeling results for the cone (9 m height, and 20 m radius) SMP with 2022 weather function

Pile Number 13

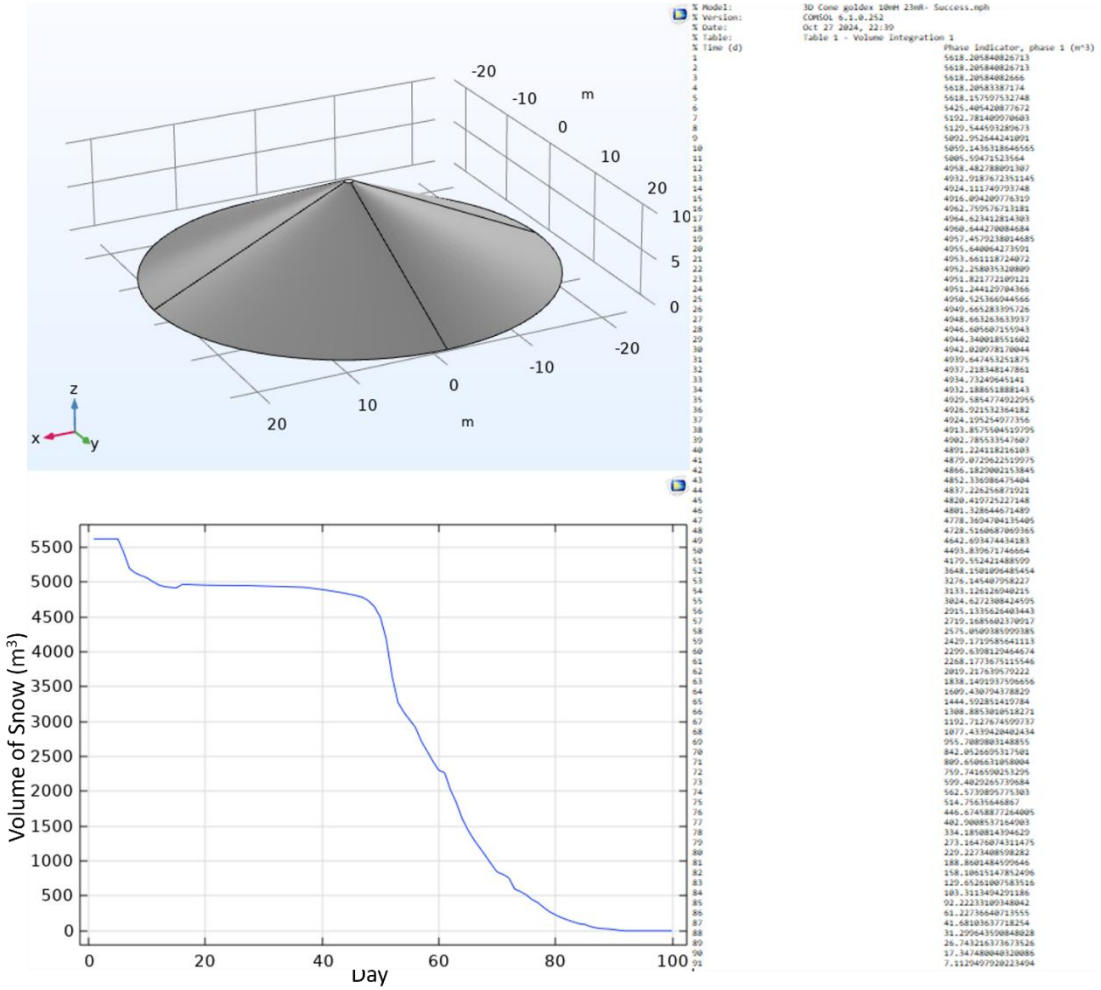

Figure E.13 Numerical modeling results for the cone (10 m height, and 23 m radius) SMP with 2022 weather function

Pile Number 14

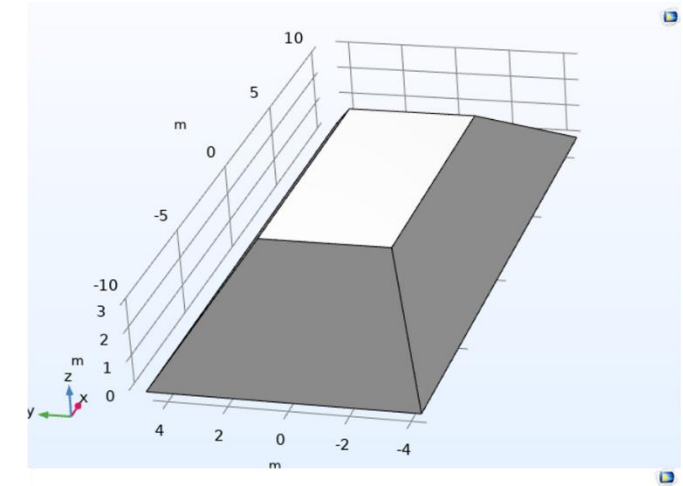

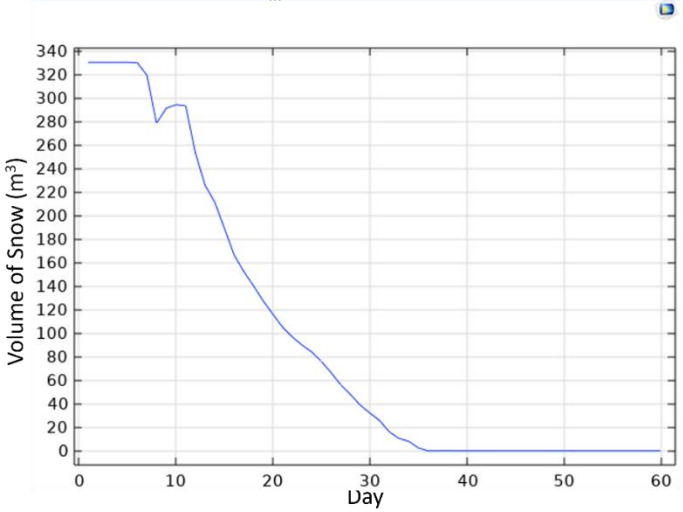

% Model:	3D Ridge Holt 21mL1 9mL2 3mH- Success .mph	
% Version:	COMSOL 6.1.0.252	
% Date:	Oct 27 2024, 22:43	
% Table:	Table 1 - Volume Integration 1	
% Time (d)		Phase indicator, phase 1 (m^3)
1		330.7499999999977
2		330.7499999999977
3		330.74999999999454
4		330.74999953108363
5		330.74856926030924
6		330.4315434949791
7		319.74877400352324
8		278.84019303870826
9		291.62038184977473
10		294.60932455538256
11		293.74271674447573
12		253.74492374467212
13		226.06289095552944
14		211.7005346531364
15		189.36725356041472
16		166.7131778838241
17		152.57526506563542
18		140.40614311964356
19		127.56050948286628
20		116.26461768910391
21		105.19660651624721
22		96.95553856610101
23		90.07851147913628
24		84.17878042357512
25		76.1123511180127
26		66.5432961943948
27		56.188603001759965
28		48.03521455585016
29		38.879528801095645
30		32.19243659017845
31		25.843588881264168
32		16.122987434911607
33		10.645613646385774
34		8.145154973696737
35		2.5814040236716354

Figure E.14 Numerical modeling results for the ramp (3m height, 9 m width, and 21 lenght) SMP with 2023 weather function

Pile Number 15

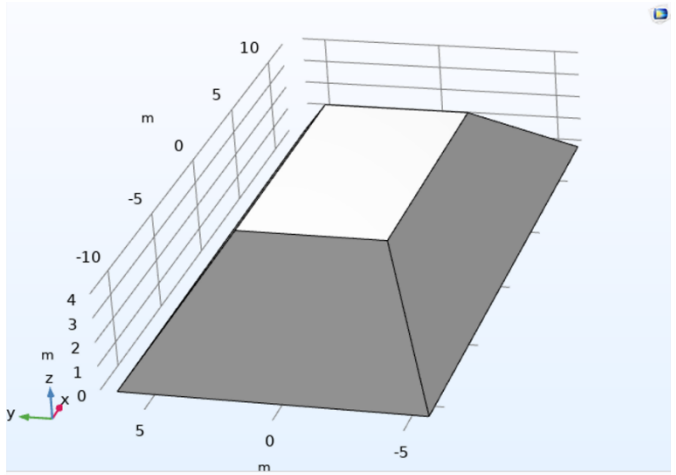

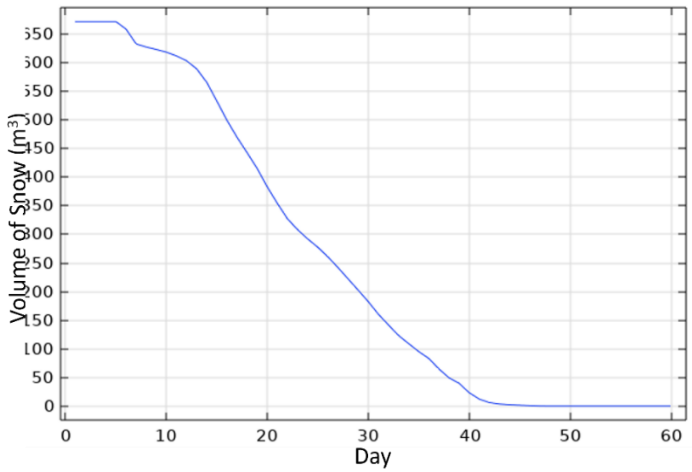

% Model:	3D Ridge Holt 24mL1 12mL2 4mH- Success .mph
% Version:	COMSOL 6.1.0.252
% Date:	Oct 27 2024, 22:45
% Table:	Table 1 - Volume Integration 1
% Time (d)	Phase indicator, phase 1 (m^3)
1	671.9999999999997
2	671.9999999999997
3	671.9999999999956
4	671.999999508967
5	671.9959282839326
6	658.977141572415
7	633.0076542153836
8	627.5944586598744
9	623.2922842852684
10	618.6391236696222
11	611.9719042286464
12	603.5219257500504
13	589.4295040786923
14	565.7899633819013
15	533.0093127066251
16	499.54566364006143
17	469.74638213831145
18	442.798787299099
19	415.1241305029945
20	382.87875999342907
21	354.09224778699627
22	327.315611725684
23	308.276213917104
24	292.1848122501956
25	277.6544339446709
26	260.932361866631
27	242.08425606265146
28	222.3890786722613
29	202.63601345564402
30	182.59914528195404
31	160.61412124367018
32	141.8217552973156
33	123.32415728869779
34	109.24425544683453
35	95.28391840770554
36	83.2791072870765
37	64.90265923861224
38	49.40455318922428
39	39.845269365428315
40	23.460988429879134
41	12.186229951525803
42	6.114830054961216
43	3.543400129207145
44	2.3514711211229256
45	1.5273221445378962

Figure E.15 Numerical modeling results for the ramp (4 m height, 12 m width, and 24 lenght) SMP with 2023 weather function

Pile Number 16

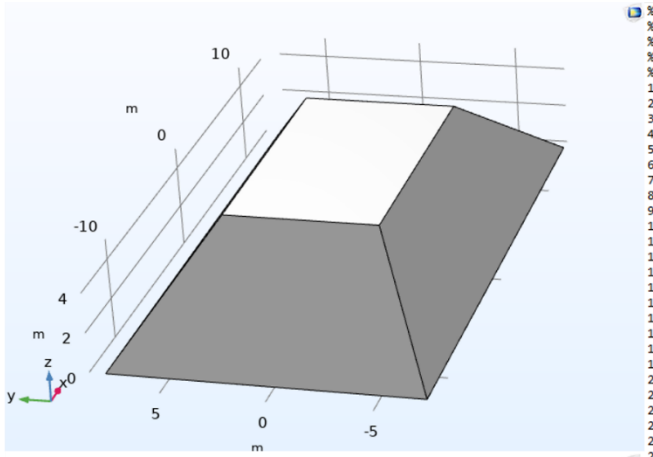

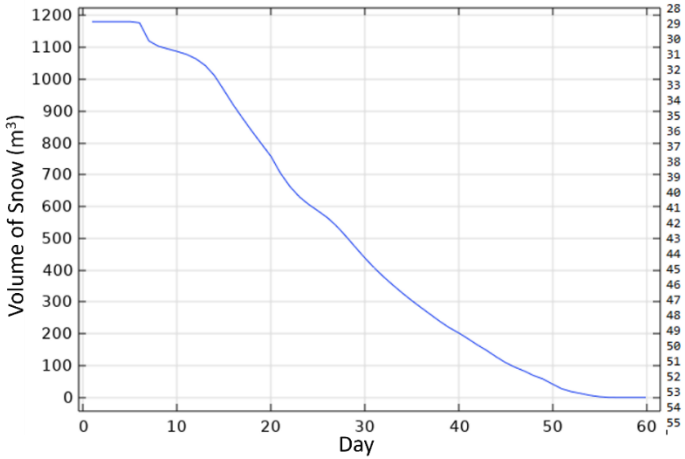

% Model:	3D Ridge Holt 27mL1 15mL2 5mH- Success .mph	
% Version:	COMSOL 6.1.0.252	
% Date:	Oct 27 2024, 22:47	
% Table:	Table 1 - Volume Integration 1	
% Time (d)		Phase indicator, phase 1 (m^3)
1		1181.250000000002
2		1181.250000000002
3		1181.2499999999966
4		1181.2499992734745
5		1181.2449335459573
6		1177.6527184125655
7		1120.3323318714038
8		1104.140867365607
9		1095.6298899857898
10		1087.6056192729448
11		1078.4022499431387
12		1064.501511320668
13		1043.6842898174175
14		1010.8856347399087
15		965.4093296785669
16		919.0919443892286
17		876.9391380465382
18		835.9659664821844
19		796.8218328513643
20		757.996213106589
21		705.6421440143914
22		664.0744673525207
23		631.3616239358369
24		607.2469269763412
25		586.7127490876693
26		565.5436028727332
27		538.7739163195209
28		506.4817831015998
29		472.29735374766125
30		438.90462076201146
31		407.6155129754678
32		379.40506104213125
33		353.27516766547143
34		328.3564603567956
35		304.8207383976345
36		282.4843556362633
37		260.9213241870897
38		239.18149496674073
39		219.54763650573318
40		202.99848107836183
41		184.65669796856264
42		165.22546286447636
43		147.64861611345935
44		127.88074821658766
45		109.68141370153329
46		95.24826427201673
47		83.01087026655334
48		68.82885359034111
49		57.99497084536591
50		42.1668161423474
51		27.289383392082758
52		18.41415055609338
53		12.692314173403869
54		6.554273085015614
55		2.3817372829554015

Figure E.16 Numerical modeling results for the ramp (5 m height, 15 m width, and 27 lenght) SMP with 2023 weather function

Pile Number 17

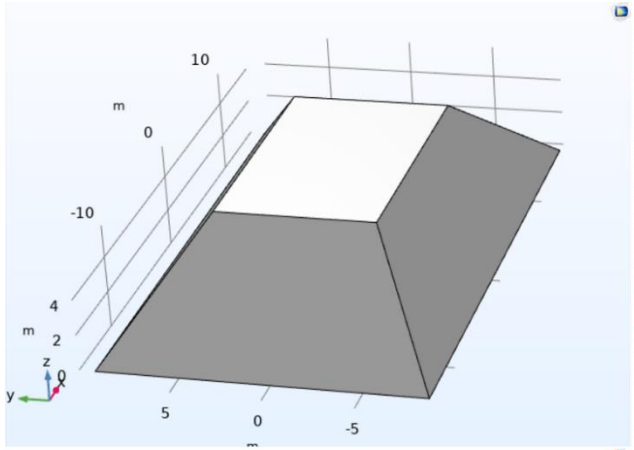

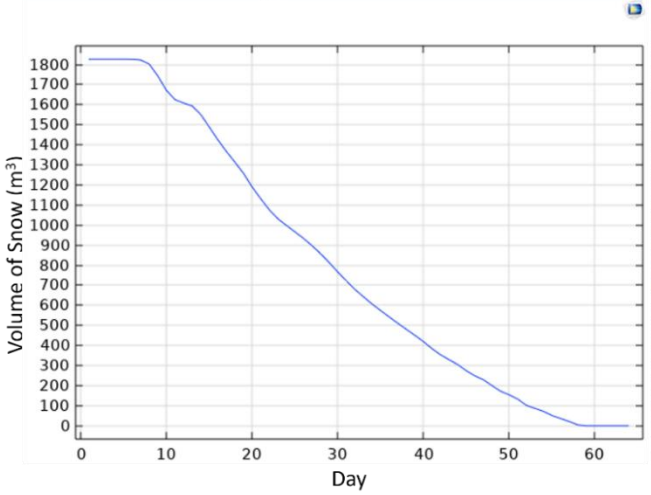


```
% Model:                    3D Ridge Holt Base- Success.mph
% Version:                  COMSOL 6.1.0.252
% Date:                     Oct 13 2024, 15:32
% Table:                    Table 1 - Volume Integration 1
% Time (d)                  Phase indicator, phase 1 (m^3)
1                           1827.0000000000007
2                           1827.0000000000007
3                           1826.9999999999925
4                           1826.9999891154446
5                           1826.99184826797
6                           1826.5517089082211
7                           1822.7832601352382
8                           1803.1550076477308
9                           1743.5527082745828
10                          1672.1130149401827
11                          1626.1166874038695
12                          1608.641177487274
13                          1594.1114281634018
14                          1552.3023240226862
15                          1489.6326819386393
16                          1426.0328997238566
17                          1367.2425213655904
18                          1313.8302546108168
19                          1258.4411289671575
20                          1190.7685644848063
21                          1132.2042251685448
22                          1077.090676132905
23                          1032.0333633115374
24                          999.0060913707352
25                          966.3592969463174
26                          934.0681039820095
27                          897.534870802109
28                          857.8450737735919
29                          813.4479905477251
30                          766.5804133054952
31                          722.2573892227641
32                          679.7720281595989
33                          643.0706974279285
34                          607.0652150268955
35                          574.2212573563964
36                          542.535768534746
37                          511.34138471167984
38                          480.8557059707842
39                          450.8689972070301
40                          419.35060429847175
41                          384.3985048661324
42                          353.74760829227023
43                          329.2478177110095
44                          304.8303113702495
45                          274.40451052669215
46                          248.76947382987453
47                          229.33673643121625
48                          200.25546848892805
49                          172.35825382733833
50                          154.38533846282502
51                          132.9891582272701
52                          101.95250997373894
53                          86.97924560663601
54                          71.86935439159686
55                          51.35782070381155
56                          36.28380680227432
57                          21.614466781396082
58                          4.537748182898285
```

Figure E.17 Numerical modeling results for the ramp (5.8 m height, 18 m width, and 30 lenght) SMP with 2023 weather function

Pile Number 18

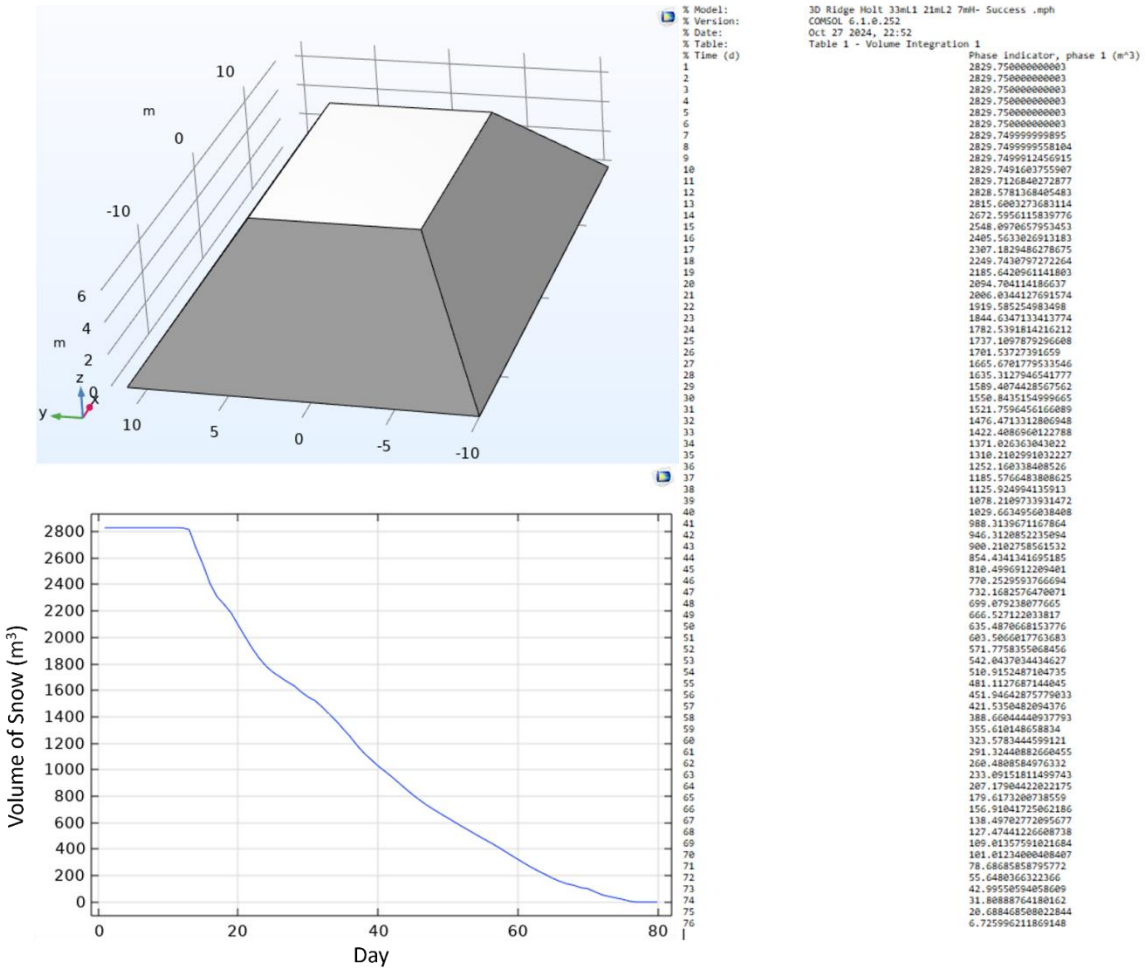

% Model:
% Version:
% Date:
% Table:
% Time (d)
3D Ridge Holt 33mL1 21mL2 7mH- Success .mph
COMSOL 6.1.0.252
Oct 27 2024, 22:52
Table 1 - Volume Integration 1
Phase indicator, phase 1 (m^3)
2829.750000000003
2829.750000000003
2829.750000000003
2829.750000000003
2829.750000000003
2829.750000000003
2829.749999999895
2829.749999958104
2829.749991245691
2829.749160375590
2829.712684027287
2828.578136840548
2815.600327368311
2672.595611583977
2548.097065795345
2405.563302691318
2307.182648627867
2249.743079727226
2185.642096114180
2094.704114186637
2006.034412769157
1919.585254983498
1844.634713341377
1782.539181421621
1737.109787929660
1701.537273916590
1665.670177953354
1635.312794654177
1589.407442856756
1550.843515499966
1521.759645616608
1476.471331280694
1422.408696012278
1371.026363043022
1310.210299103222
1252.160338408526
1185.576648380862
1125.924994135913
1078.210973391472
1029.663495603840
988.3139671167864
946.3120852235094
900.2102758561532
854.4141341695185
810.4996912209401
770.2529593766694
732.1682576470071
699.079238077665
666.5271220318170
635.4870668153776
603.5066017763683
571.7758355068456
542.0437034434627
510.9152487104735
481.1127687144045
451.9464287577903
421.5350482094376
388.6604444409377
355.6101486588340
323.5783444599121
291.3244088826604
260.4808584976332
233.0915181149974
207.1790442202217
179.6173200738559
156.9104172506218
138.4970277209567
127.4744122660873
109.0135759102168
101.0123400040840
78.68685858795772
55.64803663223660
42.99550594058609
31.80888764180162
20.68846850802284
6.725996211869148

Figure E.18 Numerical modeling results for the ramp (7 m height, 21 m width, and 33 lenght) SMP with 2023 weather function

Pile Number 19

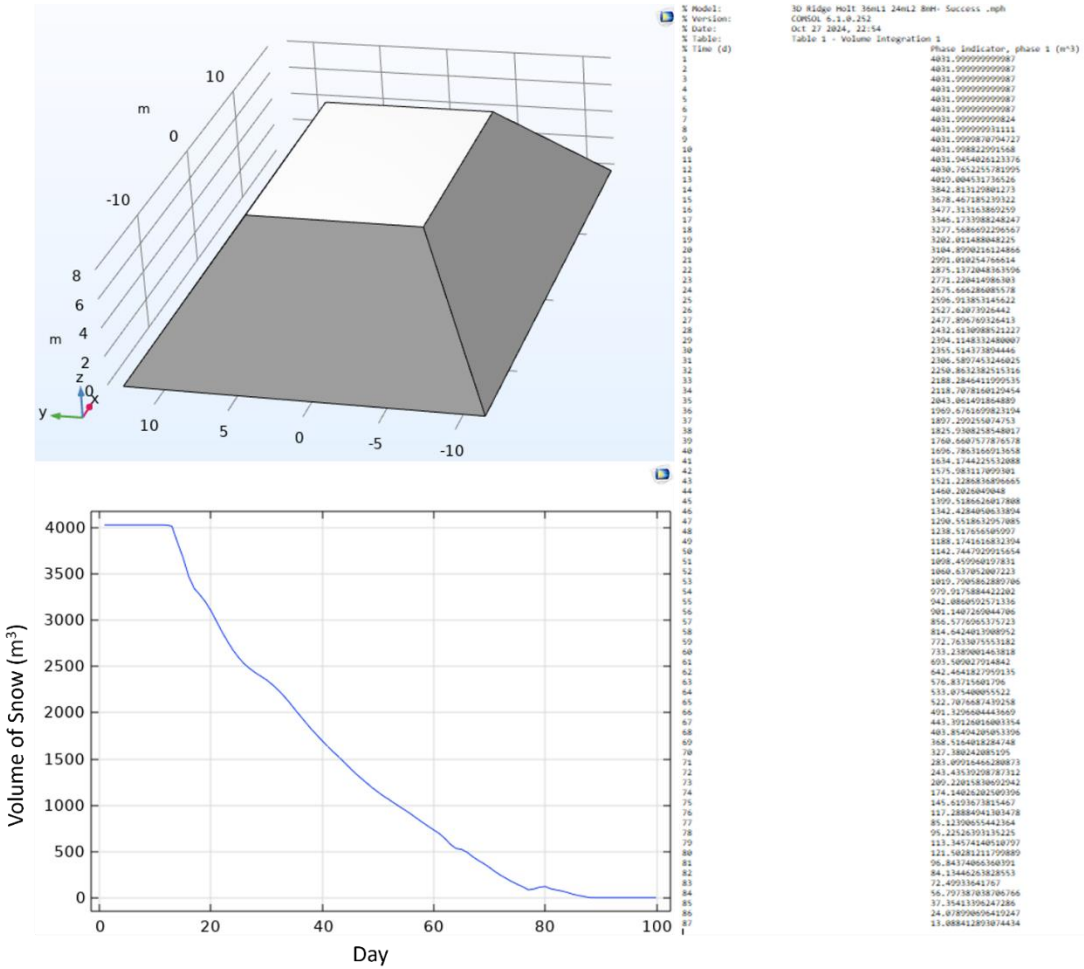

Figure E.19 Numerical modeling results for the ramp (8 m height, 24 m width, and 36 lenght) SMP with 2023 weather function

Pile Number 20

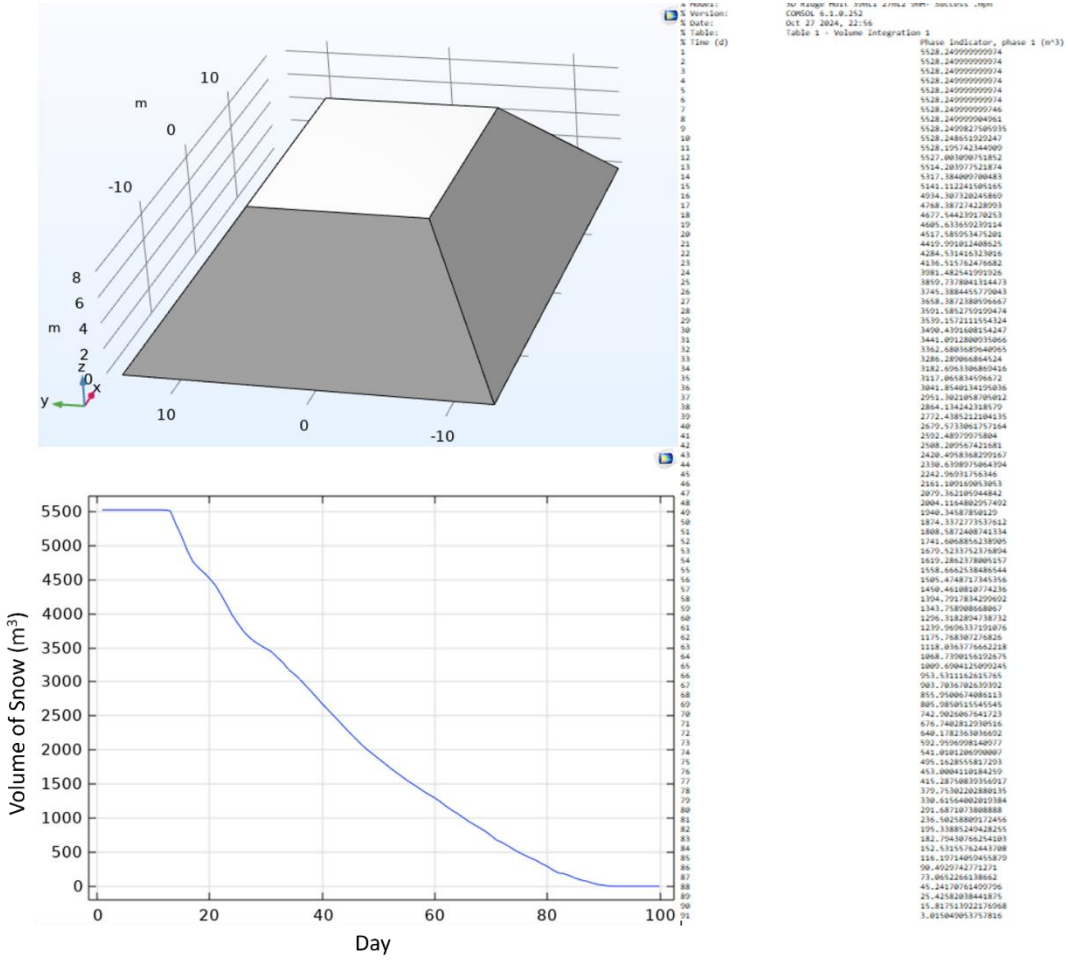

Figure E.20 Numerical modeling results for the ramp (9 m height, 27 m width, and 39 lenght) SMP with 2023 weather function

Pile Number 21

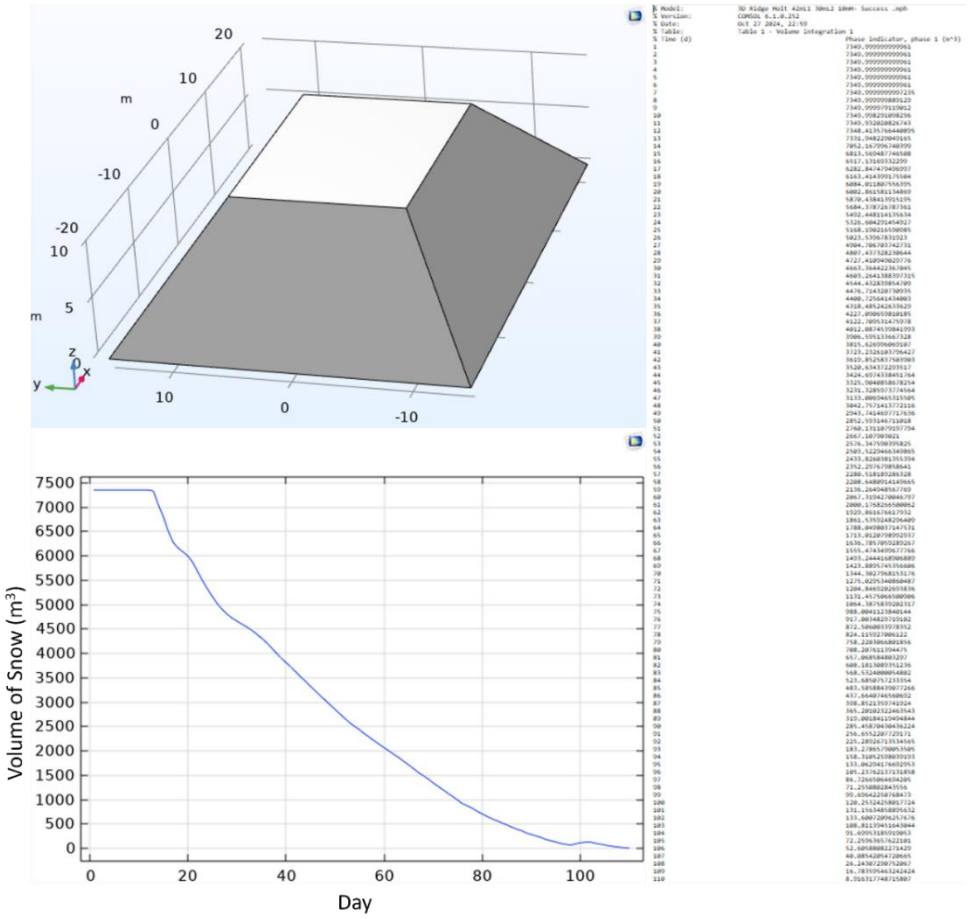

Figure E.21 Numerical modeling results for the ramp (10 m height, 30 m width, and 42 lenght) SMP with 2023 weather function

Pile Number 22

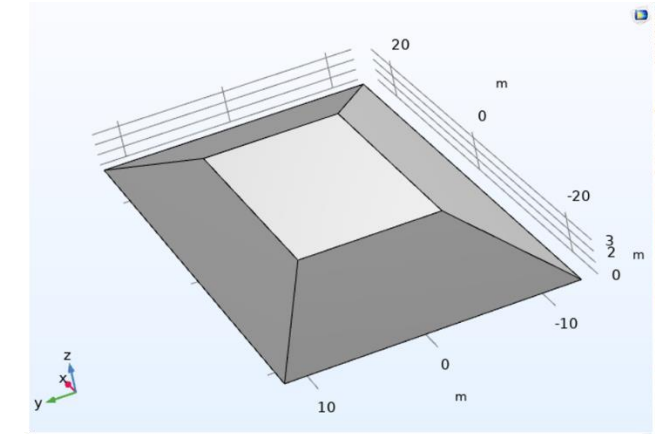

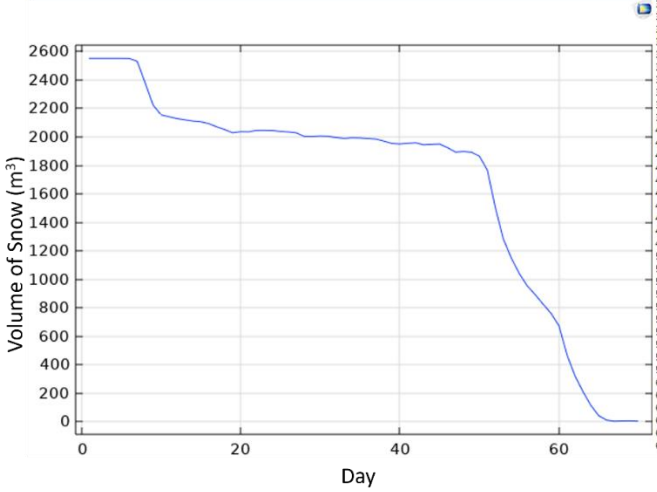

% Model:	3D Ridge goldex base - Success.mph	
% Version:	COMSOL 6.1.0.252	
% Date:	Oct 13 2024, 10:59	
% Table:	Table 1 - Volume Integration 1	
% Time (d)		Phase indicator, phase 1 (m^3)
1		2552.08333333333
2		2552.08333333333
3		2552.083333333323
4		2552.0833324054947
5		2552.0760275413404
6		2551.7037242993006
7		2546.7271215593632
8		2513.9832584352807
9		2405.7214981812945
10		2311.8835419130337
11		2257.9174543658564
12		2237.048149140262
13		2221.5290368975793
14		2207.9557437242884
15		2196.1362381681893
16		2184.8319007889254
17		2174.3265124124914
18		2164.2744596056045
19		2154.8520533620535
20		2145.924592089236
21		2137.337345780466
22		2129.917684021071
23		2122.250542664045
24		2114.316527340941
25		2106.4609122945126
26		2100.5019179904175
27		2094.326032597094
28		2087.9173532398842
29		2081.2513928899994
30		2074.296912900343
31		2067.0159083954427
32		2061.3159572231943
33		2055.4272661948307
34		2048.3359159808465
35		2039.5955728657784
36		2028.5062131706127
37		2013.920281481382
38		1990.9381694605984
39		1944.8231362205295
40		1861.3387863419475
41		1728.4810885449149
42		1606.5189464147509
43		1503.088879670118
44		1358.8183012627906
45		1251.9424990060597
46		1172.1051948872662
47		1090.0937198441125
48		994.8210090811311
49		874.5349646217012
50		757.2043458242028
51		650.1883222057116
52		543.9263739049007
53		484.56317567464095
54		436.0007407103531
55		358.13370866486676
56		268.1184347677991
57		216.58739915822284
58		124.09043684749759
59		85.58362490089287
60		73.27219050216294
61		27.719095741976737
62		41.82952350331356
63		34.12399075965517
64		37.658201786868744
65		16.340850412110264

Figure E.22 Numerical modeling results for the ridge (3.5 m height, 25 m width, and 50 m length) SMP with 2022 weather function

Pile Number 23

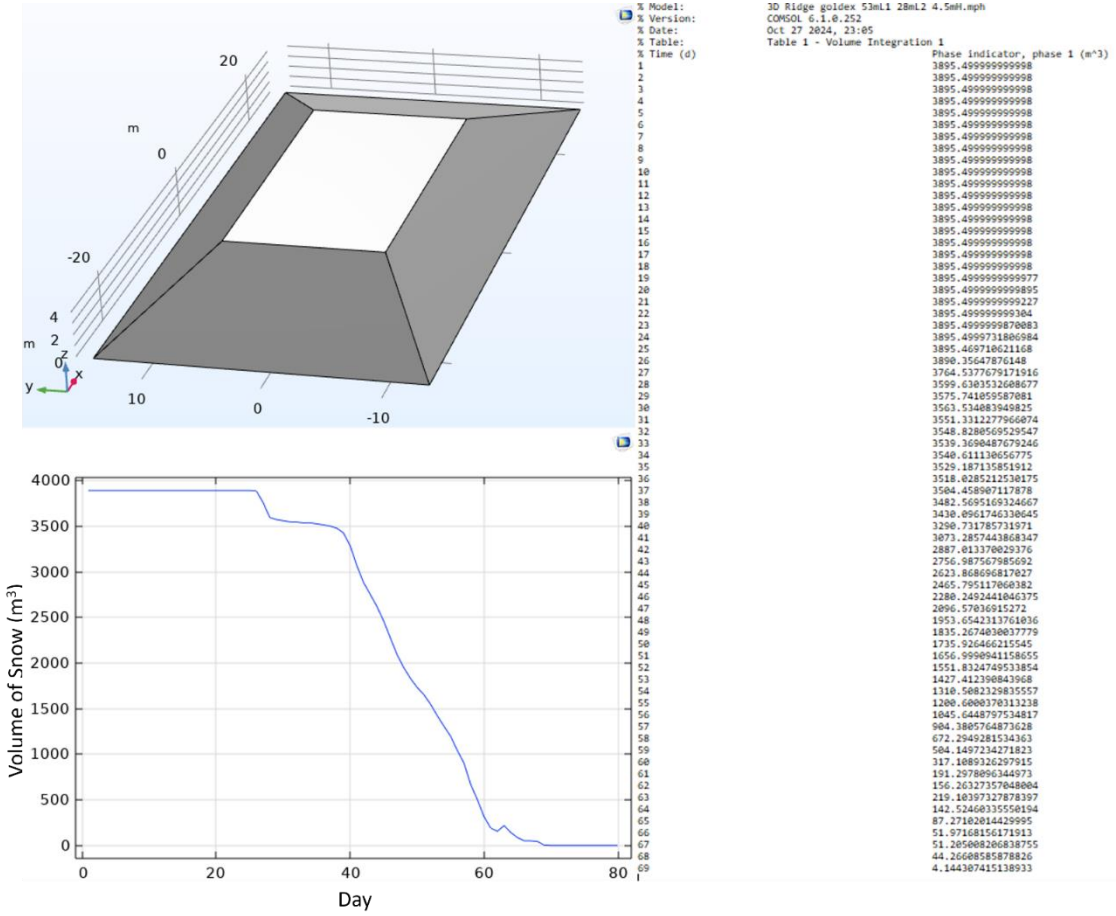


```
% Model:
% Version:
% Date:
% Table:
% Time (d)
3D Ridge goldex 53mL1 28mL2 4.5mH.mph
COMSOL 6.1.0.252
Oct 27 2024, 23:05
Table 1 - Volume Integration 1
                                                Phase indicator, phase 1 (m^3)
1                                               3895.4999999999998
2                                               3895.4999999999998
3                                               3895.4999999999998
4                                               3895.4999999999998
5                                               3895.4999999999998
6                                               3895.4999999999998
7                                               3895.4999999999998
8                                               3895.4999999999998
9                                               3895.4999999999998
10                                              3895.4999999999998
11                                              3895.4999999999998
12                                              3895.4999999999998
13                                              3895.4999999999998
14                                              3895.4999999999998
15                                              3895.4999999999998
16                                              3895.4999999999998
17                                              3895.4999999999998
18                                              3895.4999999999998
19                                              3895.4999999999977
20                                              3895.4999999999895
21                                              3895.4999999999227
22                                              3895.4999999999304
23                                              3895.4999999870083
24                                              3895.4999731806984
25                                              3895.469710621168
26                                              3890.35647876148
27                                              3764.5377679171916
28                                              3599.6303532608677
29                                              3575.7418595870881
30                                              3563.534083949825
31                                              3551.3312277966074
32                                              3548.8280569529547
33                                              3539.3690487679246
34                                              3540.611130656775
35                                              3529.187135851912
36                                              3518.0285212530175
37                                              3504.458907117878
38                                              3482.5695169324667
39                                              3430.09617463306645
40                                              3290.731785731971
41                                              3073.2857443868347
42                                              2887.0113700293776
43                                              2756.98756798569 2
44                                              2623.868696817027
45                                              2465.795117060382
46                                              2280.2492441046375
47                                              2096.57036915272
48                                              1953.6542313761036
49                                              1835.2674030037779
50                                              1735.926466215545
51                                              1656.9990941158655
52                                              1551.8324749533854
53                                              1427.412390843968
54                                              1310.5082329835557
55                                              1200.6000170113238
56                                              1045.6448797534817
57                                              904.3805764873628
58                                              672.2949281534363
59                                              504.14972342718 23
60                                              317.1089326297915
61                                              191.29788963449 73
62                                              156.26327357048004
63                                              219.10397327878397
64                                              142.52460335550194
65                                              87.27102014429995
66                                              51.97168156171913
67                                              51.205008206838755
68                                              44.266085858788826
69                                              4.144307415138933
```

Figure E.23 Numerical modeling results for the ridge (4.5 m height, 28 m width, and 53 m length) SMP with 2022 weather function

Pile Number 24

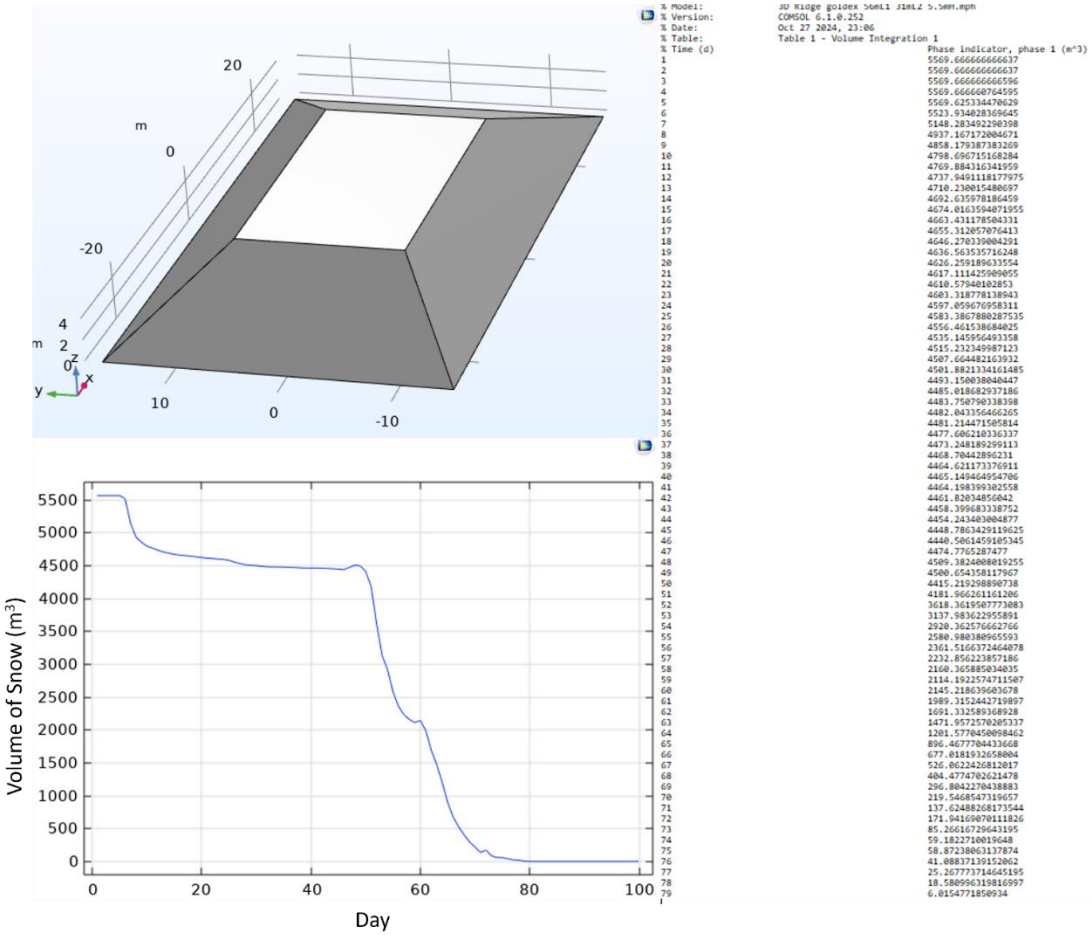

% Model:
% Version: COMSOL 6.1.0.252
% Date: Oct 27 2024, 23:06
% Table: Table 1 - Volume Integration 1
% Time (d) Phase indicator, phase 1 (m^3)
1 5569.666666666637
2 5569.666666666637
3 5569.666666666596
4 5569.666660764595
5 5569.625334470629
6 5523.934028369645
7 5148.283492290398
8 4937.167172004671
9 4858.179387383269
10 4798.696715168284
11 4769.884316341959
12 4737.94911181779975
13 4710.230015480697
14 4692.635978186459
15 4674.016359407195 5
16 4663.431178504331
17 4655.312057076413
18 4646.270339004291
19 4636.563535716248
20 4626.259189633554
21 4617.111425909055
22 4610.57940102853
23 4603.318778138943
24 4597.059676958311
25 4583.3867880287535
26 4556.461538684025
27 4535.145956493358
28 4515.213234998723
29 4507.664482163932
30 4501.88213341614 85
31 4493.150038040447
32 4485.018682937186
33 4483.758790338398
34 4482.043356466265
35 4481.214471505814
36 4477.606210136337
37 4473.248189299113
38 4468.70442896231
39 4464.621173376911
40 4465.149464954706
41 4464.198399302558
42 4461.82034856042
43 4458.399683338752
44 4454.243403004877
45 4448.786342911962 5
46 4440.506145910534 5
47 4474.7765287477
48 4509.382408001925 5
49 4500.654358117967
50 4415.219298890738
51 4181.966261161206
52 3618.361950777308 3
53 3137.983622955891
54 2920.362576662766
55 2580.980380965593
56 2361.516637246407 8
57 2232.856223857186
58 2160.365885034035
59 2114.192257471150 7
60 2145.218639603678
61 1989.315244271989 7
62 1691.312589368928
63 1471.957257020533 7
64 1201.577045009846 2
65 896.4677704433668
66 677.0181932650004
67 526.0622426812017
68 404.4774702621478
69 296.8042270438883
70 219.5468547719657
71 137.6248826817354 4
72 171.941690701118 26
73 85.26616729643195
74 59.18227100196 48
75 58.87238063137874
76 41.08837139152062
77 25.267773714645195
78 18.580996319816997
79 6.015477185093 4

Figure E.24 Numerical modeling results for the ridge (5.5 m height, 31 m width, and 56 m length) SMP with 2022 weather function

Pile Number 25

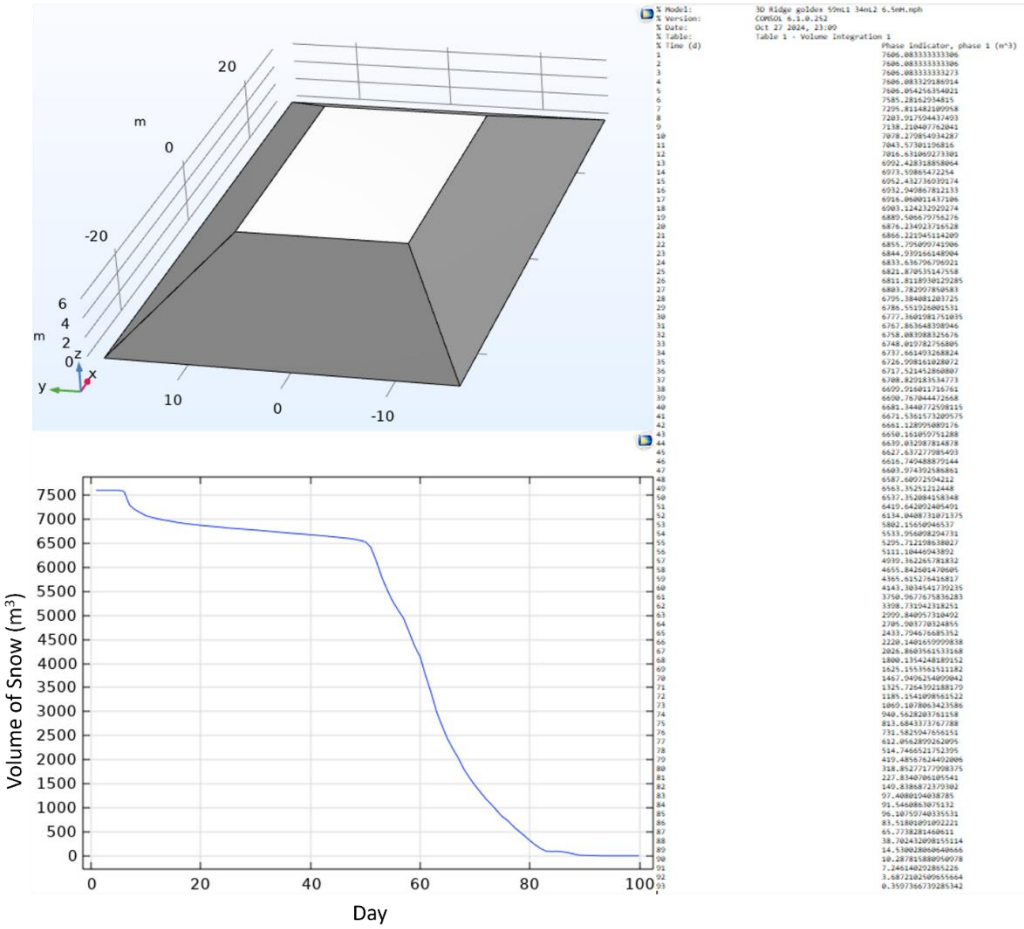

Figure E.25 Numerical modeling results for the ridge (6.5 m height, 34 m width, and 59 m length) SMP with 2022 weather function

Pile Number 26

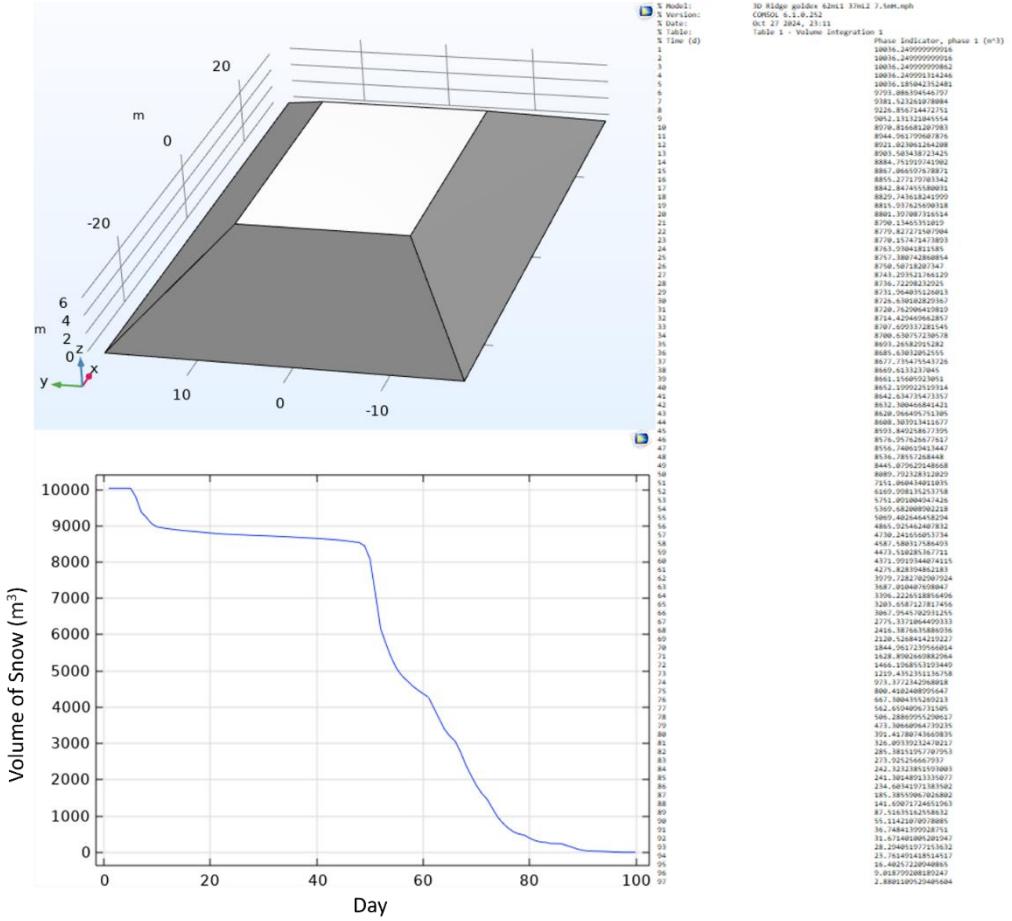

Figure E.26 Numerical modeling results for the ridge (7.5 m height, 37 m width, and 62 m length) SMP with 2022 weather function

Pile Number 27

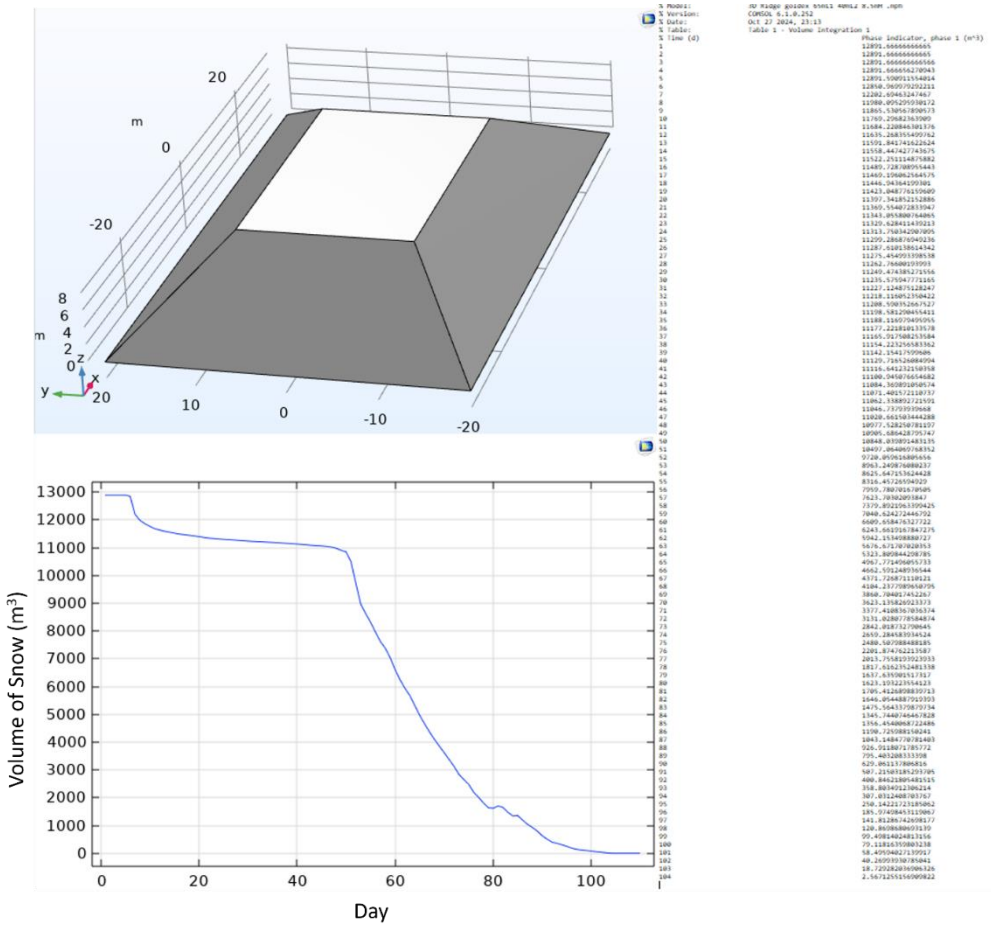

Figure E.27 Numerical modeling results for the ridge (8.5 m height, 40 m width, and 65 m length) SMP with 2022 weather function

Pile Number 28

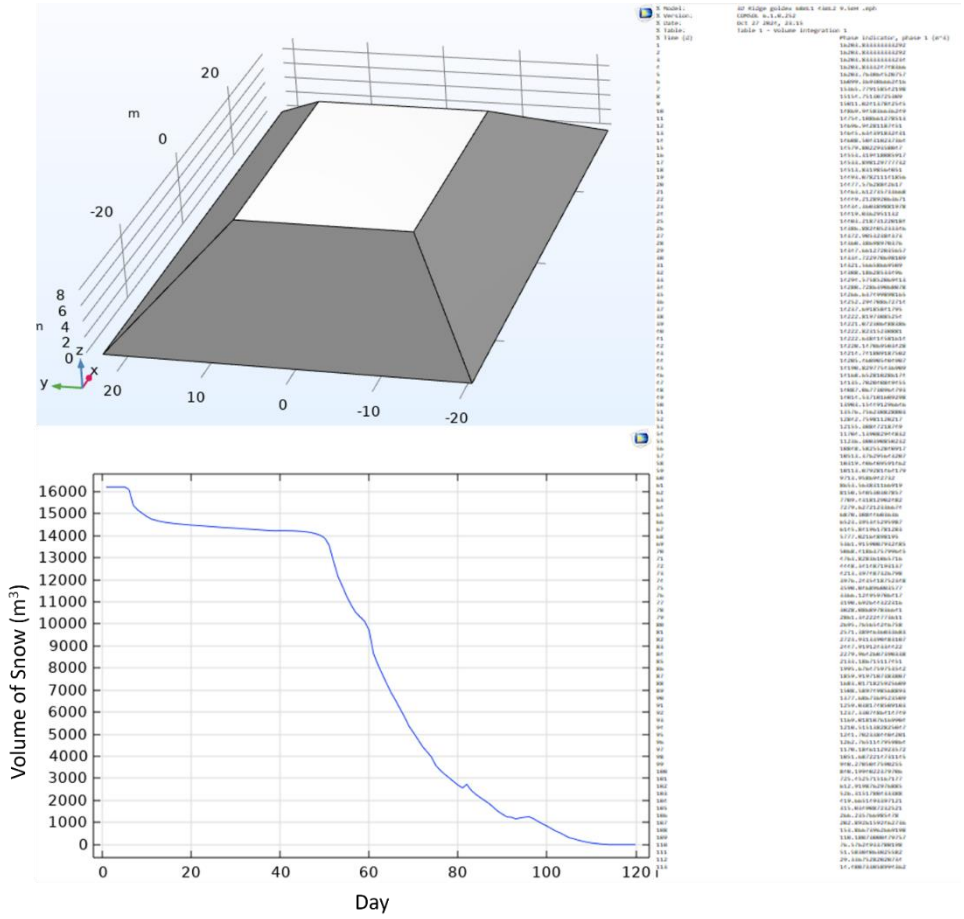

Figure E.28 Numerical modeling results for the ridge (9.5 m height, 43 m width, and 68 m length) SMP with 2022 weather function

Pile Number 29

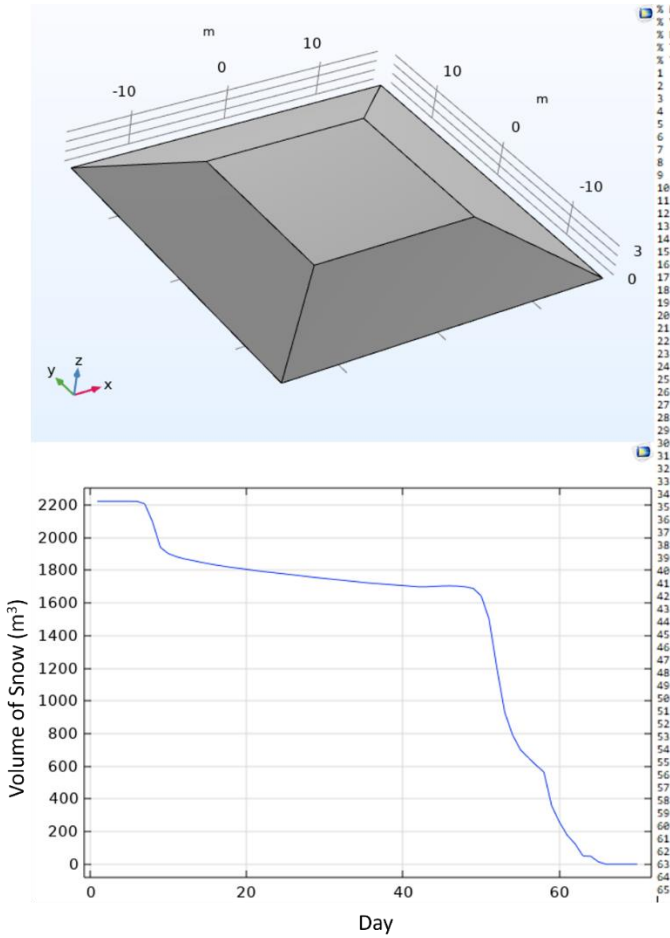


```
% Model:                 3D cubic goldex - Main.mph
% Version:               COMSOL 6.1.0.252
% Date:                  Oct 21 2024, 17:22
% Table:                 Table 1 - Volume Integration 1
% Time (d)               Phase indicator, phase 1 (m^3)
1                        2223.3749999999986
2                        2223.3749999999986
3                        2223.3749999999814
4                        2223.3749979953535
5                        2223.3677844872686
6                        2222.7773683057885
7                        2207.9520571063513
8                        2097.3697769835967
9                        1941.3435985678548
10                       1903.1118234479131
11                       1884.7703626383754
12                       1871.2739578669823
13                       1861.5089393712458
14                       1851.3299169187276
15                       1841.9764424454493
16                       1833.6648036317388
17                       1826.2050948990625
18                       1818.6853830120062
19                       1812.535253116368
20                       1806.2808672948804
21                       1799.8412657885171
22                       1793.5575188743476
23                       1788.410770258555
24                       1783.1372478557164
25                       1777.737168565363
26                       1772.2108692750812
27                       1766.558834781581
28                       1760.7817240068591
29                       1755.2636416296866
30                       1750.5052167790318
31                       1745.6713321457516
32                       1740.762127372057
33                       1735.7777992274298
34                       1730.7186092120266
35                       1725.5848905082923
36                       1721.1209820462377
37                       1717.664744797l9
38                       1714.1504204244711
39                       1710.5754171399955
40                       1706.9366388903777
41                       1703.2303672018572
42                       1699.4521185330893
43                       1699.2980585315l71
44                       1702.2155215214439
45                       1704.2871476380374
46                       1705.0562186851087
47                       1703.760409363432
48                       1699.1296363917513
49                       1688.8785872905337
50                       1643.7511012067164
51                       1501.837744257l57
52                       1202.4687383380724
53                       931.7192671161796
54                       792.815303093636
55                       702.069934592708
56                       653.3587320409864
57                       607.2634374552251
58                       565.7448080998867
59                       358.6088795641l41
60                       257.5824225410563
61                       177.4256437786968
62                       124.4049813548252
63                       50.677947374217l4
64                       48.401492297276754
65                       14.348153146747203
```

Figure E.29 Numerical modeling results for the cubic (3.5 m height, 33 m width, and 33 m length) SMP with 2022 weather function

Pile Number 30

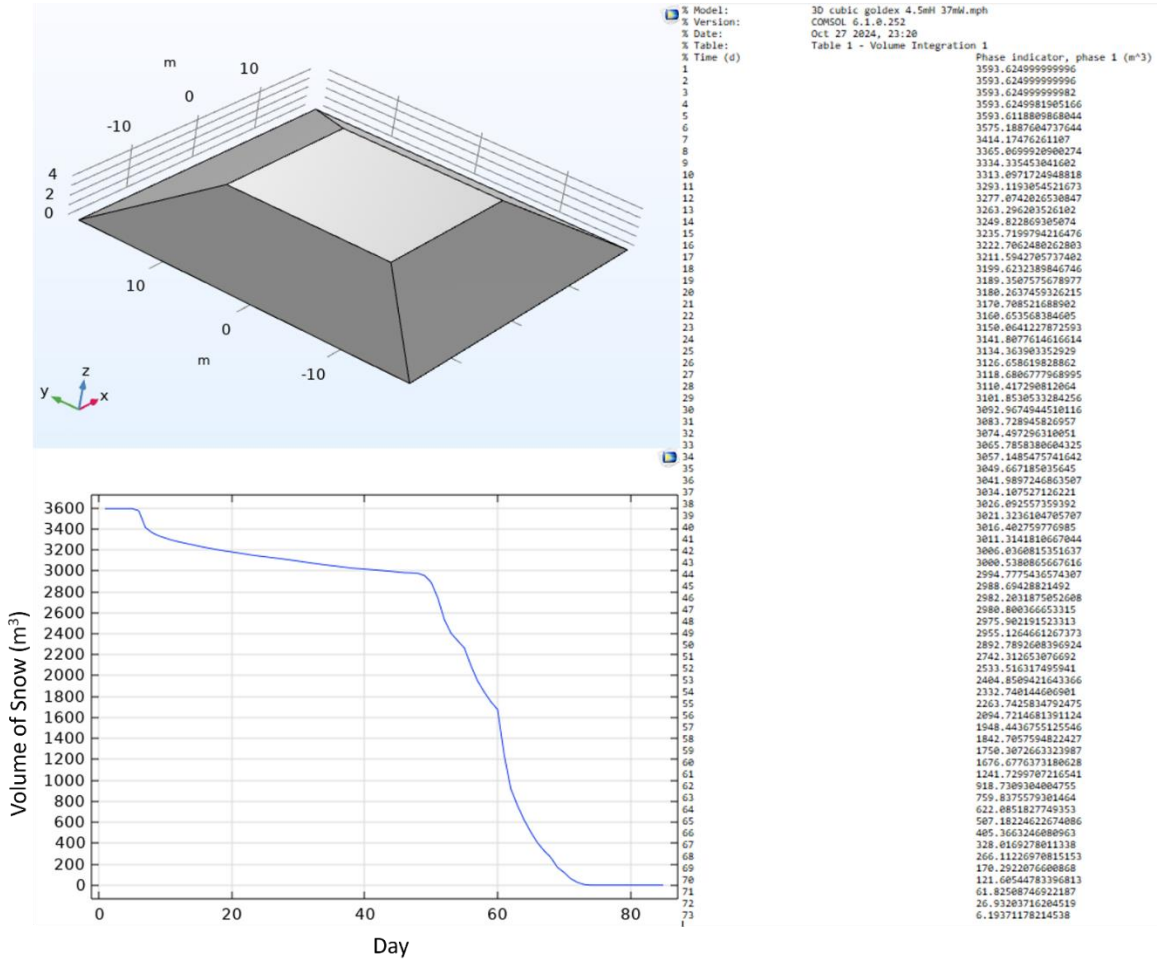

% Model:	3D cubic goldex 4.5mH 37mW.mph
% Version:	COMSOL 6.1.0.252
% Date:	Oct 27 2024, 23:20
% Table:	Table 1 - Volume Integration 1
% Time (d)	Phase indicator, phase 1 (m^3)
1	3593.624999999996
2	3593.624999999996
3	3593.624999999982
4	3593.624998196516
5	3593.611880986804
6	3575.18876047376
7	3414.17476261107
8	3365.0699920900274
9	3334.335453041602
10	3313.0971724948818
11	3293.1193054521673
12	3277.0742026530847
13	3263.296203526102
14	3249.822869305074
15	3235.7199794216476
16	3222.7062480262803
17	3211.594270573748
18	3199.6232389846746
19	3189.3507575678977
20	3180.2637459326215
21	3170.708521688902
22	3160.653568384605
23	3150.0641227872593
24	3141.8077614616614
25	3134.363903352929
26	3126.658619828862
27	3118.6806777968995
28	3110.417290812064
29	3101.8530533284256
30	3092.9674944510116
31	3083.728945826957
32	3074.497296310051
33	3065.7858380604325
34	3057.1485475741642
35	3049.667185035645
36	3041.9897246863587
37	3034.107527126221
38	3026.092557359392
39	3021.3236104705707
40	3016.402759776985
41	3011.3141810667044
42	3006.0360815351637
43	3000.5380865667616
44	2994.7775436574307
45	2988.69428821492
46	2982.2031875052608
47	2980.800366653315
48	2975.9021915233113
49	2955.1264661267373
50	2892.7892608396924
51	2742.312653076692
52	2533.5163174955941
53	2404.8509421643366
54	2332.7401446086901
55	2263.7425834792475
56	2094.7214681391124
57	1948.4436755125546
58	1842.7057594822427
59	1750.3072663323987
60	1676.6776373180628
61	1241.7299707216541
62	918.7309304004755
63	759.8375579301464
64	622.0851827749353
65	507.18224622674086
66	405.3663246080963
67	328.0169278011338
68	266.11226970815153
69	170.2922076600868
70	121.60544783396813
71	61.82508746922187
72	26.932037162045 19
73	6.193711782145 38

Figure E.30 Numerical modeling results for the cubic (4.5 m height, 37 m width, and 37 m length) SMP with 2022 weather function

Pile Number 31

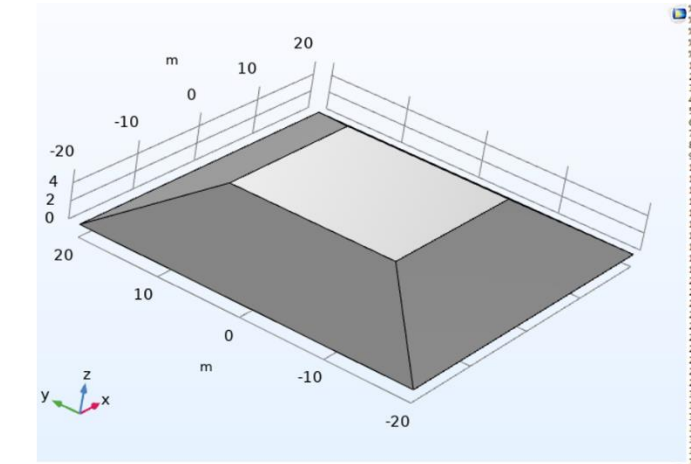

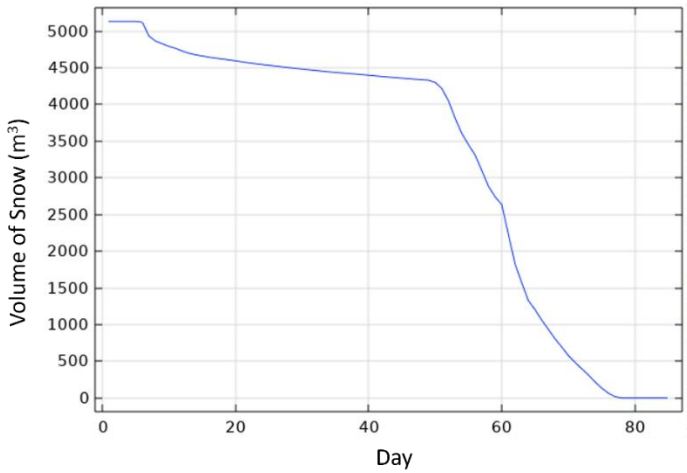


```
% Model:
% Version:
% Date:
% Table:
% Time (d)
3D cubic goldex 5.5mH 40mW.mph
COMSOL 6.1.0.252
Oct 27 2024, 23:22
Table 1 - Volume Integration 1
Phase indicator, phase 1 (m^3)
5133.333333333317
5133.333333333317
5133.333333333297
5133.333330918186
5133.316699820783
5121.912080966519
4932.90591963359
4864.728882151737
4828.129186989518
4793.585786978629
4765.547708791657
4729.931940367865 5
4699.766573157227
4678.354090315999
4662.6729983414625
4645.596897444984
4632.581223294382
4620.853471187722
4608.533232189744
4595.4694259988455
4581.568340121063
4568.430579102655
4556.248079986257
4544.815536917668
4534.90273326791
4524.62041548426
4513.955628731127
4503.16697482732
4493.113627325591
4482.938465643139
4474.002814057905
4464.841747780817
4455.450001700935
4445.822047907411
4438.341880674172
4430.8909319083
4423.261992158878
4415.464716503026
4407.499248801807
4399.361168086381
4391.043701092869
4382.537529204887 5
4374.631226617682
4367.177426022541
4359.550271879564
4352.301420837905
4344.813817614226 5
4338.034729717358
4331.546665145272 5
4301.760942745331
4218.579940984611
4049.9976556181
3813.925704033257 3
3605.794724584035
3453.008499681636 7
3312.089213166823
3102.797130985925 4
2887.357641729056
2743.139141133253
2636.672546069891
2231.323694696685 4
1827.478838115605 4
1571.901519536568 2
1327.547146649339 8
1205.112787851039 7
1064.162040283078 8
935.7531741539697
808.4822905901 02
696.987353856271 4
580.4012265774389
485.9390969928214
400.5327186400702
316.0849542578355 3
219.838475404815 3
136.230813994957 94
67.230687396596 32
18.530188186641 098
```


Figure E.31 Numerical modeling results for the cubic (5.5 m height, 40 m width, and 40 m length) SMP with 2022 weather function

Pile Number 32

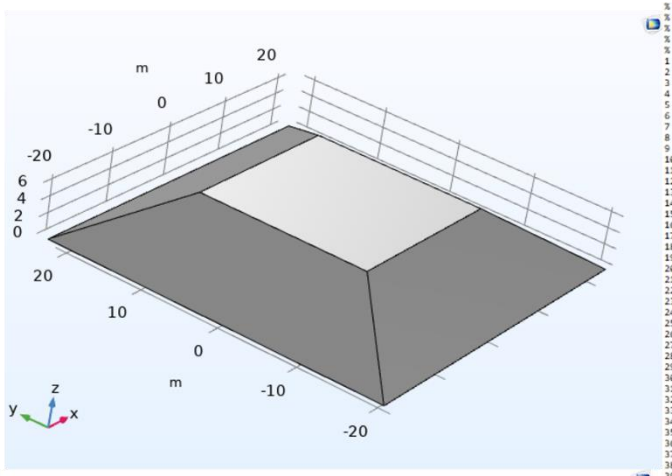

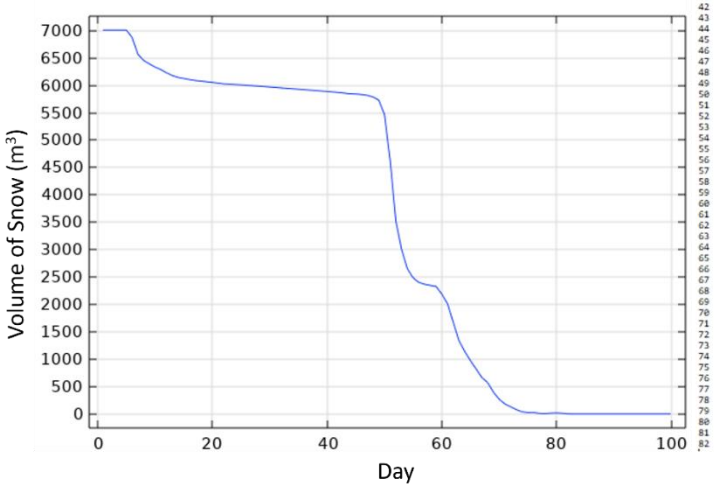


```
% Model:                 3D cubic goldex 6.5mH 43mW .mph
% Version:               COMSOL 6.1.0.252
% Date:                  Oct 27 2024, 23:24
% Table:                 Table 1 - Volume Integration 1
% Time (d)               Phase indicator, phase 1 (m^3)
1                        7010.791666666655
2                        7010.791666666655
3                        7010.791666666599
4                        7010.791659517812
5                        7010.740767541642
6                        6875.023056231683
7                        6570.9325272774795
8                        6457.44011064329
9                        6393.157004998496
10                       6335.8684216336327
11                       6289.360791799686
12                       6230.987547231222
13                       6180.7157217762
14                       6147.4718108815205
15                       6127.917316457102
16                       6107.032878380802
17                       6090.129842445797
18                       6078.874174088549
19                       6067.138121113001
20                       6054.896991682022
21                       6042.123513050614
22                       6028.863624043552
23                       6022.448406292378
24                       6015.81516813302
25                       6008.96117660496
26                       6001.883284329154
27                       5994.577885061933
28                       5987.040806725648
29                       5979.267087726133S
30                       5971.250533333683
31                       5962.982846071279
32                       5954.552072683173
33                       5946.748986163315
34                       5938.841269436312
35                       5930.826494577543
36                       5922.702016554957
37                       5914.464953709603
38                       5906.112165655231
39                       5897.648228400586
40                       5889.045406485751
41                       5880.323621913937
42                       5871.061753196162S
43                       5859.745111368342
44                       5847.480251011647
45                       5842.457773177523
46                       5835.39689238503
47                       5819.479802008478
48                       5788.970682242014
49                       5733.732094323361
50                       5472.043923665326S
51                       4624.189931842067
52                       3516.475668033379S
53                       2999.987295793288
54                       2653.616664035991G
55                       2484.419489889189
56                       2404.297664593241S
57                       2369.278010348507S
58                       2348.032525558779
59                       2329.306532007010S
60                       2189.949085214017
61                       2012.806176517305
62                       1673.835156949361S
63                       1337.306400948644G
64                       1141.885764047935S
65                       972.8744475099065
66                       819.4565017361263
67                       663.9903160801l2
68                       574.315614404
69                       399.80876542593364
70                       269.134393997417l6
71                       183.1208593774562
72                       112.326012902130S
73                       79.24451835578095
74                       39.38204209171331
75                       25.328939353615294
76                       27.467901755408874
77                       9.294631252371342
78                       4.596928190293275
79                       14.008614661732906
80                       17.921585974194855
81                       12.303715562712853
82                       1.1298178208292153
```

Figure E.32 Numerical modeling results for the cubic (6.5 m height, 43 m width, and 43 m length) SMP with 2022 weather function

Pile Number 33

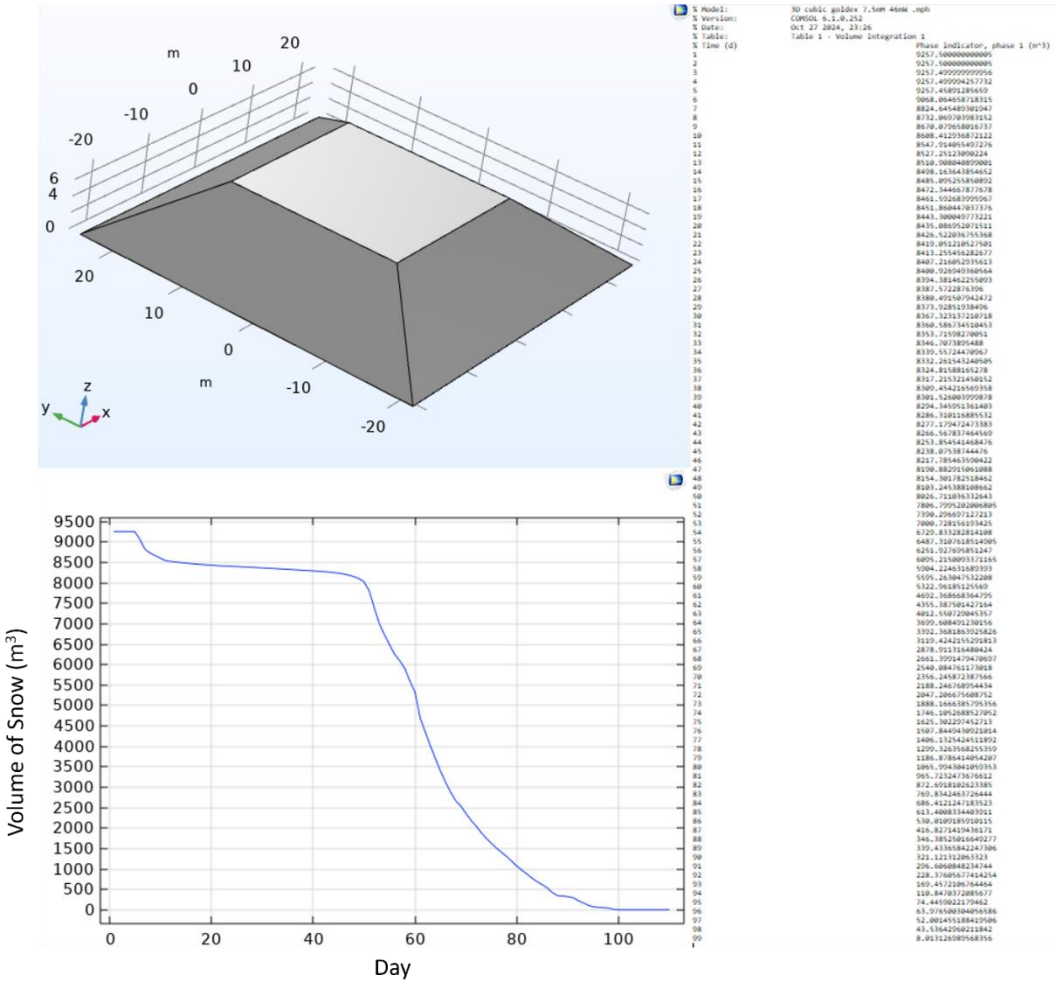

Figure E.33 Numerical modeling results for the cubic (7.5 m height, 46 m width, and 46 m length) SMP with 2022 weather function

Pile Number 34

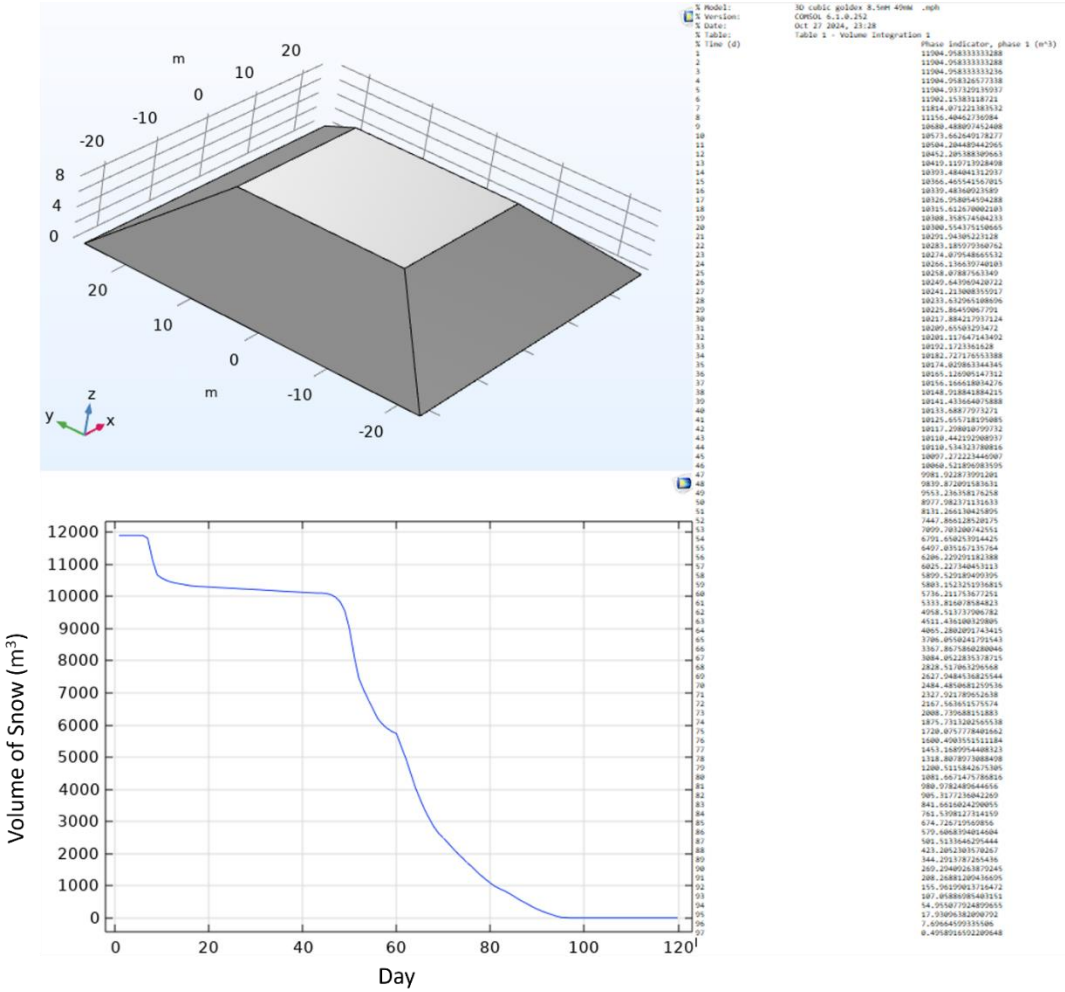

Figure E.34 Numerical modeling results for the cubic (8.5 m height, 49 m width, and 49 m length) SMP with 2022 weather function

Pile Number 35

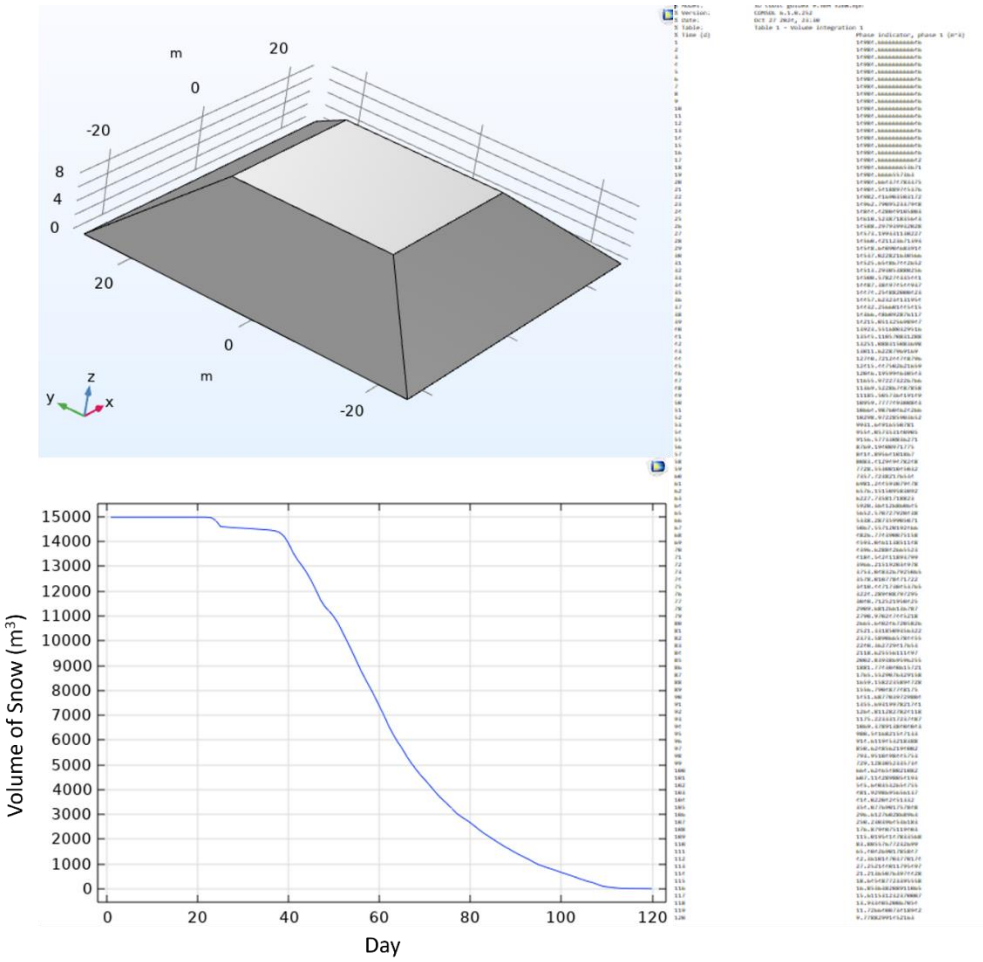

Figure E.35 Numerical modeling results for the cubic (9.5 m height, 52 m width, and 52 m length) SMP with 2022 weather function

Pile Number 36

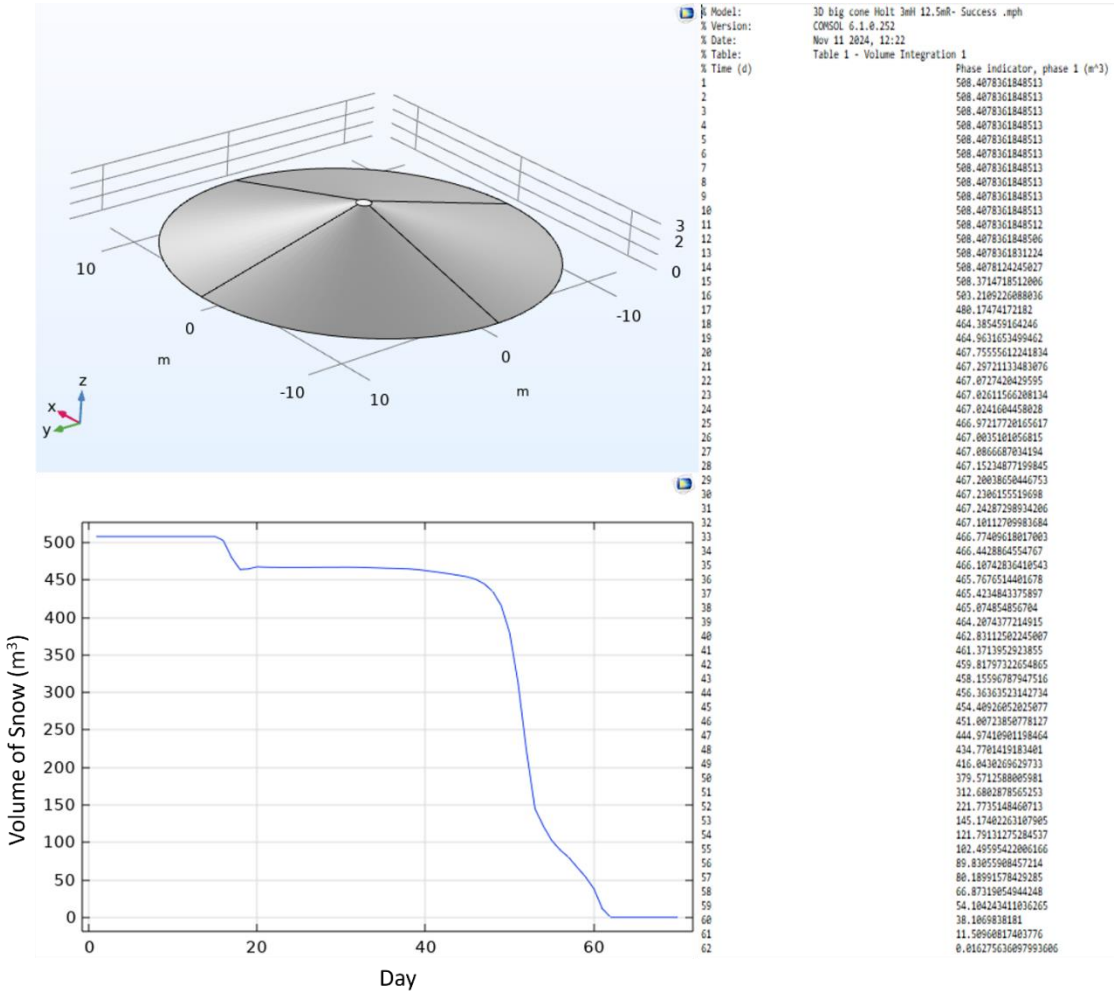

% Model:	3D big cone Holt 3mH 12.5mR- Success .mph
% Version:	COMSOL 6.1.0.252
% Date:	Nov 11 2024, 12:22
% Table:	Table 1 - Volume Integration 1
% Time (d)	Phase indicator, phase 1 (m^3)
1	508.4078361848513
2	508.4078361848513
3	508.4078361848513
4	508.4078361848513
5	508.4078361848513
6	508.4078361848513
7	508.4078361848513
8	508.4078361848513
9	508.4078361848513
10	508.4078361848513
11	508.4078361848512
12	508.4078361848506
13	508.4078361831224
14	508.4078124245027
15	508.3714718512006
16	503.2109226088036
17	480.17474172182
18	464.385459164246
19	464.96316534994462
20	467.755556122418 34
21	467.29721133483076
22	467.07274204295 95
23	467.026115662081 34
24	467.02416044580 28
25	466.97217720165617
26	467.00351010568 15
27	467.08666870341 94
28	467.15234877199845
29	467.20038650446753
30	467.2306155519698
31	467.24287298934206
32	467.10112709983684
33	466.77409618017003
34	466.44288645547 67
35	466.10742836410543
36	465.7676514401678
37	465.4234843375897
38	465.0748548567 04
39	464.2074377214915
40	462.83112502245007
41	461.3713952923855
42	459.81797322654865
43	458.15596787947516
44	456.36363523142734
45	454.40926052025077
46	451.00723850778127
47	444.97410901198464
48	434.7701419183481
49	416.0430269629733
50	379.5712588005981
51	312.6802878565253
52	221.7735148460713
53	145.17402263107905
54	121.79131275284537
55	102.49595422086166
56	89.83055908457214
57	80.18991578429285
58	66.87319054944248
59	54.104243411036265
60	38.1069838181
61	11.50960817403776
62	0.016275636097993686

Figure E.36 Numerical modeling results for the cone (3 m height, and 12.5 m radius) SMP with 2022 weather function

Pile Number 37

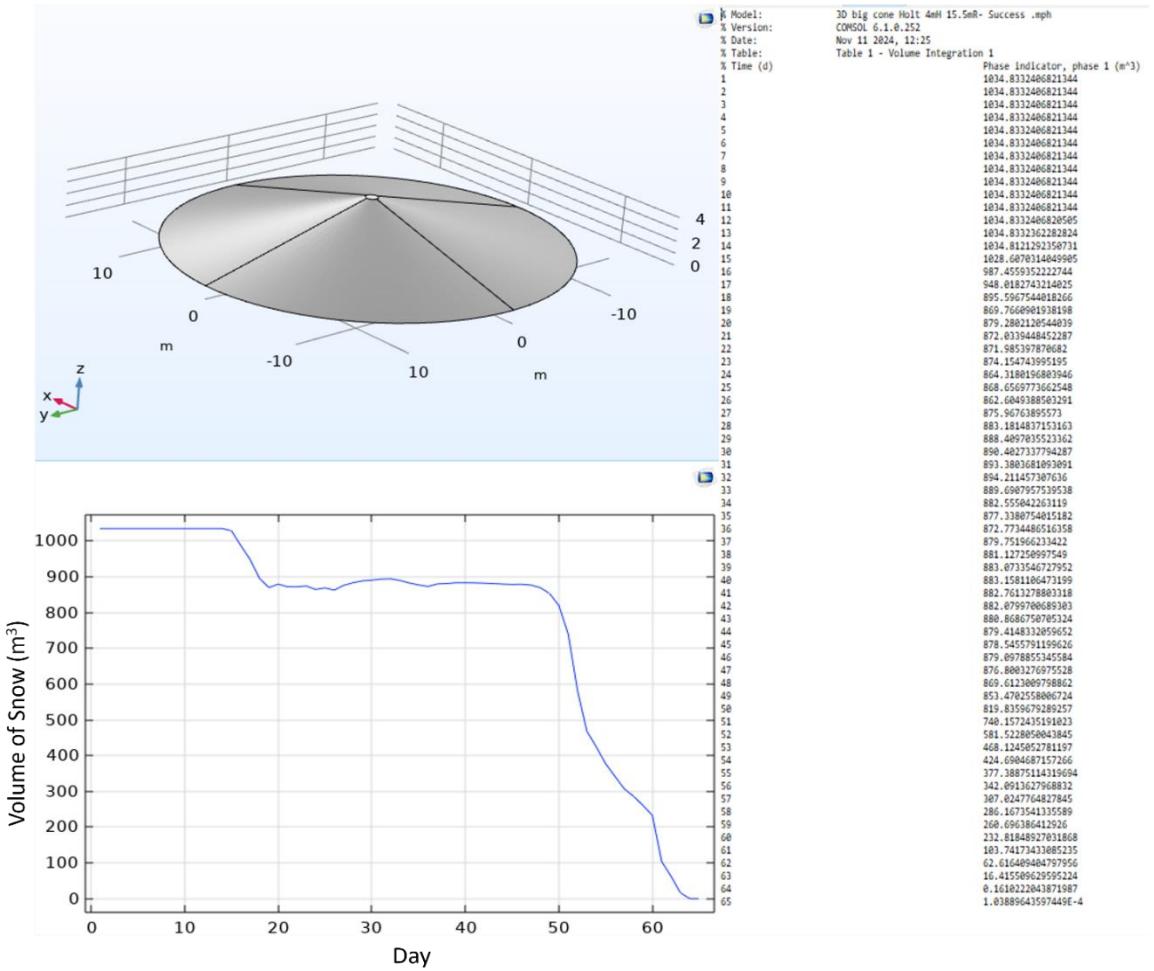

% Model: 3D big cone Holt 4mH 15.5mR- Success .mph
% Version: COMSOL 6.1.0.252
% Date: Nov 11 2024, 12:25
% Table: Table 1 - Volume Integration 1

% Time (d)	Phase indicator, phase 1 (m^3)
1	1034.8332406821344
2	1034.8332406821344
3	1034.8332406821344
4	1034.8332406821344
5	1034.8332406821344
6	1034.8332406821344
7	1034.8332406821344
8	1034.8332406821344
9	1034.8332406821344
10	1034.8332406821344
11	1034.8332406821344
12	1034.8332406820505
13	1034.8332362282824
14	1034.8121292350731
15	1028.6070314049905
16	987.4559352222744
17	948.0182743214025
18	895.5967544018266
19	869.7660901938198
20	879.2802120544039
21	872.0339448452287
22	871.9853978706482
23	874.154743995195
24	864.3180196803946
25	868.6569773662548
26	862.6049388503291
27	875.96763895573
28	883.1814837153163
29	888.4097035523362
30	890.4027337794287
31	893.3803681093091
32	894.211457307636
33	889.6907957539538
34	882.555042263119
35	877.3380754015182
36	872.7734486516358
37	879.751966233422
38	881.127250997549
39	883.0733546727952
40	883.1581106473199
41	882.7613278803318
42	882.0799700689303
43	880.868675705324
44	879.4148332059652
45	878.5455791199626
46	879.0978855345584
47	876.8003276975528
48	869.6123009798862
49	853.4702558006724
50	819.8359679289257
51	748.1572435191023
52	581.5228050043845
53	468.1245052781197
54	424.6904687157266
55	377.38875114319694
56	342.0913627968832
57	307.0247764827845
58	286.16735411335589
59	268.6963864412926
60	232.81848927031868
61	103.74173433085235
62	62.616409404797956
63	16.415509629595224
64	0.16102220437871987
65	1.0388964359744 9E-4

Figure E.37 Numerical modeling results for the cone (4 m height, and 15.5 m radius) SMP with 2022 weather function

Pile Number 38

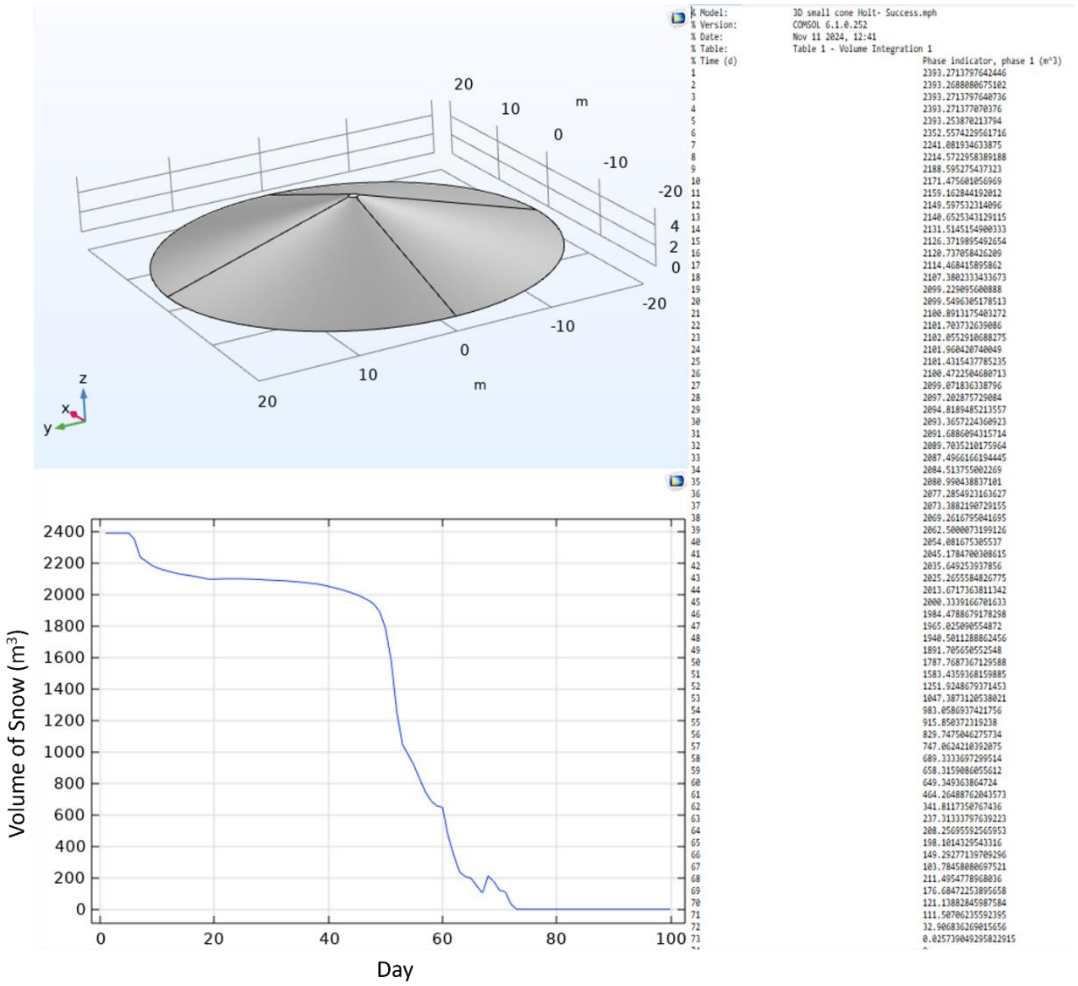

% Model: 3D small cone Holt- Success.mph
% Version: COMSOL 6.1.0.252
% Date: Nov 11 2024, 12:41
% Table: Table 1 - Volume Integration 1

% Time (d)	Phase indicator, phase 1 (m³)
1	2393.271379764244
2	2393.2688080675102
3	2393.271379764073
4	2393.271377070376
5	2393.253870213794
6	2352.5574229561716
7	2241.0819346338 75
8	2214.5722958389188
9	2188.595275437323
10	2171.4756010956969
11	2159.162844192012
12	2149.597532314096
13	2140.6525343129115
14	2131.5145154900333
15	2126.3719895492654
16	2120.737058426209
17	2114.4684158958 62
18	2107.3802333433673
19	2099.229095600888
20	2099.5496305178513
21	2100.8913175403272
22	2101.703732639086
23	2102.0552910688275
24	2101.960420740049
25	2101.4315437785235
26	2100.4722504680713
27	2099.071836338796
28	2097.202875729084
29	2094.8189485213557
30	2093.3657224360923
31	2091.6886094315714
32	2089.7035218175964
33	2087.4966166194445
34	2084.513755002269
35	2080.990438837101
36	2077.2854923163627
37	2073.3882190729155
38	2069.2616795041695
39	2062.5000071599126
40	2054.081675305537
41	2045.1784700308615
42	2035.6492539378 56
43	2025.2655584826775
44	2013.6717363811342
45	2000.3339166701633
46	1984.4788679178298
47	1965.025090554872
48	1940.5011288862456
49	1891.705650552548
50	1787.7687367129588
51	1583.4359368159885
52	1251.9248679371453
53	1047.3871128538021
54	983.0586937421756
55	915.858372319238
56	829.7475046275734
57	747.0624210392075
58	689.3333697299514
59	658.3159086055612
60	649.3493638 64724
61	464.2648876204 3573
62	341.8117350767436
63	237.3133379763922 3
64	208.2569559256595 3
65	198.1014329543316
66	149.2927713970929 6
67	103.7845808869752 1
68	211.4954778968036
69	176.6847225389565 8
70	121.1388284598758 4
71	111.5070623559239 5
72	32.906836269015656
73	0.025739049295822915

Figure E.38 Numerical modeling results for the cone (5.6 m height, and 20 m radius) SMP with 2022 weather function

Pile Number 39

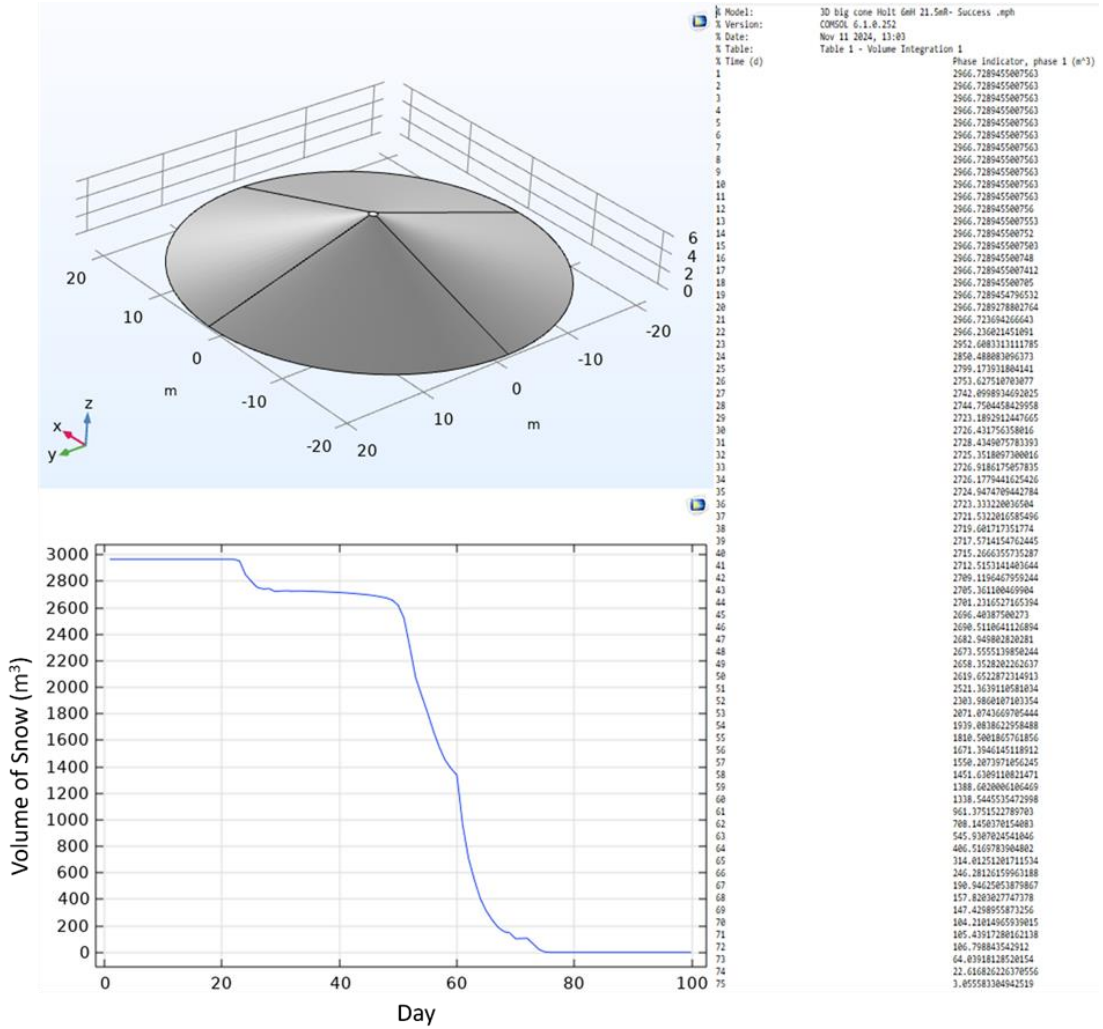

% Model: 3D big cone Holt GmH 21.5mR- Success .mph
% Version: COMSOL 6.1.0.252
% Date: Nov 11 2024, 13:03
% Table: Table 1 - Volume Integration 1

% Time (d)	Phase indicator, phase 1 (m^3)
1	2966.7289455007563
2	2966.7289455007563
3	2966.7289455007563
4	2966.7289455007563
5	2966.7289455007563
6	2966.7289455007563
7	2966.7289455007563
8	2966.7289455007563
9	2966.7289455007563
10	2966.7289455007563
11	2966.7289455007563
12	2966.7289455007556
13	2966.7289455007553
14	2966.7289455007552
15	2966.7289455007503
16	2966.7289455007748
17	2966.7289455007412
18	2966.7289455007705
19	2966.7289454796532
20	2966.7289278802764
21	2966.723694266643
22	2966.2360214510911
23	2952.6083313111785
24	2850.4880834961373
25	2799.173931804141
26	2753.627510703077
27	2742.0998934692025
28	2744.7504458429958
29	2723.1892912447665
30	2726.431756358016
31	2728.4349075783393
32	2725.3518057300016
33	2726.9186175057835
34	2726.1779441625426
35	2724.9474709442784
36	2723.333220036504
37	2721.5322016585496
38	2719.601717351774
39	2717.5714154762445
40	2715.2666355735287
41	2712.5153144403644
42	2709.1196467959244
43	2705.361100469904
44	2701.2316527165394
45	2696.40387500273
46	2690.5110641126894
47	2682.9498028202814
48	2673.5555139850244
49	2658.3528202262637
50	2619.6522872314913
51	2521.3639110581034
52	2303.9860107103354
53	2071.0743669705444
54	1939.0838622958488
55	1810.5001865761856
56	1671.3946145118912
57	1550.2073971056245
58	1451.6309110821471
59	1388.6020006106469
60	1338.5445535472998
61	961.3751522789703
62	708.1450370154083
63	545.9307024541046
64	406.5169783904802
65	314.81251201711534
66	246.28126159963188
67	190.94625053879867
68	157.8203027747378
69	147.4298955873256
70	104.21014965539015
71	105.43917280162138
72	106.798843542912
73	64.03918128520154
74	22.616826226370556
75	3.055583304942519

Figure E.39 Numerical modeling results for the cone (6 m height, and 21.5 m radius) SMP with 2022 weather function

Pile Number 40

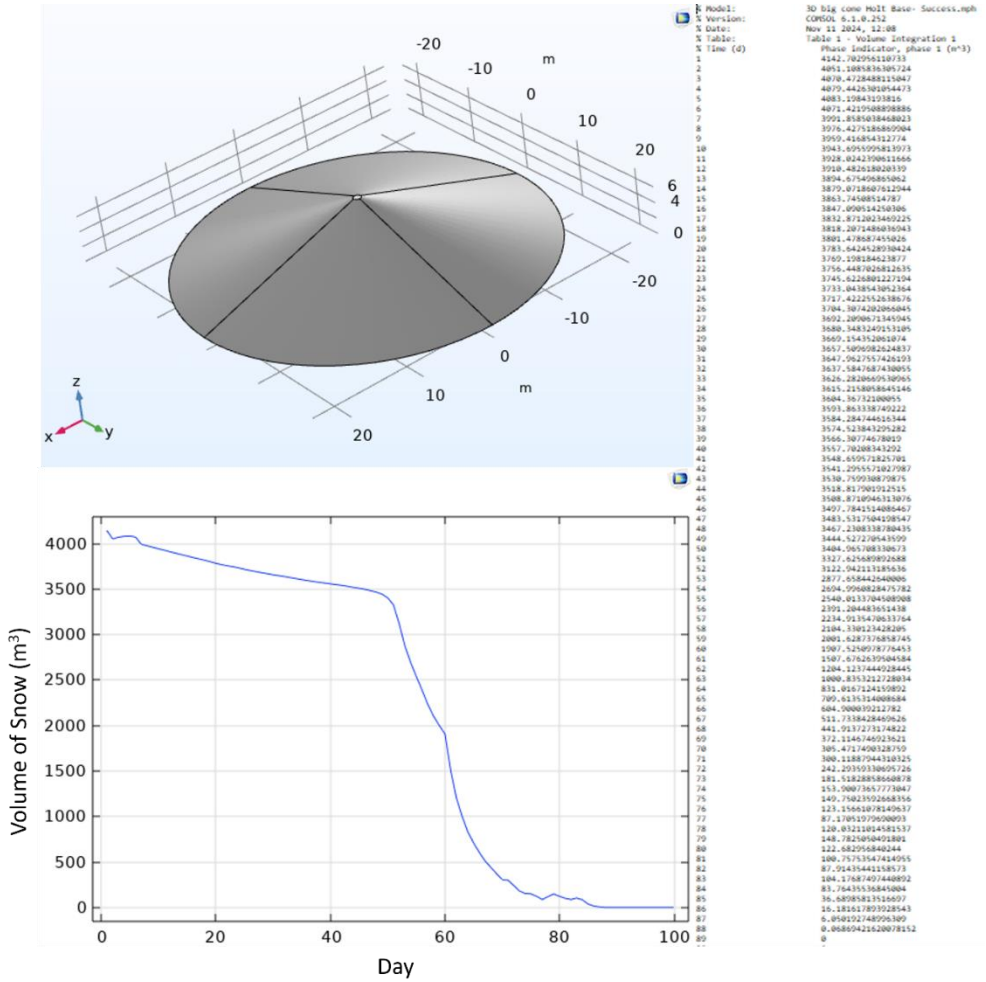

Figure E.40 Numerical modeling results for the cone (7.33 m height, and 23 m radius) SMP with 2022 weather function

Pile Number 41

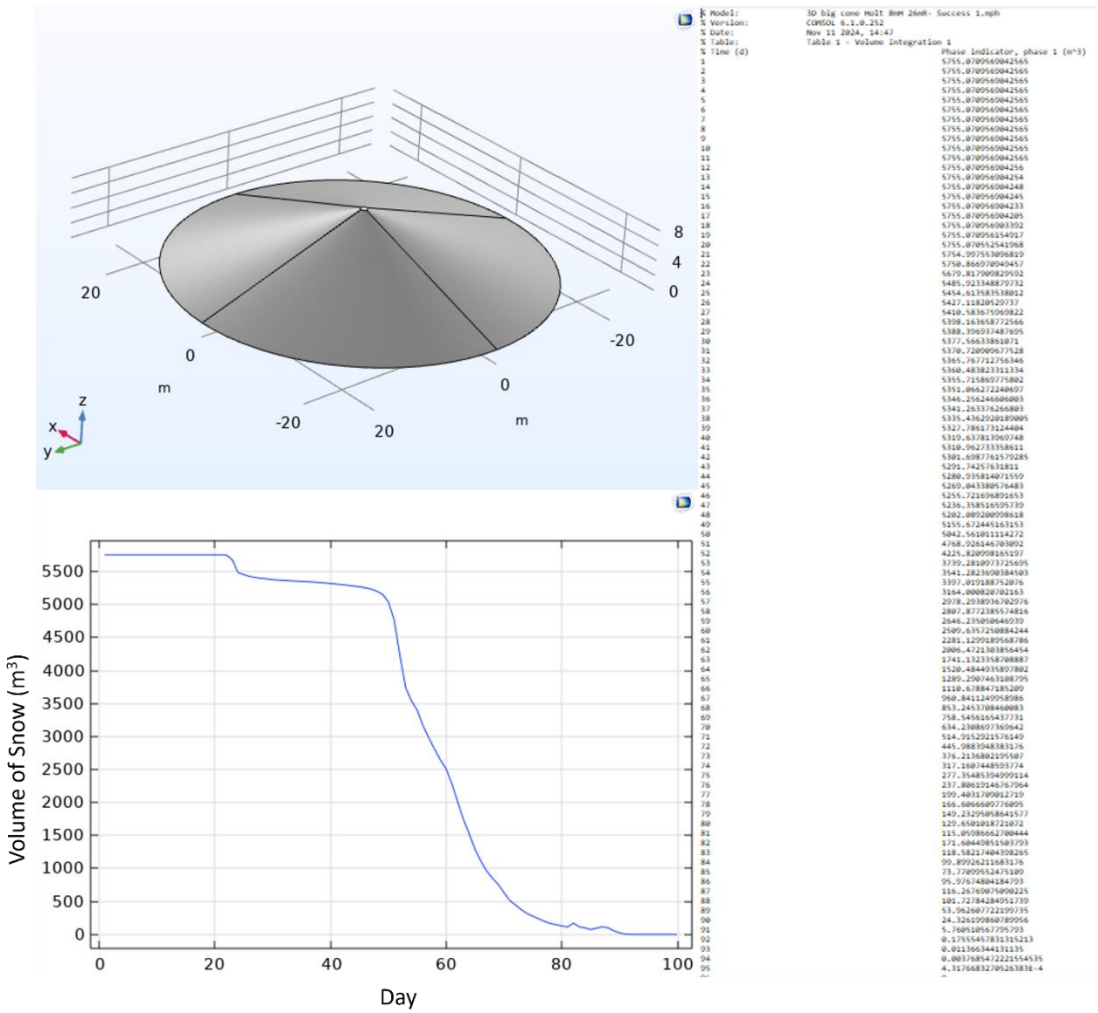

Figure E.41 Numerical modeling results for the cone (8 m height, and 26 m radius) SMP with 2022 weather function

Pile Number 42

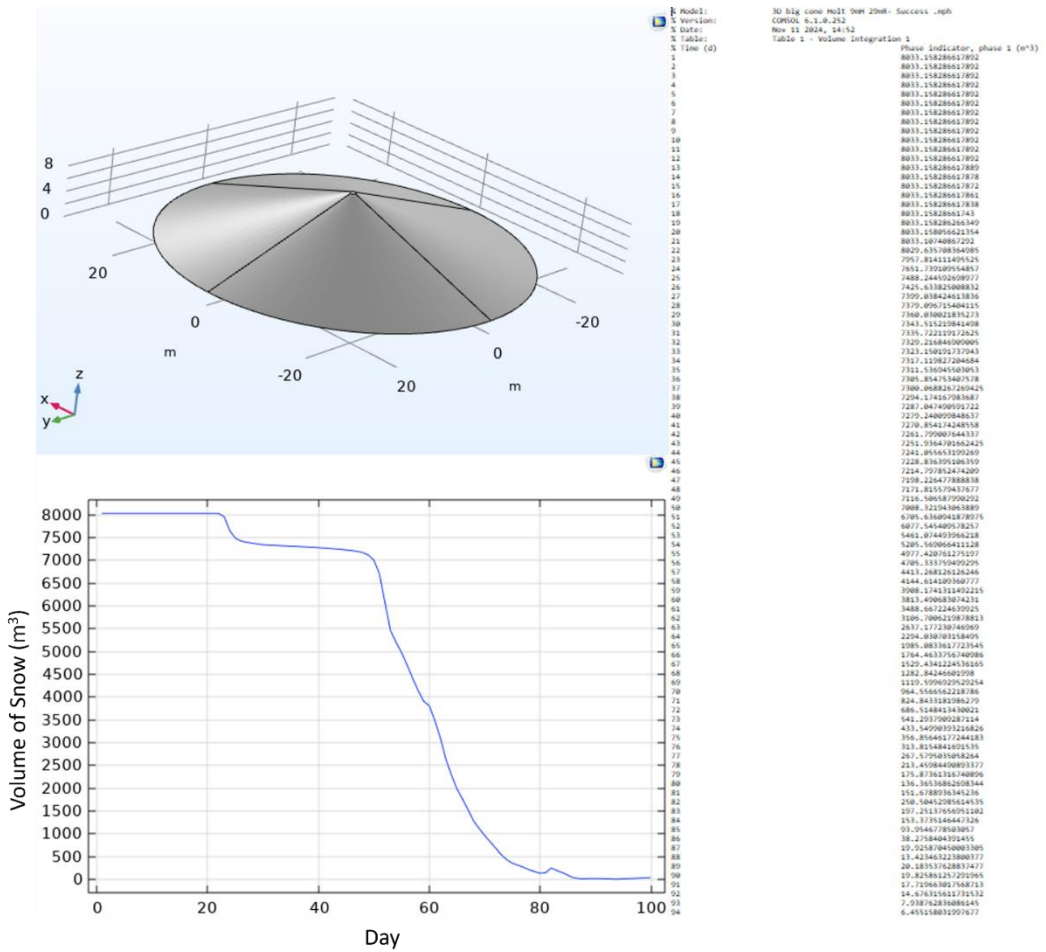

Figure E.42 Numerical modeling results for the cone (9 m height, and 29 m radius) SMP with 2022 weather function

Pile Number 43

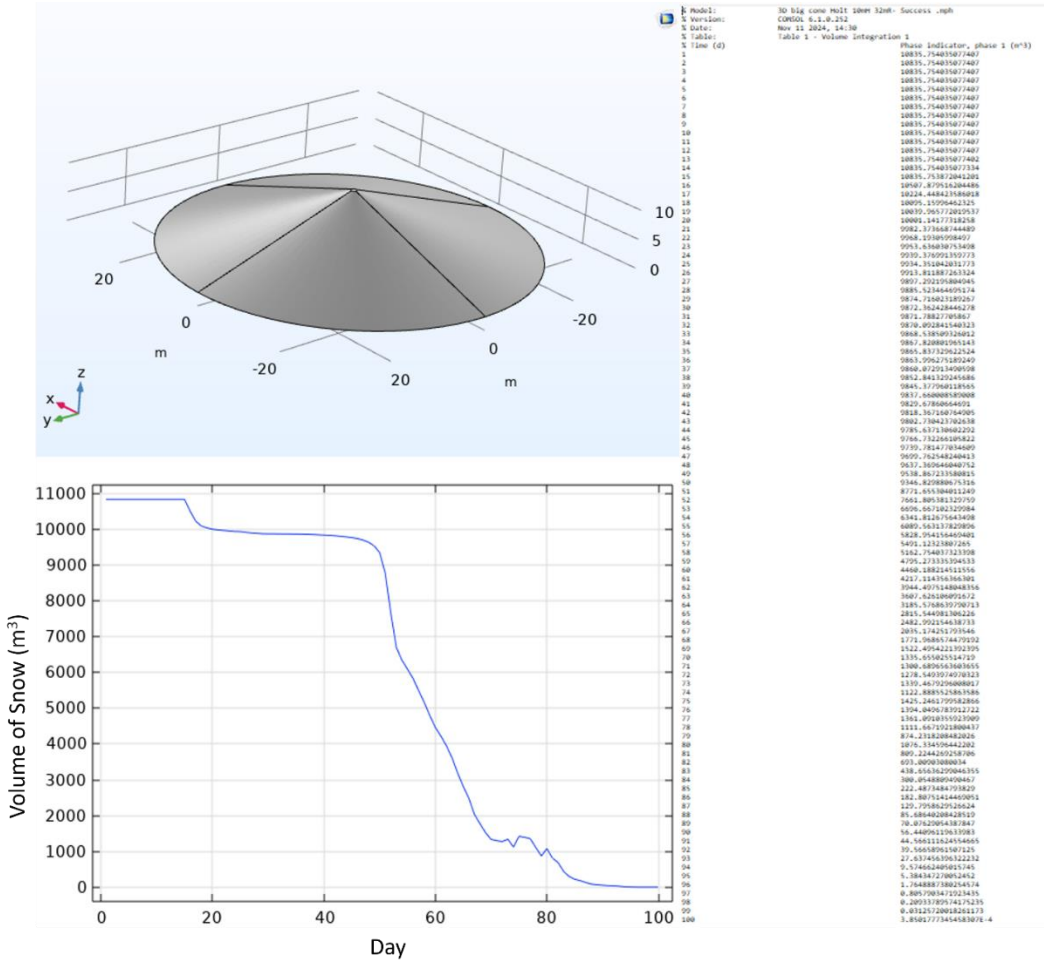

Figure E.43 Numerical modeling results for the cone (10 m height, and 32 m radius) SMP with 2022 weather function

Pile Number 44

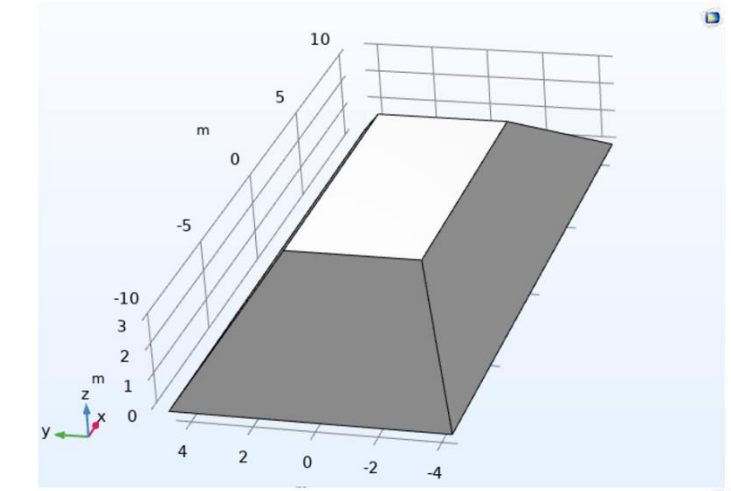

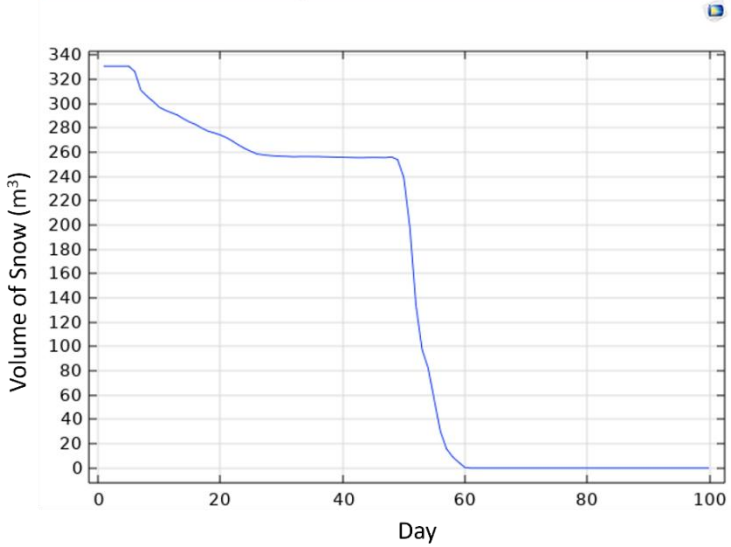

% Model:	3D Ridge Holt 21mL1 9mL2 3mH- Success .mph
% Version:	COMSOL 6.1.0.252
% Date:	Nov 11 2024, 15:02
% Table:	Table 1 - Volume Integration 1
% Time (d)	Phase indicator, phase 1 (m^3)
1	330.7499999999977
2	330.7499999999977
3	330.7499999999958
4	330.7499997175499
5	330.74806191334244
6	326.2758057620679
7	310.9881568356866
8	305.9203124466011
9	301.73052229663915
10	297.01146358044076
11	294.4519019850902
12	292.3922587171784
13	290.4472865253043
14	287.353057933211O6
15	284.676643904293G6
16	282.59227144137253
17	279.6471209809729
18	277.2030192033777
19	275.74384587590873
20	274.1445562619423
21	271.8649100292057
22	268.9695038617423
23	265.793797164O0485
24	262.92738375954116
25	260.6234210450277
26	258.4925233786849
27	257.7118807463977
28	257.190898717438З6
29	256.796118469785O3
30	256.5573638149899
31	256.40239623534546
32	256.1442773318485
33	256.29475997942234
34	256.3126687347627
35	256.27241572934355
36	256.240618105884
37	256.10714179832377
38	255.977419967530G4
39	255.82437621903134
40	255.68194386579717
41	255.5555925781183
42	255.4475208225044
43	255.35759079682902
44	255.47717468331615
45	255.5459080047805
46	255.50227594713235
47	255.4006219534951
48	255.96832105890513
49	253.712370055111
50	239.23698593979478
51	198.25176951981626
52	133.7924770348973
53	97.52202769640976
54	82.1277917643258
55	55.79044793965517
56	30.089750785026805
57	15.855829270062236
58	9.13543869881517
59	4.6941485734575235
60	0.507072280477836

Figure E.44 Numerical modeling results for the ramp (3 m height, 9 m width, and 21 lenght) SMP with 2022 weather function

Pile Number 45

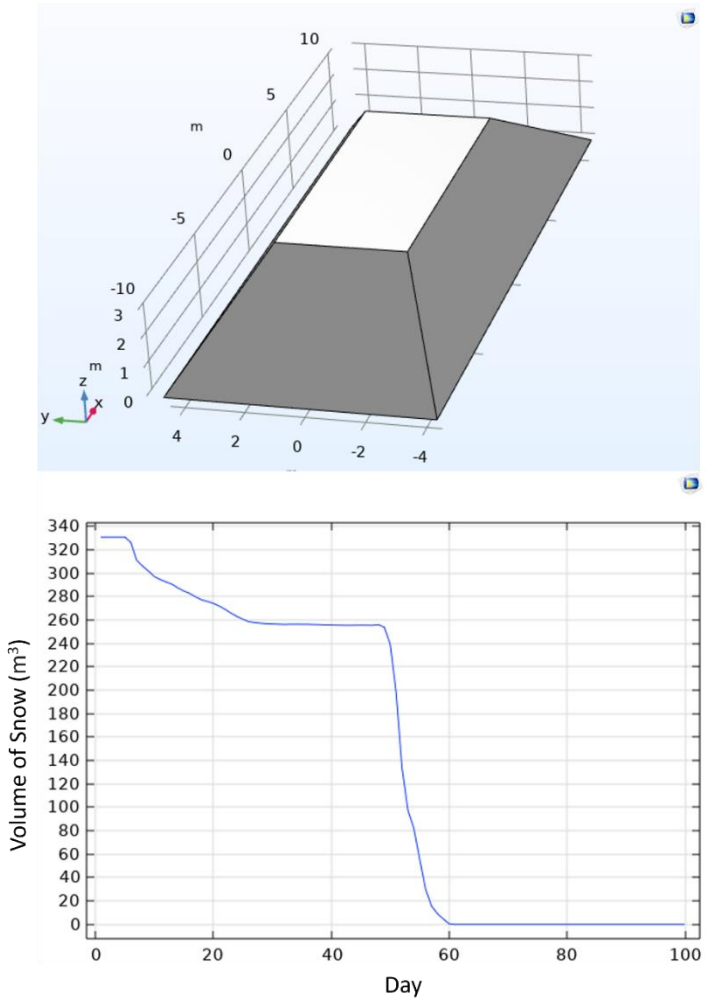

% Model:	3D Ridge Holt 21mL1 9mL2 3mH- Success .mph
% Version:	COMSOL 6.1.0.252
% Date:	Nov 11 2024, 15:02
% Table:	Table 1 - Volume Integration 1
% Time (d)	Phase indicator, phase 1 (m^3)
1	330.7499999999977
2	330.7499999999977
3	330.7499999999958
4	330.7499997175499
5	330.74806191334244
6	326.2758057620679
7	310.9881568356866
8	305.9203124466011
9	301.73052229663915
10	297.01146358044076
11	294.4519019850902
12	292.3922587171784
13	290.4472865253043
14	287.35305793321106
15	284.67664390429366
16	282.59227144137253
17	279.6471209809729
18	277.2030192033777
19	275.74384587590873
20	274.1445562619423
21	271.8649100292057
22	268.9695038617423
23	265.79379716440485
24	262.92738375954116
25	260.6234210450277
26	258.49252333786849
27	257.7118807463977
28	257.19089871743836
29	256.79611846978503
30	256.5573638149899
31	256.40239623534546
32	256.1442773318485
33	256.29475997942234
34	256.3126687347627
35	256.27241572934355
36	256.240618105884
37	256.10714179832377
38	255.97741996753064
39	255.82437621903134
40	255.68194386579717
41	255.5555925781183
42	255.4475208225044
43	255.35759079682902
44	255.47717468331615
45	255.5459080047805
46	255.50227594713235
47	255.4006219534951
48	255.96832105890513
49	253.712370055111
50	239.23698593979478
51	198.25176951981626
52	133.7924770348973
53	97.52202769640976
54	82.1277917643258
55	55.79044793965517
56	30.089750785026805
57	15.855829270062236
58	9.13543869881517
59	4.6941485734575235
60	0.507072280477836

Figure E.45 Numerical modeling results for the ramp (4 m height, 12 m width, and 24 lenght) SMP with 2022 weather function

Pile Number 46

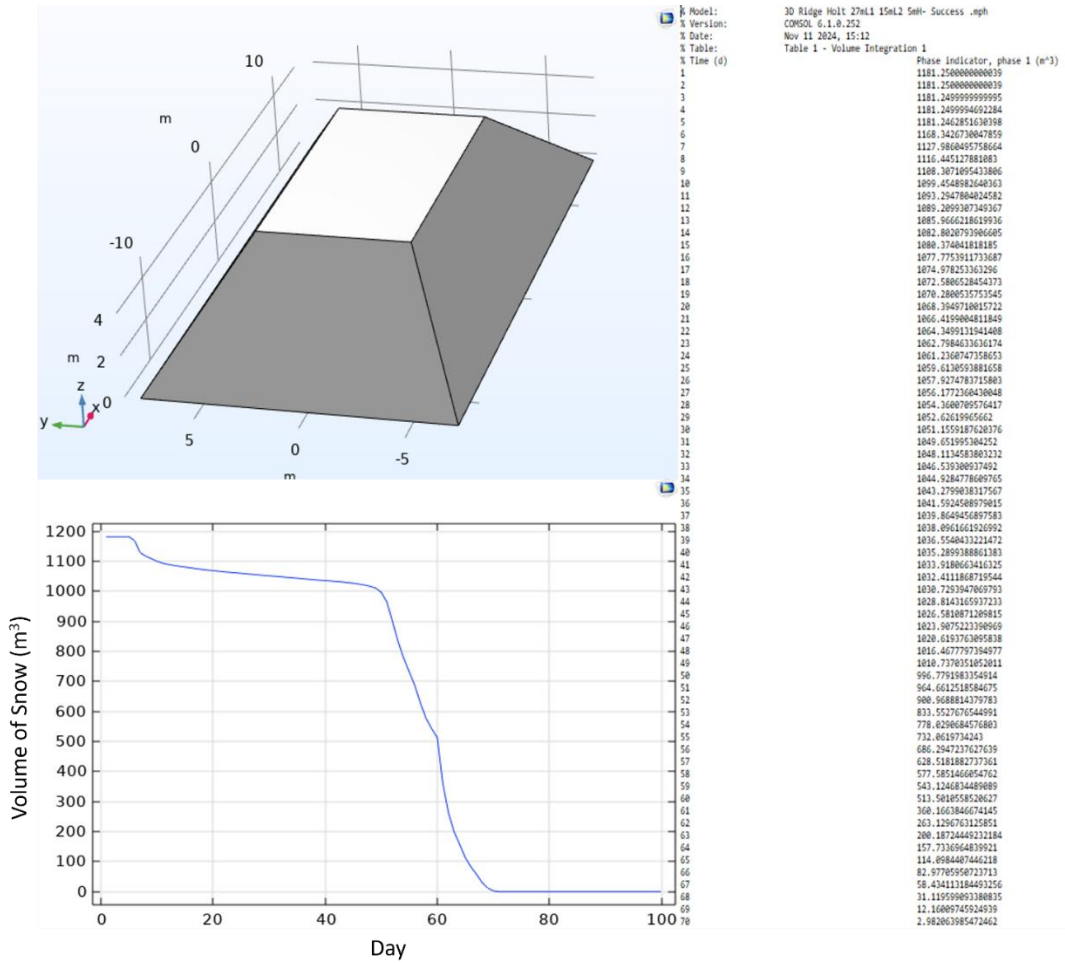

% Model: 3D Ridge Holt 27mL1 15mL2 5mH- Success .mph
% Version: COMSOL 6.1.0.252
% Date: Nov 11 2024, 15:12
% Table: Table 1 - Volume Integration 1
% Time (d) Phase indicator, phase 1 (m^3)
1 1181.2500000000039
2 1181.2500000000039
3 1181.2499999999995
4 1181.2499994692284
5 1181.2462851630398
6 1168.3426730047859
7 1127.9860495758664
8 1116.445127881083
9 1108.3071095433806
10 1099.4548982640363
11 1093.2947804024582
12 1089.2899307349367
13 1085.9666218619936
14 1082.8020793906605
15 1080.374041818185
16 1077.7753911733687
17 1074.978253363296
18 1072.5806528454373
19 1070.2800535753545
20 1068.3549710015722
21 1066.4199004811849
22 1064.3499131941408
23 1062.79846336361 74
24 1061.2360747358653
25 1059.6130593881658
26 1057.9274783715803
27 1056.1772360430048
28 1054.3600709576417
29 1052.6261996566 2
30 1051.1559187620376
31 1049.651995304252
32 1048.1134583803232
33 1046.539300937492
34 1044.9284778609765
35 1043.2795038317567
36 1041.5924508979015
37 1039.8649456897583
38 1038.0961661926992
39 1036.5540433221472
40 1035.2899388861383
41 1033.9180663416325
42 1032.4111868719544
43 1030.7293947069793
44 1028.8143165937233
45 1026.5810871269815
46 1023.9075223390969
47 1020.6193763095838
48 1016.4677797394977
49 1010.7370351052011
50 996.7791983354914
51 964.6612518584675
52 900.9688814379783
53 833.5527670544991
54 778.0290684576803
55 732.0619734243
56 686.2947237627639
57 628.5181882737361
58 577.5851466054762
59 543.1246834489089
60 513.5010558520627
61 368.1663846674145
62 263.1296763125851
63 200.18724449232184
64 157.7336964839921
65 114.0984407446218
66 82.97705950723713
67 58.434113184493256
68 31.119599093380835
69 12.160097459249 39
70 2.982063985472462

Figure E.46 Numerical modeling results for the ramp (5 m height, 15 m width, and 27 lenght) SMP with 2022 weather function

Pile Number 47

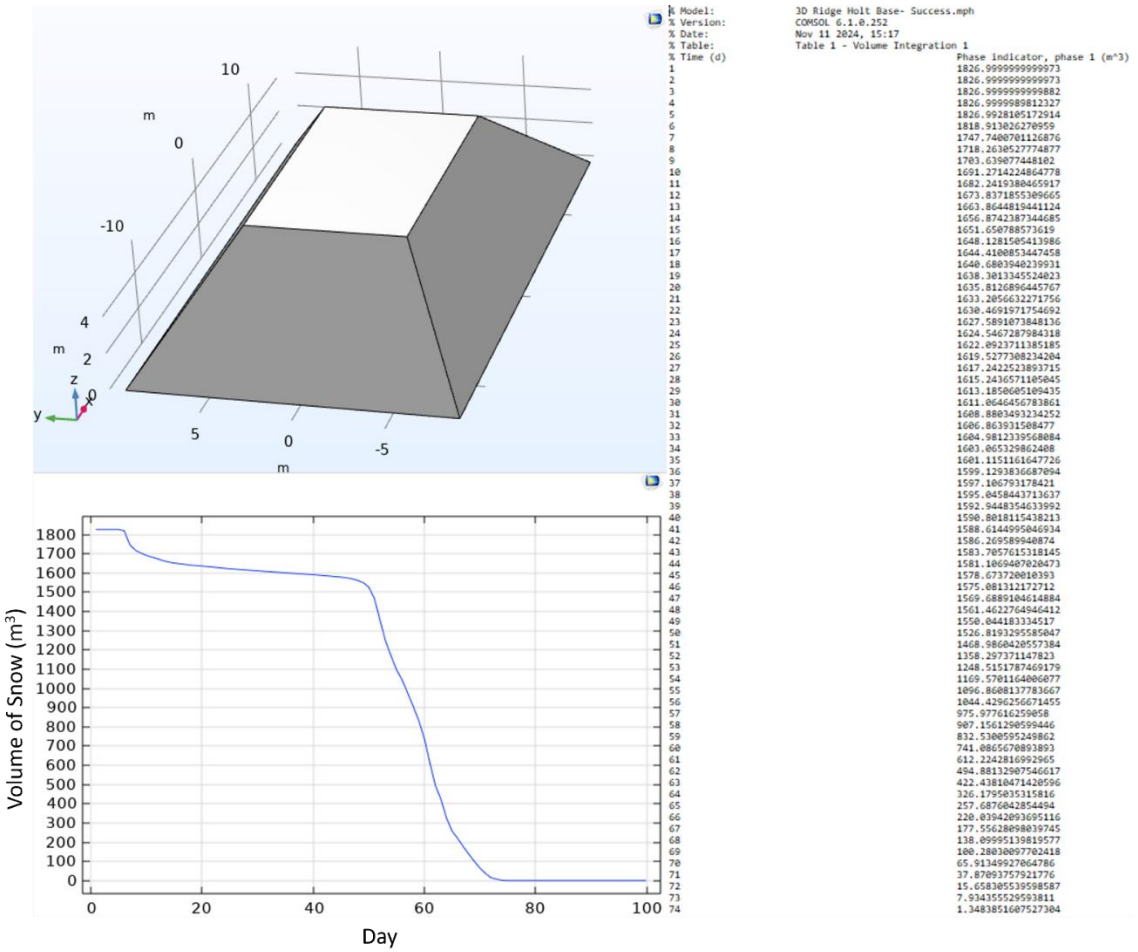


```
% Model:
% Version:
% Date:
% Table:
% Time (d)
1
2
3
4
5
6
7
8
9
10
11
12
13
14
15
16
17
18
19
20
21
22
23
24
25
26
27
28
29
30
31
32
33
34
35
36
37
38
39
40
41
42
43
44
45
46
47
48
49
50
51
52
53
54
55
56
57
58
59
60
61
62
63
64
65
66
67
68
69
70
71
72
73
74
```

```
3D Ridge Holt Base- Success.mph
COMSOL 6.1.0.252
Nov 11 2024, 15:17
Table 1 - Volume Integration 1
Phase Indicator, phase 1 (m^3)
1826.9999999999973
1826.9999999999973
1826.9999999999882
1826.9999989812327
1826.9928105172914
1818.9130262709959
1747.7400701126876
1718.2630527774877
1703.639077448102
1691.2714224864778
1682.2419380465917
1673.8371855309665
1663.8644819441124
1656.8742387344685
1651.650788573619
1648.1281505413986
1644.4100853447458
1640.6803940239931
1638.3013345524023
1635.8126896445767
1633.2056632271756
1630.4691971754692
1627.5891073848136
1624.5467287984318
1622.0923711385185
1619.5277308234204
1617.2422523893715
1615.2436571105045
1613.1850685109435
1611.0644656783861
1608.8803493234252
1606.863931508477
1604.9812339568084
1603.065329862408
1601.1151161647726
1599.1293836687094
1597.106793178421
1595.0458443713637
1592.9448354633992
1590.8018115438213
1588.6144995046934
1586.269589940874
1583.7057615318145
1581.1069407020473
1578.673720010393
1575.8813121727212
1569.6889104614884
1561.4622764946412
1550.044183334517
1526.8193295585047
1468.9860420557384
1358.297371147823
1248.5151787469179
1169.5701164006077
1096.8608137783667
1044.42962566671455
975.977616259058
907.1561290599446
832.5300595249862
741.0865670893893
612.2242816992965
494.88132907546617
422.43810471420596
326.1795035315816
257.6876042854494
220.03942093695116
177.55628098039745
138.09995139819577
100.28030097702418
65.91349927064786
37.870937577921776
15.658305539598587
7.9343555295931811
1.3483851607527304
```

Figure E.47 Numerical modeling results for the ramp (5.8 m height, 18 m width, and 30 lenght) SMP with 2022 weather function

Pile Number 48

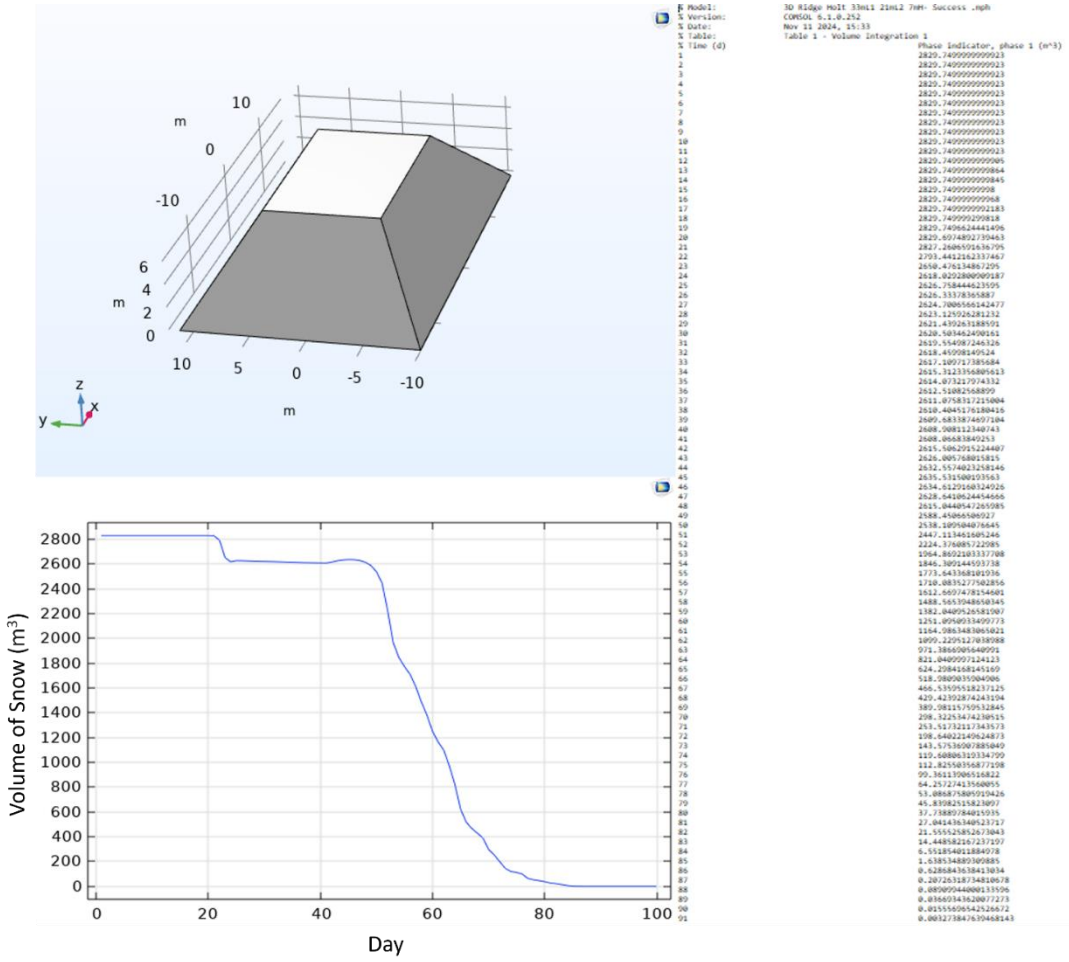

Figure E.48 Numerical modeling results for the ramp (7 m height, 21 m width, and 30=3 lenght) SMP with 2022 weather function

Pile Number 49

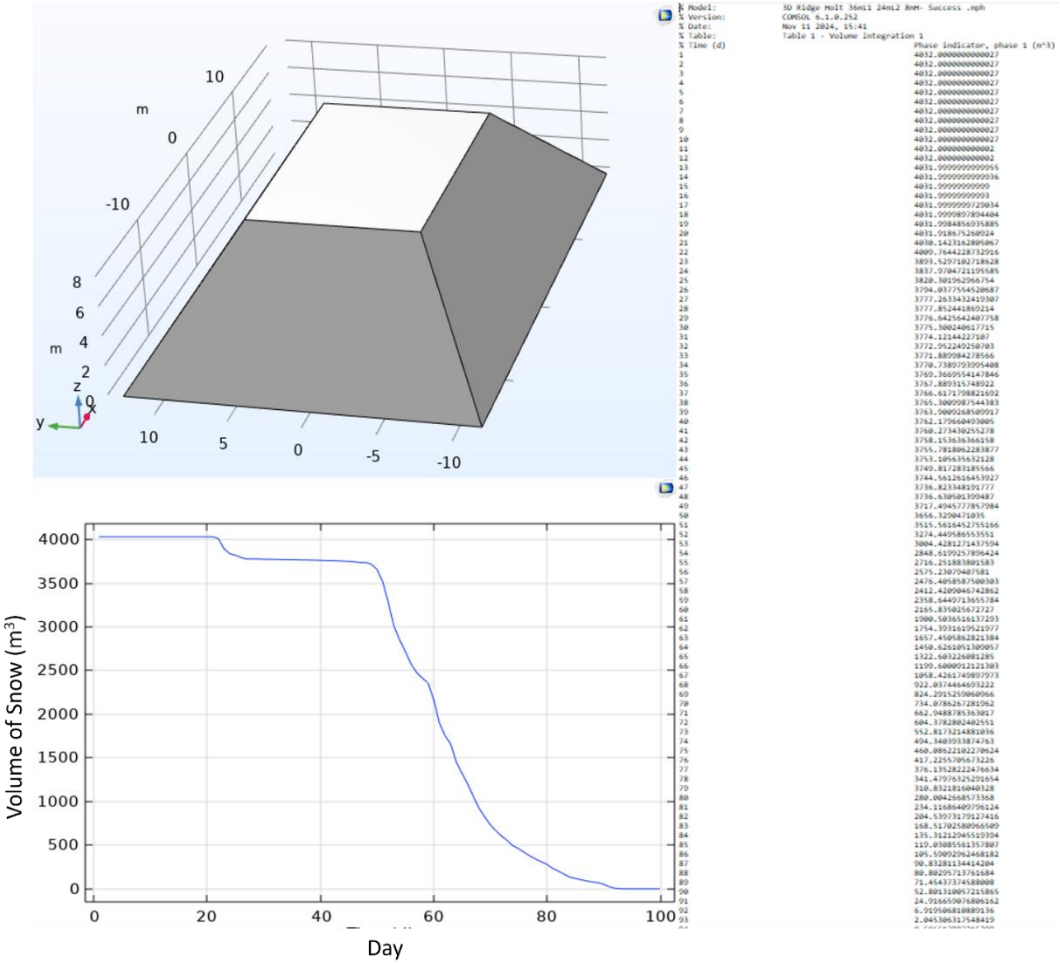

Figure E.49 Numerical modeling results for the ramp (8 m height, 24 m width, and 36 lenght) SMP with 2022 weather function

Pile Number 50

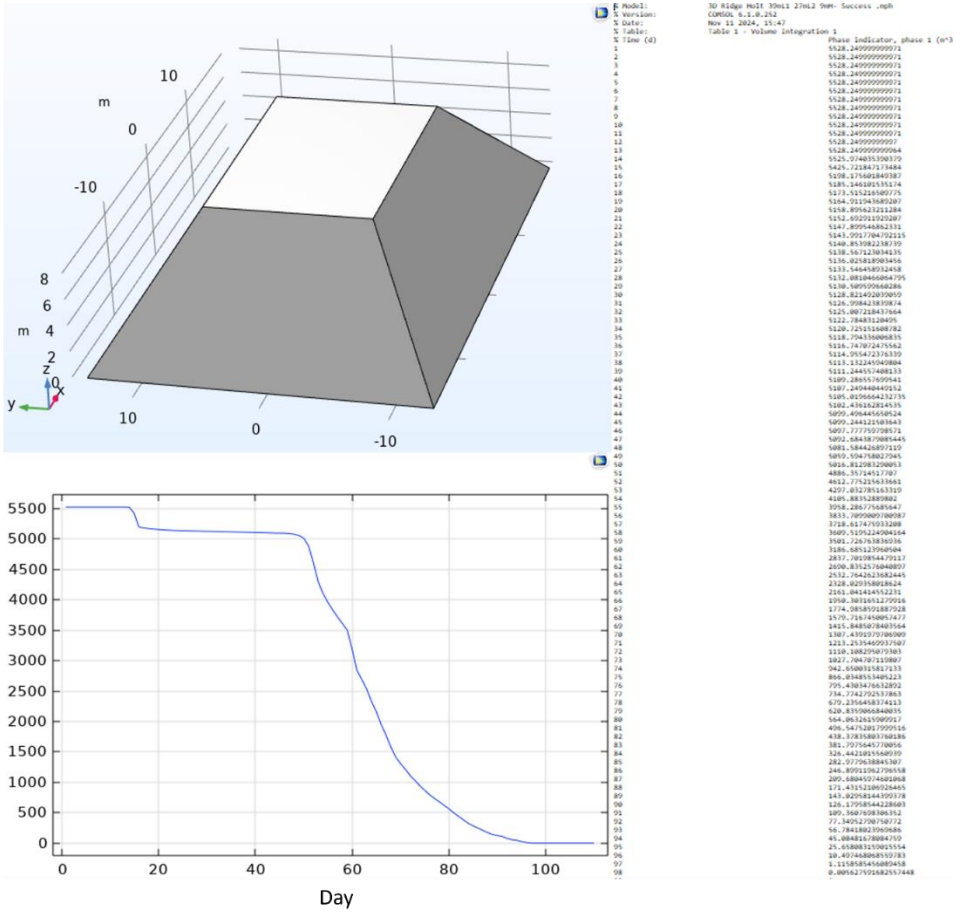

Figure E.50 Numerical modeling results for the ramp (9 m height, 27 m width, and 39 lenght) SMP with 2022 weather function

Pile Number 51

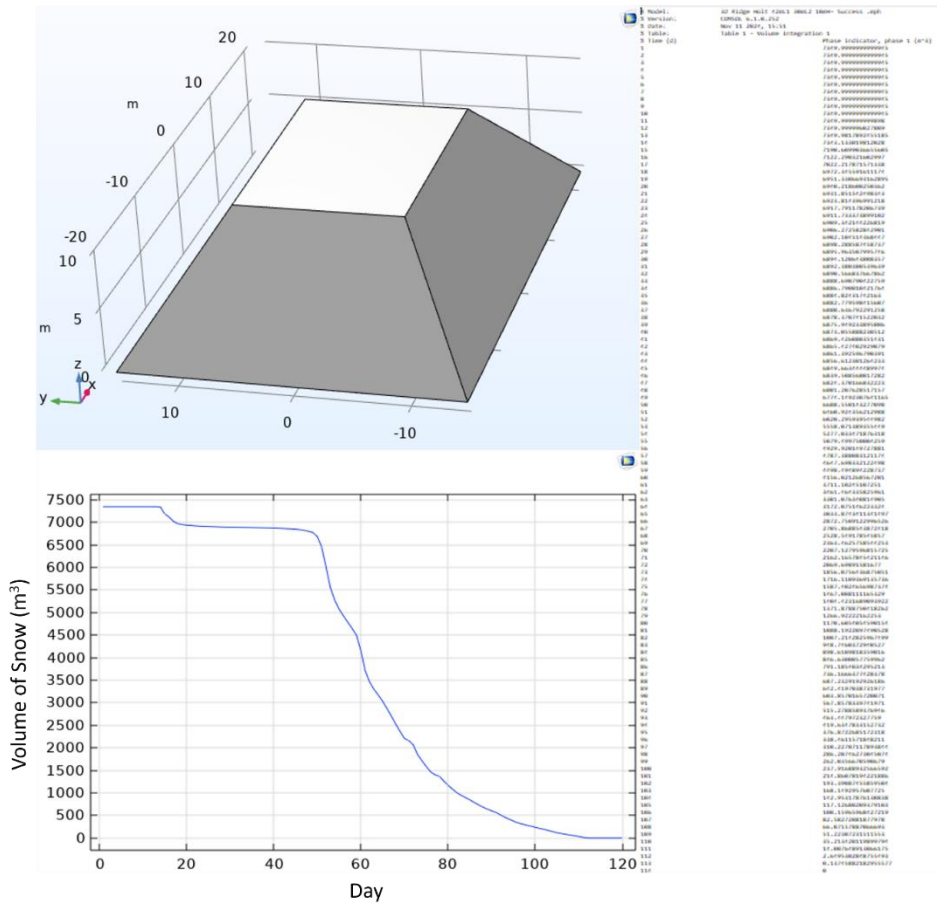

Figure E.51 Numerical modeling results for the ramp (10 m height, 30 m width, and 42 lenght) SMP with 2022 weather function

Pile Number 52

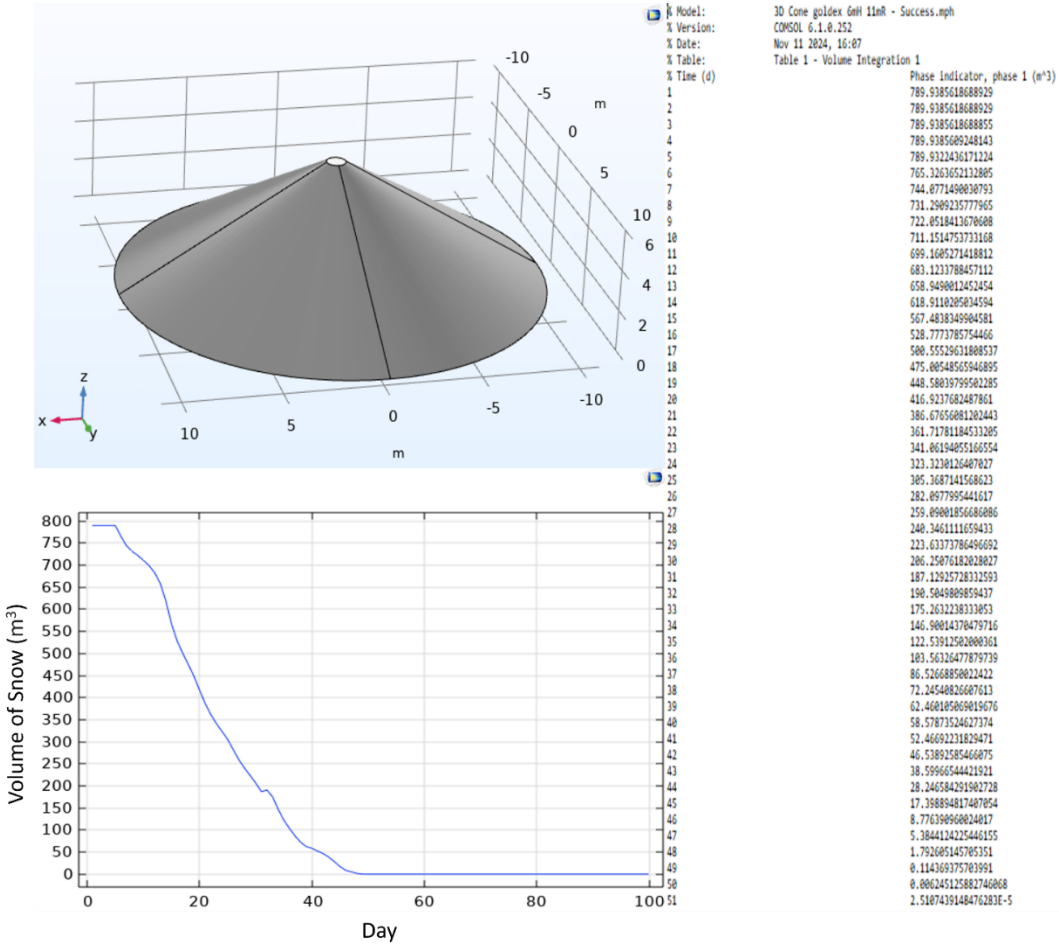

% Model: 3D Cone goldex GmH 11mR - Success.mph
% Version: COMSOL 6.1.0.252
% Date: Nov 11 2024, 16:07
% Table: Table 1 - Volume Integration 1
% Time (d) Phase indicator, phase 1 (m^3)
1 789.9385618688929
2 789.9385618688929
3 789.9385618688855
4 789.9385609248143
5 789.9322436171224
6 765.1263652132805
7 744.0771490030793
8 731.2909235777965
9 722.051841370608
10 711.1514753733168
11 699.1605271418812
12 683.1233788457112
13 658.9490012452454
14 618.9110205034594
15 567.4838349904581
16 528.7773785754466
17 500.5552963180853 7
18 475.0054856594689 5
19 448.5803979950228 5
20 416.923768248786 1
21 386.6765608120244 3
22 361.7178118453320 5
23 341.0619405516655 4
24 323.3230126407027
25 305.3687141568623
26 282.0977995441617
27 259.0900185668608 6
28 240.3461111659433
29 223.6337378649609 2
30 206.2507618202802 7
31 187.1292572833259 3
32 190.5049809859437
33 175.2632238333053
34 146.9001437047971 6
35 122.5391250200036 1
36 103.5632647787973 9
37 86.52668850022422
38 72.24540826607613
39 62.46810586901967 6
40 58.57873524627374
41 52.46692231829471
42 46.53892585466075
43 38.59966544421921
44 28.24658429190272 8
45 17.39889481740705 4
46 8.776390960824817
47 5.384412422544615 5
48 1.792605145705351
49 0.1143693757039911
50 0.0062451258274606 8
51 2.5107439148476283E-5

Figure E.52 Numerical modeling results for the cone (6 m height, and 11 m radius) SMP with 2023 weather function

Pile Number 53

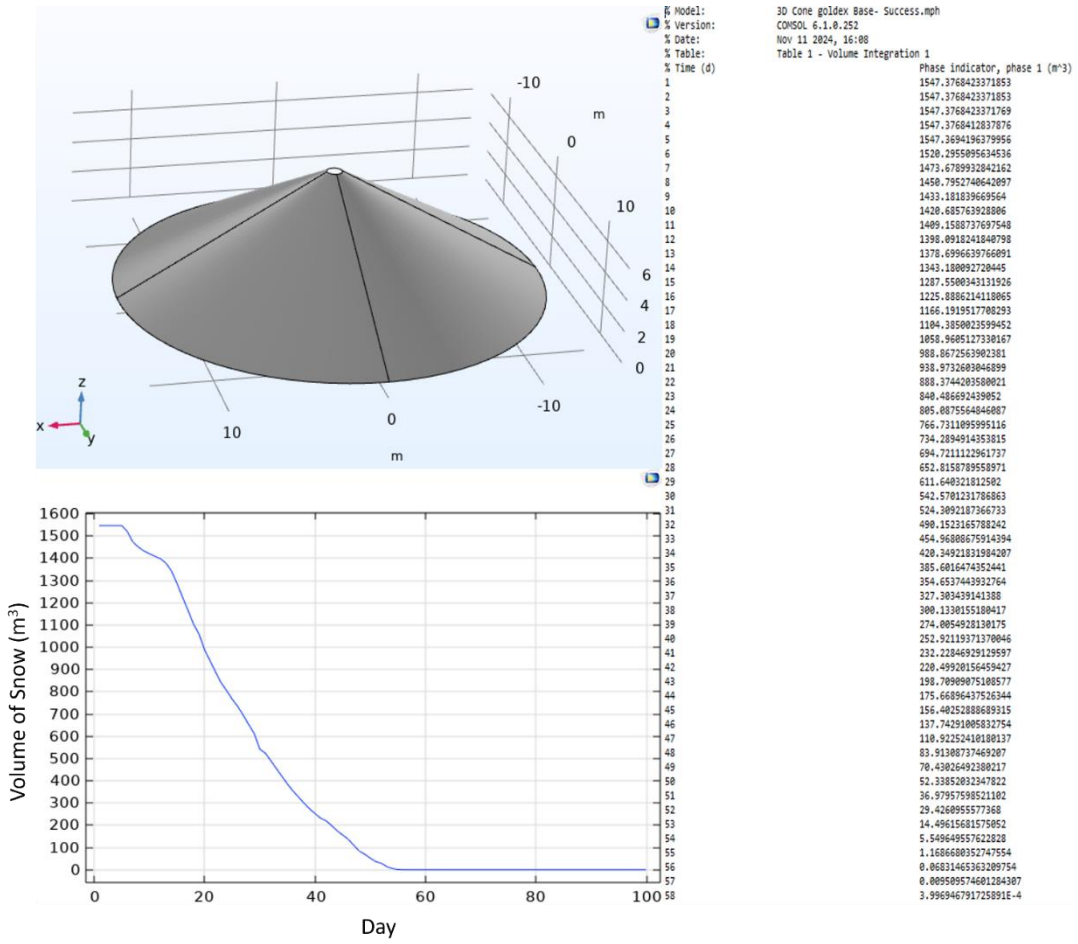

% Model: 3D Cone goldex Base- Success.mph
% Version: COMSOL 6.1.0.252
% Date: Nov 11 2024, 16:08
% Table: Table 1 - Volume Integration 1

% Time (d)	Phase indicator, phase 1 (m^3)
1	1547.3768423371853
2	1547.3768423371853
3	1547.3768423371769
4	1547.376841283787 6
5	1547.3694196379956
6	1520.2955095634536
7	1473.6789932842162
8	1450.795274064209 7
9	1433.181839669564
10	1420.685763928806
11	1409.1588737697548
12	1398.0918241840798
13	1378.6996639766091
14	1343.180092720445
15	1287.5500343131926
16	1225.8886214118065
17	1166.1919517708293
18	1104.3850023599452
19	1058.9605127330167
20	988.8672563902381
21	938.9732603046899
22	888.3744203580021
23	840.486692439052
24	805.0875564846087
25	766.7311095995116
26	734.2894914353815
27	694.7211122961737
28	652.8158789558971
29	611.640321812502
30	542.5701231786863
31	524.3092187366733
32	490.1523165788242
33	454.96808675914394
34	420.34921831984207
35	385.6016474352441
36	354.6537443932764
37	327.303439141388
38	300.1330155180417
39	274.0054928130175
40	252.92119371370046
41	232.22846929129597
42	220.49920156459427
43	198.70909075108577
44	175.66896437526344
45	156.40252888689315
46	137.74291005832754
47	110.92252410180137
48	83.91308737469207
49	70.43026492380217
50	52.33852032347822
51	36.97957598521102
52	29.4260955577368
53	14.49615681575052
54	5.5496495576228 28
55	1.1686680352747554
56	0.06831465363209754
57	0.009509574601284307
58	3.996946791725891E-4

Figure E.53 Numerical modeling results for the cone (7.3 m height, and 14 m radius) SMP with 2023 weather function

Pile Number 54

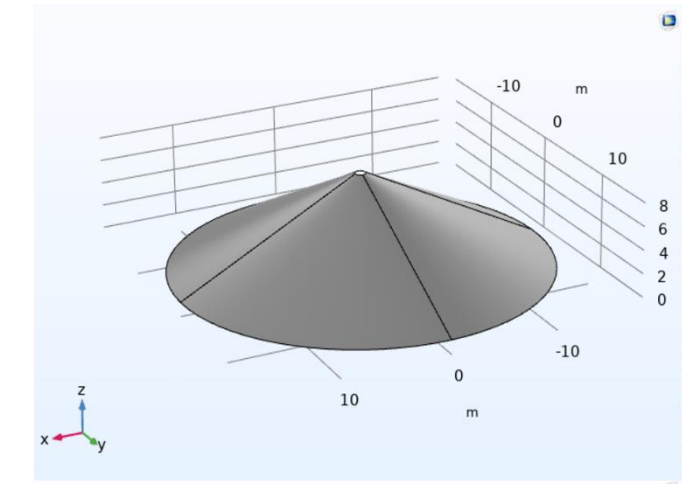

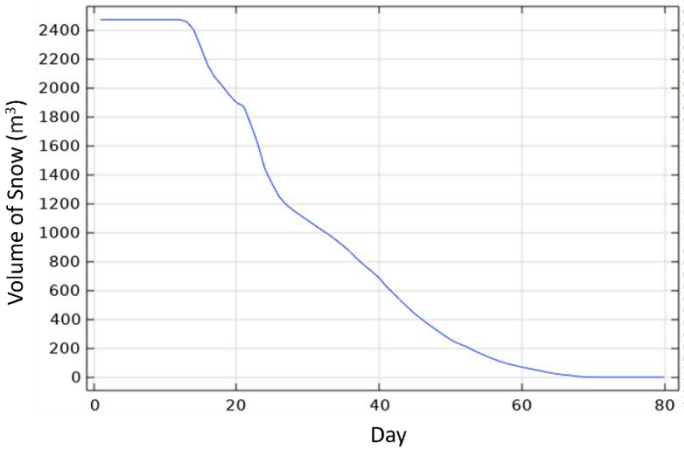

% Version: COMSOL 6.1.0.252
% Date: Nov 11 2024, 16:18
% Table: Table 1 - Volume Integration 1
% Time (d) Phase indicator, phase 1 (m^3)
1 2474.0636825608794
2 2474.0636825608794
3 2474.0636825608794
4 2474.0636825608794
5 2474.0636825608794
6 2474.0636825608794
7 2474.063682560883
8 2474.063682527014
9 2474.0636753000226
10 2474.063094159485
11 2474.03889520721
12 2473.3290992526227
13 2460.0744777860277
14 2403.3292210166596
15 2281.6916888458154
16 2154.117977557157
17 2073.04925616193
18 2015.6521213189326
19 1952.7076456116724
20 1898.8363338293355
21 1875.3984934000791
22 1751.47332829247
23 1612.0756363262349
24 1438.7807062021166
25 1337.5987443063143
26 1247.9715480720572
27 1192.3120669330035
28 1153.638494287892
29 1118.6721111820752
30 1084.8165791463061
31 1050.8434494648359
32 1016.8695366732544
33 984.4139689416387
34 947.7203387099338
35 907.4216200700371
36 864.463123016528
37 813.5274146644372
38 771.4332387224226
39 730.1222108328845
40 688.8684358914295
41 627.9588416592196
42 581.6107322806542
43 530.7167215645742
44 484.57015241706637
45 438.68767009480946
46 400.44460364562116
47 362.5391789597179
48 327.61029959659373
49 293.9942696484113
50 260.5797758029752
51 235.61784790622394
52 216.59373961108903
53 191.59161136544952
54 168.7574745689116
55 146.7009308917636
56 126.78794895055614
57 108.5669658750353
58 93.68695327084396
59 82.2377987596966
60 70.74847384653985
61 59.92799884724793
62 50.69321725177515
63 40.98333288797907
64 30.25777089166745
65 22.38882495156321
66 16.695254408918267
67 12.346924915493492
68 5.2848906111936615
69 1.5536034538206374
70 0.7719706648502966
71 0.2685179115089192
72 0.05407216344938954
73 0.007314849995288395

Figure E.54 Numerical modeling results for the cone (8 m height, and 17 m radius) SMP with 2023 weather function

Pile Number 55

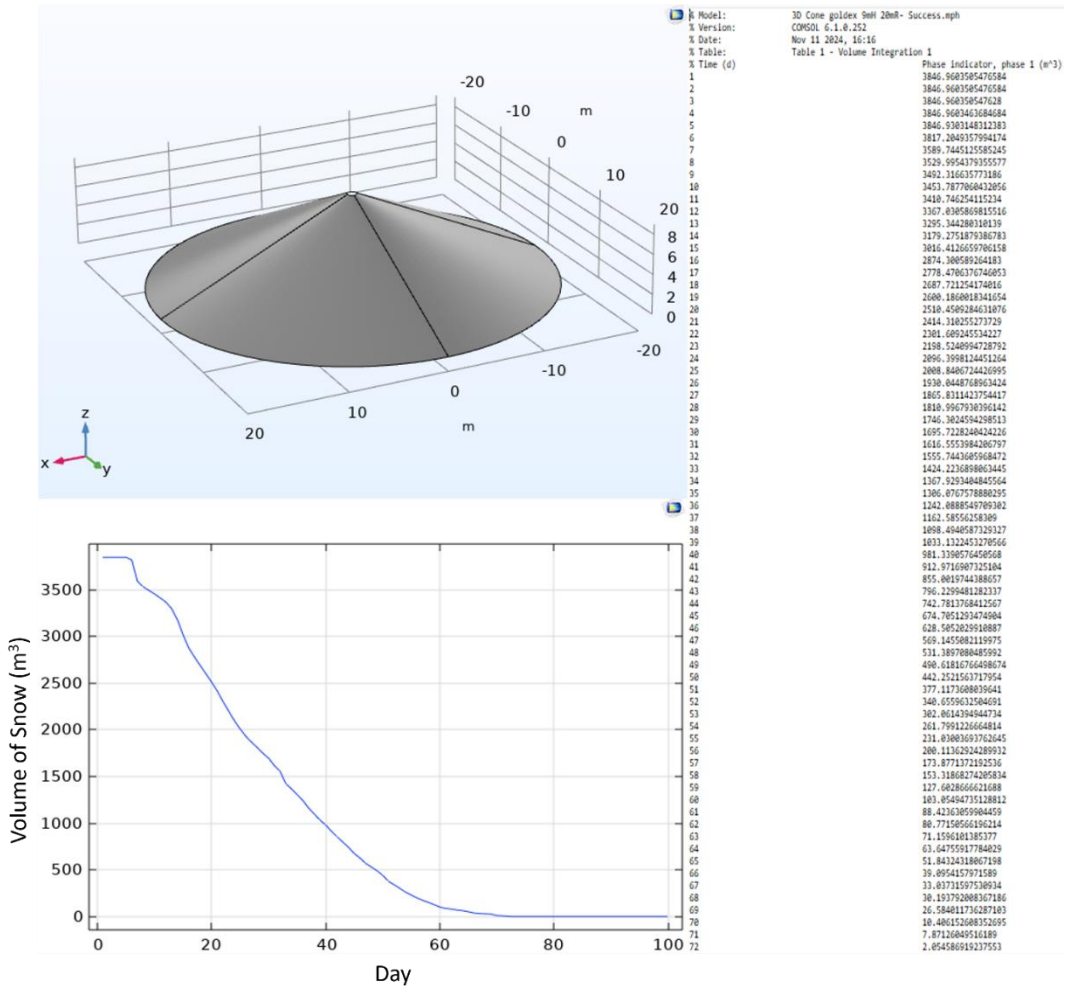

% Model: 3D Cone goldex 9mH 20mR- Success.mph
% Version: COMSOL 6.1.0.252
% Date: Nov 11 2024, 16:16
% Table: Table 1 - Volume Integration 1

% Time (d)	Phase Indicator, phase 1 (m^3)
1	3846.960350547658 4
2	3846.960350547658 4
3	3846.96035054762 8
4	3846.960346368468 4
5	3846.930314831238 3
6	3817.204935799417 4
7	3589.744512558524 5
8	3529.995437935557 7
9	3492.116635773186
10	3453.787706043205 6
11	3410.746254115234
12	3367.030586981551 6
13	3295.344280310139
14	3179.275187938678 3
15	3016.412665970615 8
16	2874.300589264183
17	2778.470637674605 3
18	2687.721254174016
19	2600.186001834165 4
20	2510.450928463107 6
21	2414.310255273729
22	2301.609245534227
23	2198.524099472879 2
24	2096.399812445126 4
25	2008.848672442699 5
26	1930.044876963424
27	1865.831142375441 7
28	1810.996793039614 2
29	1746.302459429851 3
30	1695.722824042422 6
31	1616.555398420679 7
32	1555.744360596847 2
33	1424.223689806344 5
34	1367.929340484556 4
35	1306.076757888029 5
36	1242.088854970930 2
37	1162.58556258309
38	1098.494058732932 7
39	1033.132245327056 6
40	981.339057645056 8
41	912.971690732510 4
42	855.001974438865 7
43	796.229948128233 7
44	742.781376841256 7
45	674.705129347490 4
46	628.585202991088 7
47	569.145508211997 5
48	531.389708048599 2
49	490.618167664986 7 4
50	442.252156371795 4
51	377.117360803964 1
52	340.655963250469 1
53	302.061439494473 4
54	261.799122666481 4
55	231.030036937626 4 5
56	200.113629242899 3 2
57	173.877137219253 6
58	153.318682742858 3 4
59	127.602866662168 8
60	103.054947351288 1 2
61	88.423630599044 5 9
62	80.771505661962 1 4
63	71.15961013853 7 7
64	63.647559177840 2 9
65	51.843243188671 9 8
66	39.09541579715 8 9
67	33.037315975309 3 4
68	30.193792008367 1 8 6
69	26.584011736287 1 0 3
70	10.406152608352 6 9 5
71	7.87126049516 1 8 9
72	2.054586919237 5 5 3

Figure E.55 Numerical modeling results for the cone (9 m height, and 20 m radius) SMP with 2023 weather function

Pile Number 56

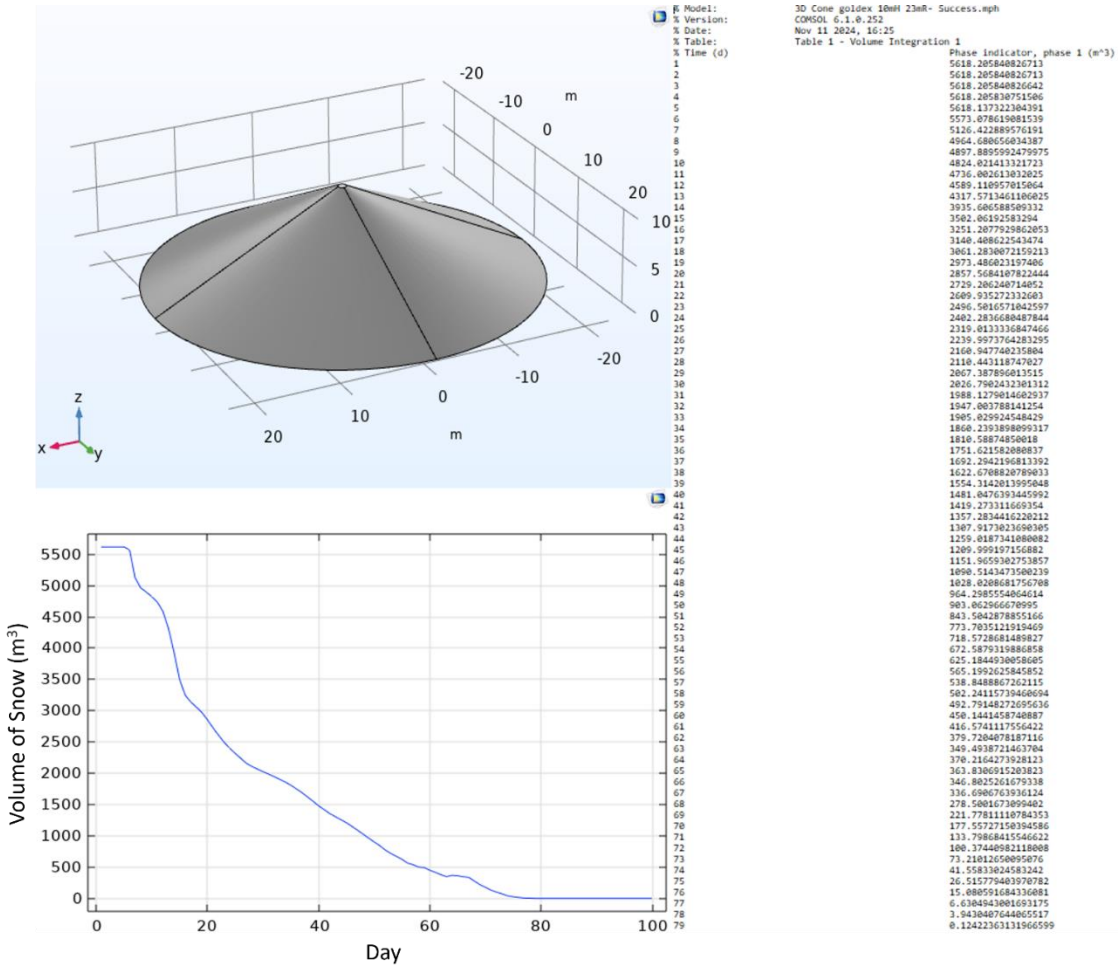

% Model:
% Version:
% Date:
% Table:
% Time (d)
3D Cone goldex 10mH 23mR- Success.mph
COMSOL 6.1.0.252
Nov 11 2024, 16:25
Table 1 - Volume Integration 1
Phase indicator, phase 1 (m^3)
5618.205840826713
5618.205840826713
5618.205840826642
5618.205830751506
5618.137122304391
5573.078619081539
5126.422889576191
4964.680056034387
4897.889599247997 5
4824.021413321723
4736.002613032025
4589.110957015064
4317.571346110602 5
3935.606588509332
3502.061925813294
3251.207792986205 3
3140.408622543474
3061.283087215921 3
2973.486023197406
2857.568410782244 4
2729.206240714052
2609.935272332603
2496.501657104259 7
2402.283668048784 4
2319.013333684746 6
2239.997376428329 5
2160.947740235804
2110.443118747027
2067.387896013515
2026.790243238131 2
1988.127901460293 7
1947.003788141254
1905.029924548429
1860.239389899317
1810.58874850018
1751.621582080837
1692.294219681339 2
1622.670882078903 3
1554.314281399504 8
1481.047639344599 2
1419.273311669354
1357.283441622021 2
1307.917302369030 5
1259.018734108008 2
1209.999197156882
1151.965930275385 7
1090.514347350023 9
1028.020868175670 8
964.2985554864614
903.062966670995
843.5042878855166
773.7035121919469
718.572868148982 7
672.5879319886858
625.1844930058605
565.1992625845852
538.848886726211 5
582.241157194686 94
492.791482726956 36
450.144145874088 7
416.5741117556422
379.720407818711 6
349.493872146370 4
370.2164273928123
363.830691520382 3
346.8025261679338
336.690676193612 4
278.500167309940 2
221.778111107843 53
177.557271503945 86
133.798684155466 22
100.374409821180 08
73.21012650095076
41.558330245832 42
26.515779403970782
15.080591684360 81
6.6384943001693175
3.9430407644065517
0.12422363131966599

Figure E.56 Numerical modeling results for the cone (10 m height, and 23 m radius) SMP with 2023 weather function

Pile Number 57

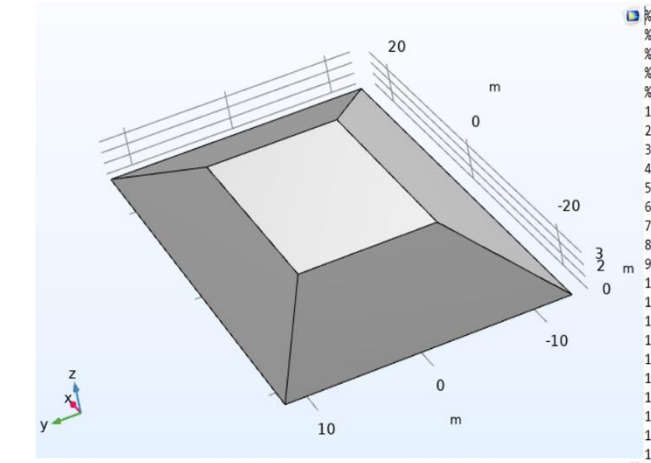

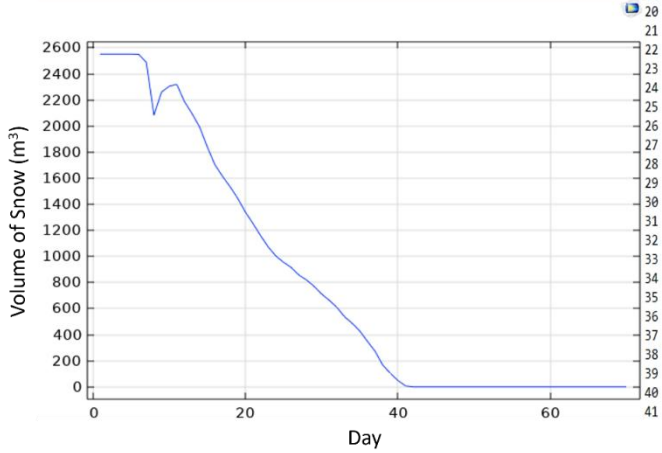

% Model:	3D Ridge goldex base - Success.mph	
% Version:	COMSOL 6.1.0.252	
% Date:	Nov 11 2024, 16:51	
% Table:	Table 1 - Volume Integration 1	
% Time (d)		Phase indicator, phase 1 (m^3)
1		2552.0833333333267
2		2552.0833333333267
3		2552.083333333294
4		2552.0833289103703
5		2552.0710700151503
6		2550.0754766197174
7		2488.3990559710483
8		2085.1357222961515
9		2260.7195360791093
10		2305.484958438838
11		2319.7971669754975
12		2187.6965383676275
13		2095.1923235404593
14		1991.3592880243066
15		1839.937009345714
16		1703.014674750771
17		1614.021108057906
18		1533.8589080862555
19		1444.4197973261373
20		1340.0983323181315
21		1251.7345822113252
22		1158.6099303267167
23		1072.249093587463
24		1003.05848771282
25		955.7410193599818
26		916.1617427456582
27		857.7229965757707
28		820.6552637662722
29		771.2645815498277
30		711.6523174519316
31		663.9388850599199
32		609.7960902819837
33		537.5479149748433
34		488.40272321725644
35		428.4275741650997
36		349.69704370283665
37		273.5090531958536
38		168.330133539086
39		104.54095115764233
40		49.24883552163618
41		7.7127540003707065

Figure E.57 Numerical modeling results for the ridge (3.5 m height, 25 m width, and 50 m length) SMP with 2023 weather function

Pile Number 58

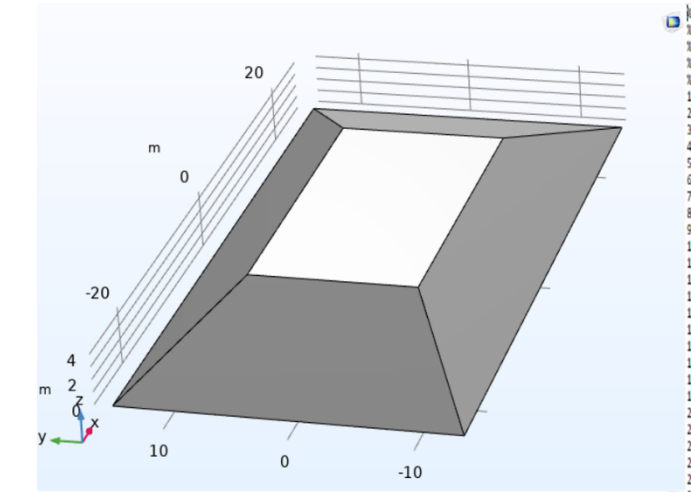

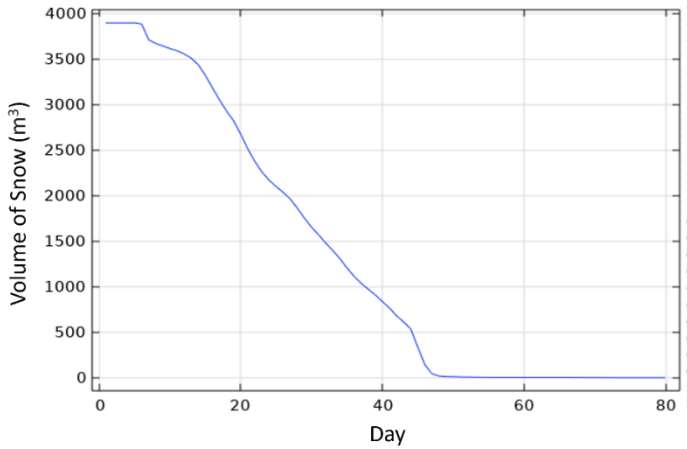

% Model:	3D Ridge goldex 53mL1 28mL2 4.5mH.mph
% Version:	COMSOL 6.1.0.252
% Date:	Nov 11 2024, 16:53
% Table:	Table 1 - Volume Integration 1
% Time (d)	Phase indicator, phase 1 (m^3)
1	3895.4999999999814
2	3895.4999999999814
3	3895.4999999999613
4	3895.499997535422
5	3895.482232436251
6	3883.142442752811
7	3708.741641589344
8	3668.3134883078897
9	3648.8896422699463
10	3612.6503219894284
11	3588.8487489451895
12	3553.941891908681
13	3508.558576452824
14	3434.1778380930045
15	3319.5494656613673
16	3181.9123527997494
17	3049.424646676923
18	2926.109578707277
19	2819.338041996154
20	2672.217467846598
21	2510.8362984821156
22	2372.3937991271837
23	2257.3940247815567
24	2167.6261639699696
25	2097.6554709069924
26	2035.5327514508185
27	1960.5079937302302
28	1859.8347343694957
29	1751.169411102531
30	1651.1507821803687
31	1568.3842819742267
32	1477.9603662209176
33	1395.24586798139
34	1306.840352928264
35	1204.7236851797768
36	1113.0806493057255
37	1035.2540061430104
38	970.9658068420217
39	909.4397469411982
40	834.6168787209276
41	765.5364229300023
42	679.9600974241781
43	612.2948462054354
44	536.025661936902
45	336.19954344917335
46	142.98488567443462
47	43.00453561368587
48	18.106893580238822
49	12.096361682466247
50	10.267647721474646
51	8.31879613508179

Figure E.58 Numerical modeling results for the ridge (4.5 m height, 28 m width, and 53 m length) SMP with 2023 weather function

Pile Number 59

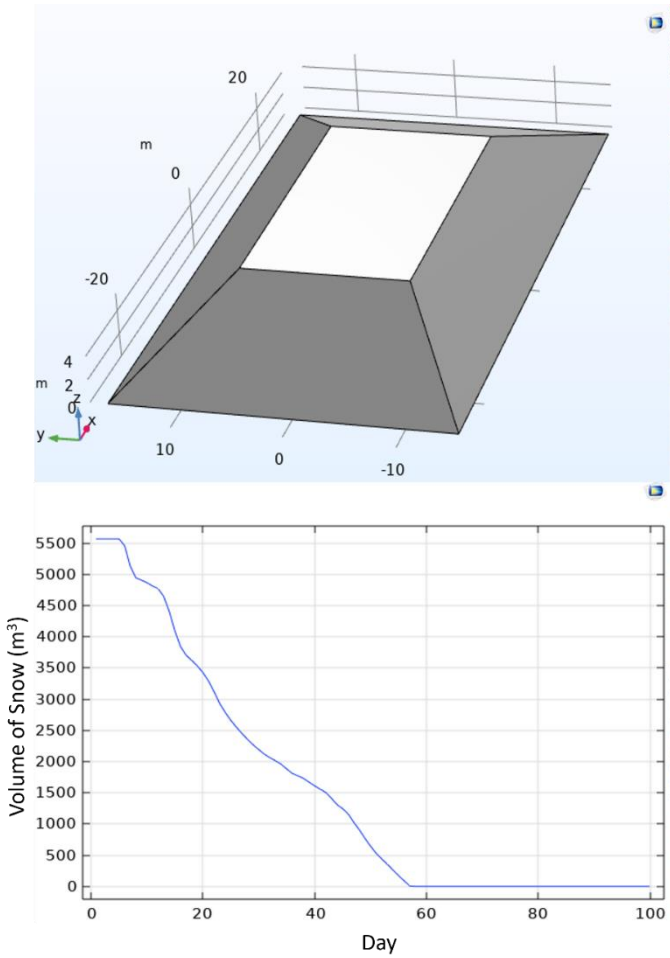

% Model:	3D Ridge goldex 56mL1 31mL2 5.5mH.mph
% Version:	COMSOL 6.1.0.252
% Date:	Nov 11 2024, 17:00
% Table:	Table 1 - Volume Integration 1
% Time (d)	Phase indicator, phase 1 (m^3)
1	5569.666666666672
2	5569.666666666672
3	5569.666666666621
4	5569.666658815648
5	5569.612174261349
6	5461.775777715172
7	5135.934892875268
8	4947.2466519192485
9	4908.796645243494
10	4868.131890496081
11	4814.670977224825
12	4772.107424942651
13	4646.695406077039
14	4404.032983031658
15	4094.2696750278774
16	3846.4573060686307
17	3704.9787928761953
18	3624.7589875142767
19	3534.7057658540716
20	3428.8313624711745
21	3294.967935114903
22	3121.6972043705964
23	2934.7895396966437
24	2789.1537155291303
25	2661.7576471896173
26	2552.46111280780655
27	2450.1830681233814
28	2356.2638101516604
29	2268.198736769192
30	2192.7719002178183
31	2119.3196386183795
32	2063.3025092839807
33	2013.0413146114965
34	1959.2605885719286
35	1882.3799780279764
36	1811.1308748487113
37	1772.2324770643452
38	1731.6027640276457
39	1670.8325662585162
40	1612.0566483991497
41	1558.1541239020285
42	1505.7154146328016
43	1413.5800564340655
44	1310.40475446751
45	1246.4276510584386
46	1162.6953422475713
47	1028.165481144696
48	906.6847798772983
49	770.9898615578054
50	644.8319091291742
51	532.3731345579686
52	439.1685413466914
53	356.418856834001
54	263.73741447459787
55	174.11416756934366
56	89.4350001042185
57	8.464995306622598

Figure E.59 Numerical modeling results for the ridge (5.5 m height, 31 m width, and 56 m length) SMP with 2023 weather function

Pile Number 60

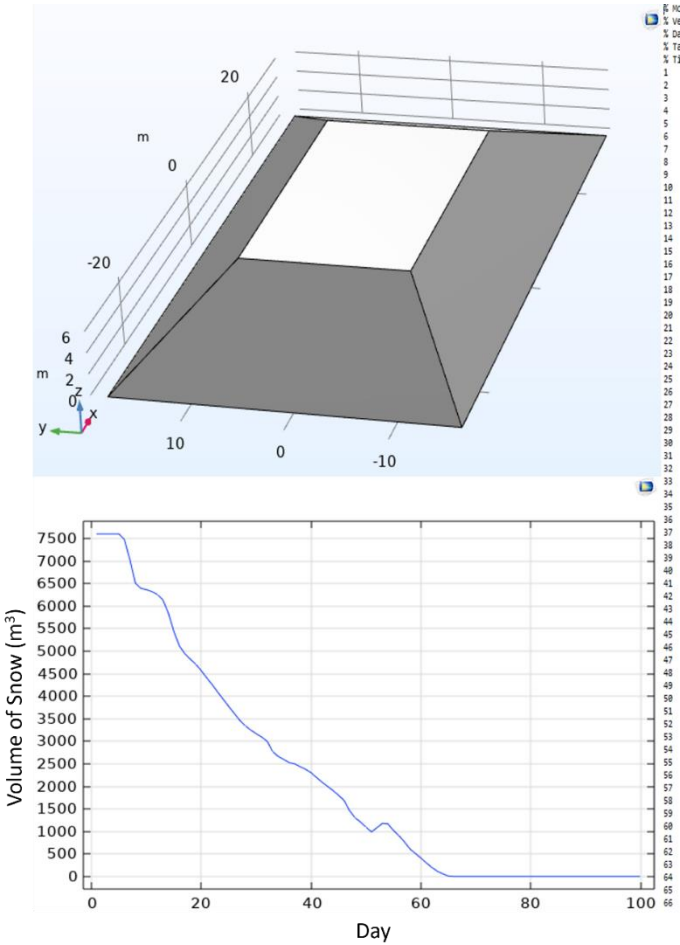

% Model: 3D Ridge goldex 59mL1 34mL2 6.5mH.mph
% Version: COMSOL 6.1.0.252
% Date: Nov 11 2024, 17:11
% Table: Table 1 - Volume Integration 1
% Time (d) Phase indicator, phase 1 (m^3)
1 7606.083333333316
2 7606.083333333316
3 7606.083333333254
4 7606.083323232483
5 7606.01297585257
6 7478.047271084407
7 7027.906409106676
8 6588.009773545626
9 6397.037882375095
10 6368.741113263209
11 6324.957466932998
12 6260.291630536225
13 6140.563597009132
14 5847.014430513635
15 5439.803386819913
16 5118.840695265312
17 4944.326833342059
18 4822.7132767521
19 4712.153425212913
20 4566.869117237049
21 4406.897590720618
22 4256.223248014053
23 4089.634292910631
24 3933.763308405590
25 3772.933140727587
26 3621.03302219305
27 3467.279933987628
28 3345.719572866315
29 3249.903607011214
30 3170.134654777081
31 3094.855649909634
32 3002.109805172958
33 2770.726558419936
34 2666.450631737914
35 2597.998654787539
36 2528.568635186971
37 2500.119717345807
38 2437.087673323389
39 2379.669456784710
40 2302.422041926816
41 2195.659938124854
42 2092.522705283071
43 1999.952216714718
44 1905.923670389
45 1802.804866604202
46 1689.417730510408
47 1462.635549271903
48 1301.603217373001
49 1209.670403586225
50 1094.806136681652
51 988.6122568354456
52 1083.522116430436
53 1179.768196538287
54 1165.018796150562
55 1019.088694246240
56 906.2303616676536
57 767.6075630979023
58 609.2650823042318
59 509.2242326908589
60 407.5110872930609
61 299.4494177437467
62 199.2503668864125
63 114.4267971309860
64 57.32059828690138
65 9.455981499577357
66 0

Figure E.60 Numerical modeling results for the ridge (6.5 m height, 34 m width, and 59 m length) SMP with 2023 weather function

Pile Number 61

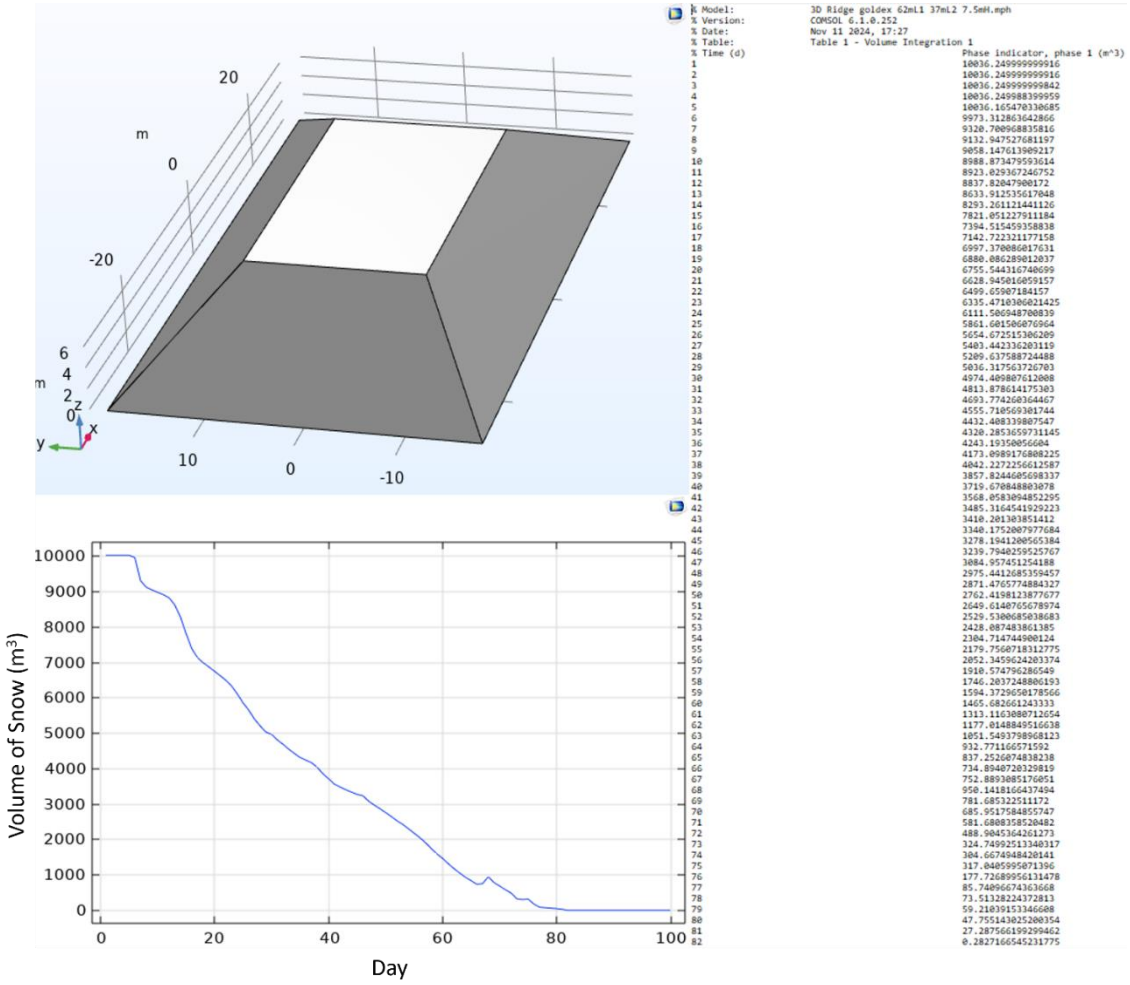

% Model: 3D Ridge goldex 62mL1 37mL2 7.5mH.mph
% Version: COMSOL 6.1.0.252
% Date: Nov 11 2024, 17:27
% Table: Table 1 - Volume Integration 1
% Time (d) Phase indicator, phase 1 (m^3)
1 10036.249999999916
2 10036.249999999916
3 10036.249999999842
4 10036.249988399959
5 10036.165470330685
6 9973.312863642866
7 9320.700968835816
8 9132.947527681197
9 9058.147613909217
10 8988.873479593614
11 8923.029367246752
12 8837.82047900172
13 8633.912535617048
14 8293.261121441126
15 7821.051227911184
16 7394.515459358838
17 7142.722321177158
18 6997.370080617631
19 6880.086228012037
20 6755.544316740699
21 6628.945016059157
22 6499.65907184157
23 6335.471030602142 5
24 6111.506948700839
25 5861.601506076964
26 5654.672515306209
27 5403.442336203119
28 5289.637588724488
29 5036.317563726703
30 4974.409807612008
31 4813.878614175303
32 4693.774260364467
33 4555.710569301744
34 4432.408339807547
35 4320.285365973114 5
36 4243.193500566 04
37 4173.098917680822 5
38 4042.227225661258 7
39 3857.824460569833 7
40 3719.670848803078
41 3568.058309485229 5
42 3485.316454192922 3
43 3410.201303851412
44 3340.175200797768 4
45 3278.194120056538 4
46 3239.794025952576 7
47 3084.957451254188
48 2975.441268535945 7
49 2871.476577488432 7
50 2762.419812387767 7
51 2649.614076567897 4
52 2529.530068503868 3
53 2428.087483861385
54 2304.714744900124
55 2179.756071831277 5
56 2052.345962420337 4
57 1910.574796280549
58 1746.203724880619 3
59 1594.372965017856 6
60 1465.682661243333
61 1313.116308071265 4
62 1177.014884951663 8
63 1051.549379896812 3
64 932.771166571592
65 837.252607483823 8
66 734.894072032981 9
67 752.889308517605 1
68 950.141816643749 4
69 781.685322511172
70 685.951758485574 7
71 581.680835852048 2
72 488.904536426127 3
73 324.749925133403 17
74 304.667494842014 1
75 317.040599507139 6
76 177.726899561314 78
77 85.7409667436366 8
78 73.513282243728 13
79 59.2103915334660 8
80 47.755143025200 354
81 27.287566199299462
82 0.2827166545231775

Figure E.61 Numerical modeling results for the ridge (7.5 m height, 37 m width, and 62 m length) SMP with 2023 weather function

Pile Number 62

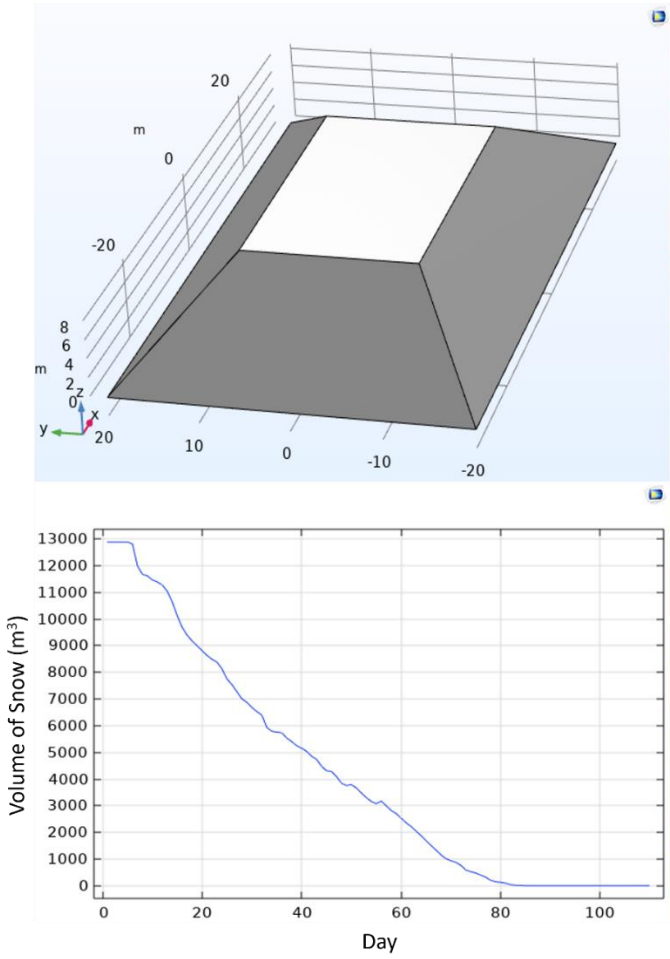

% Model: 3D Ridge goldex 65mL1 40mL2 8.5mH .mph
% Version: COMSOL 6.1.0.252
% Date: Nov 11 2024, 17:30
% Table: Table 1 - Volume Integration 1
% Time (d) Phase indicator, phase 1 (m^3)

1	12891.666666666665
2	12891.666666666665
3	12891.666666666544
4	12891.666652683549
5	12891.566303782043
6	12812.045468092907
7	11995.767470194638
8	11675.97780025316
9	11617.182607554654
10	11467.80655035377
11	11389.976353493854
12	11277.759546586005
13	11036.98755014762
14	10642.399747830246
15	10120.754392578076
16	9685.234047201044
17	9390.456492192148
18	9179.47510051573
19	8994.629736244586
20	8812.007935207619
21	8630.808569215958
22	8490.52271342647
23	8382.417132722368
24	8127.696487722216
25	7753.193284872167
26	7538.813217281113
27	7271.955748046577
28	7005.933954787575
29	6879.471233520222
30	6681.650425691401
31	6530.254151561894
32	6402.073841250103
33	5933.036612197096
34	5795.140722718623
35	5759.642314106843
36	5739.586949540019
37	5537.060341085695
38	5407.407306705947
39	5254.262803636035
40	5156.138838420941
41	5042.666281363021
42	4853.747070148629
43	4743.634118791953
44	4477.803560078312
45	4316.491589727906
46	4285.459054844439
47	4097.267995384973
48	3845.372380084961
49	3761.049590864927
50	3789.239050981623
51	3668.855827668128
52	3475.849039333097
53	3305.527480886557
54	3161.823219621322
55	3076.503280925003
56	3178.602782513822
57	2994.626023817358
58	2823.081294731469
59	2705.515121810653
60	2536.845362992661
61	2358.922954073306
62	2222.671550451295
63	2049.112076952238
64	1881.7767738132825
65	1691.0519062298176
66	1510.6404241607065
67	1340.1137279388759
68	1160.8234586874046
69	1016.0285285041903
70	937.8348974748436
71	877.3653163616384
72	763.3492866965365
73	592.0588312042094
74	524.8170774724681
75	478.87318298464845
76	398.16479419251436
77	321.8972630181824
78	202.60576773761688
79	148.34893397652826
80	131.064637499875
81	97.15015915470273
82	41.4694893783247
83	17.685548154962827
84	10.261563339087841
85	1.0298950375955864

Figure E.62 Numerical modeling results for the ridge (8.5 m height, 40 m width, and 65 m length) SMP with 2023 weather function

Pile Number 63

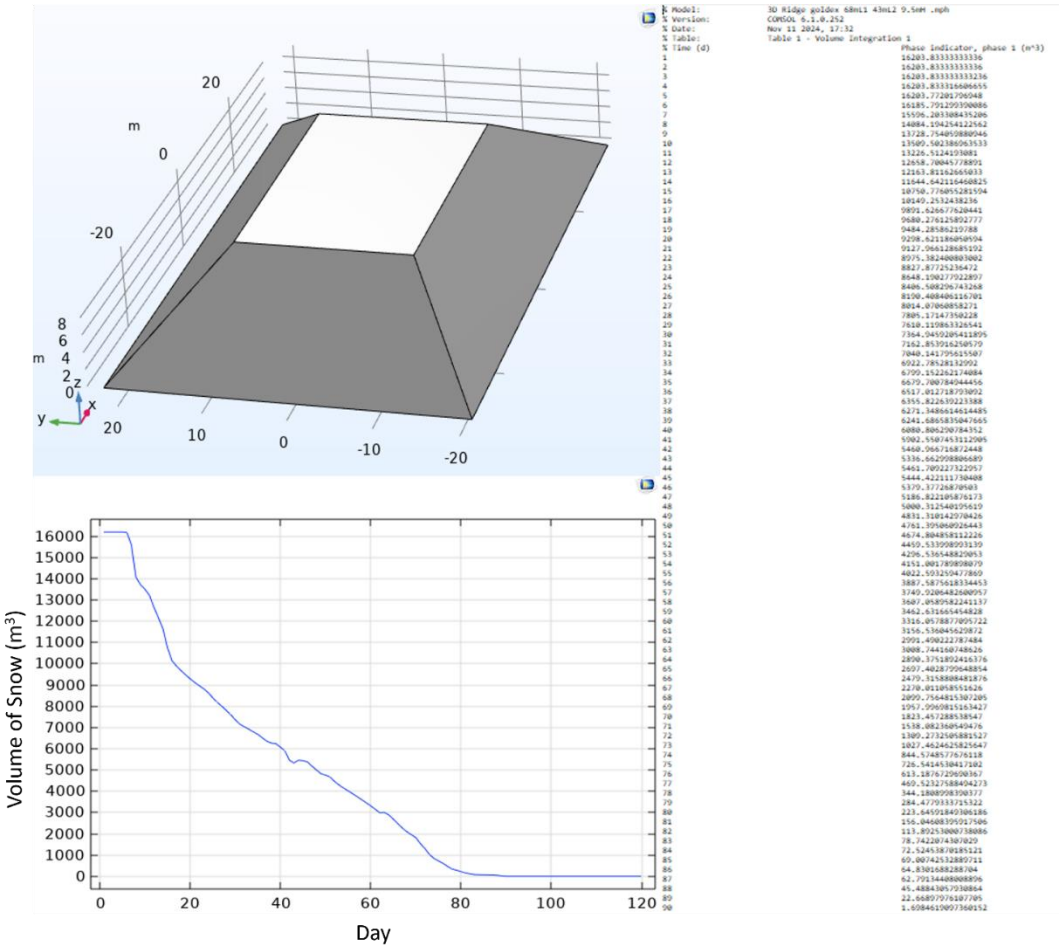

Figure E.63 Numerical modeling results for the ridge (9.5 m height, 43 m width, and 68 m length) SMP with 2023 weather function

Pile Number 64

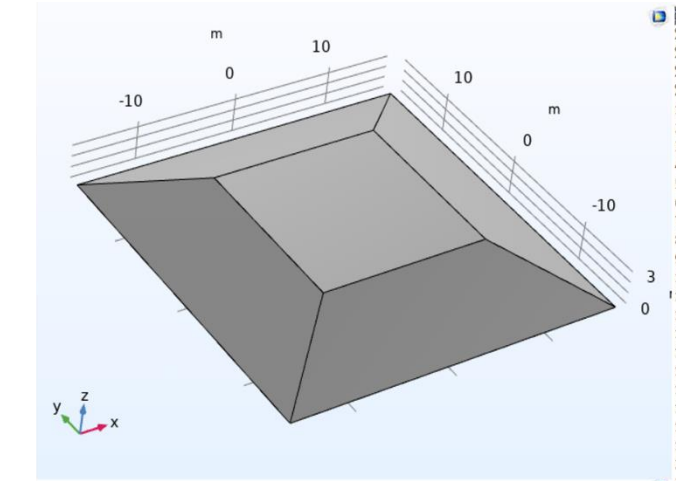

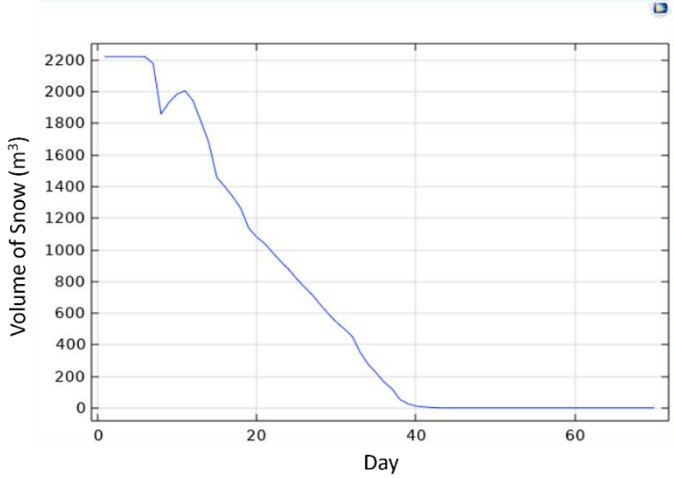

% Model:	3D cubic goldex - Main.mph	
% Version:	COMSOL 6.1.0.252	
% Date:	Nov 11 2024, 18:03	
% Table:	Table 1 - Volume Integration 1	
% Time (d)		Phase indicator, phase 1 (m^3)
1		2223.3749999999995
2		2223.3749999999995
3		2223.374999999973
4		2223.374996392146
5		2223.364672094937
6		2221.9667764006185
7		2180.458683393283
8		1860.0644228776262
9		1933.9784659928705
10		1985.6470000635095
11		2007.5237715588146
12		1944.9392916746938
13		1814.8478443376484
14		1677.5905226492555
15		1459.3969871838538
16		1401.3080177034867
17		1336.921298969327
18		1263.6879193371688
19		1139.2078761031603
20		1081.065927223977
21		1041.6929707773893
22		983.6884341214775
23		928.0206728548603
24		878.4880922709578
25		819.0597446898705
26		765.6966061520861
27		714.8949264102234
28		654.1824289416306
29		596.2478757786747
30		544.066947118139
31		500.15071522369624
32		453.2021195718156
33		352.44154959545597
34		276.5642704574126
35		222.71659070823424
36		163.72212938770662
37		121.76282304052057
38		53.31452910367108
39		26.519628180236133
40		11.647359592364317
41		6.047960440284646
42		2.5286262767755363
43		0.28884951084858757
44		0.010053213712512875

Figure E.64 Numerical modeling results for the cubic (3.5 m height, 33 m width, and 33 m length) SMP with 2023 weather function

Pile Number 65

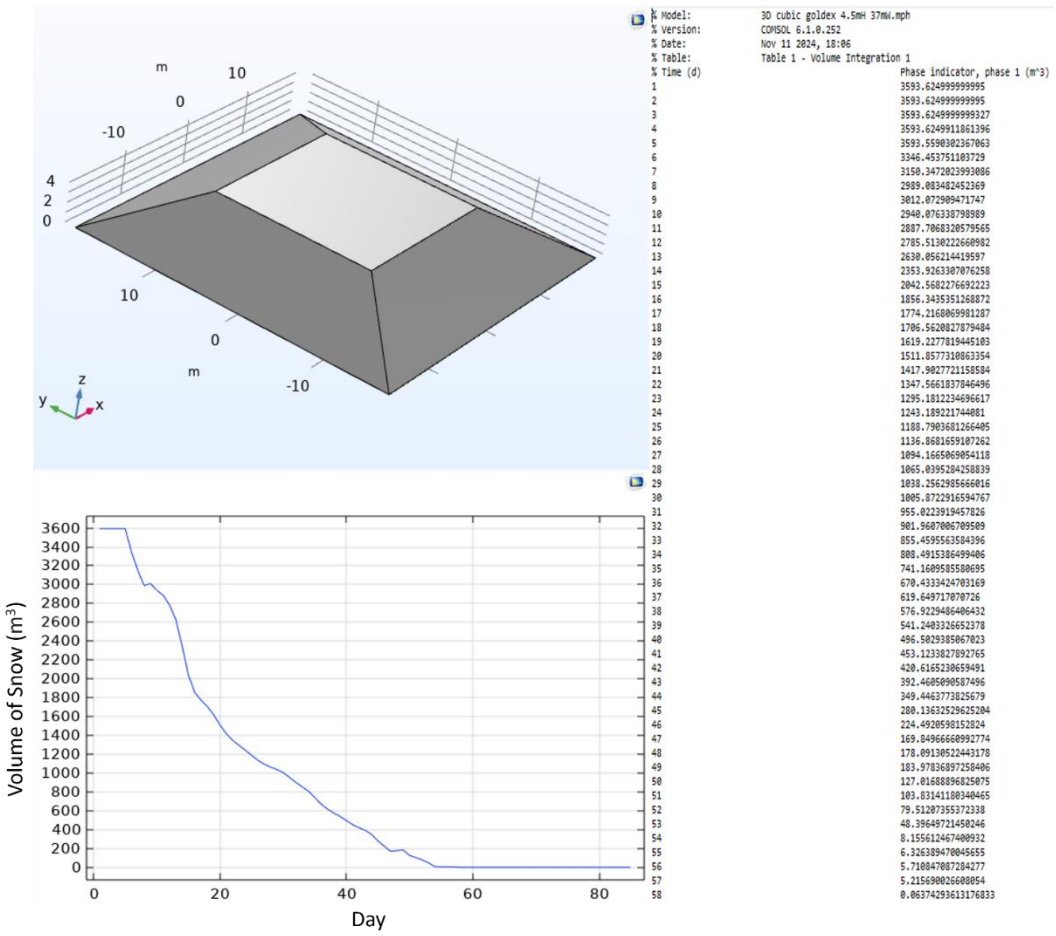


```
% Model:          3D cubic goldex 4.5mH 37mW.mph
% Version:        COMSOL 6.1.0.252
% Date:           Nov 11 2024, 18:06
% Table:          Table 1 - Volume Integration 1
% Time (d)                                Phase indicator, phase 1 (m^3)
1                                         3593.624999999995
2                                         3593.624999999995
3                                         3593.624999999327
4                                         3593.624991861396
5                                         3593.5590302367063
6                                         3346.453751103729
7                                         3150.3472023993086
8                                         2989.083482452369
9                                         3012.072909471747
10                                        2940.076338798989
11                                        2887.7068320579565
12                                        2785.5130222660982
13                                        2630.056214419597
14                                        2353.9263307076258
15                                        2042.5682276692223
16                                        1856.3435351268872
17                                        1774.2168069981287
18                                        1706.5620827879484
19                                        1619.2277819445103
20                                        1511.8577310863354
21                                        1417.9027721158584
22                                        1347.5661837846496
23                                        1295.1812234696617
24                                        1243.189221744081
25                                        1188.7903681266405
26                                        1136.8681659107262
27                                        1094.1665069054118
28                                        1065.0395284258839
29                                        1038.2562985666016
30                                        1005.8722916594767
31                                        955.0223919457826
32                                        901.9607006709509
33                                        855.4595563584396
34                                        808.4915386499406
35                                        741.1609585580695
36                                        670.4333424703169
37                                        619.649717070726
38                                        576.9229486406432
39                                        541.2403326652378
40                                        496.5029385067023
41                                        453.1233827892765
42                                        420.6165230659491
43                                        392.4605090587496
44                                        349.4463773825679
45                                        280.13632529625204
46                                        224.4920598152824
47                                        169.84966660992774
48                                        178.09130522443178
49                                        183.97836897258406
50                                        127.01688896825075
51                                        103.83141180340465
52                                        79.51207355372338
53                                        48.39649721450246
54                                        8.155612467400932
55                                        6.326389470045655
56                                        5.710047087284277
57                                        5.215690026600054
58                                        0.06374293613176833
```

Figure E.65 Numerical modeling results for the cubic (4.5 m height, 37 m width, and 37 m length) SMP with 2023 weather function

Pile Number 66

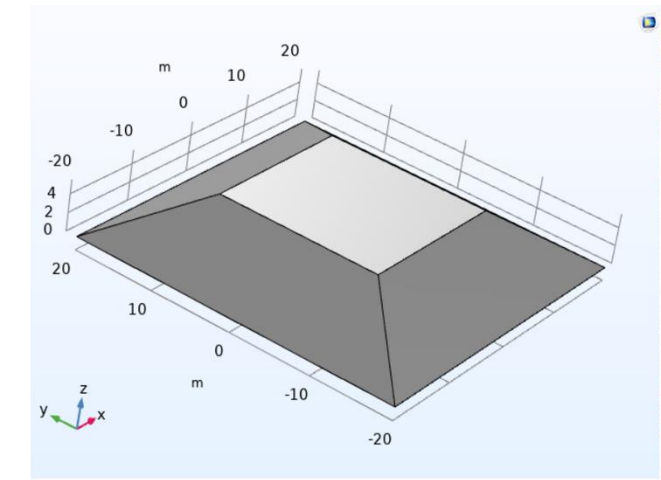

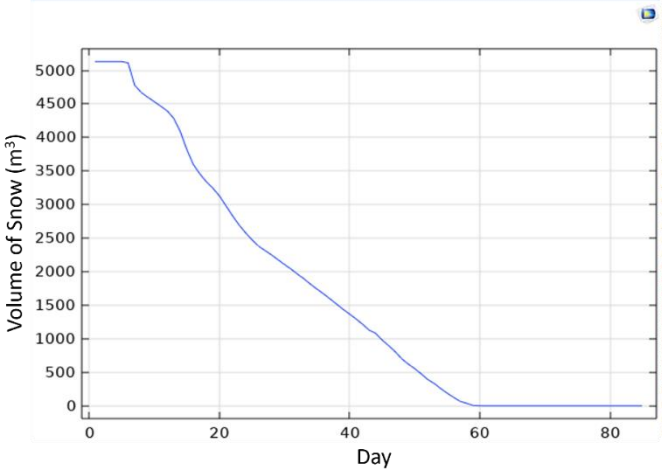


```
% Model:                 3D cubic goldex 5.5mH 40mW.mph
% Version:               COMSOL 6.1.0.252
% Date:                  Nov 11 2024, 18:08
% Table:                 Table 1 - Volume Integration 1
% Time (d)               Phase indicator, phase 1 (m^3)
1                        5133.33333333331
2                        5133.33333333331
3                        5133.333333333267
4                        5133.333327134322
5                        5133.289732988249
6                        5111.967013572903
7                        4780.548661396615
8                        4671.871200318345
9                        4601.898021337939
10                       4535.831646363764
11                       4467.185069646272
12                       4398.14412250988
13                       4286.171181638139
14                       4091.93161356551 63
15                       3824.481944461848
16                       3601.026662781266
17                       3459.761764696223
18                       3343.00183679267 14
19                       3245.83995735951 07
20                       3132.539797169324
21                       2986.451100819477
22                       2838.0040446764 35
23                       2701.77556317825 57
24                       2584.16079796139 55
25                       2478.8084355333 58
26                       2382.47925517902 38
27                       2317.9991337485 88
28                       2251.71724381491 14
29                       2180.332217686173
30                       2108.27311815446 77
31                       2040.73512183939 35
32                       1964.50734090641 87
33                       1895.09530632639 23
34                       1814.96888229419 69
35                       1741.24961785609 78
36                       1670.85683220488 45
37                       1595.921697138523
38                       1518.47792335772 33
39                       1440.89402691909 48
40                       1369.36693234731 82
41                       1296.55150555270 82
42                       1217.92805045412 98
43                       1130.32892239137 48
44                       1082.89548824365 83
45                       981.49409456037 85
46                       899.38759996857 08
47                       810.5345913604 57
48                       703.45748866087 93
49                       625.2797224720 85
50                       556.96206638838 91
51                       478.53405475972 15
52                       394.6801383914 95
53                       334.68668814942 146
54                       258.81528962378 417
55                       189.75151916891 772
56                       126.9749280780 83
57                       67.3541030674184 2
58                       38.6619129875770 2
59                       6.56026928296 1319
60                       1.20385763476748 99
61                       0.06120129815147 077
62                       0.00163941036206 05857
```

Figure E.66 Numerical modeling results for the cubic (5.5 m height, 40 m width, and 40 m length) SMP with 2023 weather function

Pile Number 67

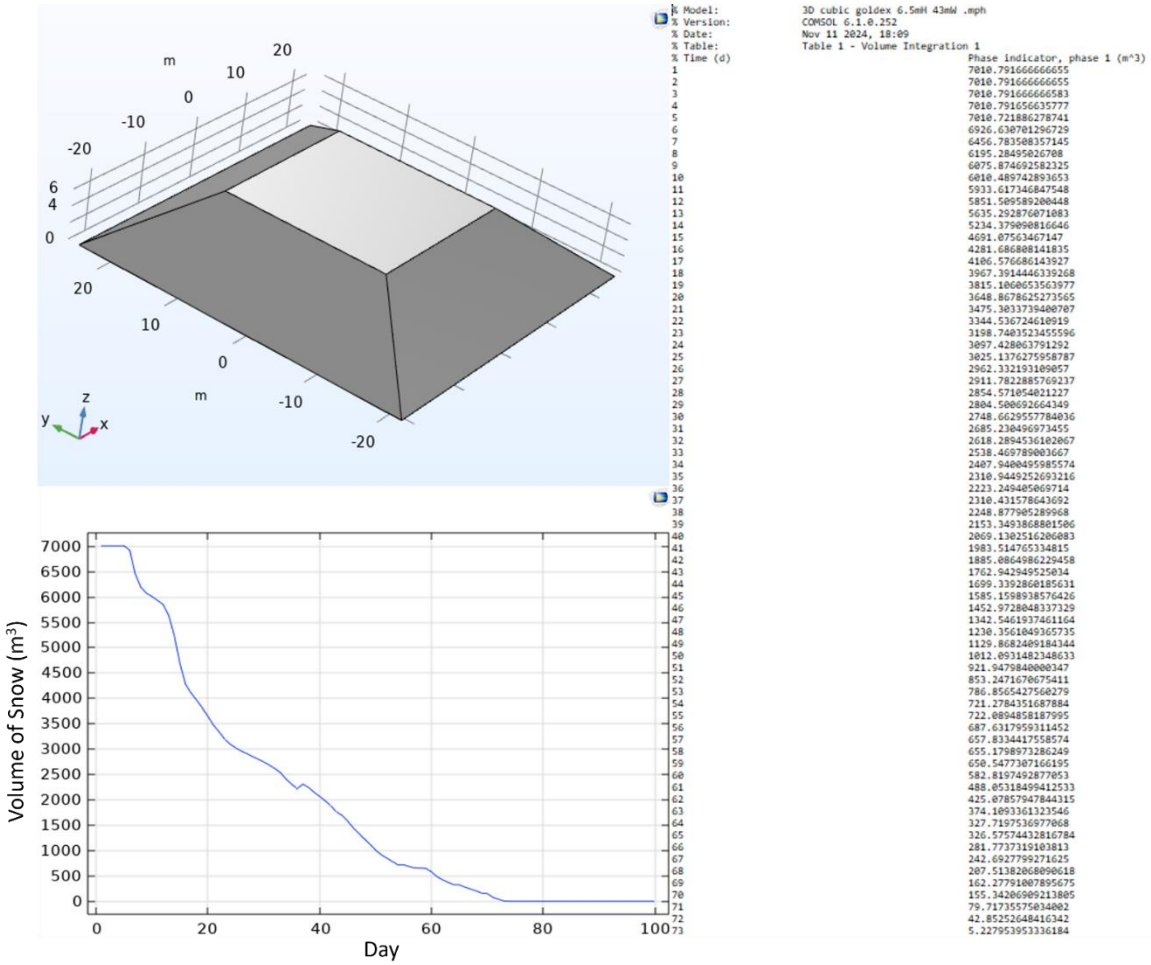


```
% Model:
% Version:
% Date:
% Table:
% Time (d)
1
2
3
4
5
6
7
8
9
10
11
12
13
14
15
16
17
18
19
20
21
22
23
24
25
26
27
28
29
30
31
32
33
34
35
36
37
38
39
40
41
42
43
44
45
46
47
48
49
50
51
52
53
54
55
56
57
58
59
60
61
62
63
64
65
66
67
68
69
70
71
72
73
```

```
3D cubic goldex 6.5mH 43mW .mph
COMSOL 6.1.0.252
Nov 11 2024, 18:09
Table 1 - Volume Integration 1
Phase indicator, phase 1 (m^3)
7010.791666666655
7010.791666666655
7010.791666666583
7010.791656635777
7010.7218862787 41
6926.630701296729
6456.783508357145
6195.28495026708
6075.874692582325
6010.489742893653
5933.617346847548
5851.509589200448
5635.292876071083
5234.379090816646
4691.07563467147
4281.686808141835
4106.576686143927
3967.3914446339268
3815.10606535639 77
3648.8678625273565
3475.303377394007 07
3344.536724610919
3198.7403523455596
3097.4280637912 92
3025.1376275958787
2962.332193109057
2911.7822885769237
2854.5710544021227
2804.500692664349
2748.6629557784036
2685.230496973455
2618.2894536102067
2538.409789003667
2407.9400495985574
2310.9449252693216
2223.249485069714
2310.431578643692
2248.877905289968
2153.3493868801506
2069.130251620 6083
1983.5147653348 15
1885.0864986229458
1762.942949525034
1699.3392860185631
1585.15989385764 26
1452.9728048337329
1342.5461937461164
1230.3561049365735
1129.8682409184344
1012.0931482348633
921.9479840000347
853.2471670675411
786.8565427560279
721.2784351687884
722.0894858187995
687.6317959311452
657.8334417558574
655.1798973286249
650.5477307166195
582.8197492877053
488.05318499412533
425.07857947844315
374.1053361323546
327.7197536977068
326.57574432816784
281.7737319103813
242.6927799271625
207.51382068090618
162.27791007895675
155.34206909213805
79.71735575034002
42.85252648416342
5.227953953336184
```

Figure E.67 Numerical modeling results for the cubic (6.5 m height, 43 m width, and 43 m length) SMP with 2023 weather function

Pile Number 68

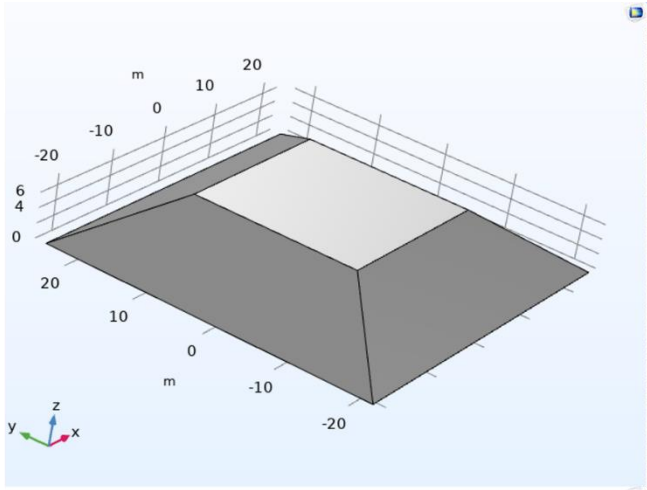

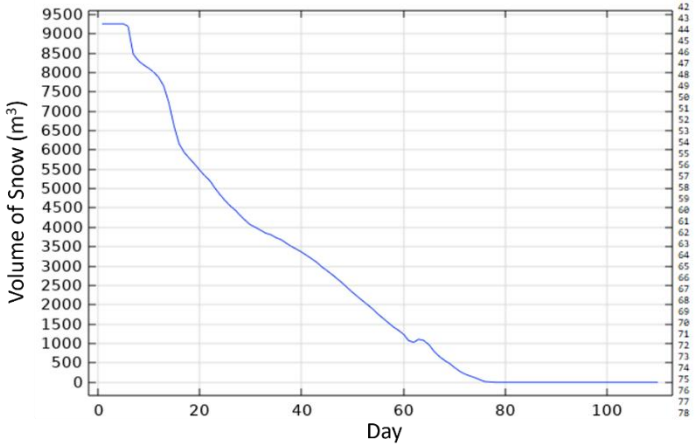


```
% Model:          3D cubic goldex 7.5mH 46mW .mph
% Version:        COMSOL 6.1.0.252
% Date:           Nov 11 2024, 18:13
% Table:          Table 1 - Volume Integration 1
% Time (d)        Phase indicator, phase 1 (m^3)
1                 9257.499999999993
2                 9257.499999999993
3                 9257.499999999858
4                 9257.499988284728
5                 9257.417878729095
6                 9195.30087099979
7                 8480.390101636141
8                 8305.126213160138
9                 8202.22794705446
10                8113.912662471873
11                8016.027966373047
12                7872.943356759776
13                7648.079856637973
14                7217.300401677576
15                6629.452069461267S
16                6161.247603082619
17                5938.64072728807
18                5788.058089976369
19                5643.967761567092
20                5487.026931517681
21                5337.809157871517S
22                5215.521116363471
23                5022.295932062828
24                4852.146338207645
25                4697.258743423728
26                4556.157922189978
27                4452.373538031781
28                4306.528068182937
29                4178.254507732774
30                4067.276070808772S
31                4000.141621066701
32                3927.465485107076
33                3852.258502450206
34                3811.981414785213
35                3736.539320627584
36                3684.304657393289S
37                3595.872006107990S
38                3510.314542636796S
39                3441.374289196819S
40                3365.514511370806S
41                3279.239307632165
42                3192.498449346708S
43                3097.919484471065S
44                2981.467029061512
45                2884.606879739981S
46                2784.284678546170S
47                2674.934662758833
48                2566.139543117772S
49                2443.055379399614
50                2324.787456542604
51                2213.533768447736S
52                2105.673161281936S
53                1999.555471405506S
54                1889.972236808375S
55                1764.246300973786S
56                1654.177289151923S
57                1543.751649922470S
58                1433.283431394049S
59                1344.156244650204S
60                1248.049161974032S
61                1077.842125735914S
62                1034.006209522976S
63                1110.441235447088S
64                1078.558532997645S
65                973.84892253964S7
66                799.861751452626S
67                670.910972293326
68                571.571024784079S
69                490.824389085128
70                385.751510590636S4
71                289.005723394638S7
72                217.626174791124S3
73                166.581538025549S3
74                121.688739723433S5
75                64.563543381204S1
76                20.292812667200S3
77                12.621923834801S7
78                0.745828757642808S
```

Figure E.68 Numerical modeling results for the cubic (7.5 m height, 46 m width, and 46 m length) SMP with 2023 weather functio

Pile Number 69

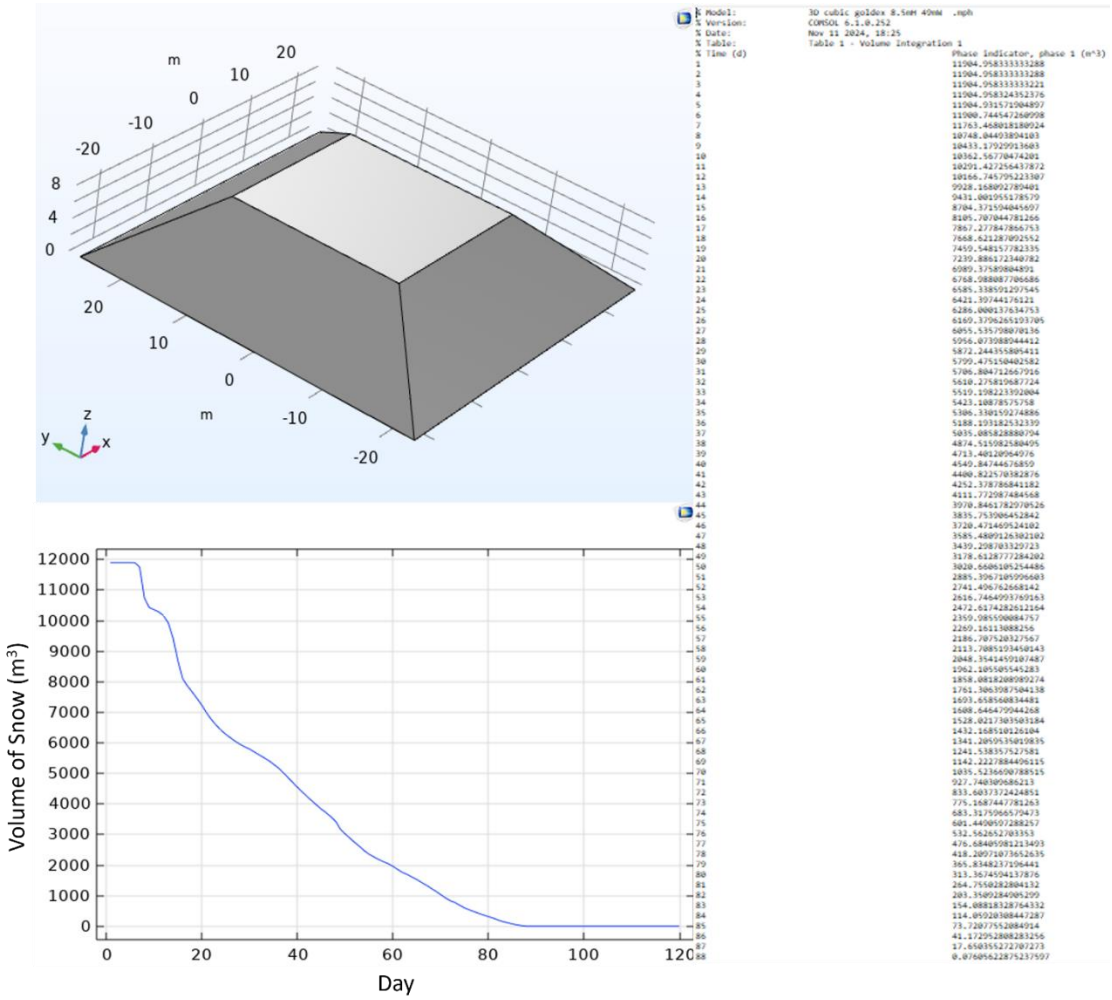

Figure E.69 Numerical modeling results for the cubic (8.5 m height, 49 m width, and 49 m length) SMP with 2023 weather function

Pile Number 70

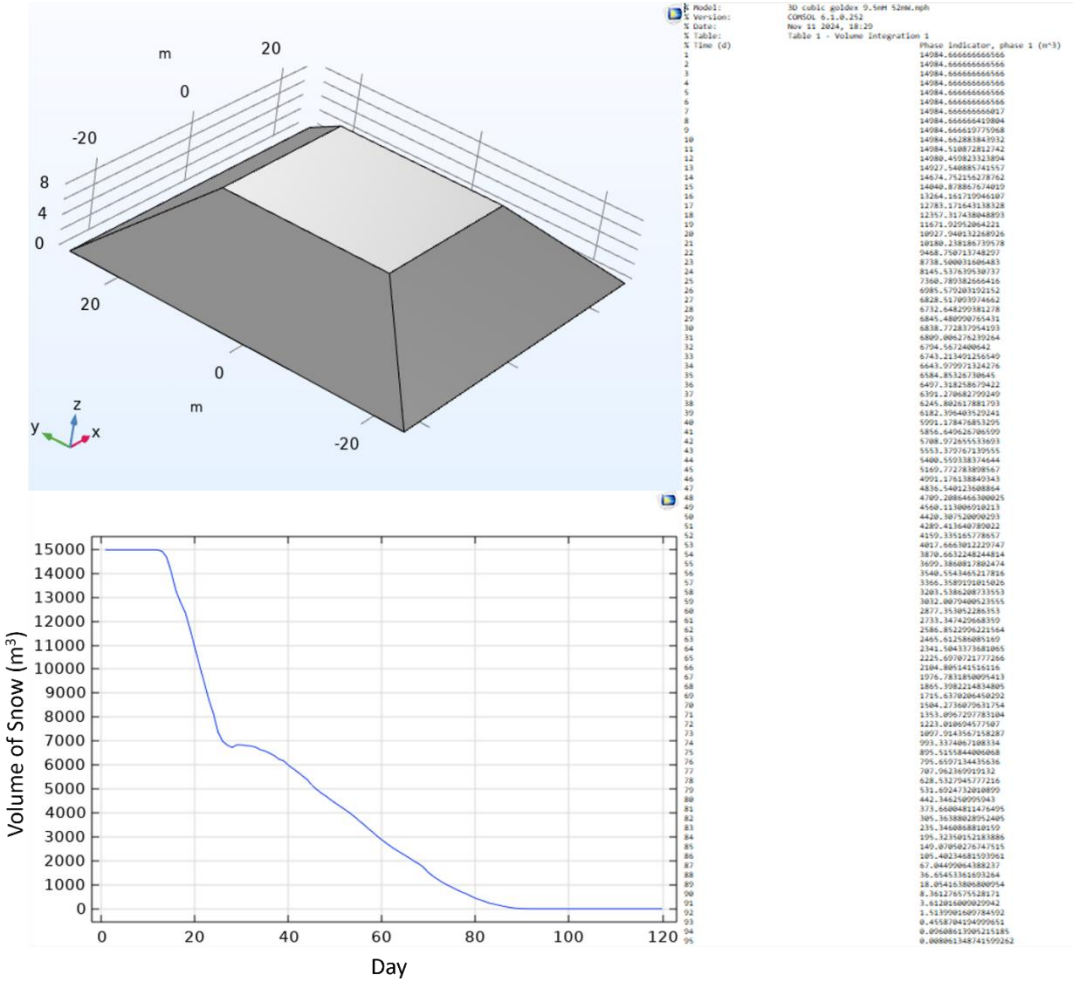

Figure E.70 Numerical modeling results for the cubic (9.5 m height, 52 m width, and 52 m length) SMP with 2023 weather function